DEPARTMENT OF GEOSCIENCES AND GEOGRAPHY A81

From partial melting to lava emplacement: the petrogenesis of some Icelandic basalts

PAAVO NIKKOLA

UNIVERSITY OF HELSINKI
FACULTY OF SCIENCE

UNIVERSITY OF ICELAND

From partial melting to lava emplacement: the petrogenesis of some Icelandic basalts

PAAVO NIKKOLA

ACADEMIC DISSERTATION
To be presented, with the permission of the Faculty of Science of the University of Helsinki and the Faculty of Earth Sciences of the University of Iceland, for public examination in auditorium E204, Physicum, Kumpula, on 20th of March 2020, at 12 noon.

This doctoral dissertation is a co-operation between the University of Helsinki and the University of Iceland and will lead to a dual degree from these universities.

DEPARTMENT OF GEOSCIENCES AND GEOGRAPHY A81/ HELSINKI 2020

Cover photo: Paavo Nikkola
Back cover photo: Elísabet Pálmadóttir

Faculty of Science, University of Helsinki
Faculty of Earth Sciences, University of Iceland

Author´s address: Paavo Nikkola
Department of Geosciences and Geography
P.O.Box 64
00014 University of Helsinki
Finland
paavo.nikkola@helsinki.fi

Supervised by: Professor O. Tapani Rämö
Department of Geosciences and Geography
University of Helsinki

Professor Thorvaldur Thordarsson
Faculty of Earth Sciences
University of Iceland

Reviewed by: Professor Christian Tegner
Department of Geoscience
Aarhus University

Professor emeritus Eero Hanski
Oulu Mining School
University of Oulu

Opponent: Professor Reidar G. Trønnes
Natural History Museum, Centre for Earth Evolution and Dynamics
University of Oslo

ISSN 1798-7911
ISBN 978-951-51-4930-5 (paperback)
ISBN 978-951-51-4931-2 (PDF)
http://ethesis.helsinki.fi
Painosalama/Turku 2020

Nikkola P., 2020. *From partial melting to lava emplacement: the petrogenesis of some Icelandic basalts.* Painosalama, Turku, 47 pages, 6 figures.

Abstract

This thesis provides insights into the petrogenesis of Iceland basalts via three subprojects. The first uses olivine macrocrysts as a proxy for mantle melting conditions below Iceland, the second utilizes petrological thermobarometry to resolve the crustal storage conditions of the most primitive basaltic rocks (ankaramites) of the Eyjafjallajökull volcano, and the third investigates basalt fractionation processes within the Hafnarhraun pāhoehoe lava lobe.

The sub-Icelandic mantle is evidently heterogeneous in composition. Yet olivine major and minor element compositions in Iceland basalts typically concur with common mantle lherzolite as the source of magmas, with the only potential exceptions being the basalts of Eyjafjallajökull and Vestmannaeyjar volcanic systems in South Iceland. These South Iceland basalts have forsterite-rich olivine with relatively high Ni and low Mn contents, together with low Sc and V and high Cr, Ti, Zn, Cu and Li contents. Elevated Ni and low Mn in olivine have been attributed to olivine-free pyroxenitic mantle source; however, the South Iceland olivine compositions are best explained by the effect of comparatively high-pressure (P_{final}>1.4 GPa) and high-temperature melting of somewhat enriched olivine-bearing mantle. I conclude this because (i) elevated Ni and low Mn in olivine can also indicate deep, high-temperature, mantle melting, (ii) the abundances of Sc, V, Ti and Zn in the South Iceland olivine are compatible with low-degree partial melts of olivine-rich mantle, and (iii) melts of olivine-free pyroxenite are, according to recent models, easily consumed in reactions with subsolidus mantle peridotite and thus unlikely to migrate to the crust and crystallize olivine. The identified high-Ni/low-Mn olivine macrocrysts suggest final mantle equilibration depths greater than 45 km for South Iceland magmas, and imply effective mantle-to-surface magma transport.

Two Eyjafjallajökull ankaramite outcrops (Hvammsmúli and Brattaskjól), rich in olivine ($Fo_{81–90}$) and clinopyroxene ($Mg\#^{cpx}$ 78–90) macrocrysts (~30 vol%) in near equal amounts, have a specifically prominent "deep mantle source signature" (high-Ni/low-Mn) in olivine. To investigate the crustal storage conditions of these and other Eyjafjallajökull basaltic magmas, I analyzed olivine, clinopyroxene, spinel and melt inclusion compositions from these volcanic units. These analyzes revealed that the olivine-hosted spinel inclusions have exceptionally high $Cr\#^{spl}$ (52–80) and TiO_2 (1–3 wt%) and low Al_2O_3 (8–22 wt%) compared to typical chromian spinels in Iceland, in line with the postulated deep and enriched mantle source of the parental magmas. According to olivine-spinel oxybarometry, these spinels crystallized under a moderate oxygen fugacity (ΔlogFMQ 0–0.5). Furthermore, jadeite-in-clinopyroxene barometry indicates clinopyroxene crystallization at a rather low pressure (1.7–4.2 kbar; external precision ±1.4 kbar), implying a magma storage depth of 10.7±5 km. Additionally, clinopyroxe-liquid, olivine-liquid and liquid only thermometry gives varying crystallization temperatures of 1120–1195 °C, 1136–1213 °C and 1155–1222 °C, respectively, for

the compositionally diverse macrocrysts. The scarcity of macrocryst plagioclase and trends in clinopyroxene compositions indicate that the mid-crustal crystallizing assemblage was olivine and clinopyroxene, and plagioclase fractionated later. Diffusive re-equilibration in Brattaskjól olivine grains suggests that this crystal assemblage mobilized and erupted from its storage within a few weeks. To conclude, the Brattaskjól and Hvammsmúli crystal cargoes are agitated wehrlitic or plagioclase-wehrlitic mushes from the mid-crust that ascended to the surface relatively rapidly.

Basaltic lavas are practically never primitive mantle melts owing to fractional crystallization in the crust, which, at low pressure, may be aided by volatile exsolution. Deciphering magma fractionation processes from solidified crustal intrusions is hampered by their often complex emplacement history. The emplacement of pāhoehoe lavas, however, is simpler and well understood, and hence I investigated the mechanisms of basalt fractionation from a differentiated pāhoehoe lava lobe in Hafnarhraun lava flow field. Here, volatile exsolution had facilitated separation of basaltic residual melts to form three types of melt segregations: vesicle cylinders (VC) in the core of the lobe and two types of horizontal vesicle sheets (HVS1 and HVS2) in the upper part of the lobe. Interestingly, the VC do not match chemically with the modelled residual melts of the lobe, and their formation seems to have included two stages: volatile-aided melt separation from crystallizing base of the lobe and later contamination by primitive macro- and microphenocrysts in the lava core. HVS1, which resemble VC, were formed as the ascending VC diapirs accumulated to the upper solidification front of the lava lobe. HVS2, in turn, are distinctly evolved in compositions compared to other units in the lobe and were formed as highly fractionated residual melts seeped to voids in the upper crust of the lobe. Processes analogous to segregation formation at Hafnarhraun may contribute to genesis of evolved basalts and silicic rocks in shallow magmatic systems.

Overall, my work highlights the exceptional nature of South Iceland among other volcanically active regions in Iceland. Furthermore, analyses of the Hafnarhraun pāhoehoe lava reveal the processes of melt segregation formation in pāhoehoe lava lobes. I hope future research will expand on these findings, further resolving the nature of mantle melting below South Iceland and the significance of volatile-aided processes in crustal magma differentiation.

Tiivistelmä

Tämä väitöskirja käsittelee Islannin basalttisten laavojen syntyä ja kehitystä. Väitöskirjan ensimmäisessä osassa käytän laavoissa esiintyvien oliviinihajarakeiden koostumuksia Islannin alaisen maapallon vaipan sulamisolosuhteiden indikaattorina, toisessa selvitän Eyjafjallajökull-tulivuoren ankaramiitti-laavojen purkautumista edeltäviä säilytysolosuhteita maankuoressa, ja kolmannessa tutkin pāhoehoe-laavan fraktioitumisprosesseja Hafnarhraun-laavakentällä.

Maapallon vaippa Islannin alla on todennäköisesti koostumukseltaan vaihteleva. Tästä huolimatta oliviinihajarakeiden koostumus Islannin basalteissa on tyypillisesti yhtenevä vain lherzoliittisen magmojen vaippalähteen kanssa. Tähän ainoa poikkeus ovat eteläisen Islannin Eyjafjallajökull- ja Vestmannaeyjar-tulivuorten laavoissa esiintyvät oliviinihajarakeet, joissa on korkea nikkeli- ja matala mangaanipitoisuus, mutta myös alhainen skandium ja vanadium, sekä korkea kromi, titaani, sinkki, kupari ja litium. Vaikka oliviinin korkea nikkeli- ja matala mangaanipitoisuus voidaan nähdä oliviinista köyhän pyrokseniittiseen vaipan indikaattorina, eteläisen Islannin poikkeavat oliviinikoostumukset selittyvät parhaiten vaipan syvällä sulamisella korkeassa lämpötilassa. Esitän näin sillä (i) korkea nikkeli ja matala mangaani oliviinissa voi olla myös seurausta vaipan korkeasta sulamislämpötilasta, (ii) Sc-, V-, Ti- ja Zn-pitoisuudet eteläisen Islannin oliviinihajarakeissa viittaavat oliviinirikkaaseen vaipan lähteeseen, ja (iii) uusimpien vaipan sulamisen mallien mukaan pyrokseniittivaipan sulat reagoivat helposti ympäröivän lherzoliittivaipan kanssa ja näin ne tuskin säilyvät muuttumattomina noustessaan kohti maapallon kuorta. Löydetyt korkean nikkelin ja matalan mangaanin oliviinihajarakeet viittaavat siihen, että eteläisen Islannin magmat tasapainottuvat vaipan lähteen kanssa yli 45 km syvyydessä ja nousevat tämän jälkeen tehokkaasti litosfäärin läpi.

Erityisen voimakas syvän vaipan sulamisen signaali (korkea nikkeli ja matala mangaani oliviinissa) havaittiin kahdesta ankaramiitti-laavasta (Hvammsmúli ja Brattaskjól) Eyjafjallajökull-tulivuoren rinteiltä. Selvittääkseni näiden laavojen purkautumista edeltävät säilytysolosuhteet maankuoressa, analysoin niistä oliviini-, klinopyrokseeni-, spinelli- ja sulasulkeumakoostumuksia. Havaitsin, että oliviinihajarakeiden spinellisulkeumilla on poikkeuksellisen korkea $Cr\#^{spl}$ (52–80) ja TiO_2 (1–3 m–%) sekä matala Al_2O_3 (8–22 m–%) verrattuna Islannista aiemmin analysoituihin Cr-spinelleihin, mikä on yhtenevää näiden ankaramiittien oletetun syvän ja rikastuneen vaippalähteen kanssa. Oliviini-spinelli oxybarometrian mukaan spinellit kiteytyivät hapen fugasiteetin ollessa ΔlogFMQ 0–0,5. Klinopyrokseenin jadeiittipitoisuuteen perustuva barometria puolestaan indikoi verrattain matalaa (1,7–4,2 kbar; metodin tarkkuus ±1,4 kbar) klinopyrokseenien kiteytymispainetta, mikä vastaa 10,7±5 km syvyyttä maapallon kuoressa. Klinopyrokseenin, oliviinin ja sulan koostumukseen perustuvat termometrit antavat hajarakeille vaihtelevia kiteytymislämpötiloja: 1120–1195 °C, 1136–1213 °C ja 1155–1222 °C. Hajarae plagioklaasin harvinaisuus ja klinopyrokseenihajarakeiden koostumuksellinen vaihtelu osoittavat, että keskikuoressa kiteytyvä mineraaliseurue koostui oliviinista ja klinopyrokseenista, ja plagioklaasi kiteytyi magmoista myöhemmin. Näin ollen tutkittujen ankaramiittien hajarakeet ovat luultavasti peräisin keskikuoren wehrliittisistä tai plagioklaasi-wehrliittisistä kidepuuroista.

Näihin kidepuuroihin tunkeutuvat magmat nostattivat hajarakeet muutaman viikon sisällä maanpintaan, mikä voidaan arvioida diffusiivisen tasapainottumisen määrästä Brattaskjól-ankaramiitin oliviinihajarakeiden vyöhykkeellisyydessä.

Pintaan purkautuvat basalttiset laavat eivät käytännössä koskaan enää edusta vaipan sulia, sillä fraktioiva kiteytyminen on muuttanut niiden koostumusta niiden noustessa maankuoren läpi. Magman fraktioitumisprosessien tutkiminen maankuoren plutoneista on haastavaa niiden usein monimutkaisen muodostumishistorian vuoksi. Pāhoehoe-laavojen asettuminen on yksinkertaisempaa ja näin ollen tutkin basalttisen magma fraktioitumisprosesseja pāhoehoe-laavapatjasta Hafnarhraun-laavakentällä. Tutkitussa laavassa volatiilien erottuminen magmasta oli edesauttanut jäännössulien erottumista ja muodostanut kolmen tyyppisiä segregaatiosulia laavan sisään: rakkulapiippuja (VC) pāhoehoe-laavan ytimeen ja kahden tyyppisiä horisontaalisia rakkulapatjoja (HVS1 ja HVS2) laavapatjan yläosiin. VC koostumukset eivät vastannut laavan mallinnutettuja jäännössulia, mutta ne voitiin selittää kaksivaiheisella syntyhistorialla, jossa VC ensin erottuvat volatiiliavusteisesti isäntämagmasta laavan pohjaosissa ja tämän jälkeen niihin kertyy oliviini- ja plagioklaasikiteitä laavapatjan keskiosissa. HVS1 muodostuivat, kun nousevat VC levittäytyivät laavan kiteytyvän yläkuoren alapintaa vasten, ja HVS2 ovat pitkälle fraktioituneita isäntälaavan jäännösulia, joita tihkui laavan yläkuoreen muodostuneisiin aukkoihin ja rakoihin. Hafnarhraun pāhoehoe-laavan segregaatiosulien erottumista muistuttavat prosessit saattavat johtaa kehittyneiden basalttisten magmojen muodostumiseen maanpinnan läheisissä magmasäiliöissä.

Väitöskirjatutkimuksessani paljastui eteläisen Islannin ainutlaatuisuus verrattuna Islannin muihin magmaattisesti aktiivisiin alueisiin. Tämän lisäksi Hafnarhraun pāhoehoe laava osoitti volatiilien merkityksen sulasegregaatioiden synnyssä. Toivon, että löydöksieni päälle rakennetaan uutta tutkimusta, joka vie ymmärrystämme eteenpäin selvittäen eteläisen Islannin magmojen vaippalähteen luonnetta ja volatiilien merkitystä magmojen fraktioitumisessa.

Ágrip

Í þessari ritgerð er ljósi varpað á uppruna basaltkviku á Íslandi með þremur rannsóknarþemum. Í fyrsta þemanu er snefilefnainnihald ólívíndíla notað til að skýra hvaða skilyrði ríkja við hlutbræðslu möttulsins undir Íslandi. Í öðru þemanu er stuðst við jarðefnafræðilega hita- og þrýstimæla til þess að meta eiginleika kvikuhólfa/-þróa sem innihalda frumstæða basaltkviku (þ.e. ankaramít) í skorpunni undir Eyjafjallajökli. Þriðja þemað varðar þróunarferli basaltbráðar í helluhraunssepa í Hafnarhrauni við Þorlákshöfn.

Möttulinn undir Íslandi er að samsetningu misleitur. Samt samræmist aðal- og snefilefnasamsetning ólívíndíla í íslensku basalti kviku sem á uppruna sinn að rekja til hlutbræðslu á venjulegum lherzólítmöttli. Hugsanleg undantekning frá þessari reglu er basaltkvikan sem kemur upp í eldstöðvakerfunum Eyjafjallajökli og Vestmannaeyjum, sem innihalda mjög forsterítríka ólívíndíla með tiltölulega háan Ni-styrk og lágan Mn-styrk, ásamt lágum styrk Sc og V og háum styrk Cr, Ti, Zn, Cu og Li. Þrátt fyrir að hár Ni-styrkur og lágur Mn-styrkur í frumstæðum ólívíndílum sé gjarnan rakinn til kviku sem myndast við hlutbráðnun á ólívínlausum pyroxenítmöttli, þá er samsetning umræddra ólívíndíla best skýrð með háhitabráðnun á auðguðum, ólívínríkum perídótítmöttli við háan þrýsting (P_{final} > 1,4 GPa). Ég dreg þessa ályktun vegna þess að (i) hár Ni-styrkur og lágur Mn-styrkur í ólívíni samræmist einnig bráðnun við háan hita djúpt í möttlinum, (ii) tiltölulega hár styrkur Sc, V, Ti og Zn í ólívíndílunum er í samræmi við litla hlutbráðnun á ólívínríkum möttli, og (iii) samkvæmt nýjustu líkönum hvarfast pýroxenítbráð auðveldlega við möttulperidótít og því ólíklegt að slík bráð komist upp í jarðskorpuna og kristalli ólívín. Þessi hái styrkur Ni og lágur styrkur Mn í ólívíndílunum bendir til þess að kvikan hafi síðast verið í jafnvægi við möttulefnið á meira en 45 km dýpi og að kvikan hafi flust hratt frá möttli til yfirborðs.

Tvær ankaramítmyndanir í Eyjafjöllum, Hvammsmúli og Brattaskjól, sem auðugar eru af ólívíndílum ($Fo_{81–90}$) og klínópýroxendílum ($Mg\#^{cpx}$ 78–90) (~ 30%), nokkurn veginn í sama magni, sýna merki um uppruna djúpt í möttlinum, þ.e. hátt Ni-magn / lágt Mn-magn í ólívíndílunum. Efnasamsetning ólívíns, klínópýroxens, spínils og bráðarinnlyksna var greind í sýnum frá þessum myndunum til þess að meta dýpi kvikuþróa þar sem þessar kvikur safnast fyrir í skorpunni fyrir gos. Þessar greiningar sýna að spínilkristallarnir, sem eru til staðar sem innlyksur í ólívíndílum, hafa óvenju hátt $Cr\#^{spl}$ (52–80) og mikið af TiO_2 (1–3 þ.%) og lítið af Al_2O_3 (8–22 þ.%) í samanburði við dæmigerða krómspínla í íslensku basalti. Þetta er í takt við ályktunina um djúpstæðan uppruna móðurkvikunnar frá auðguðum möttli. Samkvæmt ólívín-spínil súrefnisþrýstingsmælinum kristölluðust þessir spínlar við hóflegan súrefnisstyrk (ΔlogFMQ 0–0,5). Jafnframt bendir þrýstimælir sem byggir á magni jaðeitþáttar í klínópýroxeni til að kristöllun klínópýroxens hafi átt sér stað við frekar lágan þrýsting (1,7–4,2 ± 1,4 kbar), sem gefur til kynna 10,7 ± 5 km dýpi fyrir kvikuþróna. Að auki gefa hitamælar fyrir klínópýroxen-gler, ólívín-gler og gler eingöngu mismunandi kristöllunarhitastig fyrir hinar mismundi gerðir fasa, nefnilega 1120–1195 °C, 1136–1213 °C og 1155–1222 °C. Lítið magn plagíóklasdíla ásamt samsetningu klínópýroxendílanna bendir til þess að þessar kvikur hafi kristallað ólívín og klínópýroxen í kvikuþrónni og myndun plagíóklasdíla hafist síðar. Líkanreikningar á efnasveimi í ólívíni frá Brattaskjóli bendir til að þessi dílafarmur hafi farið að stað úr geymslurýminu og borist til yfirborðs í eldgosi innan nokkurra vikna. Niðurstaðan er að dílafarmurinn í Brattaskjóli

og Hvammsmúla sé að uppruna kristalríkur massi í miðskorpunni með steindafylki wehrlíts eða plagíóklas-wehrlíts sem reis tiltölulega hratt til yfirborðs.

Basalthraun eru nær aldrei með sömu samsetningu og frumstæðar möttulbráðir vegna hlutkristöllunar sem á sér stað í jarðskorpunni, en hlutkristöllunin getur við lágan þrýsting orðið fyrir áhrifum af aðskilnaði gastegunda. Erfitt getur verið að greina áhrif þróunarferla í kviku með því að skoða storknuð innskot vegna flókinnar sögu þeirra oft á tíðum. Hins vegar er myndun helluhrauna vel skilin og hef ég því rannsakað kvikuþróunarferli basalts með því að skoða þróaðan helluhraunssepa í Hafnarhrauni. Í þessu tilfelli átti aðskilnaður gass þátt í aðskilnaði afgangsbráðar með samsetningu basalts. Bráðaraðskilnaðurinn var af þrennu tagi: blöðrusívalningar (VC) í kjarna hraunsepans og tvær gerðir láréttra blöðrulaga (HVS1 og HVS2) í efri hluta sepans. Áhugavert er að efnasamsetning VC fellur ekki að líkanreikningum fyrir sepann og myndun þeirra virðist hafa orðið í tveimur þrepum: bráðaraðskilnaður með hjálp gass í botni sepans þar sem kristöllun átti sér stað og síðar mengun af frumstæðum stór- og smádílum í kjarna hraunsins. HVS1 líkjast VC og mynduðust þegar VC-sívalningar risu og söfnuðust fyrir á storknunarmörkum hraunsepans. Hins vegar eru HVS2 greinilega þróaðir í samanburði við hinar gerðirnar í sepanum og mynduðust við að mjög þróaðar afgangsbráðir seytluðu í holrými í efri skorpu sepans. Ferli lík þeim sem mynduðu afgangsbráðirnar í Hafnarhrauni gætu komið við sögu við myndun þróaðs basalt og súrs bergs í grunnstæðum kvikukerfum.

Heilt yfir litið þá sýna rannsóknir mínar hversu einstakt Suðurgosbeltið er meðal virkra gosbelta á Íslandi. Þá hafa rannsóknirnar á Hafnarhrauni leitt í ljós ferli bráðaraðskilnaðar í helluhraunssepum. Ég vona að framtíðarrannsóknir muni byggja á þessum uppgötvunum og leiða til betri skilnings á eðli möttulbráðnunar undir Suðurlandi og því hversu mikilvægt gas er fyrir kvikuþróunarferli í skorpunni.

Acknowledgements

I want to thank my supervisors Thorvaldur (Thor) Thordarsson and Tapani Rämö. Thor kindly took me under his wing when I decided to start a PhD in Iceland. He encouraged me to start on this path and supported me through thick and thin. Tapani, in turn, was invaluable for finishing this project with his deadlines and tireless supervision, especially during the last two years. Tapani was also the first, already eons ago, who got me interested in igneous petrology.

Secondly, my life-long gratitude goes to Enikő Bali and Guðmundur H. Guðfinnsson who contributed immensely to two of my thesis manuscripts and helped me back on track when my thesis topic changed in 2016. Without their help and vision, my thesis would not be as it is today, and I may have never become obsessed over olivine macrocrysts.

Furthermore, I thank my co-authors Tobias Fusswinkel, Maren Kahl, Quinten van der Meer and Pasi Heikkilä who helped me during these years. My gratitude also goes to the following, who aided me on the thesis research: Jussi Heinonen, Sanni Turunen, Sæmundur Ari Halldórsson, Matthew Pankhurst, David Neave, Leó Kristjánsson, Atli Hjartarson, Robert Askew and Maja Bar Rasmussen.

Then I want to mention Rikke Pedersen who was the boss during my years working for the Nordic Volcanological Center. She was there when needed.

Others were there also, and as they hang around long enough, they became friends. In fact, friends are likely the best thing I got from this endeavor they call a PhD. It boggles my mind how many good moments we have shared. I kid you not, once a lava tornado nearly roasted some of us. As listing you all by name would be too wordy, I announce the following: greatest thanks to the First-response team Holuhraun, Petrosquad, Vesturbæjarlaug swimmers, Da running club, Flóki and Folda, and Room 227.

This work would have not been possible without the support of my family: the one in Alavus, the one in Njarðvík, and the one in Espoo. This thesis is dedicated to Gadidjah and Aaron.

Contents

List of original publications

This thesis is based on the following publications:

I Nikkola P., Guðfinnsson G.H., Bali E., Rämö O.T., Fusswinkel T., Thordarson T. 2019. Signature of deep mantle melting in South Iceland olivine. Contributions to Mineralogy and Petrology 174:43.

II Nikkola P., Bali E., Kahl M., Quinten H. A. van der Meer, Rämö O.T., Guðfinnsson G.H., Thordarson T. 2019. Mid-crustal storage and crystallization of Eyjafjallajökull ankaramites, South Iceland. Jökull 69:77–96.

III Nikkola P., Thordarson T., Rämö O.T., Heikkilä P. 2019. Formation of segregation structures in Hafnarhraun pāhoehoe lobe, SW Iceland: a window into crystal–melt separation in basaltic magma. Bulletin of Volcanology 81:70.

The publications are referred to in the text by their roman numerals.

Author's contribution to the publications

I The original idea for the research came from EB and GHG. Collection of the samples was done by PN, EB and GHG. PN conducted all microanalyses and related laboratory work with the guidance of GHG and TF. PN is fully responsible for all geochemical modelling and he wrote the manuscript with contributions from the co-authors.

II PN, EB, MK and GHG planned the study. PN and QM did the microanalyses of mineral compositions, EB performed the melt inclusion experiments and analyses, and MK conducted the EBSD analyses of olivine crystallographic orientation. PN did the thermobarometric and diffusion modelling and wrote the manuscript with input from the co-authors.

III The idea of the study came from TT and was developed by PN. PN is fully responsible of all fieldwork, sampling, geochemical modelling and interpretations. He conducted all microanalyses of mineral phases and performed the whole rock analyses with the guidance of PH. PN wrote the manuscript with input from the co-authors.

Abbreviations

An	anorthite
CaTs	calcium Tschermak component
cf.	*confer*
$Cr\#^{spl}$	chromium number in spinel
D	distribution coefficient
DiHd	diopside hedenbergite
EBSD	electron backscatter diffraction
ED	energy dispersive
EnFs	enstatite ferrosilite
EPMA	electron probe microanalyzer
EVZ	Eastern Volcanic Zone
e.g.	*exempli gratia*
F	degree of partial melting
Fo	forsterite
fO_2	oxygen fugacity
G	Gibb's free energy
HVS	horizontal vesicle sheets
i.e.	*id est*
ICP–MS	inductively coupled plasma mass spectrometer
Jd	jadeite
KDE	kernel density estimation
$Kd^{Mg–Fe}$(cpx–liq)	Mg/Fe exchange coefficient between clinopyroxene and melt
LAB	lithosphere-asthenosphere boundary
LA–ICP–MS	laser ablation inductively coupled plasma mass spectrometry
LLD	liquid line of decent
Ma	million years (mega-annum) before present
$Mg\#^{cpx}$	magnesium number of clinopyroxene
$Mg\#^{liquid}$	magnesium number of liquid
Moho	Mohorovičić discontinuity
MORB	mid-ocean ridge basalt
MIB	Mid-Iceland Belt
NVZ	Northern Volcanic Zone
OIB	ocean island basalt
ÖVZ	Öræfajökull Volcanic Zone
P	pressure
ppm	parts per million
RVZ	Reykjanes Volcanic Zone
SEM	secondary electron microscope

SEVZ	Southern tip of the Eastern Volcanic Zone
SISZ	South Iceland Seismic Zone
SVZ	Snæfellsness Volcanic Zone
T	temperature
VC	vesicle cylinders
WD	wavelength dispersive
WVZ	Western Volcanic Zone
X_{px}	relative contribution of olivine-free pyroxenite-derived melt
XRF	X-ray fluorescence
1SEE	one standard error of estimate
ΔlogFMQ	logarithmic deviation from the Fayalite-Magnetite-Quartz oxygen buffer

List of figures

1 Introduction

1.1 Aims, motivation and outcome

The overarching aim of my thesis is to improve the understanding of basaltic magma genesis in Iceland. This is a broad goal, as the origin of basalts is one of the core topics of igneous petrology and Iceland is a classical locus of basalt research. Nonetheless, I have tackled this aim with three separate projects that each have independent goals as follows:

(i) To evaluate the variability in olivine minor and trace element contents in various geotectonic localities in Iceland and use this to infer compositional heterogeneity in the mantle source of Icelandic basalts (PAPER I).

(ii) To estimate conditions and timescales of the crustal storage of macrocrysts in Eyjafjallajökull ankaramites for a model of crustal magma transport in South Iceland (PAPER II).

(iii) To study a differentiated pāhoehoe lava lobe to decipher and describe mechanisms of crystal-melt separation in a typical olivine tholeiite basalt (PAPER III).

Investigating these topics of basaltic magma genesis is important, because they are essential for our understanding of the workings of the Earth's upper mantle and crust. Furthermore, estimating the conditions of crustal magma storage below active volcanoes is required for identifying the mechanisms leading to possibly hazardous volcanic eruptions. In the inners of our planet, intricacies of silicate partial melting and crystallization determine how material circulates and behaves, and Iceland is a good location to study these processes.

The most significant outcome of my thesis is the identification of an anomalous, in the context of previous Iceland data, deep mantle melting signature in olivine from South Iceland volcanic rocks (PAPER I). PAPER II shows that the clinopyroxene macrocrysts of Eyjafjallajökull ankaramites crystallized at surprisingly low mid- and upper-crustal pressures (3.0±1.4 kbar). This suggests that early clinopyroxene fractionation from primitive South Iceland magmas can occur shallower in the crust than previously thought. Furthermore, the Hafnarhraun pāhoehoe lava lobe (PAPER III) revealed the mechanisms of crystal-melt separation in this differentiated basalt, potentially analogous to mechanisms occurring in shallow crustal intrusions, thus providing valuable insights into basalt magma genesis.

1.2 Anatomy of the thesis

In PAPER I, I investigate mantle melting below Iceland by analyzing major, minor and trace element compositions of primitive olivine crystals from various tectonic settings in Iceland (eight sampling locations and 482 analyzed olivine grains in total). Olivine analyses were performed with high-precision EPMA and LA-ICP-MS, and the results were compared to numerical models of mantle melting and olivine crystallization. Olivine crystals are a valuable proxy of the mantle mode (i.e., rock type) and melting conditions, as they are the first phase to crystallize from a primitive basaltic magma, and thus record a nearly unmodified, initial composition of the mantle-derived partial melt. Knowledge on the composition of these near-primary mantle melts can be further used to infer the nature of their mantle source.

In addition to mantle processes, my thesis explores how basaltic magmas reside and differentiate in the Earth's crust. This—crustal storage of magmas—is the topic of PAPER II, for which I analyzed clinopyroxene, olivine, spinel and melt inclusions in the most primitive rocks of Eyjafjallajökull to determine at what pressure and temperature these crystals crystallized. Compositional analyses were performed with EPMA, and pressure and temperature estimates were de-

rived using the most recent thermobarometric models. In addition, I analyzed compositional zonation patterns in olivine crystals, formed by magma mixing-induced growth and subsequent solid-state diffusion, to estimate how long these crystals spent in the magmatic system after the magma-mixing event. The necessary crystallographic orientation data for these diffusion models were acquired with EBSD.

PAPER III is a thorough description of a differentiated pāhoehoe lava lobe. It focuses on the question of how residual melts of the partly crystalline lava separated to form evolved units (melts segregations) within the lava lobe. Composition of whole-rock samples and main minerals in the pertinent units within the lava lobe were analyzed using WD-XRF and EPMA. Pāhoehoe lavas are useful for this type of a study, as they are modest in size, crystallize at atmospheric pressure, and have a relatively simple emplacement mechanism in comparison to exposed crustal basaltic intrusions.

2 Basaltic magmatism in Iceland

2.1 The volcanic setting

Basaltic magmas are partial melts of the Earth's upper mantle. These melts have a low density in comparison to common mantle rocks; therefore, they ascend through Earth's upper layers and sometimes erupt as lava flows. At mid-ocean ridges, basalt differentiation and solidification generate the oceanic crust (Wilson, 1963). Ultimately, basaltic magmatism also contributes to the formation of continental crust, atmosphere and oceans, making Earth as we know it (Allègre et al., 1987; Hofmann, 1988).

Globally, Iceland is one of the most proficient producers of basaltic magma (Thordarson and Larsen, 2007). It is a volcanic island situated in the North Atlantic between the Eurasian and North-American lithospheric plates that diverge by a rate of 18–19 mm/year (Sigmundsson et al., 2018). This spreading is concentrated at rift zones, 50–100 km in width, which cross Iceland from southwest to northeast (Fig. 1). In the southern half of Iceland, there are two parallel rift zones, Eastern Volcanic Zone (EVZ) and Western Volcanic Zone (WVZ). Between these resides a crustal block, called the Hreppar Formation, which is bordered by the Mid-Iceland Belt (MIB) in the north and the South Iceland Seismic Zone (SISZ) in the south. SISZ, as the name suggests, is an earthquake-prone transform, and here lithospheric spreading is accommodated as a left-lateral shear in "bookshelf" type faulting (Einarsson, 2010). At its western extremity, the SISZ fuses with the WVZ, and this part of the plate boundary is the Reykjanes Volcanic Belt (RVB). Here, the plate boundary trends characteristically oblique (~30°) to the plate spreading direction (Clifton and Kattenhorn, 2006). The tectonic setting in the northern half of Iceland is generally simpler than in the south, featuring a single rift zone that accommodates all deformation: Northern Volcanic Zone (NVZ). In the northernmost Iceland, this simplicity is lost again, as NVZ converts to a complex transform zone—the Tjörnes Fracture Zone (TFZ)—that accommodates both right-lateral shear and extension (Stefansson et al., 2008).

Owing to magmatism focused at the spreading rifts, the age of the Iceland crust increases away from them (Fig. 1), such that the oldest rocks are at the eastern and western extremities of the island, being 12–13 Ma old at the eastern coast and 15–16 Ma in the northwest (Moorbath et al., 1968). This pattern is broken by volcanic flank zones (also called off-rift volcanic zones), where magmas erupt off-rift and accumulate unconformably on older strata (Fig. 1). The three major flank zones are Snæfellsness

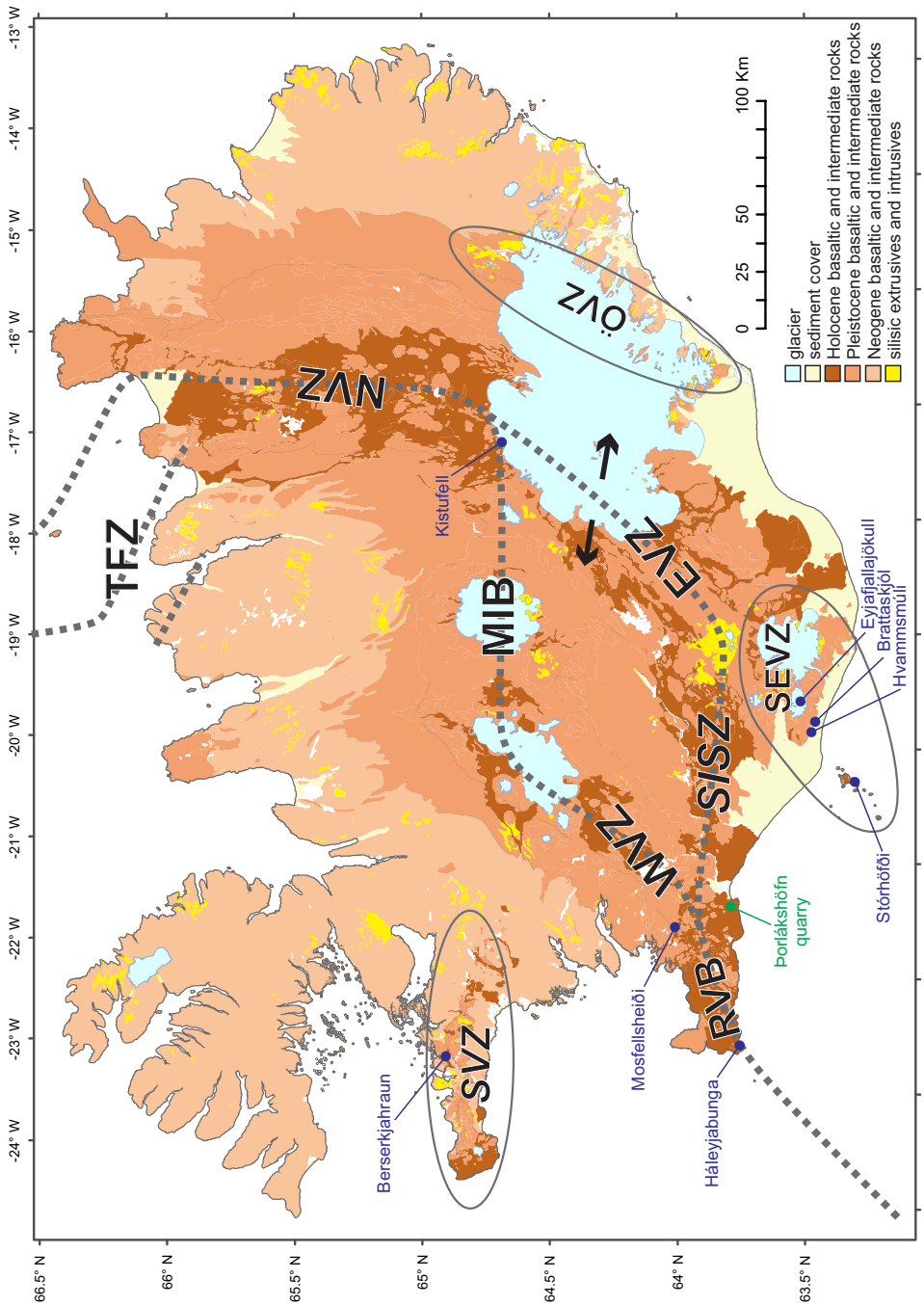

Figure 1. Geological map of Iceland. Stippled line marks the active plate boundary. Arrows show the direction of crustal spreading. Ovoids delineate the volcanic flank zones (i.e., off-rift zones) with little or no rifting. Pertinent sampling locations of the thesis are marked. Acronyms: SVZ = Snæfellsness Volcanic Zone, RVB = Reykjanes Volcanic Belt, WVZ = Western Volcanic Zone, SISZ = South Iceland Seismic Zone, MIB = Mid-Iceland Belt, TFZ = Tjörnes Fracture Zone, EVZ = Eastern Volcanic Zone, NVZ = Northern Volcanic Zone, ÖVZ = Öræfajökull Volcanic Zone.

Volcanic Zone (SVZ), Southern tip of the Eastern Volcanic Zone (SEVZ) and Öræfajökull volcanic zone (ÖVZ). The reasons behind the magmatism in off-rift volcanic zones are not completely clear. However, SVZ has been interpreted as a remnant of the now extinct Snæfellsnes-Skagi rift segment, and as such a zone of weakness in the crust (Hardarson et al., 1997), while SEVZ has been suggested to be the off-rift tip of the southward propagating EVZ (Oskarsson et al., 1982). Furthermore, ÖVZ has been suggested to be a recently-developed locus of rifting (Hards et al., 2000) parallel to EVZ. Of the volcanic flank zones, SEVZ has been the most active during historical times (Thordarson and Larsen, 2007).

92 volume% of the Iceland magmas erupted in the Holocene have been basalts (Thordarson and Larsen, 2007), and silicic rocks are a minority in the rock record (Fig. 1). Basalts of the rift zones are olivine tholeiite or tholeiite, whereas basalts erupted from off-rift volcanoes tend to be alkali basalts or so-called transitional alkali basalts, meaning that they plot close to the alkalic-tholeiitic transition on a TAS diagram (see Jakobsson, 1972; Jakobsson et al., 2008). This compositional variation is likely due to varying mantle melting conditions during the genesis of these basalts.

2.2 Mantle origin of Iceland basalts

Abyssal peridotites, ophiolites and mantle xenoliths indicate that the Earth's upper mantle is dominantly composed of lherzolite with olivine, pyroxenes, and spinel or garnet as the dominant phases (e.g., Green and Ringwood, 1963, 1967; McDonough and Sun, 1995). Basaltic lavas, although nearly never primary partial mantle melts (O'Hara, 1968), typically conform as fractionated partial melts of mantle lherzolite, as shown by the plethora of melting experiments and numerical models (e.g., Green and Ringwood, 1967; Langmuir et al., 1977; Jaques and Green, 1980; Baker and Stolper, 1994).

The sub-Icelandic mantle melts in response to plate spreading induced upwelling and decompression. Additionally, it has been suggested that Iceland is underlain by a hot mantle plume (Schilling, 1973), which increases the melting rate at least in central Iceland (Maclennan et al., 2001a). Icelandic basalts commonly have an "enriched" isotopic signature with high $^{87}Sr/^{86}Sr$, $^{206}Pb/^{204}Pb$, $^{3}He/^{4}He$ and low $^{143}Nd/^{144}Nd$ compared to MORB (Hart et al., 1973; Sun and Jahn, 1975), although some basalts also reveal a depleted signature—with low $^{87}Sr/^{86}Sr$ and high $^{143}Nd/^{144}Nd$—distinct from MORB (e.g., Fitton et al., 1997; Thirlwall et al., 2004b). This compositional deviance from MORB is typically seen indicative of the presence of trace element enriched and undegassed mantle below Iceland brought up by the mantle plume (Chauvel and Hémond, 2000; Kokfelt et al., 2006; Harðardóttir et al., 2018), although alternative views do also exist (e.g., Hole and Natland, 2019). Further evidence for the Iceland plume comes from seismic tomography that indicates a low-velocity zone below Iceland, interpreted to represent the tail of the ascending plume (e.g., Wolfe et al., 1997; French and Romanowicz, 2015). Moreover, petrological thermometry suggests a hot mantle beneath Iceland, with estimated mantle potential temperatures of 1430–1630 °C compared to 1250–1400 °C for typical Mid-Oceanic Ridges (White and McKenzie, 1989; Mckenzie and O'Nions, 1991; Maclennan et al., 2001a; Putirka, 2008a, 2016; Brown and Lesher, 2014; Shorttle et al., 2014; Herzberg and Asimow, 2015; Jenkins et al., 2016).

When ascending mantle melts in response to plate spreading, it melts over a pressure (P) range, such that the degree of partial melting (F) progressively increases with lowering pressure (see Langmuir and Forsyth, 2007; and references therein). This induces variation in generated partial melt compositions, such that alkali basalts are produced at higher P and lower F, and tholei-

itic to picritic melts form at higher F and lower P. Some variation in basalt compositions is also derived from mantle heterogeneity. In Iceland, this is indicated by correlation in incompatible trace elements and long-lived radiogenic isotopes in basalts (Zindler et al., 1979; Hemond et al., 1993; Chauvel and Hémond, 2000; Kokfelt et al., 2006), which suggests that the enriched and fusible mantle components are distinct units from the depleted mantle and have been separated for hundreds of millions of years to attain their different isotopic signature. Because the fusibility of a mantle rock is governed by its major element composition (including water content), it can be assumed that these isotopically distinct and fusible mantle components are also their own rock types in the melting regime. Furthermore, the newest models indicate that the Icelandic mantle indeed needs to be modally heterogenous (Shorttle and Maclennan, 2011; Shorttle et al., 2014), as a minor (4–15%) contribution from olivine-poor mantle in the form of pyroxenite or pyroxenite-peridotite hybrid is required to generate the major and trace element compositional variation in erupted Iceland basalts.

The isotopically distinct and incompatible trace element-rich basalt compositions of the volcanic flank zones have been explained by contamination with lower crustal melts (Oskarsson et al., 1985; Steinthorsson et al., 1985), or by a lower degree of melting and greater average melting depth of compositionally heterogenous mantle (e.g., Furman et al., 1991a; Hemond et al., 1993; Kokfelt et al., 2006a). Although both processes are likely to have an effect on the genesis of flank zone basalts, the latter of these ideas, sketched in Fig. 2, has attained popularity, as it best explains the correlation between incompatible trace elements and isotopic enrichment in Iceland basalts (Sigmarsson and Steinthórsson, 2007; and references therein). Due to the thin lithosphere at the locus of rifting, mantle melting extends shallower and occurs over a greater pressure interval below rift zones compared to volcanic flank zones (green columns). Consequently, the degree of mantle melting is higher in rift zones, and the low-degree melts from fusible enriched mantle sources (yellow ellipses) are diluted by abundant shallow partial melts of depleted mantle. However, at volcanic flank zones, this dilution does not occur to the same extent, and thus the erupted magmas are (i) deep low-degree partial melts of the mantle, and (ii) more typically composed of partial melts of fusible, major and trace element-enriched mantle sources.

2.3 Basalt differentiation

After their formation in the sub-Icelandic mantle, the mantle melts need to transect 20 to 50 km of lithosphere (Darbyshire et al., 2000) before they erupt on surface. During this ascent, magmas accumulate at various depths and extended volumes of melts are stored and partially or completely crystallized. This crystallization is commonly fractional, meaning that the crystallizing mineral phases separate from the host melt soon after their formation, and thus the host melt composition alters due to the removal of elements by the fractionating crystal phases. This fractional crystallization is the key compositional modifier of magmas and so ubiquitous that completely non-fractionated magmas, so-called primary magmas, are rare on the surface of the Earth (O'Hara, 1968). Indeed, most erupted basaltic magmas in Iceland have already crystallized to reach the olivine + plagioclase cotectic (Hartley and Maclennan, 2018) or the phase assemblage olivine-plagioclase-clinopyroxene (Presnall and Gudfinnsson, 2011). The common order of fractionating mineral phases from reduced Icelandic tholeiitic magmas is olivine (±spinel), olivine + plagioclase and olivine + plagioclase + clinopyroxene (Herzberg, 2004). In addition, if the fractionating magma is sufficiently oxidized and

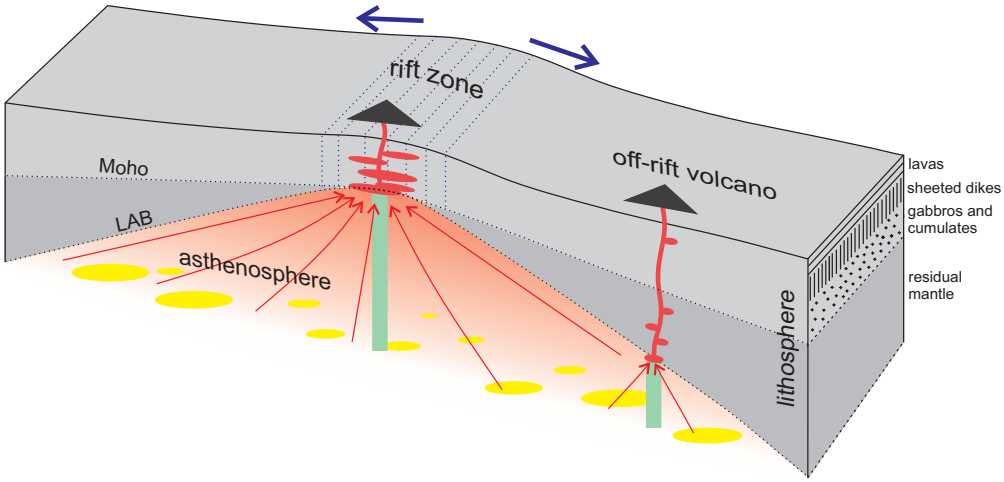

Figure 2. Conceptual model of mid-ocean ridge mantle melting and lithospheric structure. Yellow colored ovoids are modally and chemically enriched material in the mantle and triangles are volcanic edifices that tap the mantle melts. The strength of the red tone displays the degree of melting, fully red portions being dominantly molten. Red arrows are melt trajectories, and blue arrows illustrate the lithospheric spreading. The green bar shows the depth range of melting beneath rift and off-rift zones. Moho = Mohorovičić discontinuity, LAB = lithosphere-asthenosphere boundary.

poor in Ca and Al, and the crystallization pressure is sufficient, plagioclase crystallization may be suppressed to allow preferential crystallization of clinopyroxene after olivine (Presnall et al., 1978; Stolper, 1980; Presnall et al., 2002; Neave et al., 2019b).

Variably differentiated magmas from variable mantle sources are also prone to mix with each other during crustal storage. Primitive phenocryst phases commonly have melt inclusions that record high variability in trace element and isotopic contents. This variability, however, diminishes in more evolved phenocrysts. This has been interpreted as the result of 'concurrent mixing and crystallization' of magmas derived from various depths and sources from the mantle, which homogenizes magmas in crustal intrusions (Maclennan, 2008a, b; Neave et al., 2013). During this process, a large degree of the chemical variability inherited from polybaric mantle melting is lost.

Besides crystallization and mixing, intrusive magmas tend to interact with crustal rocks surrounding them. The stored magma can disaggregate rock fragments (xenoliths) or crystals (xenocrysts) and partially melt or resorb, i.e., assimilate, the surrounding crustal material. In Iceland, the limited compositional variability and the high melting point of the gabbroic crust limits this process and its effects on magma compositions, but isotopic and trace element studies nonetheless suggest that at least some Icelandic magmas have assimilated hydrothermally altered crust (Hemond et al., 1993; Brounce et al., 2012). In addition, Icelandic magmas commonly carry mineral cargoes that are not in chemical equilibrium with the carrier melt (Halldorsson et al., 2008; Thomson and Maclennan, 2013; Neave et al., 2014). These 'accumulated' non-equlibrium crystals can be xenocrysts: crystals not related to the host magma (Sollas, 1894), potentially derived by assimilation of fragments of crustal gabbro (e.g., Bédard, 1993). In addition, they can be antecrysts, co-genetic with the host magma but crystallized at an earlier evolutionary stage or in partial separation from the magma (Davidson et al., 2007). All these accumulated crystals affect the erupted magma compositions.

2.4 Storage of magmas in the Iceland crust

The storage of magmas in oceanic crust is evidently transcrustal, meaning that magmas reside in pockets in the Earth's crust at a range of depths (Maclennan et al., 2001b; Kelley and Barton, 2008; Maclennan, 2019; White et al., 2019). This view of multi-level magma storage conforms to detected seismicity during volcanic eruptions and sill emplacements (e.g., Tarasewicz et al., 2012; Greenfield and White, 2015), and to petrological barometry relying on final equilibration of a suite of magmatic liquids (Herzberg, 2004) and mineral-melt equilibrium in magmas (e.g., Neave and Putirka, 2017; Hartley and Maclennan, 2018; Neave et al., 2019a). Despite the consensus on variable magma storage depths, conceptual models of the nature and size of the crustal intrusions vary. Some envision an oceanic crust with melt lenses in a pervasive crystal-liquid mush—a mixture of interconnected crystals and magma (Cashman et al., 2017)—whereas others visualize an oceanic crust layered with sills surrounded by solid rock with only trivial crystal-liquid mush on intrusion margins (Maclennan, 2019). In addition, the 'temporal rigidity' of deep magmatic storage is largely unknown. Are the deep roots of volcanoes spatially and temporally fixed, or do the deep portions of the magma transport system reorganize themselves on eruption-to-eruption basis? At least the magmatic systems seem to be flexible in changing their architecture in response to altering surficial loading caused by recurring glaciations (Caracciolo et al., 2019). Shallow silicic magmatic intrusions, typical of evolved central volcanoes, may be long-lived and rigid features in the crust (Flude et al., 2010), whereas magma emplacement in the ductile middle and lower crust may be more indefinite and random.

3 Sampling and laboratory analysis of rocks and minerals

3.1 Samples

For PAPER I, samples containing olivine macrocrysts were gathered from eight locations representing different volcano-tectonic environments in Iceland. From the rift zones (WVZ and NVZ, Fig. 1), I sampled Háleyjabunga lava shield, Mosfellsheiði lava flow field and Kistufell table mountain. From the off-rift volcanic flank zones, I analyzed olivine macrocrysts from Berserkjahraun, Hvammsmúli, Brattaskjól and Stórhöfði lavas and Eyjafjallajökull 2010 tephra (Fig. 1). I separated olivine crystals by handpicking from crushed and sieved (Ø = 0.1–4.0 mm) rock samples, after which they were mounted into epoxy molds or on glass slides. A total of 482 olivine macrocrysts were analyzed for their minor elements (Ni, Mn and Ca specifically) with EPMA, 64 were analyzed for their trace elements with LA-ICP-MS, and analysis of the zoning patterns in olivine was conducted for 34 macrocrysts.

In PAPER II, I further studied the Brattaskjól and Hvammsmúli ankaramite crystal cargo for which the composition of olivine macrocryst cores (n=192) had been determined in PAPER I. Compositions of 51 macrocryst clinopyroxene, 38 spinel and 21 melt inclusions in olivine, and 47 concentration profiles across olivine zonation were measured from thin sections and crystal separates in epoxy molds. As the melt inclusions were partly crystalline in all olivine crystals, they were homogenized by heating to 1200–1220 °C in graphite crucibles prior mounting to epoxy (see Methods in PAPER II).

For the study of the Hafnarhraun lava flow (PAPER III), I initially gathered 54 hand samples, of which 23 were analyzed for whole-rock composition and six thin sections were made for

microchemical examinations and compositional analysis of main minerals (olivine, clinopyroxene and plagioclase). Samples were collected with a steam-hammer developed for taking paleo-magnetic drillcore samples or by rock and chisel, and often by hanging from a rope on the eight-meter-tall quarry wall.

3.2 XRF

X-ray fluorescence (XRF) is the emission of secondary X-rays with characteristic energies and wavelengths, dependent on the atomic structure, when a material is excited with high-energy radiation (X-rays or gamma rays). The compositions of whole-rock samples from the Hafnarhraun pāhoehoe lava lobe (PAPER III) were measured utilizing the XRF phenomenon with a PANalytical Axios mAX 151 4kW WD-XRF spectrometer at the Department of Geosciences and Geography, University of Helsinki. The samples were first crushed using an iron-jawed crusher, wet-sieved with deionized water, and fine-powdered with an agate mill. The rock powders were then mixed in a ratio of 1-part sample powder with 10-parts Li-Borate ultrapure flux (49.5 wt% $Li_2B_4O_7$, 49.5 wt% $LiBO_2$, and 1.0 wt% LiBr) and fused to glass beads using Claisse M4 fluxer. These glass beads were then bombarded with X-rays and the intensity of the X-ray peaks in the secondary X-ray spectra were measured to quantify their major oxide and trace element composition. A total analysis time of 2.5 hours per sample was used to attain an uncertainty of less than <0.05 wt% for all major oxides.

3.3 EPMA

Electron probe microanalyzer (EPMA) is an apparatus for precise non-destructive microanalyses of solid samples. In EPMA, a beam of electrons is produced by an electron source (tungsten filament, Lanthanum Hexaborate crystal cathode, or field emission electron source), accelerated with an anode plate, and directed with electromagnetic condenser lenses to a solid sample. The electron beam interacts with the studied material in various ways, including the production of heat, light (cathodoluminescence), backscattered electrons, secondary electrons, auger electrons, and X-rays. Whereas the electrons and light are useful for imaging purposes, the characteristic X-rays emitted are indicative of the sample composition. To quantify the composition, one can measure the intensity of X-rays of varying energies by energy-dispersive (ED) or wavelength-dispersive (WD) detectors, the difference being that an ED detector counts the intensity of the whole X-ray spectrum at once, while WD detectors can isolate and quantify specific X-ray wavelengths/energies separately.

All EPMA analyses pertinent to this thesis were conducted using a JEOL JXA-8230 electron microprobe at the University of Iceland, equipped with five WD and one silicon drift ED detectors, and a lanthanum hexaborate electron source. For the procedures of major element analyses in olivine, clinopyroxene, plagioclase, spinel and melt inclusions, the reader is referred to the attached papers. Anyhow, the advanced high-precision measurements of minor and trace elements in olivine deserve to be described in some detail here. For these analyses, I used a modified version of a setup of Batanova et al. (2015) and bombarded olivine macrocrysts with unusually high probe-current of 500 nA (compared to 20 nA in standard analyses) and 20 keV acceleration voltage. Analyses were performed with a focused electron beam, and they took 13.25 min per sample spot. Minor and trace elements (Ni, Mn, Ca, Al, Cr, Co, Ti, Zn, P, Na) were measured with WD detectors with peak count times varying from 90 to 150 s, and the EDS was utilized for Si, Mg and Fe measurements with a counting time of 300 s. Grains of San Carlos olivine were measured between every 20–50 analyses

to check for instrumental stability. The setup delivered minor and trace element detection limits of 3–10 ppm, and, crucially, high mean instrumental precisions for Ni (0.52%), Mn (0.48%) and Ca (0.34%). I compared the resulting olivine compositions to earlier analyses of Sobolev et al. (2007), and these were found to be an outstanding match (Electronic Appendix in PAPER I). The success of these olivine minor and trace element analyses was a significant building block for this thesis.

3.4 LA-ICP-MS

For precise trace element analyses of olivine macrocrysts, I utilized laser ablation inductively coupled plasma mass spectrometry (LA-ICP-MS) at the Department of Geosciences and Geography, University of Helsinki. In LA-ICP-MS, a high-intensity laser is used to ablate a small portion (a typical analysis spot diameter of 1-100 μm) of a solid sample, and the produced fine particles are brought to a plasma torch to be ionized and fed to a mass spectrometer. Mass spectrometer is an analytical tool that separates ions based on their mass-to-charge ratio, typically by subjecting them to electromagnetic fields. The amount of deflection in ion paths is mass-to-charge dependent and thus distinct for a specific ion. There are numerous instruments (mass analyzers) to deflect the ions, e.g., the quadrupole mass analyzer utilized in the LA-ICP-MS facility of the University of Helsinki. At the end of the mass spectrometer, the intensity of arriving ions is measured, commonly with an electron multiplier.

I conducted the LA-ICP-MS olivine analyses of PAPER I with the Coherent GeoLas Pro MV 193 nm laser ablation system coupled to an Agilent 7900 s quadrupole ICP–MS at the University of Helsinki. Olivine grains were ablated with a laser spot size of 44 μm and energy density of 7 J/cm^2, and the measurement program included the isotopes: ^{7}Li, ^{23}Na, ^{24}Mg, ^{25}Mg, ^{27}Al, ^{29}Si, ^{43}Ca, ^{31}P, ^{43}Ca, ^{44}Ca, ^{45}Sc, ^{49}Ti, ^{51}V, ^{52}Cr, ^{55}Mn, ^{56}Fe, ^{57}Fe, ^{59}Co, ^{60}Ni, ^{62}Ni, ^{63}Cu, ^{66}Zn, ^{85}Rb, ^{88}Sr and ^{137}Ba. The external standardization was done using GSE 1G synthetic basalt glass, and the Si concentrations determined with high-probe current EPMA analyses were used as internal standards. The data reduction was performed with the SILLS software package (Guillong et al., 2008), and Si-normalized fractionation factors (Fryer et al., 1995) were used to monitor for significant down-hole fractionation or down-hole compositional zonation. The trace element composition of olivine from one location, Háleyjabunga, had been previously analyzed by LA-ICP-MS by Neave et al. (2018). My analyses were found to be slightly higher in Co, but for other elements, the results concurred.

3.5 EBSD

The rate of diffusion in a crystal lattice in olivine is dependent on the crystallographic directions, being nearly three times faster along the olivine c-axis than the a- or b-axes (Dohmen and Chakraborty, 2007; Dohmen et al., 2007). Hence, to use the amount of diffusion in crystal zoning in olivine grains as an indicator of diffusion timescales (PAPER II), the crystallographic orientation of these crystals had to be determined. This was done using electron backscatter diffraction (EBSD, Prior et al., 1999) with FEI Quanta 650 SEM and HKL CHANNEL 5 EBSD software at the University of Leeds. EBSD is a technique of automated analysis of diffraction patterns produced when electrons scatter in a crystal lattice, which can be used to resolve the mineral crystallographic orientation (see Humphreys, 2001).

4 Numerical modelling

4.1 Major, minor and trace elements in olivine as a mantle proxy

Forsterite-rich olivine is typically the first mineral (along with minor spinel) to crystallize from a mantle-derived melt. Therefore, the first-to-crystallize high-Fo olivine is expected to record the composition of its near-primary parental melt before it is masked by crustal magma differentiation. Consequently, high-Fo olivine should store information about the mantle source from which its parental magma was derived (e.g., Sobolev et al., 2007; Herzberg et al., 2016; Matzen et al., 2017b).

Sobolev et al. (2005) were the first to suggest that minor element concentrations in olivine (specifically Ni, Mn and Ca contents) can be used to derive the relative amount of olivine-free pyroxenite in the mantle source of magmas. Since this work, olivine compositions have been used to infer mantle lithology for a wide variety of volcanic settings (e.g., Sobolev et al., 2007; Gurenko et al., 2010; Trela et al., 2015; Herzberg et al., 2016). However, this view of olivine as a proxy of mantle mineralogy has been recently challenged, as new evidence suggests that shifts in partitioning coefficients during mantle melting and subsequent olivine crystallization may in fact be accountable for most, if not all, global variability in olivine compositions (Matzen et al., 2013, 2017a, b; Putirka et al., 2018).

Various mantle rocks produce compositionally diverse mantle melts. For example, partial melts of olivine-free pyroxenites are expected to be richer in Ni than melts of mantle lherzolite, as the abundant olivine in lherzolite effectively sequesters Ni during melting (e.g., Sobolev et al., 2005; Herzberg, 2011). Additionally, the nature of mantle melts varies as a function of the degree and depth of melting. Continuing with Ni as an example, olivine sequesters Ni less effectively at higher T at greater mantle depths (i.e., $D_{Ni}^{ol/liq}$ is lower at higher T, Matzen et al. (2013, 2017a)), and consequently, deep and hot partial melts of lherzolite are higher in Ni compared to lherzolite melts generated at shallower mantle levels. Mildly incompatible elements, for example Sc and Ti that are relevant for olivine studies, are in turn highly susceptible to the degree of mantle melting due to their high incompatibility to mantle minerals (Putirka et al., 2018).

Because influenced by numerous parameters of melting and crystallization, it is challenging to derive a unique explanation for an olivine with a certain minor and trace element composition. High Ni and low Mn in a certain olivine population, for example, may either signal melting of an olivine-poor sources or a deep mantle source region for the magma (see PAPER I). Anyhow, as the knowledge of the partitioning of various elements during mantle melting increases, joint analysis of multiple minor and trace elements (e.g., Ni, Mn, Ca, Sc, Ti, Zn) in olivine may be used to better constrain mantle source characteristics. Furthermore, parameterizations of the temperature- and pressure-dependence of elemental partitioning between olivine and melt can be used to constrain the depth of mantle melting (Matzen et al., 2017b), as attempted in PAPER I.

4.2 Thermodynamic modelling of melting and crystallization

A large part of my thesis revolves around comparing compositional data of rocks and minerals to thermodynamic models of magmatic processes. These models are quantifications of the stability of solid and liquid phases over a range of P and T conditions relevant to igneous systems, rooted to experimentally determined phase stabilities of igneous minerals.

Three thermodynamic modelling programs were used in this thesis: Petrolog3 (Danyush-

evsky and Plechov, 2011), COMAGMAT-5.2.2 (Ariskin et al., 2018), and MELTS (Ghiorso et al., 2002) with ALPHAMELTS 1.8. front end (Smith and Asimow, 2005). Petrolog3 was used to a lesser extent and only to calculate olivine compositions crystallizing from evolving basaltic magmas using the model of Beattie et al. (1993) (e.g., Fig. 8 in PAPER I) and to correct melt inclusion compositions for post-entrapment olivine crystallization and diffusion (see Danyushevsky et al., 2000). The strength of Petrolog3 is that it allows comparison of published mineral-melt equilibrium models (for example, it includes 14 models for olivine-melt equilibrium) and simple calculations can be performed with clearly defined setup. In contrast, the model procedure is fixed in MELTS and COMAGMAT, relying on finding the minimum Gibb's Free Energy (G) of the system under given conditions. MELTS does this directly by testing the stability of phases (whether changes lead to lower G) at a given T using nonlinear mathematical programming (Ghiorso, 1994), whereas COMAGMAT does this indirectly by finding equilibrium for a pre-defined crystallization degree using experimentally determined liquidus temperatures of minerals (Ariskin, 1999; Ariskin et al., 2018). The practical difference between these thermodynamic programs is that MELTS is extremely flexible; it can perform numerous different modelling schemes (to name a few: adiabatic melting, reverse crystallization, near-fractional crystallization) in a large P, T and compositional range. COMAGMAT, in contrast, is calibrated only for basaltic compositions at 1 atm (although usable up to 3 kbar, Ariskin et al. 2018) and tuned for crystallization modelling. Maybe due to this high level of specification, fractional crystallization modelling with COMAGMAT reproduced the compositional trends in the Hafnarhraun lava lobe better than MELTS, and therefore all fractional crystallization modelling was done with the former in PAPER III. MELTS, however, was the only program capable of performing the sophisticated near-fractional adiabatic decompression melting calculations in PAPER I.

4.3 Thermobarometry – probing the crystallization conditions of minerals

The composition of magmatic mineral phases is dependent on the composition of the liquid phase and conditions of crystallization including P, T and fO_2. A prime example of a P-dependent mineral component is jadeite ($NaAlSi_2O_6$; Jd) in clinopyroxene. The stability of Jd increases with increasing pressure, which stems from the significant volume decrease as Jd is produced in the reaction $NaO_{0.5}^{liq} + AlO_{1.5}^{liq} + 2SiO_2^{liq} = NaAlSi_2O_6^{cpx}$, where $NaAlSi_2O_6^{cpx}$ is Jd, and the superscripts denote liquid (liq) and clinopyroxene (cpx). Experimental quantification of this P-sensitive incorporation of Jd in clinopyroxene makes it possible to use measured clinopyroxene-liquid equilibria in volcanic rocks as a barometer, i.e., as a tool to estimate the pressure of crystallization. The most recent formulation of the so-called Jd-in-clinopyroxene barometer (Neave and Putirka, 2017) is as follows (**Equation 1**):

$$\mathrm{P(kbar)} =$$

$$-26.27 + 39.16\frac{\mathrm{T(K)}}{10^4}\ln\left[\frac{\mathrm{X_{Jd}^{Cpx}}}{\mathrm{X_{NaO_{0.5}}^{liq}}\,\mathrm{X_{AlO_{1.5}}^{liq}}\left(\mathrm{X_{SiO_2}^{liq}}\right)^2}\right]$$

$$-4.22\ln\left(X_{DiHd}^{Cpx}\right) + 78.43\mathrm{X_{AlO_{1.5}}^{liq}}$$

$$+393.81\left(\mathrm{X_{NaO_{0.5}}^{liq}}\,\mathrm{X_{KO_{0.5}}^{liq}}\right)^2$$

Here X^{liq} are cation fractions (normalized to 1) and X^{cpx} are clinopyroxene components calculated on the 6 oxygen basis (cation sum close to 4). Jd and DiHd components are calculated using a normative procedure of Putirka et al. (2003). From this formulation, one can see that, in ad-

dition to the compositions of clinopyroxene and host liquid, the barometer is dependent on T. Fortunately, clinopyroxene-liquid equilibrium can also be used as a thermometer, as the partitioning of Diopside-Hedenbergite ($Ca(Mg,Fe)Si_2O_6$; DiHd) and Jd component between clinopyroxene and silicate melt is temperature sensitive (Putirka et al., 1996, 2003). As given in Eq. 33 in Putirka (2008b), the expression of this so-called Jd-DiHd exchange thermometer is (**Equation 2**):

$$\frac{10^4}{T(K)} =$$

$$7.53 - 0.14\ln\left[\frac{X_{\mathrm{Jd}}^{\mathrm{cpx}} X_{CaO}^{liq} X_{Fm}^{liq}}{X_{DiHd}^{\mathrm{cpx}} X_{\mathrm{Na}}^{\mathrm{liq}} X_{Al}^{liq}}\right]$$

$$+0.07(H_2O^{liq}) - 14.9\left(X_{CaO}^{liq} X_{SiO_2}^{liq}\right)$$

$$-0.08\ln\left(X_{TiO_2}^{liq}\right) - 3.62\left(X_{NaO_{0.5}}^{liq} + X_{KO_{0.5}}^{liq}\right)$$

$$-1.1(Mg\#^{liq}) - 0.18ln\left(X_{EnFs}^{cpx}\right) - 0.027P(kbar)$$

Here $X_{\mathrm{Fm}}^{\mathrm{liq}}$ is the Mg+Fe in liquid (cation fractions), H_2O^{liq} is in wt%, and $Mg\#^{\mathrm{liq}}$ is Mg/(Mg+Fe^{2+}) in liquid. Remaining terms are as in Equation 1. Solving Equations 1 and 2 iteratively, using the output of a one model as the input to the other, allows simultaneous estimation of P and T. This, however, requires that the parental melt composition of the studied clinopyroxene crystals is known.

Lava-hosted clinopyroxene macrocrysts are most applicable to thermobarometric studies, as their composition reflects the magmatic storage conditions and subsurface architecture of volcanoes. In these cases, however, the macrocrystic clinopyroxene grains are typically no longer in equilibrium with their carrier lavas, as these lavas tend to have evolved by fractional crystallization and magma mixing after the macrocryst crystallization (Hansen and Grönvold, 2000; Halldorsson et al., 2008; Thomson and Maclennan, 2013). In addition, the macrocryst cargo may have never been in equilibrium with their carrier lavas if the macrocrysts are xenocrysts, i.e., picked by the ascending magmas from unrelated, compositionally distinct magmas or wall rocks. A further problem arises from the presumption of equilibrium crystallization. Numerous experiments have shown that in undercooled magmas, the rapid crystallization of minerals (e.g., clinopyroxene) results in disequilibrium partitioning of elements (e.g., Hammer, 2008; Mollo et al., 2010; Welsch et al., 2016). Furthermore, textural and microchemical evidence indicates that high undercooling and disequilibrium crystallization are common in volcanic magma systems (e.g., Welsch et al., 2016; Ubide et al., 2019).

The challenges related to selecting suitable melts for Jd-in-clinopyroxene thermobarometry require that clinopyroxene-melt equilibrium has to be evaluated using experimentally defined parameters, such as Fe–Mg equilibrium (Wood and Blundy, 1997), minor element contents Ti (e.g., Ti; Hill et al., 2011), and deviation from predicted and measured clinopyroxene componentry (Putirka, 1999; Mollo et al., 2013). In addition, textural inspections of minerals are required to avoid analyzing rapidly crystallized domains that may have disequilibrium compositions (Welsch et al., 2016; Ubide et al., 2019).

In PAPER II, I utilized Jd-in-clinopyroxene thermobarometry to estimate the crystallization pressure and temperature of primitive clinopyroxene crystals in two Eyjafjallajökull ankaramites. As these ankaramites have accumulated macrocrysts (~30% macrocrysts in total), their whole-rock composition does not represent a melt composition, being thus not representative as an equilibrium liquid to be used in thermobarometry. I thus advanced by fitting clinopyroxene compositions to Eyjafjallajökull whole-rock and melt inclusion compositions from Loughin (1995), Moune et al. (2012) and my study, on the basis of chemical equilibrium. First, putative

clinopyroxene-melt pairs were selected with a threshold of ±10 % Fe–Mg equilibrium assuming $Kd^{Mg–Fe}$(cpx-liq) = 0.27±0.6, for which "pseudo" P and T were calculated. Then, these results were filtered to only include the clinopyroxene-melt pairs that have a measured clinopyroxene composition that concurs with the composition predicted to crystallize from the melt at the given P and T. Specifically, the measured and predicted clinopyroxene compositions had to be in Fe–Mg equilibrium according to Eq. 35 in Putirka (2008b) and agree with respect to CaTs, EnFs and DiHd components within ±0.03 for CaTs (Putirka, 1999), and ±0.05 for EnFs and ±0.06 for DiHd (Mollo et al., 2013). Additionally, the clinopyroxene-liquid pairs had to be within ±40 % of Ti equilibrium (Hill et al., 2011).

Complementary to the Jd-in-clinopyroxene thermobarometry, I used liquid-only (Eq. 15, Putirka, 2008) and olivine-liquid thermometry (Eq. 4, Putirka et al., 2007) for calculating the temperature of olivine crystallization in these ankaramites. I also determined oxygen fugacity during crystallization by comparing compositions of co-crystallized olivine and spinel and using the most recent calibration (Nikolaev et al., 2016) of the Ballhaus-Berry-Green olivine-orthopyroxene-spinel oxybarometer equation (Ballhaus et al., 1991; Beattie, 1993).

4.4 Kinetic modelling of diffusion time scales

Diffusion chronometry (Costa et al., 2008; Zhang and Cherniak, 2010; Dohmen et al., 2017) is a tool for solving magmatic timescales from the amount of diffusion over compositional boundaries in crystals. When being crystallized, a magmatic mineral commonly develops zones of varying composition in response to changes in magma composition and crystallization conditions. While the mineral resides at magmatic temperatures, the initially sharp chemical boundaries diffuse and diminish (Fig. 3a) with a rate typically dependent on T, P, fO_2 and crystallographic orientation. When these are known, the degree of the subsolidus diffusion can be related to the time elapsed between mineral crystallization (e.g., formation of a compositionally distinct rim) and cooling of the crystal. Consequently, the amount of diffusion in minerals can be used to constrain internal dynamics of magma plumbing systems (Kahl et al., 2011, 2015, 2017; Pankhurst et al., 2018), and magma ascent (Rae et al., 2016; Mutch et al., 2019b) and residence times (Mutch et al., 2019a).

In PAPER II, I utilized diffusion chronometry to solve the Fe–Mg diffusion time over compositional boundaries in olivine macrocrysts from Eyjafjallajökull ankaramites. To conduct the iterative calculations of diffusion, I used the Mathematica finite difference diffusion code developed by Maren Kahl (Kahl et al., 2015), and used Fe–Mg inter-diffusion coefficients of Dohmen et al. (2007) and Dohmen and Chakrabortny (2007). Fig. 3b gives an example of the model-fitting for olivine crystal BR02_Ol82 with a so called 'complex reverse zonation', which refers to a core-to-rim zonation pattern where the forsterite content first increases and then sharply decreases in the outer-edge of the crystal. The initial model compositions were set at $Fo_{85.4}$ for the rim and $Fo_{82.4}$ for the core (stippled line). Then, the diffusion model defined the time (9.2 days) of diffusive re-equilibration that is required to produce a zonation pattern (red line) fitting the measured compositional zonation (filled black circles with error bars). The outermost rims in the studied olivine grains have formed, at least partly, by crystallization from cooling and evolving host magma, and not by diffusive re-equilibration only. Therefore, I opted to model the time of diffusive re-equilibration between the olivine core and the high-Fo zone near the crystal edge (Fig. 3b) rather than the re-equilibration between the

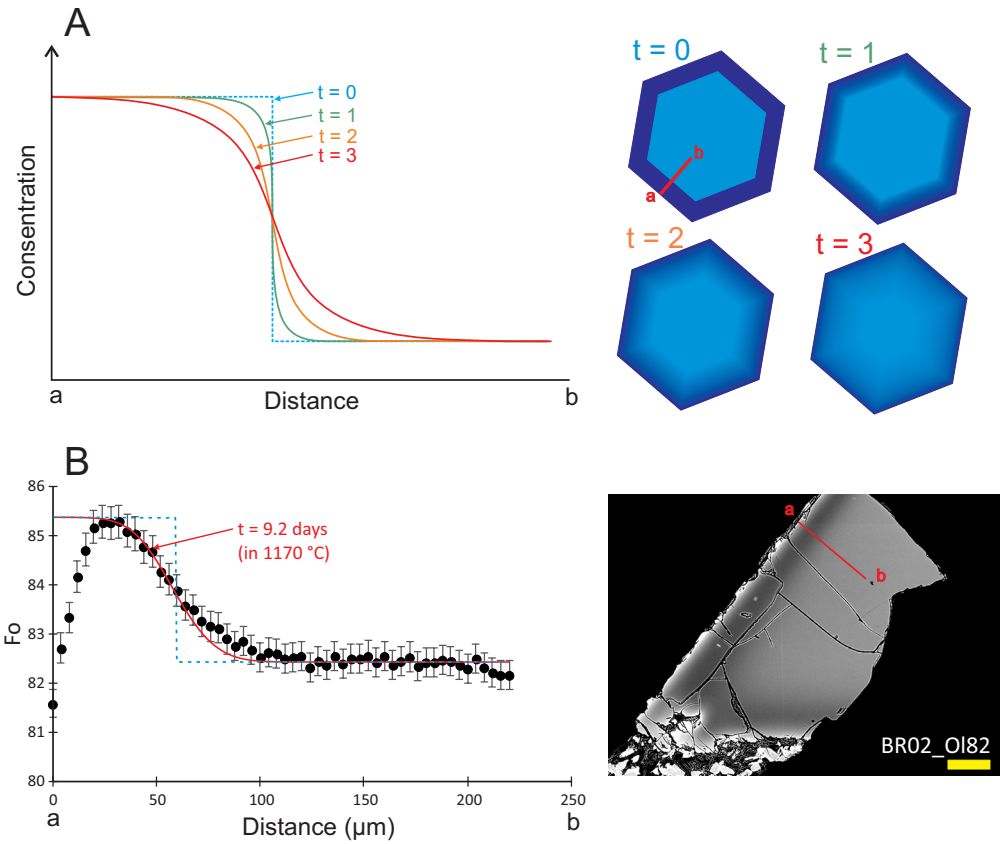

Figure 3. a) Diffusion profile of an element along a traverse a–b in zoned olivine with higher concentration rims (dark blue) and a lower concentration core (light blue). t=0 is the initial state of the system without any diffusive equilibration, t=3 is the last state with the most abundant diffusion. b) An example of diffusion model fitted for an olivine crystal BR02_Ol82. Black dots are the measured forsterite (Fo = 100 × atomic Mg/(Mg + Fe^{2+})) contents in olivine along traverse a–b that is illustrated with a red bar in the BSE image on the right. Error bars correspond to the propagated 2σ error in Fo. The blue stippled line is the model initial state, and the red curve represents the modelled Fo distribution after 9.2 days of diffusive equilibration. The yellow bar is a 100-µm scale bar.

high-Fo zone and the outer crystal rim.

5 Review of original papers

5.1 PAPER I

The compositional variability in basalts erupted in the different volcanic zones of Iceland suggests that the underlying mantle is heterogeneous in composition (Shorttle and Maclennan, 2011; Shorttle et al., 2014). Furthermore, it has been suggested that pyroxenitic mantle domains of recycled oceanic crust contribute to the genesis of Icelandic magmas (Chauvel and Hémond, 2000; Kokfelt et al., 2006). I investigated the mantle source of Iceland basalts by determining the minor and trace element compositions of primitive olivine grains from eight locations around Iceland. As primitive forsteritic olivine is the first mineral to crystallize from most basaltic magmas, it records the composition of its near-primary mantle-derived parental magma and is useful as a mantle proxy. Minor and trace element abundances in olivine, however, do not reflect the mantle source composition only, as they are

dependent on varying olivine-melt distribution coefficients affected by the P–T conditions of melting and subsequent olivine crystallization (Putirka et al., 2018).

Mainly, the new olivine data obtained in this work concur with earlier data, suggesting shallow melting of typical lherzolite mantle as the dominant source of Iceland basalts. However, I also discovered that olivine macrocrysts from the Eyjafjallajökull and Vestmanneyjar volcanic systems in SEVZ are distinctly Mn-poor and Ni-rich compared to olivine from elsewhere in Iceland. Compared to olivine from depleted Iceland rift tholeiite, these SEVZ olivines are also relatively low in Ca, Sc and V and high in Cr, Ti, Zn, Cu and Li. This compositional signature is not easily explained by crustal processes and must be mantle-derived, either indicating the presence of olivine-free mantle domains or high-temperature melting relatively deep in the mantle below the SEVZ.

To examine the cause of the SEVZ olivine signature, I modelled Sc, V, Ti, and Zn partitioning in melting of mantle lherzolite (KLB-1) and pyroxenite-peridotite hybrid (KG2). These numerical models suggest that SEVZ olivine macrocrysts could have been formed by crystallization from low degree lherzolite melts, and only the Zn enrichment may require input from modally enriched mantle domains (e.g., KG2). In the light of these and other results from recent mantle melting models (Lambart, 2017), the SEVZ olivine compositions likely signal high-temperature and high-pressure melting of somewhat enriched olivine-bearing mantle, not an olivine-free mantle source.

The Ni enrichment in the SEVZ olivine macrocrysts suggests melt equilibration depths greater than 45 km, possibly as deep as 66–81 km. Crucial for the survival of this mantle signature in olivine, these deep-derived magmas must have also ascended to the surface relatively fast to avoid re-equilibration and mixing with other mantle derived melts. Seemingly, the off-rift setting at SEVZ favors low-degree melting of deep mantle and swift ascent of these melts, and this is reflected in the olivine compositions in SEVZ basalts.

5.2 PAPER II

To elucidate the conditions of magma storage and differentiation below SEVZ, I analyzed compositions of minerals, mineral zoning patterns, and melt inclusions from the most primitive volcanic rocks identified from Eyjafjallajökull volcanic system: Brattaskjól and Hvammsmúli ankaramites. These ankaramites have ~30 vol% magnesian olivine (up to $Fo_{89.8}$) and clinopyroxene (up to $Mg\#^{cpx}$ 89.8) in near equal proportions and olivine-hosted spinel inclusions that have high $Cr\#^{spl}$ (52–80) and TiO_2 (1–3 wt%) and low Al_2O_3 (8–22 wt%), in comparison with typical Icelandic chromian spinel.

The mineral cargo in these ankaramites is suggestive of mid-crustal crystallization at 10.4±5 km depth over a large temperature interval. Spinel-olivine oxybarometry suggests that olivine-spinel co-crystallization occurred under a moderate oxygen fugacity of ΔlogFMQ 0–0.5. The clinopyroxene-compositions imply crystallization pressures of 1.7–4.2 kbar, averaging at 3.0±1.4 kbar, and crystallization temperatures in the interval 1120–1195 °C. Liquid-only thermometry and olivine-liquid thermometry give somewhat higher crystallization temperatures of 1155–1222 °C and 1136–1213 °C, respectively. Diffusion modelling of the compositional re-equilibration in Brattaskjól olivine macrocrysts suggests that the macrocrysts were mobilized and transported from their crustal storage to the surface within few weeks (within 9–37 days).

Thermobarometric estimations and compositional trends in clinopyroxene suggest that the crystal cargo in Brattaskjól and Hvammsmú-

li ankaramites represents agitated wehrlitic or plagioclase wehrlitic mid-crustal crystal mushes. Evidently, the mid-crustal cotectic assemblage was olivine and clinopyroxene and plagioclase joined the fractionating mineral assemblage later. Compositional trends suggestive of clinopyroxene-dominated crystallization are a known phenomenon in SEVZ lavas, typically regarded as indicative of high (>8 kbar) crystallization pressures (Furman et al., 1991b; Mattsson and Oskarsson, 2005). Our mid-crustal crystallization pressures for Brattaskjól and Hvammsmúli clinopyroxene crystals raise a question whether these high pressures are required to produce clinopyroxene-dominated fractionating assemblages in SEVZ.

5.3 PAPER III

Numerous mechanisms have been suggested that separate crystals and melts from each other in magmatic systems, including gravitational crystal settling (Darwin, 1844), liquid convection (Sparks et al., 1984), filter-pressing (Philpotts et al., 1996), and gas filter-pressing (also called vapor differentiation; Anderson et al., 1984; Sisson and Bacon, 1999; Pistone et al., 2015; Parmigiani et al., 2016). There are two main approaches to the study of these mechanisms: analog experiments and research conducted on solidified differentiated magmatic systems. I took the latter approach and determined the whole-rock and main mineral compositions of a partly differentiated pāhoehoe lava lobe in Hafnarhraun lava flow field, SW Iceland.

The studied 8-m-thick lava lobe (Fig. 4a) includes abundant segregation features: vesicle cylinders (VC) and horizontal vesicle sheets (HVS), commonly interpreted as separated residual melts of the lobe (e.g., Goff, 1996; Caroff et al., 2000; Hartley and Thordarson, 2009). VC are pipe-like, continuous structures up to ~5 cm in diameter that ascend from the base of the lobe and transect the whole lava core (Fig. 4b and d), whereas HVS are vesicular sheets in the upper part of the lava lobe (Fig. 4c), generally a few centimeters thick.

It was found that the whole-rock compositions of VC do not correspond to residual melts generated by fractional crystallization, but rather suggest selective fractionation of plagioclase from the host lava. In addition, the presence of olivine phenocrysts ($Fo_{73–79}$) and microphenocrysts of Ca-plagioclase (An_{77}) in VC indicates that the VC had accumulated primitive crystals in some stage of their evolution. HVS, in turn, were found to occur as two compositional variants in the lava lobe: HVS1 and HVS2. HVS1 are only mildly differentiated in relation to the host lava, commonly include olivine phenocrysts, and are holocrystalline. HVS2, in contrast, correspond to residual melts of the host lava after over 50 % crystallization, and are mineralogically distinct, displaying a texture of flow-aligned plagioclase and having no olivine nor phenocrysts.

Based on the compositional and field evidence, it seems that the VC in the Hafnarhraun lava lobe formed via a two-stage process. First, a combination of residual melt and vapor detached as buoyant diapirs near the lobe base from a mush of olivine, plagioclase, melt and vapor, and later these diapirs accumulated primitive olivine and plagioclase in the lava core. HVS1 represent VC that accumulated at the top of the lava core and spread out as sheets, whereas HVS2 formed independently of VC when residual melts seeped into voids within the upper crust of the lobe. At shallow crustal levels, volatile-aided differentiation processes, such as described from the Hafnarhraun lava lobe, might contribute to the generation of the diversity of basaltic magmas.

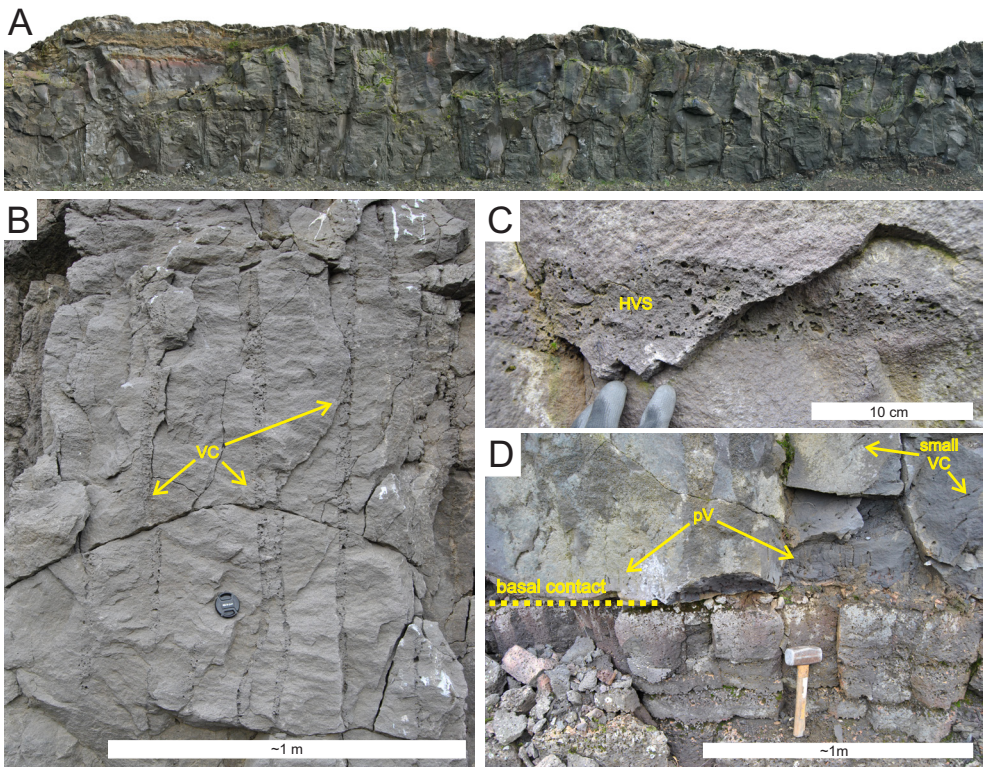

Figure 4. Internal structures of the Hafnarhraun pāhoehoe lobe: a) the studied elongated lava lobe dissected along its crest by a quarry wall, b) vesicle cylinders (VC) in the lava core, c) horizontal vesicle sheet (HVS) in the upper crust d) pipe-vesicles (pV) at the base of the lobe. Photographs by Paavo Nikkola.

6 Discussion

6.1 Dynamics of mantle melting (PAPER I)

The analyses of major, minor and trace elements in olivine macrocrysts from seven Icelandic lavas and one tephra revealed that although most olivine compositions are consistent with a lherzolite mantle as the source of the Iceland basalts, volcanic rocks erupted from Eyjafjallajökull and Vestmannaeyjar in SEVZ carry olivine macrocrysts potentially suggestive of olivine-free, pyroxenitic, mantle source at depth. This is depicted as a kernel density estimation (KDE) in Fig. 5, where I show the compositional parameter of olivine indicating the 'degree of melt derived from olivine-free pyroxenite mantle source' (X_{px}), as parametrized by Gurenko et al. (2010), for Iceland basalts. X_{px} represents the Ni-enrichment and Mn-depletion in olivine at given Fo compared to model-olivines crystallizing from 'canonical' mantle peridotite-derived melts. The Eyjafjallajökull and Vestmannaeyjar olivines show X_{px} values of 0.2–0.7, which are high relative to the X_{px} values of 0–0.4 calculated for olivine grains from the other studied volcanic systems in Iceland.

The X_{px} works well to quantify the difference from olivine expected to crystallize from melts of mantle peridotite, and some have argued for its usefulness as an indicator of the amount of pyroxenite in the mantle source (e.g., Sobolev et al. 2007). However, it is highly doubtful that

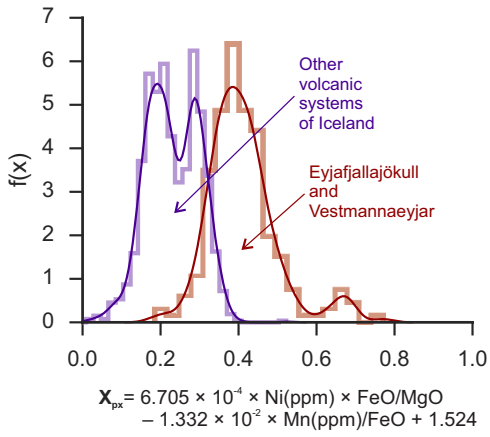

Figure 5. Contribution of melts from pyroxenite mantle to parental magmas (X_{px}) as calculated using the formulation of Gurenko et al. (2010). The curves are kernel density estimates (KDE) fitted with the corresponding histograms of the olivine compositional data. SEVZ olivine data in red and all other Iceland olivine data in violet. Higher X_{px} values can be regarded as representing greater contribution of pyroxenite mantle to aggregated mantle melts (e.g., Sobolev et al., 2007) or higher mantle melting temperatures and greater depth (Matzen et al., 2017b, 2013).

X_{px} has this simple significance, as recent studies demonstrate that higher X_{px} can also reflect an increasing temperature difference between mantle melting and olivine crystallization (Matzen et al., 2017a, b). In addition, mixing between primary and derivate lherzolite magmas can elevate X_{px} (Herzberg et al., 2016). Essentially, in the SEVZ, elevated X_{px} in olivines may simply be attributed to high temperature melting at a great mantle depth caused by the thickened lithosphere in off-rift setting.

Despite the exceptional Ni and Mn contents in SEVZ olivine macrocrysts, other elements in them mainly concur with deep melting of typical olivine-rich lherzolite mantle (KLB-1, Hirose and Kushiro, 1993). I derived this conclusion by modelling the partitioning of Sc, Ti, V and Zn in near-fractional partial melting of a lherzolitic mantle (KLB-1) and then calculating the equilibrium olivine compositions crystallizing from these partial melts, which separate from the mantle at different extents of melting at different depths. In addition, I modelled the composition of olivine crystallizing from partial melts of an olivine-depleted peridotite-pyroxenite hybrid (KG2, Kogiso et al., 1998). The element concentrations of model olivine crystallized from deep-derived, low-degree melts of lherzolite concur with those of the analyzed SEVZ olivine crystals, with the possible exception of Zn, whereas model olivine crystallizing from shallow, high-degree mantle melts are similar to olivine from depleted rift-zone basalt (Háleyjabunga). Even the high Zn in SEVZ olivine grains is not directly indicative of the presence of olivine-free pyroxenite in the mantle source, as an input from KG2 peridotite-pyroxenite hybrid source seems to explain this Zn enrichment.

As nothing in the composition of SEVZ olivine macrocrysts conclusively necessitate olivine-barren pyroxenitic mantle at depth, the deep melting of an olivine-bearing mantle is a more likely candidate in explaining the SEVZ olivine signature. This conclusion is also supported by recent mantle melting models, indicating that relatively silicic melts of olivine-free pyroxenites are prone to react with the surrounding peridotite and hence unlikely to preserve their coherence and compositional signature (Lambart et al., 2012; Lambart, 2017). The high Ni content of the most forsteritic olivine grains suggests a temperature difference between mantle melting and olivine crystallization of 75 ± 3 °C, which, assuming a 55 °C/GPa slope of olivine-saturated liquidus (Sugawara, 2000), translates to a 1.4 GPa pressure difference. Thus, the final mantle equilibration depth of the olivine parental melts must be 45 km or more, if olivine crystallization occurred near the surface, or at depths of 66–81 km, if olivine crystallization occurred in the lower crust (0.6–1.0 GPa pressure). Essentially, I view the SEVZ high-Ni/low-Mn olivine macrocrysts as an indication of the survival of

mantle melts from the deep parts of the mantle melting column, where relatively enriched mantle components like KG2 may reside, to the shallow T–P conditions of olivine crystallization.

Besides SEVZ magmas, deep melting of relatively enriched mantle has been indicated for some rift-zone (Shorttle and Maclennan, 2011) and especially SVZ off-rift magmas (Kokfelt et al., 2006), but there olivine still have MORB-like low-Ni and high-Mn compositions (Herzberg et al., 2016). This is a conundrum: Why the apparent signature of deep mantle melting in olivine from South Iceland magmas in particular? Although I fail to deliver a definitive answer, I suggest that the existence and survival of this signature is due to a favorable crustal and mantle structure below SEVZ. SEVZ is the youngest (activated >3 Ma, Martin et al., 2011) volcanically active zone in Iceland, and hence the underlying mantle may have not yet been depleted in the most fusible domains (e.g., KG2), biasing the melt production to increased depth. In addition, the juvenility of volcanism and low crustal geothermal gradient at SEVZ (Flóvenz and Saemundsson, 1993) is likely reflected in embryonic, small and ephemeral (Sigmarsson, 1996; Mattsson and Oskarsson, 2005) magma storage systems in the crust and upper mantle. These poorly developed magma storage zones favor relatively fast ascent of magmas and allow deep mantle melts to transect the lithosphere with little mixing with mantle melts of shallower origin. This should promote preservation of the deep mantle melting signature in olivine. In contrast, at rift zones and SVZ, magmas derived from different mantle depths and their olivine macrocryst cargo may thoroughly mix and equilibrate in extensive and long-lived crustal magma storage zones, suppressing the potential deep mantle signature in olivine.

This study joins the growing number of other studies expressing skepticism about olivine as a proxy for mantle mineralogy and instead prefer to explain the olivine compositional record as related to the conditions of mantle melting (F, T and P) and subsequent basalt crystallization (Li and Ripley, 2010; Niu et al., 2011; Putirka et al., 2011, 2018; Matzen et al., 2013, 2017b; Heinonen and Fusswinkel, 2017). Nevertheless, major and trace element, as well as isotopic evidence from Iceland lavas suggest the presence of enriched component(s) in the sub-Icelandic mantle (Thirlwall et al., 2004; Shorttle et al., 2014). Moreover, the high-Zn and low-Ca in the analyzed SEVZ olivine grains can be seen suggestive of modally enriched (olivine-poor) mantle source. Therefore, some compositional heterogeneity likely exists in the mantle beneath Iceland.

Recently, Rasmussen et al. (2020) have confirmed the existence of SEVZ olivine signature published in PAPER I, while also presenting a somewhat divergent interpretation regarding the high-Ni and low-Mn in SEVZ olivine macrocrysts. They argue that the SEVZ olivine compositions are, at least partly, indicating pyroxenitic or pyroxenite-peridotite hybrid mantle source, as the lithospheric thickness below SEVZ (~45 km; Árnadóttir et al., 2009; Barnhoorn et al., 2011) is less than the mantle melting depths (up to ~90 km) indicated by NiO/MnO ratios in some of the SEVZ olivine macrocrysts. This argument is reasonable considering the aforementioned notion of the likely existence of enriched mantle components below Iceland; however, it ignores that Icelandic magmas can originate from deeper than the lithosphere-asthenosphere boundary (LAB) and mantle melts do not necessarily equilibrate at LAB before ascending to the lithosphere. Below Iceland, partial melts are sampled from various mantle depths and these melts can keep their compositional coherence at least until mixing and crystallization in crustal intrusions. This is indicated in the trace element and isotopic heterogeneity in melt inclusions (e.g., Maclennan,

2008b, a; Neave et al. 2018) and in geochemical variations in basalts erupted in Iceland rift zones (e.g., Zindler et al., 1979; Shorttle and Maclennan, 2011; Shorttle et al., 2014). SEVZ melts that crystallized the highest Ni and lowest Mn olivine macrocrysts may have been derived deeper than LAB, depths of up to 90 km being still realistic (e.g., Lambart, 2017), and hence elevated NiO/MnO in some olivine macrocrysts at SEVZ does not, by itself, necessitate pyroxenitic mantle source (or any other enriched mantle source) for the region. In addition, the reliability of NiO/MnO in olivine as a mantle indicator, as used in Rasmussen et al. (2020), is hampered in evolved olivine macrocrysts ($Fo_{<88}$), because NiO contents—and thus also NiO/MnO ratios—in olivine crystals are prone to increase in mixing of variably differentiated magmas of a similar mantle source (see Herzberg et al., 2016). Overall, caution is warranted when utilizing NiO and MnO in olivine as an indicator of compositional heterogeneity in the mantle.

For all geochemical mantle proxies (i.e., major and trace element and isotopic composition of magmas), separating the signal of large-scale mantle heterogeneity from that of locally variable conditions of mantle melting is difficult, as the mode of the mantle source and degree and depth of partial melting are expected to be intertwined properties in the production of mantle melts. This dependence is derived from the greater fusibility of modally enriched mantle. Modally enriched mantle domains are only expected to reside in the deep mantle, as partial melting depletes them at a lower pressure. In addition, partial melts of the enriched mantle domains are tapped effectively only at low degrees of partial melting, when they are not diluted by melts of the prevalent depleted mantle. Therefore, if an area—such as SEVZ—erupts magmas suggestive of modally (and isotopically) enriched mantle component at depth, it is not clear whether this component really is (more than usual) abundant below, or if its melts are just tapped effectively by favorable mantle melting (e.g., low melting degree) and transport (e.g. channelized melt flow) conditions. A signal of modally enriched mantle in erupted basalts at a certain area does not necessarily indicate exceptional chemistry in the underlying mantle, as this signal may be due to favorable melting and transport processes, dependent on the physical state of the mantle.

6.2 Magma storage and crystallization in the South Iceland crust (PAPER II)

Analysis of crystals from Eyjafjallajökull ankaramites indicates that at least most of the clinopyroxene and olivine macrocrysts in these rocks have crystallized in mid-crustal pressures (3.0±1.4 kbar), in a large temperature interval (1120–1220 °C), and mostly in absence of plagioclase. In PAPER I, the olivine with high Ni and low Mn contents in these ankaramites did set a minimum mantle equilibration depth of 45 km for the South Iceland magmas. However, if we take 3.0±1.4 kbar as the crystallization pressure of the high-Ni olivine, the final mantle equilibration depth of the olivine host melt is refined to 56±7 km below surface. Furthermore, the high $Cr\#^{spl}$ and TiO_2, and low Al_2O_3 in olivine hosted spinel inclusions identified in PAPER II conform to a deep and enriched mantle source for the olivine host melt suggested by PAPER I.

Fig. 6 depicts the preferred model of crustal ascent and differentiation for Eyjafjallajökull ankaramites. Assuming that the magmatic plumbing system during the formation of Hvammsmúli and Brattaskjól ankaramites resembles the modern volcanic roots of Eyjafjallajökull, multiple lenses of magma reside in the lower crust (A). The degree of solidification of the country rocks at these mid-crustal depths is not certain; however, considering the relatively cold crust at SEVZ

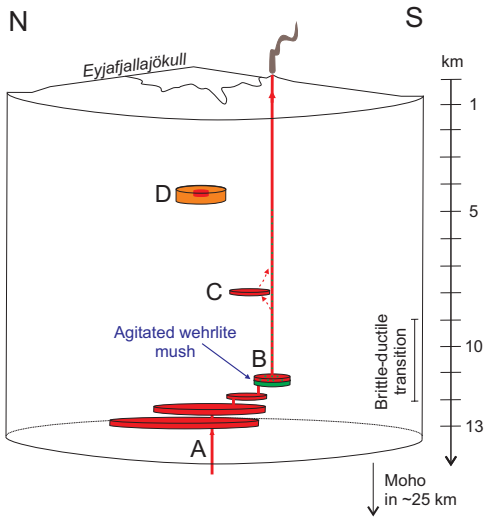

Figure 6. Conceptual model of magma storage below the Eyjafjallajökull volcano. The mantle-derived host magma of the ankaramites ascended and differentiated in mid-crustal magma storage zones (A), agitated a wehrlite crystal-melt mush at 10.7±5 km depth (B), potentially ascended through a shallower intrusion (C), and erupted on the surface. The depth of brittle-ductile transition under Eyjafjallajökull according to Hjaltadóttir et al. (2009). The Eyjafjallajökull 2010 eruption revealed the existence of a benmoreitic magma chamber (D) below the volcano at 5 km depth. It is uncertain whether this evolved magma chamber existed when Hvammsmúli and Brattaskjól ankaramites erupted.

(Flóvenz and Saemundsson, 1993), I envision most of the crust to be below the solidus, and that melt mushes exist only at boundaries of intrusions and near channels of recurring melt transport (see Maclennan, 2019). Somewhere here, a wehrlite mush was agitated and disaggregated to an ascending magma (B). Although all crystallization pressures fall within the 1SEE uncertainty of the Jd-in-clinopyroxene thermometry (±1.4), clinopyroxene with $Mg\#^{cpx}$<83 has the tendency to record lower crystallization pressures. It is thus possible that some clinopyroxene crystallized shallower, maybe in a short-term storage of the magma during magma ascent (C). If the Eyjafjallajökull volcano had a shallow magma chamber (D) during the formation of the Hvammsmúli and Brattaskjól ankaramites, alike it has today, these ankaramite magmas, full of cumulus clinopyroxene and olivine, bypassed it with no interaction.

Identification of mid-crustal formation of a clinopyroxene and olivine-rich mineral assemblage below Eyjafjallajökull is important, in part because clinopyroxene and olivine co-crystallization from SEVZ magmas have been earlier interpreted as indicative of elevated (>8 kbar) magma differentiation pressures (Furman et al., 1991a; Thy, 1991; Mattsson and Oskarsson, 2005). Now, in the light of the new clinopyroxene crystallization pressures, it appears that these lower crustal or upper mantle crystallization conditions are not necessary. This discovery is also timely, as a recent experimental work suggests the co-crystallization of olivine and clinopyroxene from an "enriched end-member" Iceland magma before arrival of plagioclase at the liquidus at only 3 kbar (Neave et al., 2019b). Here, the enriched end-member magma refers to a basaltic magma with high FeO, TiO_2, K_2O and Na_2O contents, and low SiO_2 and CaO contents, compared to depleted end-member basalt in the two-end-member major element classification of Shorttle and Maclennan (2011). SEVZ, where Eyjafjallajökull is located, produce basalts similar to the enriched end-member series (Shorttle and Maclennan, 2011; Shorttle et al., 2014).

If considered in terms of fractional crystallization, the key to stabilizing clinopyroxene before plagioclase in the fractionation assemblage at relatively low pressures is the Ca, Al and H_2O contents in the host magma (Neave et al., 2019b). Addition of water decreases the liquidus temperature of all minerals, but especially plagioclase, suppressing plagioclase crystallization in favor of clinopyroxene and olivine (Gaetani et al., 1993; Feig et al., 2006). Magnesian clinopyroxene could also become stable in intrusive basaltic magma as it evolves while mixing with residual liquids of crystal mushes crystallizing *in situ* near cooling edges of the intrusion (Langmuir, 1989; Hammer et al., 2016). However, yet

there is no need to invoke such a complex model for SEVZ magma genesis, as crystallization experiments with enriched basalts show co-crystallizing olivine and clinopyroxene (Neave et al., 2019b) at 3 kbar. Future research on mush nodules and crustal xenoliths, hosted in many Iceland lavas, should provide deeper insight into how magmatic differentiation really takes place in the Iceland crust.

6.3 Insights to basalt differentiation from the Hafnarhraun lava lobe (PAPER III)

Magmatic differentiation aided by the exsolution of a vapor phase has been invoked to explain differentiated magma lenses and sheets in intrusions (e.g., Carman and Alle, 1994; White, 2007; Zavala et al., 2011), and the formation of crystal-poor Fe-Ti basalts (Sigmarsson et al., 2009) and rhyolites (Parmigiani et al., 2016). In addition, in crustal intrusions, it has been suggested that water vapor can produce density differences in a crystallizing magma body and hence accommodate "bubble-driven convection" (Cardoso and Woods, 1999). The observations from the Hafnarhraun pāhoehoe lobe indicate that vapor exsolution can indeed induce partial convection and compositional variation in solidifying basaltic magma. The effect of vapor on melt circulation was relatively limited, seen as ta sluggish upward movement of segregated material from the solidifying lava base to the upper solidification front, whereas vapor exsolution was efficient in separating residual melts from the bulk crystallizing magma.

In the Hafnarhraun pāhoehoe lobe, vapor-induced differentiation produced two morphological types of vesicular segregation: vesicular cylinders (VC) in the lava core and horizontal vesicle sheets (HVS) in the upper half of the lava lobe. Field evidence and the chemical composition of the segregations suggest that the VC formed as diapirs of residual melt and vapor detached from the lower solidification front of the lava lobe and buoyantly ascended through the lava core. Interestingly, the compositions of VC do not match residual liquids expected to be formed via fractional crystallization of the lobe, as they had accumulated relatively primitive phenocrysts of olivine and microphenocrysts of plagioclase during their ascent in the lava core. HVS, in contrast, developed by two mechanisms, which explains some of the diverging interpretations on the HVS genesis in earlier studies (for example, compare Hartley and Thordarson, 2009; Kuritani et al., 2010). Specifically, HVS can form by accumulation of VC to the upper solidification front of the lobe (mechanism to form HVS1) or when evolved interstitial melts seep into voids in the lava crust (mechanism to form HVS2).

Although volatile exsolution is evidently the culprit in generating chemical heterogeneity within basaltic pāhoehoe lavas, it is uncertain how significant it is for magma differentiation in crustal magmatic systems. Primitive Iceland basalts are expected to be CO_2-saturated but H_2O-undersaturated at mid-crustal (~2–4 kbar) pressures (Lowenstern, 2001), which is their typical pre-ascent storage (Neave and Putirka, 2017; White et al., 2019). Mainly CO_2 (as CO_2-rich fluid) exsolves in response to basalt crystallization at these pressures, and the amount of generated volatiles remains relatively minor. Hence, shallow upper crustal magma storage zones, where H_2O vapor may exist, are more likely environments for volatile-aided differentiation to occur. For example, geophysical anomalies below the Katla volcano are suggestive of a magma chamber at a depth as shallow as 2–3 km (Gudmundsson et al., 1994; Sturkell et al., 2008), and Katla typically produces eruptions of crystal-poor Fe-Ti basalts (Óladóttir et al., 2008). At these low-pressure conditions, and considering the H_2O-en-

riched nature of South Iceland magmas (Moune et al., 2012), differentiation could be aided by exsolution of vapor (Sigmarsson et al., 2009). Furthermore, in more silicic magmas, such as crystal-poor rhyolites, volatile-aided processes of magmatic differentiation are likely important (see Parmigiani et al., 2016) in part due to their higher H_2O content and expansion during volatile saturation (Sisson and Bacon, 1999).

7 Conclusions and future directions

The mantle underneath Iceland must be compositionally heterogeneous. This study, however, did not find evidence of olivine-free domains in the sub-Icelandic mantle. Although an anomalous mantle-source signature in olivine macrocrysts from South Iceland was identified, a closer inspection revealed that these olivines likely crystallized from deep low-degree melts of—potentially somewhat enriched—garnet-peridotite mantle, and an olivine-free mantle source is not necessitated. Future research utilizing isotopic and trace element compositions of South Iceland lavas can build on these findings and better constrain the character of the enriched end-member mantle source below Iceland.

Crystallization of the macrocryst cargo in the Eyjafjallajökull ankaramites Brattaskjól and Hvammsmúli occurred dominantly, if not fully, in the mid-crust (3.0±1.4 kbar; 10.7±5 km). The parental magma (or magmas) had a moderate oxygen fugacity (ΔlogFMQ 0–0.5) and the crystallization occurred over a temperature interval of 1120–1230 °C. The mid-crustal crystallization assemblage was clinopyroxene and olivine, followed by plagioclase, which suggests that elevated lower-crustal pressures (>8 kbar) are not required to produce wehrlitic cumulus assemblages from South Iceland magmas.

At shallow crustal levels, exsolution of volatiles produces density variation in solidifying crystal mushes, which can aid separation of crystals and residual melt. When vapor exsolution occurred within the crystallizing Hafnarhraun pāhoehoe lava lobe, it did not only facilitate separation of residual melt from the bulk crystallizing lava but led to mixing of primitive crystals with these residual melts. As an outcome, magma compositions not predicted by simple models of fractional crystallization were produced. The importance of volatile-aided differentiation in basalt genesis could be elucidated by research on shallow-intrusive bodies aimed to constrain the extent at which vapor exsolution accommodates separation of melts from crystal mushes at various crustal settings.

References

Allègre, J. C., Staudacher, T. and Sarda, P. 1987 Rare gas systematics: formation of the atmosphere, evolution and structure of the Earth's mantle. Earth Planet Sci Lett 81, 127–150. https://doi.org/10.1016/0012-821X(87)90151-8

Anderson, A. T., Swihart, G. H., Artioli, G. and Geiger, C. A. 1984 Segregation vesicles, gas filterpressing, and igneous differentiation. J Geol 92, 55–72. https://doi.org/10.1086/628834

Ariskin, A. A. 1999 Phase equilibria modeling in igneous petrology: use of COMAGMAT model for simulating fractionation of ferro-basaltic magmas and the genesis of high-alumina basalt. J Volcanol Geotherm Res 90, 115–162. https://doi.org/10.1016/S0377-0273(99)00022-0

Ariskin, A. A., Bychkov, K. A., Nikolaev, G. S. and Barmina, G. S. 2018 The COMAGMAT-5: Modeling the effect of Fe-Ni sulfide immiscibility in crystallizing magmas and cumulates. J Petrol 59, 283–298. https://doi.org/10.1093/petrology/egy026

Árnadóttir, T., Lund, B., Jiang, W., et al. 2009 Glacial rebound and plate spreading: Results from the first countrywide GPS observations in Iceland. Geophys J Int 177, 691–716. https://doi.org/10.1111/j.1365-246X.2008.04059.x

Baker, M. B. and Stolper, E. M. 1994 Determining the composition of high-pressure mantle melts using diamond aggregates. Geochim Cosmochim Acta 58, 2811–2827. https://doi.org/10.1016/0016-

7037(94)90116-3
Ballhaus, C., Berry, R. F. and Green, D. H. 1991 High pressure experimental calibration of the olivine-orthopyroxene-spinel oxygen geobarometer: implications for the oxidation state of the upper mantle. Contrib Mineral Petrol 107, 27–40
Barnhoorn, A., van der Wal, W. and Drury, M. R. 2011 Upper mantle viscosity and lithospheric thickness under Iceland. J Geodyn 52, 260–270. https://doi.org/10.1016/j.jog.2011.01.002
Batanova, V. G., Sobolev, A. V. and Kuzmin, D. V. 2015 Trace element analysis of olivine: High precision analytical method for JEOL JXA-8230 electron probe microanalyser. Chem Geol 419, 149–157. https://doi.org/10.1016/j.chemgeo.2015.10.042
Beattie, P. 1993 Olivine-melt and orthopyroxene-melt equilibria. Contrib Mineral Petrol 115, 103–111. https://doi.org/10.1007/BF00712982
Bédard, J. H. 1993 Oceanic crust as a reactive filter: Synkinematic intrusion, hybridization, and assimilation in an ophiolitic magma chamber, western Newfoundland. Geology 21, 77. https://doi.org/10.1130/0091-7613(1993)021<0077:OCAARF>2.3.CO;2
Brounce, M., Feineman, M., LaFemina, P. and Gurenko, A. 2012 Insights into crustal assimilation by Icelandic basalts from boron isotopes in melt inclusions from the 1783-1784 Lakagígar eruption. Geochim Cosmochim Acta 94, 164–180. https://doi.org/10.1016/j.gca.2012.07.002
Brown, E. L. and Lesher, C. E. 2014 North Atlantic magmatism controlled by temperature, mantle composition and buoyancy. Nat Geosci 7, 820–824. https://doi.org/10.1038/ngeo2264
Caracciolo, A., Bali, E., Guðfinnsson, G. H., et al. 2019 Temporal evolution of magma and crystal mush storage conditions in the Bárðarbunga-Veiðivötn volcanic system, Iceland. Lithos. https://doi.org/10.1016/j.lithos.2019.105234
Cardoso, S. S. S. and Woods, A. W. 1999 On convection in a volatile-saturated magma. Earth Planet Sci Lett 168, 301–310. https://doi.org/10.1016/S0012-821X(99)00057-6
Carman, M. F. and Alle. 1994 Mechanisms of differentiation in shallow mafic alkaline instrusions, as illustrated in the Big Bend area, western Texas. J Volcanol Geotherm Res 61, 1–44. https://doi.org/10.1016/0377-0273(94)00008-5
Caroff, M., Maury, R. C., Cotten, J., et al. 2000 Segregation structures in vapor-differentiated basaltic flows. Bull Volcanol 62, 171–187. https://doi.org/10.1007/s004450000077
Cashman, K. V., Sparks, R. S. J. and Blundy, J. D. 2017 Vertically extensive and unstable magmatic systems: A unified view of igneous processes. Science 355, 1–9. https://doi.org/10.1126/science.aag3055
Chauvel, C. and Hémond, C. 2000 Melting of a complete section of recycled oceanic crust: Trace element and Pb isotopic evidence from Iceland. Geochem, Geophys Geosys 1, 1–22. https://doi.org/10.1029/1999GC000002
Clifton, A. E. and Kattenhorn, S. A. 2006 Structural architecture of a highly oblique divergent plate boundary segment. Tectonophysics 419, 27–40. https://doi.org/10.1016/j.tecto.2006.03.016
Costa, F., Dohmen, R. and Chakraborty, S. 2008 Time scales of magmatic processes from modeling the zoning patterns of crystals. Rev Mineral Geochem 69, 545–594. https://doi.org/10.2138/rmg.2008.69.14
Danyushevsky, L. V., Della-Pasqua, F. N. and Sokolov, S. 2000 Re-equilibration of melt inclusions trapped by magnesian olivine phenocrysts from subduction-related magmas: Petrological implications. Contrib Mineral Petrol 138, 68–83. https://doi.org/10.1007/PL00007664
Danyushevsky, L. V. and Plechov, P. 2011 Petrolog3: Integrated software for modeling crystallization processes. Geochem, Geophys Geosys 12. https://doi.org/10.1029/2011GC003516
Darbyshire, F. A., White, R. S. and Priestley, K. F. 2000 Structure of the crust and uppermost mantle of Iceland from a combined seismic and gravity study. Earth Planet Sci Lett 181, 409–428. https://doi.org/10.1016/S0012-821X(00)00206-5
Darwin CR (1844) Geological observations on the volcanic islands visited during the voyages of 519 H.M.S. Beagle, with brief notices on the geology of Australia and the Cape of Good Hope, being the second part of the Voyage of the Beagle. Smith Elder & Co., London.
Davidson, J. P., Morgan, D. J., Charlier, B. L. A., et al. 2007 Microsampling and isotopic analysis of igneous rocks: Implications for the study of magmatic systems. Ann Rev Earth Planet Sci 35, 273–311. https://doi.org/10.1146/annurev.earth.35.031306.140211
Dohmen, R. and Chakraborty, S. 2007 Fe–Mg diffusion in olivine II: point defect chemistry, change of diffusion mechanisms and a model for calculation of diffusion coefficients in natural olivine. Phys Chem Miner 34, 409–430. https://doi.org/10.1007/s00269-007-0158-6
Dohmen, R., Becker, H.-W. and Chakraborty, S. 2007 Fe–Mg diffusion in olivine I: experimental determination between 700 and 1,200°C as a function of composition, crystal orientation and oxygen fugacity. Phys Chem Miner 34, 389–407. https://doi.org/10.1007/s00269-007-0157-7
Dohmen, R., Faak, K. and Blundy, J. D. 2017 Chronometry and speedometry of magmatic processes using chemical diffusion in olivine, plagioclase and pyroxenes. Rev Mineral Geochem. https://doi.org/10.2138/rmg.2017.83.16
Einarsson, P. 2010 Mapping of Holocene surface ruptures in the South Iceland Seismic Zone. Jökull 60, 117–134

Feig, S. T., Koepke, J. and Snow, J. E. 2006 Effect of water on tholeiitic basalt phase equilibria: An experimental study under oxidizing conditions. Contrib Mineral Petrol 152, 611–638. https://doi.org/10.1007/s00410-006-0123-2

Fitton, J., Saunders, A., Norry, M., et al. 1997 Thermal and chemical structure of the Iceland plume. Earth Planet Sci Lett Planet Sci Lett 153, 197–208. https://doi.org/10.1016/S0012-821X(97)00170-2

Flóvenz, Ó. G. and Saemundsson, K. 1993 Heat flow and geothermal processes in Iceland. Tectonophysics 225, 123–138. https://doi.org/10.1016/0040-1951(93)90253-G

Flude, S., McGarvie, D. W., Burgess, R. and Tindle, A. G. 2010 Rhyolites at Kerlingarfjöll, Iceland: The evolution and lifespan of silicic central volcanoes. Bull Volcanol 72, 523–538. https://doi.org/10.1007/s00445-010-0344-0

French, S. W. and Romanowicz, B. 2015 Broad plumes rooted at the base of the Earth's mantle beneath major hotspots. Nature 525, 95–99. https://doi.org/10.1038/nature14876

Fryer, B. J., Jackson, S. E. and Longerich, H. P. 1995 The design, operation and role of the laser-Ablation microprobe coupled with an inductively-coupled plasma - mass-spectrometer (LAM–ICP–MS) in the Earth-Sciences. Can Mineral 33:303–312

Furman, T., Frey, F. A. and Park, K. H. 1991a Chemical constraints on the petrogenesis of mildly alkaline lavas from Vestmannaeyjar, Iceland: the Eldfell (1973) and Surtsey (1963-1967) eruptions. Contrib Mineral Petrol 109, 19–37. https://doi.org/10.1007/BF00687198

Furman, T., Frey, F. A. and Park, K. H. 1991b Chemical constraints on the petrogenesis of mildly alkaline lavas from Vestmannaeyjar, Iceland: the Eldfell (1973) and Surtsey (1963-1967) eruptions. Contrib Mineral Petrol 109, 19–37. https://doi.org/10.1007/BF00687198

Gaetani, G. A., Grove, T. L. and Bryan, W. B. 1993 The influence of water on the petrogenesis of subduction related igneous rocks. Nature 365, 332–334. https://doi.org/10.1038/365332a0

Ghiorso, M. S. 1994 Algorithms for the estimation of phase stability in heterogeneous thermodynamic systems. Geochim Cosmochim Acta 58, 5489–5501. https://doi.org/10.1016/0016-7037(94)90245-3

Ghiorso, M. S., Hirschmann, M. M., Reiners, P. W. and Kress, V. C. 2002 The pMELTS: A revision of MELTS for improved calculation of phase relations and major element partitioning related to partial melting of the mantle to 3 GPa. Geochem, Geophys Geosys 3, 1–35. https://doi.org/10.1029/2001GC000217

Goff, F. 1996 Vesicle cylinders in vapor-differentiated basalt flows. J Volcanol Geotherm Res 71, 167–185. https://doi.org/10.1016/0377-0273(95)00073-9

Green, D. H. and Ringwood, A. E. 1963 Mineral assemblages in a model mantle composition. J Geophys Res 68, 937–945. https://doi.org/10.1029/JZ068i003p00937

Green, D. H. and Ringwood, A. E. 1967 The genesis of basaltic magmas. Contrib Mineral Petrol 15, 103–190. https://doi.org/10.1007/BF00372052

Greenfield, T. and White, R. S. 2015 Building Icelandic igneous crust by repeated melt injections. J Geophys Res Solid Earth 120, 7771–7788. https://doi.org/10.1002/2015JB012009

Gudmundsson, O., Brandsdottir, B., Menke, W. and Sigvaldason, G. E. 1994 The crustal magma chamber of the Katla volcano in south Iceland revealed by 2-D seismic undershooting. Geophys J Int 119, 277–296. https://doi.org/10.1111/j.1365-246X.1994.tb00928.x

Guillong, M., Meier, D. L., Allan, M. M., et al. 2008 SILLS: A matlab-based program for the reduction of laser ablation ICP–MS data of homogeneous materials and inclusions. Mineral Assoc Canada Short Course 40, 328–333

Gurenko, A. A., Hoernle, K. A., Sobolev, A. V., et al. 2010 Source components of the Gran Canaria (Canary Islands) shield stage magmas: evidence from olivine composition and Sr–Nd–Pb isotopes. Contrib Mineral Petrol 159, 689–702. https://doi.org/10.1007/s00410-009-0448-8

Halldorsson, S. A., Oskarsson, N., Gronvold, K., et al. 2008 Isotopic-heterogeneity of the Thjorsa lava-Implications for mantle sources and crustal processes within the Eastern Rift Zone, Iceland. Chem Geol 255, 305–316. https://doi.org/10.1016/j.chemgeo.2008.06.050

Hammer, J. E. 2008 Experimental studies of the kinetics and energetics of magma crystallization. Rev Mineral Geochem 69, 9–59. https://doi.org/10.2138/rmg.2008.69.2

Hammer, J., Jacob, S., Welsch, B., et al. 2016 Clinopyroxene in postshield Haleakala ankaramite: 1. Efficacy of thermobarometry. Contrib Mineral Petrol 171, 1–23. https://doi.org/10.1007/s00410-015-1212-x

Hansen, H. and Grönvold, K. 2000 Plagioclase ultraphyric basalts in Iceland: The mush of the rift. J Volcanol Geotherm Res 98, 1–32. https://doi.org/10.1016/S0377-0273(99)00189-4

Harðardóttir, S., Halldórsson, S. A. and Hilton, D. R. 2018 Spatial distribution of helium isotopes in Icelandic geothermal fluids and volcanic materials with implications for location, upwelling and evolution of the Icelandic mantle plume. Chem Geol 480, 12–27. https://doi.org/10.1016/j.chemgeo.2017.05.012

Hardarson, B. S., Fitton, J. G., Ellam, R. M. and Pringle, M. S. 1997 Rift relocation — A geochemical and geochronological investigation of a palaeo-rift in northwest Iceland. Earth Planet Sci Lett

153, 181–196. https://doi.org/10.1016/S0012-821X(97)00145-3
Hards, V., Kempton, P., Thompson, R. and Greenwood, P. 2000 The magmatic evolution of the Snæfell volcanic centre; an example of volcanism during incipient rifting in Iceland. J Volcanol Geotherm Res 99, 97–121. https://doi.org/10.1016/S0377-0273(00)00160-8
Hart, S. R., Schilling, J. G. and Powell, J. L. 1973 Basalts from Iceland and along the Reykjanes Ridge: Sr isotope geochemistry. Nat Phys Sci 246, 104–107. http://doi.org10.1038/physci246104a0
Hartley, M. and Maclennan, J. 2018 Magmatic densities control erupted volumes in Icelandic volcanic systems. Front Earth Sci 6, 1–9. https://doi.org/10.3389/feart.2018.00029
Hartley, M. E. and Thordarson, T. 2009 Melt segregations in a Columbia River Basalt lava flow: A possible mechanism for the formation of highly evolved mafic magmas. Lithos 112, 434–446. https://doi.org/10.1016/j.lithos.2009.04.003
Heinonen, J. S. and Fusswinkel, T. 2017 High Ni and low Mn/Fe in olivine phenocrysts of the Karoo meimechites do not reflect pyroxenitic mantle sources. Chem Geol 467, 134–142. https://doi.org/10.1016/j.chemgeo.2017.08.002
Hemond, C., Arndt, N. T., Lichtenstein, U., et al. 1993 The heterogeneous Iceland plume: Nd-Sr-O isotopes and trace element constraints. J Geophys Res 98, 15833. https://doi.org/10.1029/93JB01093
Herzberg, C. T. 2004 Partial crystallization of mid-ocean ridge basalts in the crust and mantle. J Petrol 45, 2389–2405. https://doi.org/10.1093/petrology/egh040
Herzberg, C. T. 2011 Identification of source lithology in the Hawaiian and Canary Islands: Implications for origins. J Petrol 52, 113–146. https://doi.org/10.1093/petrology/egq075
Herzberg, C. T. and Asimow, P. D. 2015 PRIMELT3 MEGA.XLSM software for primarymagma calculation: Peridotite primarymagma MgO contents fromthe liquidus to the solidus. Geochem, Geophys Geosys 16, 563–578. https://doi.org/10.1002/2014GC005631
Herzberg, C. T., Vidito, C., Starkey, N. A., et al. 2016 Nickel-cobalt contents of olivine record origins of mantle peridotite and related rocks. Am Mineral 101, 1952–1966. https://doi.org/10.2138/am-2016-5538
Hill, E., Blundy, J. D. and Wood, B. J. 2011 Clinopyroxene-melt trace element partitioning and the development of a predictive model for HFSE and Sc. Contrib Mineral Petrol 161, 423–438. https://doi.org/10.1007/s00410-010-0540-0
Hirose, K. and Kushiro, I. 1993 Partial melting of dry peridotites at high pressures: Determination of compositions of melts segregated from peridotite using aggregates of diamond. Earth Planet Sci Lett 114, 477–489. https://doi.org/10.1016/0012-821X(93)90077-M
Hjaltadóttir, S., Vogfjörð, K. S. and Slunga, R. 2009 Seismic signs of magma pathways through the crust in the Eyjafjallajökull volcano, South Iceland. Icelandic Meteorol Off Rep Vi 2009-013, 1–33
Hofmann, A. W. 1988 Chemical differentiation of the Earth: the relationship between mantle, continental crust, and oceanic crust. Earth Planet Sci Lett. https://doi.org/10.1016/0012-821X(88)90132-X
Hole, M. J. and Natland, J. H. 2019 Magmatism in the North Atlantic Igneous Province; mantle temperatures, rifting and geodynamics. Earth-Sci Rev 1–24. https://doi.org/10.1016/j.earscirev.2019.02.011
Humphreys, F. J. 2001 Grain and subgrain characterisation by electron backscatter diffraction. J Mater Sci 36, 3833–3854. https://doi.org/10.1023/A:1017973432592
Jakobsson, S. P. 1972 Chemistry and distribution pattern of recent basaltic rocks in Iceland. Lithos 5, 365–386. https://doi.org/10.1016/0024-4937(72)90090-4
Jakobsson, S. P., Jónasson, K. and Sigurðsson, I. 2008 The three igneous rock series of Iceland. Jökull 58, 117–138
Jaques, A. L. and Green, D. H. 1980 Anhydrous melting of peridotite at 0-15 Kb pressure and the genesis of tholeiitic basalts. Contrib Mineral Petrol 73, 287–310. https://doi.org/10.1007/BF00381447
Jenkins, J., Cottaar, S., White, R. S. and Deuss, A. 2016 Depressed mantle discontinuities beneath Iceland: Evidence of a garnet controlled 660 km discontinuity? Earth Planet Sci Lett 433, 159–168. https://doi.org/10.1016/j.epsl.2015.10.053
Kahl, M., Chakraborty, S., Costa, F. and Pompilio, M. 2011 Dynamic plumbing system beneath volcanoes revealed by kinetic modeling, and the connection to monitoring data: An example from Mt. Etna. Earth Planet Sci Lett 308, 11–22. https://doi.org/10.1016/j.epsl.2011.05.008
Kahl, M., Chakraborty, S., Pompilio, M. and Costa, F. 2015 Constraints on the nature and evolution of the magma plumbing system of Mt. Etna volcano (1991–2008) from a combined thermodynamic and kinetic modelling of the compositional record of minerals. J Petrol 56, 2025–2068. https://doi.org/10.1093/petrology/egv063
Kahl, M., Viccaro, M., Ubide, T., et al. 2017 A branched magma feeder system during the 1669 eruption of Mt Etna: Evidence from a time-integrated study of zoned olivine phenocryst populations. J Petrol 58, 443–472. https://doi.org/10.1093/petrology/egx022
Kelley, D. F. and Barton, M. 2008 Pressures of crystallization of Icelandic magmas. J Petrol 49, 465–492. https://doi.org/10.1093/petrology/egm089
Kogiso, T., Hirose, K. and Takahashi, E. 1998 Melting experiments on homogeneous mixtures of perido-

tite and basalt: application to the genesis of ocean island basalts. Earth Planet Sci Lett 162, 45–61. https://doi.org/10.1016/S0012-821X(98)00156-3

Kokfelt, T. F., Hoernle, K., Hauff, F., et al. 2006 Combined trace element and Pb-Nd-Sr-O isotope evidence for recycled oceanic crust (upper and lower) in the Iceland mantle plume. J Petrol 47, 1705–1749. https://doi.org/10.1093/petrology/egl025

Kuritani, T., Yoshida, T. and Nagahashi, Y. 2010 Internal differentiation of Kutsugata lava flow from Rishiri Volcano, Japan: Processes and timescales of segregation structures' formation. J Volcanol Geotherm Res 195, 57–68. https://doi.org/10.1016/j.jvolgeores.2010.06.003

Lambart, S. 2017 No direct contribution of recycled crust in Icelandic basalts. Geochemical Perspect Lett 7–12. https://doi.org/10.7185/geochemlet.1728

Lambart, S., Laporte, D., Provost, A. and Schiano, P. 2012 Fate of pyroxenite-derived melts in the peridotitic mantle: Thermodynamic and experimental constraints. J Petrol 53, 451–476. https://doi.org/10.1093/petrology/egr068

Langmuir, C. H., Bender, J. F., Bence, A. E., et al. 1977 Petrogenesis of basalts from the FAMOUS area: Mid-Atlantic Ridge. Earth Planet Sci Lett 36, 133–156. https://doi.org/10.1016/0012-821X(77)90194-7

Langmuir, C. H. 1989 Geochemical consequences of in situ crystallization. Nature 340, 199–205. https://doi.org/10.1038/340199a0

Langmuir, C. and Forsyth, D. 2007 Mantle melting beneath mid-ocean ridges. Oceanography 20, 78–89. https://doi.org/10.5670/oceanog.2007.82

Li, C. and Ripley, E. M. 2010 The relative effects of composition and temperature on olivine-liquid Ni partitioning: Statistical deconvolution and implications for petrologic modeling. Chem Geol 275, 99–104. https://doi.org/10.1016/j.chemgeo.2010.05.001

Loughlin, S. C. 1995 The evolution of the Eyjafjoll volcanic system, southern Iceland. Geology 319

Lowenstern, J. B. 2001 Carbon dioxide in magmas and implications for hydrothermal systems. Mineral Deposita 36, 490–502. https://doi.org/10.1007/s001260100185

Maclennan, J. 2008a Lead isotope variability in olivine-hosted melt inclusions from Iceland. Geochim Cosmochim Acta 72, 4159–4176. https://doi.org/10.1016/j.gca.2008.05.034

Maclennan, J. 2008b Concurrent mixing and cooling of melts under Iceland. J Petrol 49, 1931–1953. https://doi.org/10.1093/petrology/egn052

Maclennan, J. 2019 Mafic tiers and transient mushes: Evidence from Iceland. Philos Trans R Soc A Math Phys Eng Sci 377, 1–20. https://doi.org/10.1098/rsta.2018.0021

Maclennan, J., Mckenzie, D. and Gronvold, K. 2001a Plume-driven upwelling under Central Iceland. Earth Planet Sci Lett 194, 67–82. https://doi.org/10.1016/S0012-821X(01)00553-2

Maclennan, J., McKenzie, D., Gronvöld, K. and Slater, L. 2001b Crustal accretion under Northern Iceland. Earth Planet Sci Lett 191, 295–310. https://doi.org/10.1016/S0012-821X(01)00420-4

Martin, E., Paquette, J. L., Bosse, V., et al. 2011 Geodynamics of rift-plume interaction in Iceland as constrained by new $^{40}Ar/^{39}Ar$ and in situ U-Pb zircon ages. Earth Planet Sci Lett 311, 28–38. https://doi.org/10.1016/j.epsl.2011.08.036

Mattsson, H. B. and Oskarsson, N. 2005 Petrogenesis of alkaline basalts at the tip of a propagating rift: Evidence from the Heimaey volcanic centre, south Iceland. J Volcanol Geotherm Res 147, 245–267. https://doi.org/10.1016/j.jvolgeores.2005.04.004

Matzen, A. K., Baker, M. B., Beckett, J. R. and Stolper, E. M. 2013 The temperature and pressure dependence of nickel partitioning between olivine and silicate melt. J Petrol 54, 2521–2545. https://doi.org/10.1093/petrology/egt055

Matzen, A. K., Baker, M. B., Beckett, J. R., et al. 2017a The effect of liquid composition on the partitioning of Ni between olivine and silicate melt. Contrib Mineral Petrol 172, 3. https://doi.org/10.1007/s00410-016-1319-8

Matzen, A. K., Wood, B. J., Baker, M. B. and Stolper, E. M. 2017b The roles of pyroxenite and peridotite in the mantle sources of oceanic basalts. Nat Geosci 10, 530–535. https://doi.org/10.1038/ngeo2968

McDonough, W. F. and Sun, S. s. 1995 The composition of the Earth. Chem Geol 120, 223–253. https://doi.org/10.1016/0009-2541(94)00140-4

Mckenzie, D. and O'nions, R. K. 1991 Partial melt distributions from inversion of rare earth element concentrations. J Petrol. https://doi.org/10.1093/petrology/32.5.1021

Mollo, S., Del Gaudio, P., Ventura, G., et al. 2010 Dependence of clinopyroxene composition on cooling rate in basaltic magmas: Implications for thermobarometry. Lithos 118, 302–312. https://doi.org/10.1016/j.lithos.2010.05.006

Mollo, S., Putirka, K., Misiti, V., et al. 2013 A new test for equilibrium based on clinopyroxene-melt pairs: Clues on the solidification temperatures of Etnean alkaline melts at post-eruptive conditions. Chem Geol 352, 92–100. https://doi.org/10.1016/j.chemgeo.2013.05.026

Moorbath, S., Sigurdsson, H. and Goodwin, R. 1968 K–Ar ages of the oldest exposed rocks in Iceland. Earth Planet Sci Lett 4, 197–205. https://doi.org/10.1016/0012-821X(68)90035-6

Moune, S., Sigmarsson, O., Schiano, P., et al. 2012 Melt inclusion constraints on the magma source of Eyjafjallajökull 2010 flank eruption. J Geophys Res Solid Earth 117, 1–13. https://doi.org/10.1029/2011JB008718

Mutch, E. J. F., Maclennan, J., Holland, T. J. B. and

Buisman, I. 2019a Millennial storage of near-Moho magma. Science 365, 260–264. https://doi.org/10.1126/science.aax4092

Mutch, E. J. F., Maclennan, J., Shorttle, O., et al. 2019b Rapid transcrustal magma movement under Iceland. Nat Geosci 12, 569–574. https://doi.org/10.1038/s41561-019-0376-9

Neave, D. A., Passmore, E., Maclennan, J., et al. 2013 Crystal-melt relationships and the record of deep mixing and crystallization in the ad 1783 laki eruption, Iceland. J Petrol 54, 1661–1690. https://doi.org/10.1093/petrology/egt027

Neave, D. A., Maclennan, J., Hartley, M. E., et al. 2014 Crystal storage and transfer in basaltic systems: The Skuggafjöll eruption, Iceland. J Petrol 55, 2311–2346. https://doi.org/10.1093/petrology/egu058

Neave, D. A. and Putirka, K. D. 2017 A new clinopyroxene-liquid barometer, and implications for magma storage pressures under Icelandic rift zones. Am Mineral 102, 777–794. https://doi.org/10.2138/am-2017-5968

Neave, D. A., Shorttle, O., Oeser, M., et al. 2018 Mantle-derived trace element variability in olivines and their melt inclusions. Earth Planet Sci Lett 483, 90–104. https://doi.org/10.1016/j.epsl.2017.12.014

Neave, D. A., Bali, E., Guðfinnsson, G. H., et al. 2019a Clinopyroxene–liquid equilibria and geothermobarometry in natural and experimental tholeiites: the 2014–2015 Holuhraun eruption, Iceland. J Petrol. https://doi.org/10.1093/petrology/egz042

Neave, D. A., Namur, O., Shorttle, O. and Holtz, F. 2019b Magmatic evolution biases basaltic records of mantle chemistry towards melts from recycled sources. Earth Planet Sci Lett 520, 199–211. https://doi.org/10.1016/j.epsl.2019.06.003

Nikolaev, G. S., Ariskin, A. A., Barmina, G. S., et al. 2016 Test of the Ballhaus–Berry–Green Ol–Opx–Sp oxybarometer and calibration of a new equation for estimating the redox state of melts saturated with olivine and spinel. Geochemistry Int 54, 301–320. https://doi.org/10.1134/S0016702916040078

Niu, Y., Wilson, M., Humphreys, E. R. and O'Hara, M. J. 2011 The origin of intra-plate ocean island basalts (OIB): The lid effect and its geodynamic implications. J Petrol 52, 1443–1468. https://doi.org/10.1093/petrology/egr030

O'Hara, M. J. 1968 The bearing of phase equilibria studies in synthetic and natural systems on the origin and evolution of basic and ultrabasic rocks. Earth-Sci Rev 4, 69–133. https://doi.org/10.1016/0012-8252(68)90147-5

Óladóttir, B. A., Sigmarsson, O., Larsen, G. and Thordarson, T. 2008 Katla volcano, Iceland: Magma composition, dynamics and eruption frequency as recorded by Holocene tephra layers. Bull Volcanol 70, 475–493. https://doi.org/10.1007/s00445-007-0150-5

Oskarsson, N., Sigvaldason, G. E. and Steinthórsson, S. 1982 A dynamic model of rift zone petrogenesis and the regional petrology of Iceland. J Petrol 23, 28–74. https://doi.org/10.1093/petrology/23.1.28

Oskarsson, N., Steinthorsson, S. and Sigvaldason, G. E. 1985 Iceland geochemical anomaly: Origin, volcanotectonics, chemical fractionation and isotope evolution of the crust. J Geophys Res 90, 10011. https://doi.org/10.1029/JB090iB12p10011

Pankhurst, M. J., Morgan, D. J., Thordarson, T. and Loughlin, S. C. 2018 Magmatic crystal records in time, space, and process, causatively linked with volcanic unrest. Earth Planet Sci Lett 493, 231–241. https://doi.org/10.1016/j.epsl.2018.04.025

Parmigiani, A., Faroughi, S., Huber, C., et al. 2016 Bubble accumulation and its role in the evolution of magma reservoirs in the upper crust. Nature 532, 492–495. https://doi.org/10.1038/nature17401

Philpotts, A. R., Carroll, M. and Hill, J. M. 1996 Crystal-mush compaction and the origin of pegmatitic segregation sheets in a thick flood-basalt flow in the Mesozoic Hartford Basin, Connecticut. J Petrol 37, 811–836. https://doi.org/10.1093/petrology/37.4.811

Pistone, M., Arzilli, F., Dobson, K. J., et al. 2015 Gas-driven filter pressing in magmas: Insights into in-situ melt segregation from crystal mushes. Geology 43, 699–702. https://doi.org/10.1130/G36766.1

Presnall, D. C. and Gudfinnsson, G. H. 2011 Oceanic volcanism from the low-velocity zone - without mantle plumes. J Petrol 52, 1533–1546. https://doi.org/10.1093/petrology/egq093

Presnall, D. C., Dixon, S. A., Dixon, J. R., et al. 1978 Liquidus phase relations on the join diopside-forsterite-anorthite from 1 atm to 20 kbar: Their bearing on the generation and crystallization of basaltic magma. Contrib Mineral Petrol 66, 203–220. https://doi.org/10.1007/BF00372159

Presnall, D. C., Gudfinnsson, G. H. and Walter, M. J. 2002 Generation of mid-ocean ridge basalts at pressures from 1 to 7 GPa. Geochim Cosmochim Acta 66, 2073–2090. https://doi.org/10.1016/S0016-7037(02)00890-6

Prior, D. J., Boyle, A. P., Brenker, F., et al. 1999 The application of electron backscatter diffraction and orientation contrast imaging in the SEM to textural problems in rocks. Am Mineral 84, 1741–1759. https://doi.org/10.2138/am-1999-11-1204

Putirka, K. 1999 Clinopyroxene + liquid equilibria to 100 kbar and 2450 K. Contrib Mineral Petrol 135, 151–163. https://doi.org/10.1007/s004100050503

Putirka, K. 2008a Excess temperatures at ocean islands: Implications for mantle layering and convection. Geology 36, 283. https://doi.org/10.1130/G24615A.1

Putirka, K. D. 2008b Thermometers and barometers

for volcanic systems. Rev Mineral Geochem 69, 61–120. https://doi.org/10.2138/rmg.2008.69.3

Putirka, K. 2016 Rates and styles of planetary cooling on Earth, Moon, Mars, and Vesta, using new models for oxygen fugacity, ferric-ferrous ratios, olivine-liquid Fe-Mg exchange, and mantle potential temperature. Am Mineral 101, 819–840. https://doi.org/10.2138/am-2016-5402

Putirka, K., Johnson, M., Kinzler, R., et al. 1996 Thermobarometry of mafic igneous rocks based on clinopyroxene-liquid equilibria, 0-30 kbar. Contrib Mineral Petrol 123, 92–108. https://doi.org/10.1007/s004100050145

Putirka, K., Ryerson, F. J., Perfit, M. and Ridley, W. I. 2011 Mineralogy and composition of the oceanic mantle. J Petrol 52, 279–313. https://doi.org/10.1093/petrology/egq080

Putirka, K. D., Mikaelian, H., Ryerson, F. and Shaw, H. 2003 New clinopyroxene-liquid thermobarometers for mafic, evolved, and volatile-bearing lava compositions, with applications to lavas from Tibet and the Snake River Plain, Idaho. Am Mineral 88, 1542–1554. https://doi.org/10.2138/am-2003-1017

Putirka, K. D., Perfit, M., Ryerson, F. J. and Jackson, M. G. 2007 Ambient and excess mantle temperatures, olivine thermometry, and active vs. passive upwelling. Chem Geol 241, 177–206. https://doi.org/10.1016/j.chemgeo.2007.01.014

Putirka, K., Tao, Y., Hari, K. R. R., et al. 2018 The mantle source of thermal plumes: Trace and minor elements in olivine and major oxides of primitive liquids (and why the olivine compositions don't matter). Am Mineral 103, 1253–1270. https://doi.org/10.2138/am-2018-6192

Rae, A. S. P., Edmonds, M., Maclennan, J., et al. 2016 Time scales of magma transport and mixing at Kīlauea Volcano, Hawai'i. Geology 44, 463–466. https://doi.org/10.1130/G37800.1

Rasmussen, M. B., Halldórsson, S. A., Gibson, S. A. and Guðfinnsson, G. H. 2020 Olivine chemistry reveals compositional source heterogeneities within a tilted mantle plume beneath Iceland. Earth Planet Sci Lett 531, 116008. https://doi.org/10.1016/j.epsl.2019.116008

Schilling, J. G. 1973 Iceland mantle plume: Geochemical study of Reykjanes Ridge. Nature 242, 565–571. https://doi.org/10.1038/242565a0

Shorttle, O. and Maclennan, J. 2011 Compositional trends of Icelandic basalts: Implications for short-length scale lithological heterogeneity in mantle plumes. Geochem, Geophys Geosys 12. https://doi.org/10.1029/2011GC003748

Shorttle, O., Maclennan, J. and Lambart, S. 2014 Quantifying lithological variability in the mantle. Earth Planet Sci Lett 395, 24–40. https://doi.org/10.1016/j.epsl.2014.03.040

Sigmarsson, O. 1996 Short magma chamber residence time at an Icelandic volcano inferred from U-series disequilibria. Nature 382, 440–442. https://doi.org/10.1038/382440a0

Sigmarsson, O. and Steinthórsson, S. 2007 Origin of Icelandic basalts: A review of their petrology and geochemistry. J Geodyn 43, 87–100. https://doi.org/10.1016/j.jog.2006.09.016

Sigmarsson, O., Thordarson, T. and Jakobsson, S. P. 2009 Segregations in Surtsey lavas (Iceland) reveal extreme magma differentiation during late stage flow emplacement. Spec Publ IAVCEI 85–104. https://doi.org/10.1182/blood-2015-09-672774

Sigmundsson, F., Einarsson, P., Rut, Á., et al. 2018 Geodynamics of Iceland and the signatures of plate spreading. J Volcanol Geotherm Res. https://doi.org/10.1016/j.jvolgeores.2018.08.014

Sisson, T. W. and Bacon, C. R. 1999 Gas-driven filter pressing in magmas. Geology 27, 613–616. https://doi.org/10.1130/0091-7613(1999)027<0613:GDFPIM>2.3.CO

Smith, P. M. and Asimow, P. D. 2005 Adiabat-1ph: A new public front-end to the MELTS, pMELTS, and pHMELTS models. Geochem, Geophys Geosys 6, 1–8. https://doi.org/10.1029/2004GC000816

Sobolev, A. V., Hofmann, A. W., Sobolev, S. V. and Nikogosian, I. K. 2005 An olivine-free mantle source of Hawaiian shield basalts. Nature 434, 590–597. https://doi.org/10.1038/nature03411

Sobolev, A. V., Hofmann, A. W., Kuzmin, D. V., et al. 2007 The amount of recycled crust in sources of mantle-derived melts. Science 316, 412–7. https://doi.org/10.1126/science. 1138113

Sollas,W. J. (1894). On the volcanic district of Carlingford and Slieve Gullion. Part I: On the relation of the granite to the gabbro of Barnavave, Carlingford. Transactions of the Royal Irish Academy 30: 477–512.

Sparks, R. S. J., Huppert, H. E., Turner, J. S., et al. 1984 The fluid dynamics of evolving magma chambers. Philos Trans R Soc Lond 310, 511–534. https://doi.org/10.1098/rsta.1984.0006

Stefansson, R., Gudmundsson, G. B. and Halldorsson, P. 2008 Tjörnes fracture zone. New and old seismic evidences for the link between the North Iceland rift zone and the Mid-Atlantic ridge. Tectonophysics 447, 117–126. https://doi.org/10.1016/j.tecto.2006.09.019

Steinthorsson, S., Oskarsson, N. and Sigvaldason, G. E. 1985 Origin of alkali basalts in Iceland: A plate tectonic model. J Geophys Res 90, 10027. https://doi.org/10.1029/JB090iB12p10027

Stolper, E. 1980 A phase diagram for mid-ocean ridge basalts: Preliminary results and implications for petrogenesis. Contrib Mineral Petrol 74, 13–27. https://doi.org/10.1007/BF00375485

Sturkell, E., Einarsson, P., Roberts, M. J., et al. 2008 Seismic and geodetic insights into magma accumulation at Katla subglacial volcano, Iceland: 1999 to 2005. J Geophys Res Solid Earth 113, 1–17. https://doi.org/10.1029/2006JB004851

Sugawara, T. 2000 Empirical relationships between temperature, pressure, and MgO content in olivine and pyroxene saturated liquid. J Geophys Res 105, 8457. https://doi.org/10.1029/2000JB900010

Sun, S.-S. and Jahn, B. 1975 Lead and strontium isotopes in post-glacial basalts from Iceland. Nature 255, 527–530. https://doi.org/10.1038/255527a0

Tarasewicz, J., Brandsdóttir, B., White, R. S., et al. 2012 Using microearthquakes to track repeated magma intrusions beneath the Eyjafjallajökull stratovolcano, Iceland. J Geophys Res Solid Earth 117, 1–13. https://doi.org/10.1029/2011JB008751

Thirlwall, M. F., Gee, M. A. M., Taylor, R. N. and Murton, B. J. 2004 Mantle components in Iceland and adjacent ridges investigated using double-spike Pb isotope ratios. Geochim Cosmochim Acta 68, 361–386. https://doi.org/10.1016/S0016-7037(03)00424-1

Thomson, A. and Maclennan, J. 2013 The distribution of olivine compositions in Icelandic basalts and picrites. J Petrol 54, 745–768. https://doi.org/10.1093/petrology/egs083

Thordarson, T. and Larsen, G. 2007 Volcanism in Iceland in historical time: Volcano types, eruption styles and eruptive history. J Geodyn 43, 118–152. https://doi.org/10.1016/j.jog.2006.09.005

Thy, P. 1991 High and low pressure phase equilibria of a mildly alkalic lava from the 1965 Surtsey eruption: Experimental results. Lithos 26, 223–243. https://doi.org/10.1016/0024-4937(91)90030-O

Trela, J., Vidito, C., Gazel, E., et al. 2015 Recycled crust in the galápagos plume source at 70 ma: Implications for plume evolution. Earth Planet Sci Lett 425, 268–277. https://doi.org/10.1016/j.epsl.2015.05.036

Ubide, T., Mollo, S., Zhao, J., et al. 2019 Sector-zoned clinopyroxene as a recorder of magma history, eruption triggers, and ascent rates. Geochim Cosmochim Acta 251, 265–283. https://doi.org/10.1016/j.gca.2019.02.021

Welsch, B., Hammer, J., Baronnet, A., et al. 2016 Clinopyroxene in postshield Haleakala ankaramite: 2. Texture, compositional zoning and supersaturation in the magma. Contrib Mineral Petrol 171, 1–19. https://doi.org/10.1007/s00410-015-1213-9

White, C. M. 2007 The graveyard point intrusion: An example of extreme differentiation of snake river plain basalt in a shallow crustal pluton. J Petrol 48, 303–325. https://doi.org/10.1093/petrology/egl062

White, R. and McKenzie, D. 1989 Magmatism at rift zones: The generation of volcanic continental margins and flood basalts. J Geophys Res 94, 7685. https://doi.org/10.1029/JB094iB06p07685

White, R. S., Edmonds, M., Maclennan, J., et al. 2019 Melt movement through the Icelandic crust. Philos Trans R Soc A Math Phys Eng Sci 377, 1–22. https://doi.org/10.1098/rsta.2018.0010

Wilson, J. T. 1963 Evidence from islands on the spreading of ocean floors. Nature 197, 536–538

Wolfe, C. J., Bjarnason, I. T., VanDecar, J. C. and Solomon, S. C. 1997 Seismic structure of the Iceland mantle plume. Nature 385, 245–247. https://doi.org/10.1038/385245a0

Wood, B. J. and Blundy, J. D. 1997 A predictive model for rare earth element partitioning between clinopyroxene and anhydrous silicate melt. Contrib Mineral Petrol 129, 166–181. https://doi.org/10.1007/s004100050330

Zavala, K., Leitch, A. M. and Fisher, G. W. 2011 Silicic segregations of the Ferrar Dolerite sills, Antarctica. J Petrol 52, 1927–1964. https://doi.org/10.1093/petrology/egr035

Zhang, Y. and Cherniak, D. 2010 Diffusion in Minerals and Melts. Rev Mineral Geochem. https://doi.org/10.2138/rmg.2010.72.2

Zindler, A., Hart, S. R., Frey, F. A. and Jakobsson, S. P. 1979 Nd and Sr isotope ratios and rare earth element abundances in Reykjanes Peninsula basalts evidence for mantle heterogeneity beneath Iceland. Earth Planet Sci Lett 45, 249–262. https://doi.org/10.1016/0012-821X(79)90127-4

Appendix I. Compositions of clinopyroxene of Brattaskjól ankaramite (data related to Paper II)

Brattaskjól

Analysis[1]	Anal. Loc[2]	Mg#^{cpx}	SiO_2	TiO_2	Al_2O_3	FeO	MnO	MgO	CaO	Na2O	Cr_2O_3	NiO	Total
BR02cpx_cp1_AVG	CORE	84.7	50.96	0.80	4.26	5.25	0.10	16.31	21.29	0.25	0.06	0.01	99.28
BR02cpx_cp2_AVG	CORE	85.7	51.68	0.72	3.57	4.99	0.10	16.73	21.14	0.24	0.39	0.04	99.60
BR02cpx_cp3_AVG	CORE	84.2	50.96	0.76	4.50	5.36	0.10	16.06	21.36	0.25	0.35	0.02	99.71
BR02cpx_cp4_AVG	CORE	83.3	50.40	0.97	4.50	5.61	0.11	15.73	21.48	0.26	0.49	0.02	99.59
BR02cpx_cp5_AVG	CORE	84.3	51.32	0.75	4.00	5.39	0.11	16.23	21.26	0.26	0.45	0.03	99.79
BR02cpx_cp6_AVG	CORE	86.0	51.26	0.62	3.62	4.84	0.11	16.67	21.16	0.27	0.75	0.03	99.33
BR02cpx_cp7_AVG	CORE	84.8	50.60	0.85	4.16	5.12	0.11	16.03	21.43	0.29	0.68	0.04	99.32
BR02cpx_cp8_AVG	CORE	82.4	50.42	1.01	4.00	5.98	0.11	15.71	21.18	0.26	0.46	0.03	99.16
BR02cpx_cp9_AVG	CORE	85.1	50.99	0.76	4.13	5.08	0.11	16.34	21.29	0.25	0.64	0.03	99.62
BR02cpx_cp10_AVG	CORE	80.8	50.30	1.09	3.91	6.58	0.14	15.58	21.22	0.28	0.16	0.03	99.29
BR02cpx_cp11_AVG	CORE	86.7	51.08	0.59	3.68	4.58	0.09	16.70	20.88	0.27	1.23	0.03	99.13
BR02cpx_cp13_AVG	CORE	80.4	51.11	1.04	3.42	6.81	0.13	15.72	21.34	0.26	0.08	0.01	99.91
BR02cpx_cp14_AVG	CORE	89.8	53.04	0.36	2.25	3.68	0.10	18.11	20.63	0.27	1.10	0.04	99.59
BR02cpx_cp15_AVG	CORE	89.8	53.05	0.38	2.19	3.68	0.09	18.17	20.47	0.26	1.12	0.03	99.43
BR02cpx_cp16_AVG	CORE	83.9	51.29	0.62	3.49	5.64	0.12	16.46	20.98	0.26	0.44	0.02	99.31
BR02cpx_cp17_AVG	CORE	83.6	50.92	0.86	4.20	5.60	0.11	16.01	21.56	0.27	0.13	0.02	99.68
BR02cpx_cp18_AVG	CORE	89.7	53.18	0.36	2.22	3.71	0.09	18.17	20.76	0.28	1.09	0.05	99.92
BR02cpx_cp19_AVG	CORE	82.4	50.96	0.92	3.63	6.09	0.12	16.01	21.13	0.26	0.35	0.01	99.48
BR02cpx_cp20_AVG	CORE	82.5	50.57	1.00	3.90	5.98	0.12	15.82	21.61	0.25	0.38	0.02	99.64
BR02cpx_cp21_AVG	CORE	85.5	51.15	0.73	4.00	4.97	0.10	16.43	21.29	0.27	0.76	0.04	99.74
BR02cpx_cp22_AVG	CORE	81.7	50.81	1.02	3.75	6.26	0.13	15.68	21.45	0.28	0.19	0.03	99.59
BR02cpx_cp23_AVG	CORE	86.4	51.57	0.64	3.63	4.67	0.09	16.63	21.18	0.28	0.87	0.03	99.59
BR02cpx_cp24_AVG	CORE	86.7	52.26	0.57	3.15	4.68	0.10	17.18	20.82	0.28	0.68	0.02	99.76
BR02cpx_cp25_AVG	CORE	83.1	50.84	1.04	3.95	5.71	0.11	15.72	21.57	0.25	0.46	0.01	99.67
BR02cpx_cp26_AVG	CORE	86.9	52.14	0.52	2.97	4.62	0.10	17.21	20.97	0.27	0.87	0.03	99.70
BR02cpx_cp27_AVG	CORE	83.2	50.31	0.89	4.58	5.66	0.11	15.76	21.38	0.27	0.39	0.02	99.38
BR02cpx_cp28_AVG	CORE	84.3	51.05	0.78	4.25	5.34	0.12	16.04	21.37	0.25	0.39	0.02	99.61
BR02cpx_cp29_AVG	CORE	86.0	51.20	0.74	3.77	4.81	0.11	16.57	21.44	0.25	0.66	0.03	99.56
BR02cpx_cp30_AVG	CORE	83.9	50.71	0.80	4.27	5.53	0.12	16.14	21.53	0.26	0.14	0.02	99.50
BR02cpx_cp31_AVG	CORE	85.5	51.54	0.62	3.56	5.05	0.11	16.70	21.11	0.25	0.52	0.02	99.49
BR02cpx_cp12_GM_AVG	GM	76.8	50.39	1.40	3.04	7.98	0.18	14.84	20.89	0.39	0.35	0.03	99.50
BR02cpx_cp2_RIM_AVG	RIM	78.2	50.93	1.29	2.90	7.49	0.15	15.09	20.97	0.31	0.25	0.04	99.41
BR02cpx_cp3_RIM_AVG	RIM	84.1	51.09	0.86	4.23	5.29	0.09	15.74	21.71	0.23	0.70	0.01	99.93
BR02cpx_cp7_RIM_AVG	RIM	77.2	50.45	1.52	2.92	7.88	0.16	14.94	20.79	0.35	0.20	0.03	99.24
BR02cpx_cp9_RIM_AVG	RIM	77.4	50.04	1.80	3.09	7.75	0.15	14.93	20.78	0.38	0.22	0.01	99.15
BR02cpx_cp18_RIM_AVG	RIM	77.4	50.25	1.73	3.02	7.82	0.17	15.00	20.82	0.35	0.28	0.02	99.45
BR02cpx_cp19_RIM_AVG	RIM	74.6	47.44	1.62	6.58	8.56	0.16	14.09	20.21	0.31	0.13	0.02	99.11
BR02cpx_cp25_RIM_AVG	RIM	77.3	50.50	1.54	3.08	7.87	0.16	15.06	20.84	0.35	0.27	0.02	99.67

[1]Clinopyroxene core compositions are averages of three microprobe analysis spots, whereas clinopyroxene rim compositions are averages of 1–3 analysis spots.
[2]CORE = macrocryst core analysis, GM = groundmass crystal core analysis, RIM = macrocryst rim analysis
Compositions are in weight percentages.

Appendix II. Compositions of clinopyroxene of Hvammsmúli ankaramite (data related to Paper II)

Hvammsmúli

Analysis[1]	Anal. Loc[2]	$Mg\#^{cpx}$	SiO_2	TiO_2	Al_2O_3	FeO	MnO	MgO	CaO	Na2O	Cr_2O_3	NiO	Total
Hva01_cp1_AVG	CORE	86.03	51.69	0.64	3.63	4.90	0.10	16.92	20.94	0.26	0.57	0.04	99.69
Hva01_cp2_AVG	CORE	81.78	51.09	0.95	3.72	6.24	0.12	15.72	21.48	0.27	0.19	0.02	99.79
Hva01_cp3_AVG	CORE	85.71	51.56	0.68	3.98	4.90	0.12	16.48	21.00	0.30	0.80	0.04	99.85
Hva01_cp4_AVG	CORE	85.41	51.83	0.74	3.89	5.07	0.10	16.64	21.48	0.25	0.24	0.02	100.25
Hva01_cp5_AVG	CORE	83.26	51.02	0.82	4.04	5.79	0.13	16.17	21.39	0.25	0.25	0.01	99.86
Hva01_cp6_AVG	CORE	83.54	51.29	0.79	4.02	5.68	0.12	16.18	21.50	0.25	0.21	0.02	100.05
Hva01_cp7_AVG	CORE	84.30	50.81	0.85	4.34	5.31	0.10	15.99	21.58	0.26	0.26	0.03	99.52
Hva01_cp8_AVG	CORE	78.47	50.47	1.18	3.45	7.47	0.17	15.27	20.94	0.29	0.16	0.02	99.42
Hva01_cp9_AVG	CORE	81.88	51.09	0.91	3.57	6.28	0.14	15.91	21.52	0.24	0.14	0.01	99.81
Hva01_cp10_AVG	CORE	79.20	50.62	1.20	3.44	7.21	0.14	15.39	21.16	0.27	0.15	0.00	99.59
Hva01_cp11_AVG	CORE	86.09	51.86	0.64	3.64	4.83	0.10	16.76	21.45	0.24	0.44	0.03	99.99
Hva01_cp12_AVG	CORE	86.01	52.24	0.55	3.03	5.00	0.11	17.26	21.00	0.24	0.48	0.03	99.95
Hva01_cp13_AVG	CORE	86.32	51.86	0.58	3.23	4.79	0.11	16.94	21.13	0.26	0.63	0.02	99.55
Hva01_cp14_AVG	CORE	87.21	52.06	0.55	2.96	4.48	0.11	17.14	21.01	0.26	0.88	0.03	99.48
Hva01_cp15_AVG	CORE	84.21	51.07	0.78	4.12	5.46	0.11	16.33	21.27	0.24	0.39	0.02	99.78
Hva01_cp16_AVG	CORE	84.50	51.57	0.70	3.71	5.42	0.12	16.58	21.21	0.24	0.26	0.02	99.82
Hva01_cp17_AVG	CORE	82.47	51.01	0.94	3.89	6.08	0.12	16.03	21.59	0.27	0.21	0.01	100.15
Hva01_cp18_AVG	CORE	86.10	51.57	0.64	3.52	4.80	0.11	16.67	21.34	0.26	0.69	0.02	99.60
Hva01_cp19_AVG	CORE	83.07	50.99	0.87	3.97	5.86	0.11	16.14	21.31	0.24	0.20	0.03	99.73
Hva01_cp20_AVG	CORE	84.88	51.33	0.68	3.82	5.23	0.11	16.49	21.11	0.26	0.54	0.02	99.61
Hva01_cp1_RIM_AVG	RIM	70.55	49.89	1.80	2.88	10.34	0.21	13.90	20.35	0.37	0.01	0.01	99.76
Hva01_cp2_RIM_AVG	RIM	72.68	50.55	1.72	2.86	9.51	0.21	14.19	20.61	0.34	0.12	0.02	100.10
Hva01_cp3_RIM_AVG	RIM	73.59	50.52	1.60	2.96	9.18	0.20	14.35	20.63	0.35	0.14	0.01	99.93
Hva01_cp5_RIM_AVG	RIM	73.85	50.68	1.49	2.69	9.21	0.20	14.59	20.53	0.36	0.13	0.01	99.86
Hva01_cp9_RIM_AVG	RIM	73.35	50.53	1.54	2.63	9.38	0.19	14.48	20.50	0.35	0.07	0.02	99.67
Hva01_cp11_RIM_AVG	RIM	72.51	51.14	1.47	2.25	9.79	0.21	14.49	20.41	0.35	0.00	0.02	100.14
Hva01_cp13_RIM_AVG	RIM	70.64	49.80	1.82	2.94	10.30	0.21	13.90	20.22	0.36	0.02	0.02	99.59
Hva01_cp15_RIM_AVG	RIM	72.16	50.96	1.37	2.08	10.04	0.23	14.60	20.16	0.33	0.03	0.01	99.79
Hva01_cp16_RIM_AVG	RIM	72.45	50.77	1.48	2.29	9.83	0.21	14.50	20.44	0.33	0.02	0.02	99.91
Hva01_cp5_RIM_AVG	RIM	72.97	50.42	1.37	2.81	9.57	0.19	14.50	20.41	0.35	0.07	0.01	99.69
Hva01_cp10_RIM_AVG	RIM	73.48	50.25	1.61	2.94	9.20	0.19	14.29	20.73	0.34	0.18	0.02	99.74
Hva01_cp9_RIM_AVG	RIM	74.19	50.69	1.53	2.84	9.03	0.18	14.56	20.70	0.33	0.17	0.01	100.02

[1]Clinopyroxene core compositions are averages of 3 microprobe analysis spots, whereas clinopyroxene rim analyses are averages of 1–3 analysis spots.

[2]CORE = macrocryst core analysis, RIM = macrocryst rim analysis

Compositions are in weight percentages.

Appendix III. Electron microprobe analyses of spinel of Brattaskjól ankaramite (data related to Paper II)

Analysis	SiO_2	TiO_2	Al_2O_3	FeO	MnO	MgO	V_2O_3	Cr_2O_3	NiO	Total
BR02_Ol92_sp1_1	0.10	1.52	14.70	20.49	0.18	13.87	0.11	46.93	0.17	98.06
BR02_Ol92_sp1_2	0.12	1.56	15.21	20.21	0.21	14.05	0.18	47.07	0.20	98.79
BR02_Ol93_sp1_1	0.12	1.53	13.32	20.19	0.20	13.58	0.15	48.39	0.23	97.71
BR02_Ol94_sp1_1	0.08	1.55	13.88	22.20	0.20	12.92	0.18	45.97	0.19	97.17
BR02_Ol41_sp1_1	0.08	1.57	12.11	20.81	0.19	13.25	0.14	50.94	0.16	99.25
BR02_Ol41_sp1_2	0.08	1.56	12.06	21.63	0.19	12.56	0.15	51.18	0.19	99.60
BR02_Ol41_sp2_1	0.09	1.50	12.13	24.22	0.24	10.93	0.14	50.09	0.14	99.47
BR02_Ol41_sp3_1	0.07	1.58	12.13	20.05	0.20	13.59	0.14	51.60	0.20	99.56
BR02_Ol35_sp1_1	0.10	1.49	14.51	23.49	0.21	11.84	0.15	47.70	0.18	99.67
BR02_Ol35_sp1_2	0.10	1.53	14.67	23.37	0.24	11.74	0.14	47.96	0.16	99.91
BR02_Ol03_sp1_1	0.09	1.43	10.80	23.28	0.27	11.64	0.17	50.17	0.14	97.99
BR02_Ol03_sp2_1	0.10	1.41	13.46	21.89	0.22	12.84	0.14	48.82	0.16	99.03
BR02_Ol03_sp3_1	0.08	1.52	13.42	22.98	0.21	11.96	0.15	48.12	0.16	98.61
BR02_Ol03_sp4_1	0.10	1.45	12.45	21.81	0.23	12.51	0.16	48.87	0.18	97.76
BR02_Ol03_sp5_1	0.07	1.46	13.56	22.25	0.21	12.52	0.15	48.40	0.14	98.75
BR02_Ol03_sp6_1	0.11	1.54	13.40	21.94	0.23	12.94	0.16	48.84	0.17	99.33
BR02_Ol04_sp1_1	0.11	1.61	13.31	21.94	0.22	12.86	0.15	48.24	0.14	98.57
BR02_Ol72_sp1_1	0.07	1.25	11.50	25.65	0.24	9.82	0.13	49.97	0.09	98.73
BR02_Ol95_sp1_1	0.10	1.40	11.92	27.76	0.30	8.86	0.14	47.04	0.10	97.61
BR02ts_Ol01_sp1_1	0.11	1.60	15.03	20.04	0.19	14.13	0.15	47.30	0.20	98.75
BR02ts_Ol01_sp1_2	0.12	1.68	15.01	19.79	0.18	13.92	0.15	47.29	0.20	98.34
BR02ts_Ol02_sp2_1	0.46	1.47	11.87	21.17	0.23	13.71	0.14	49.25	0.17	98.47
BR02ts_Ol04_sp1_1	0.07	1.39	11.91	21.15	0.23	12.34	0.15	51.35	0.17	98.74
BR02ts_Ol04_sp1_2	0.07	1.39	11.88	20.48	0.24	12.70	0.13	52.27	0.15	99.31
BR02ts_Ol04_sp1_3	0.09	1.38	11.88	20.83	0.20	12.55	0.14	50.48	0.16	97.70

Compositions are in weight percentages.

Appendix IV. Electron microprobe analyses of spinel of Hvammsmúli ankaramite (data related to Paper II)

Analysis	SiO_2	TiO_2	Al_2O_3	FeO	MnO	MgO	V_2O_3	Cr_2O_3	NiO	Total
Pos-1a_Ol01_sp1_1	0.07	1.57	13.38	25.63	0.24	9.94	0.17	48.20	0.19	99.39
Pos-1a_Ol01_sp2_1	0.08	1.62	13.54	24.72	0.26	10.25	0.14	48.21	0.17	98.97
Pos-1a_Ol01_sp2_2	0.08	1.64	13.53	25.00	0.23	10.31	0.18	48.64	0.18	99.79
Pos-1a_Ol06_sp1_1	0.04	2.64	14.64	20.83	0.23	12.45	0.22	48.69	0.22	99.96
Pos-1a_Ol45_sp1_1	0.06	2.04	17.43	21.64	0.22	12.76	0.18	44.79	0.16	99.28
Pos-1a_Ol45_sp3_1	0.11	1.47	17.39	22.30	0.20	12.03	0.15	45.41	0.16	99.22
Pos-1a_Ol45_sp2_2	0.08	1.51	18.12	21.54	0.22	12.85	0.16	45.10	0.18	99.75
Pos-1a_Ol45_sp4_1	0.09	1.73	16.00	22.52	0.23	11.96	0.20	47.08	0.18	99.97
Pos-1a_Ol19_sp1_1	0.07	1.44	18.42	19.07	0.20	13.79	0.14	46.19	0.21	99.54
Pos-1a_Ol19_sp2_1	0.09	1.61	20.69	18.89	0.19	14.32	0.15	44.25	0.22	100.41
Pos-1a_Ol20_sp1_1	0.07	1.35	21.78	22.57	0.24	12.63	0.18	39.83	0.16	98.81
Pos-1a_Ol20_sp2_1	0.06	1.38	21.48	22.81	0.21	12.55	0.21	39.58	0.16	98.44
Pos-1a_Ol20_sp3_1	0.05	1.50	21.13	24.12	0.19	11.89	0.23	40.61	0.16	99.87
Pos-1a_Ol20_sp5_1	0.06	1.58	21.92	24.33	0.24	12.02	0.20	39.97	0.17	100.49
Pos-1a_Ol20_sp4_1	0.05	1.46	22.30	23.52	0.20	12.39	0.23	39.74	0.15	100.03
Pos-1a_Ol22_sp1_1	0.09	1.40	15.86	20.33	0.21	12.83	0.17	47.87	0.19	98.95
Pos-1a_Ol46_sp1_1	0.06	1.50	16.71	22.62	0.24	11.98	0.21	46.28	0.16	99.76
Pos-1a_Ol26_sp1_1	0.08	1.56	16.09	21.64	0.23	12.48	0.20	47.66	0.12	100.05
Pos-1a_Ol47_sp1_1	0.07	1.42	12.70	21.20	0.21	11.50	0.18	51.69	0.15	99.11
Pos-1a_Ol48_sp1_1	0.06	1.64	19.37	25.92	0.24	11.08	0.22	40.86	0.17	99.55
Pos-1a_Ol49_sp1_1	0.05	1.11	9.03	28.54	0.31	7.78	0.18	52.24	0.13	99.38
Pos-1a_Ol49_sp2_1	0.05	1.18	9.31	28.65	0.27	7.55	0.17	50.67	0.14	97.99
Pos-1a_Ol50_sp1_1	0.08	1.47	11.67	27.15	0.27	8.90	0.23	49.13	0.13	99.02

Compositions are in weight percentages.

Paper I

Nikkola P., Guðfinnsson G.H., Bali E., Rämö O.T., Fusswinkel T., Thordarson T. 2019. *Signature of deep mantle melting in South Iceland olivine.* Contributions to Mineralogy and Petrology 174:43.

Contributions to Mineralogy and Petrology (2019) 174:43
https://doi.org/10.1007/s00410-019-1580-8

ORIGINAL PAPER

Signature of deep mantle melting in South Iceland olivine

Paavo Nikkola[1,2] · Guðmundur H. Guðfinnsson[2] · Enikő Bali[2,3] · O. Tapani Rämö[1] · Tobias Fusswinkel[4] · Thorvaldur Thordarson[2,3]

Received: 1 December 2018 / Accepted: 26 April 2019 / Published online: 13 May 2019

Abstract

We present new high-precision major and trace element data on olivine macrocrysts from various volcano-tectonic settings in Iceland and use these data as a proxy for mantle mode and melting conditions. Within individual sampling sites examined (seven lavas and one tephra) olivine-dominated fractional crystallization, magma mixing and diffusive re-equilibration control observed variability in olivine composition. High-pressure fractional crystallization of clinopyroxene may have lowered Ca and increased Fe/Mn in one olivine population and subsolidus diffusion of Ni and Fe–Mg affected the mantle-derived Ni/Fo ratio in some compositionally zoned olivine macrocrysts. Interestingly, magmas erupted at the southern tip of the Eastern Volcanic Zone (SEVZ), South Iceland, have olivines with elevated Ni and low Mn and Ca contents compared to olivines from elsewhere in Iceland, and some of the SEVZ olivines have relatively low Sc and V and high Cr, Ti, Zn, Cu and Li in comparison to depleted Iceland rift tholeiite. In these olivines, the high Ni and low Mn indicate relatively deep melting ($P_{\text{final}} > 1.4$ GPa, ~ 45 km), Sc, Ti and V are compatible with low-degree melts of lherzolite mantle, and elevated Zn may suggest modal (low-olivine) or geochemical (high Zn) enrichment in the source. The SEVZ olivine macrocrysts probably crystallized from magmas derived from olivine-bearing but relatively deep, enriched and fertile parts of the sub-Icelandic mantle, and indicate swift ascent of magma through the SEVZ lithosphere.

Keywords Olivine · Trace elements · Mantle heterogeneity · Mantle melting · Iceland

Introduction

Icelandic mantle

Although many of the details remain obscure, Earth's mantle is evidently heterogeneous in mineralogy and chemical composition (Allègre and Turcotte 1986). A major source of this heterogeneity is subducted oceanic crust that contributes to the mantle source of oceanic island basalts (Hofmann and White 1982; Hauri 1996; Chauvel et al. 2008). In Iceland, there is abundant isotopic evidence for recycled oceanic crustal material in the upper mantle (Fitton et al. 1997; Chauvel and Hémond 2000; Kokfelt et al. 2006; Peate et al. 2010). Anyhow, isotope systematics do not yield straightforward information about mantle lithology, and it is yet unclear whether the recycled oceanic crust resides in the mantle as a discrete rock type, i.e. pyroxenite or eclogite, or if it has been completely mixed with the dominant mantle peridotite (Green and Ringwood 1963).

Insights into the modal composition of the mantle can be acquired by studying the major and trace element

Communicated by Mark S Ghiorso.

Electronic supplementary material The online version of this article (https://doi.org/10.1007/s00410-019-1580-8) contains supplementary material, which is available to authorized users.

✉ Paavo Nikkola
paavo.nikkola@helsinki.fi

[1] Department of Geosciences and Geography, Geology and Geophysics Research Group, University of Helsinki, P. O. Box 64, 00014 Helsinki, Finland

[2] Nordic Volcanological Center, Institute of Earth Sciences, Sturlugata 7, 101 Reykjavík, Iceland

[3] Faculty of Earth Sciences, University of Iceland, Sturlugata 7, 101 Reykjavík, Iceland

[4] Institute of Applied Mineralogy and Economic Geology, RWTH Aachen University, Wüllnerstr. 2, 52062 Aachen, Germany

composition of magmas that represent partial melts of the mantle. This is, however, prone to uncertainty, as the nature of mantle melts is dependent on not only the modal composition of the mantle but also melting temperature (T), pressure (P) and the degree of melting (F). In addition, mantle-derived magmas are usually modified in the crust by low-P fractional crystallization, magma mixing and crustal contamination, which may obscure the traits they inherited from the source. Nevertheless, with careful treatment of the data, the quantity of possible end-member mantle source rock-types can be estimated, and the inferred mantle components can be further assessed by comparing their assumed melt productivity to crustal thickness (Shorttle and Maclennan 2011; Brown and Lesher 2014; Shorttle et al. 2014; Lambart 2017). Using this approach, it has been established that melting of depleted lherzolite alone is unlikely to produce the compositional variability (especially the high Fe and low Ca) in Icelandic lavas (Shorttle and Maclennan 2011). A minor (4–15%) olivine-free pyroxenite or mixed pyroxenite–peridotite hybrid seem to be required in the mantle source (Shorttle et al. 2014).

Besides utilizing the major and trace element composition of magmas, the nature of the mantle source can be probed by analyzing forsteritic olivine macrocrysts. The composition of forsteritic olivine reflects the composition of its near-primary parental magma, and hence the mode (Sobolev et al. 2005) and/or melting conditions (Li and Ripley 2010; Matzen et al. 2013, 2017a, b) in the mantle source. In Iceland, olivine compositions have been found to be rather consistent with shallow melting of lherzolite (Herzberg et al. 2016), although some lavas have olivines with higher Ni than expected by models of fractional crystallization of peridotite-derived melts (Shorttle and Maclennan 2011; Herzberg et al. 2016; Neave et al. 2018). These Ni-rich olivines have been suggested to indicate melting of enriched, olivine-free or olivine-poor, mantle below Iceland (Sobolev et al. 2007, 2008; Shorttle and Maclennan 2011), or explained by mixing of variably differentiated lherzolite-derived melts in the crust (Herzberg et al. 2016).

We present new olivine trace element data from various volcano-tectonic settings in Iceland, gathered using high probe current microprobe and laser ablation inductively coupled plasma mass spectrometry (LA–ICP–MS) methods. The primary finding are the relatively Ni-enriched and Mn- and Ca-poor olivine macrocrysts from Eyjafjallajökull and Vestmannaeyjar volcanic systems, exceptional in the context of pre-existing data (Sobolev et al. 2007; Shorttle and Maclennan 2011; Neave et al. 2018). Some of these olivine crystals are also enriched in Ti, Zn, Cu, Li, Cr and depleted in Sc and V compared to olivines from rift zone tholeiite (Háleyjabunga). We propose that the parental magma of these olivine macrocrysts equilibrated at high temperatures and pressures with a fertile olivine-bearing mantle source.

Olivine as indicator of mantle mode and melting conditions

In mantle lherzolite, abundant residual olivine limits the Ni content of partial melts by effectively sequestering Ni. In contrast, low-degree partial melts of olivine-free pyroxenite are, in most cases, rich in Ni, and poor in Mn and Ca as garnet and clinopyroxene in the residuum preferentially sequester Mn and Ca, but not Ni. Ni, Mn and Ca are stored in early-formed Fo-rich olivine in proportion to their content in primitive melts, even if the melt is later modified by fractional crystallization and magma mixing. Because of this, trace elements in olivine should record the lithology of the mantle source. Sobolev et al. (2005) were the first to use high-Ni, low-Mn and low-Ca in olivine as an indicator of olivine-free pyroxenite in the mantle. Since this work, olivine composition has been used to estimate the mantle lithology for a wide range of volcanic provinces (e.g. Sobolev et al. 2007, 2008; Herzberg 2011; Herzberg et al. 2014; Trela et al. 2015).

Using olivine as a mantle proxy is complicated by variation in T, P, and oxygen fugacity (fO_2) that affects element partitioning in mantle melting and subsequent olivine crystallization. Recent experimental work suggests that Ni and Mn distribution coefficients between olivine and melt ($D_{Ni}^{ol/liq}$, $D_{Mn}^{ol/liq}$) are, directly or indirectly, dependent on temperature of mantle melting (Li and Ripley 2010; Putirka et al. 2011; Matzen et al. 2013, 2017a, b). $D_{Ni}^{ol/liq}$ is relatively low for high-temperature peridotite melting at high pressures, which results in partial melts relatively enriched in Ni. Consequently, when a deep mantle-derived magma rises to a lower temperature and pressure environment, $D_{Ni}^{ol/liq}$ is higher, resulting in crystallization of Ni-rich olivine (Matzen et al. 2013, 2017a). $D_{Mn}^{ol/liq}$ correlates positively with MgO in the melt, and MgO-rich melts of peridotite are generated at higher temperature; therefore, high-temperature mantle melts have lower MnO and they crystallize low-Mn olivine macrocrysts (Matzen et al. 2017b). This, and the global correlation between lithospheric thickness and olivine compositions, has sparked a debate on whether the variation in Ni and Mn in olivines reflect the depth of mantle melting or variation in mantle mode (Niu et al. 2011; Heinonen and Fusswinkel 2017; Putirka et al. 2018). Mn partitioning between partial melts and mantle residue may also be susceptible to water content in the mantle (Balta et al. 2011), and the extent of parental melt polymerization (NBO/T) has been proposed to affect Ni partitioning during olivine crystallization (Wang and Gaetani 2008). Also, the slower diffusion of

Ni compared to Mg and Fe in olivine lattice during crustal storage can affect element ratios in zoned olivine (Lynn et al. 2017).

Because complexly influenced by parameters of melting and crystallization, olivine compositions need not to be directly related to the volume of a certain rock type in the mantle, e.g. olivine-free pyroxenite. Nevertheless, olivine macrocrysts are useful, as their composition echoes the evolutionary history of an individual melt, i.e. they record fractional crystallization and magma mixing, and the most primitive olivines in a system mirror the composition of the original mantle-derived melt in a way glass or whole-rock composition of magmas nearly never do. Olivine composition is a high-detail mantle proxy, valuable when treated in view of other mantle source indicators, such as major, trace element and isotopic composition of magmas.

Sampling and geological background

Sample locations

We analyzed olivines from eight locations, which represent varying volcano-tectonic environments in Iceland. These include Háleyjabunga and Mosfellsheiði lavas in southwestern Iceland; Kistufell hyaloclastite in the central highlands; Berserkjahraun lava of the Snæfellsnes Volcanic Zone (SVZ); and Stórhöfði, Hvammsmúli, Brattaskjól lavas and Eyjafjallajökull 2010 summit tephra from the southern tip of the Eastern Volcanic Zone (SEVZ, Table 1, Fig. 1). The majority of olivine trace element data gathered earlier from Iceland are from the neovolcanic lavas of SVZ and the Northern Rift Zone (Sobolev et al. 2007, 2008). To gain new insights, we focused our sampling efforts on SEVZ (Fig. 1), where high-precision olivine analyzes had not been done earlier. Olivine major and trace element compositions from Háleyjabunga and Kistufell have been presented by Sobolev et al. (2007), and Háleyjabunga has also been revisited by Shorttle and Maclennan (2011) and Neave et al. (2018). Háleyjabunga and Kistufell are the end-members in terms of Ni and Mn content in the earlier Sobolev et al. (2007) high-precision data set from Iceland, and we re-analyzed them for assessment of data quality (cf. Supplementary Material).

Olivines from rift-zone tholeiites

The sampling locations Háleyjabunga, Mosfellsheiði and Kistufell represent the central parts of the mid-oceanic rift that lies across Iceland (Fig. 1); here the amount of decompression melting is generally the largest (Sæmundsson 1979). Háleyjabunga is a 13 ka (Sæmundsson 1995) lava shield situated near the tip of the Reykjanes Peninsula, known for its depleted isotopic and trace element character (Thirlwall et al. 2004). Our Háleyjabunga sample has the most magnesian olivines in our sample suite with forsterite (Fo) content up to 91 ($Fo = 100 \times$ atomic $Mg/(Mg + Fe^{2+})$). Mosfellsheiði is a younger than 700 ka (Sæmundsson et al. 2010) olivine-tholeiite lava flow field from the outskirts of

Table 1 The sample locations in this study with a collection of available geochemical data (Jakobsson 1979; Wiese 1992; Jóhannesson 1994; Breddam et al. 2000; Thirlwall et al. 2004, 2006; Peate et al. 2009, 2010; Sæmundsson et al. 2010; Sigmarsson et al. 2011)

	Rift-zones			SVZ	SEVZ			
	Háleyjabunga	Mosfellsheiði	Kistufell	Berserkjahraun	Hvammsmúli	Brattaskjól	Eyjafjallajökull 2010	Stórhöfði
Rock type[a]	Olivine tholeiite	Olivine tholeiite	Olivine tholeiite	Alkali basalt	Transitional basalt	Transitional basalt	Benmoreite/basalt[b]	Alkali basalt
Volcanic zone	WVZ	WVZ	NVZ	SVZ	EVZ	EVZ	EVZ	EVZ
Volcanic system	Reykjanes	Hengill	Bárðarbunga	Ljósufjöll	Eyjafjallajökull	Eyjafjallajökull	Eyjafjallajökull	Vestmannaeyjar
Fo	89.3–91.0	71.8–86.0	85.7–88.7	83.2–90.1	83.0–89.8	80.7–89.2	78.7–86.9	85.07–89.03
$^{3}He/^{4}He$	10.29–11.49	–	15.33–16.79	8.54	17.13	–	–	13.11–14.51
$^{206}Pb/^{204}Pb$	18.297	–	18.343–18.361	19.1335	19.2155	–	–	19.0467
$^{207}Pb/^{204}Pb$	15.48	–	15.420–15.427	15.5388	15.5566	–	–	15.5419
$^{208}Pb/^{204}Pb$	38.061	–	37.935–37.964	38.7567	38.8690	–	–	38.6541
$^{87}Sr/^{86}Sr$	0.703039	–	0.703036–0.703079	0.703400	0.703335	–	0.703241–0.703259	0.703138–0.703196
$^{143}Nd/^{144}Nd$	0.51313	–	0.513058–0.513099	0.512934	0.512987	–	0.512985–0.513004	0.513015–0.513019
$\delta^{18}O_{olivine}$	4.68–5.03	–	4.43–4.74	5.00	4.74	–	5.43–5.96	5.01
$^{176}Hf/^{177}Hf$	–	–	–	0.283113	0.283093	–	–	0.283103–0.283152
Age	10–13 ka	< 730 ka	< 730 ka	4000 a	587 ± 31 ka	< 730 ka	2010 AD	~ 5000–6000 ka

See Supplementary Material for data sources affiliated to respective cells

[a]Rock types according to Jakobsson et al. (2008). All samples are in fact subalkaline in composition

[b]Eyjafjallajökull 2010 summit eruption tephra is a mixture of benmoreite and basalt

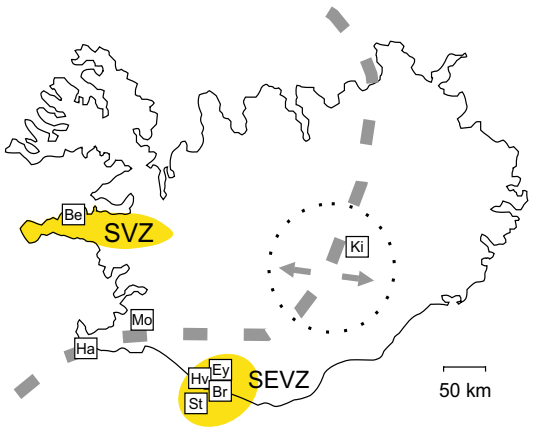

Fig. 1 Map of Iceland with sample locations: *Be* Berserkjahraun, *Ha* Háleyjabunga, *Mo* Mosfellsheiði, *Ki* Kistufell, *Hv* Hvammsmúli, *Ey* Eyjafjallajökull 2010, *Br* Brattaskjól, and *St* Stórhöfði. Approximate location of the plate boundary and the locus of the Iceland mantle plume (Wolfe et al. 1997) are marked with grey and black stippled lines, respectively. The major off-rift volcanic zones, Snæfellsnes Volcanic Zone (SVZ) and the southern tip of Eastern Volcanic Zone (SEVZ), are marked in yellow

Reykjavík with $Fo_{71.8–86.0}$ olivines. Kistufell is a monogenetic table mountain located at the NW margin of the Vatnajökull ice cap (Breddam 2002), close to the inferred center of the Iceland plume at the rift axis (Wolfe et al. 1997). The Kistufell magma has been interpreted as plume-derived near-primary melt, and it has up to $Fo_{88.7}$ olivines (Breddam 2002). The exact age of Kistufell is unknown, but is probably close to the end of the last glacial period (Breddam 2002).

Olivines from off-rift volcanic zones

The sampled lavas and tephra from SVZ and SEVZ (Berserkjahraun, Hvammsmúli, Brattaskjól and Stórhöfði lavas, and Eyjafjallajökull 2010 tephra) were erupted from off-rift volcanic systems situated in areas of minimal crustal extension (Fig. 1). Off-rift volcanoes are peripheral to the main rift zone and they produce alkaline or mildly alkaline lavas enriched in incompatible elements compared to rift tholeiites (Jakobsson 1972; Hemond et al. 1993). This indicates relatively small degree of mantle melting (Sæmundsson 1979), while isotopic composition (especially high $^{206}Pb/^{204}Pb$) suggests a more enriched mantle source (Kokfelt et al. 2006; Peate et al. 2010). This covariation of small degree mantle melting and enriched isotopic composition is commonly explained by a model where smaller degree melting allows preferential tapping of enriched and fusible veins set in a more refractory mantle (Chauvel and Hémond 2000; Fitton et al. 2003; Kokfelt et al. 2006).

The tectonic setting of the two major off-rift volcanic zones, SVZ and SEVZ (Fig. 1), is different. SVZ has been interpreted as a zone of weakness that is the remnant of the Snæfellsnes-Skagi paleo-rift (Hardarson et al. 1997), active from 15–20 to 10–12 Ma (Martin et al. 2011). In contrast, magmatism in South Iceland is related to the southward propagation of the Eastern Volcanic Zone (EVZ), which is the youngest (activated > 3 Ma, Martin et al. 2011) volcanically active zone in Iceland, and the most profuse magma producer in historical times (Thordarson and Larsen 2007). In this area, including the Eyjafjallajökull and Vestmannaeyjar volcanic systems, active extension is minimal. Of SEVZ and SVZ lavas, the latter have higher La/Yb_N (2–12 vs 2–7), indicating smaller degrees of melting, as well as lower ε_{Nd}, and lower $^3He/^4He$ (Peate et al. 2010).

Three locations from SVZ were analyzed for olivine trace elements compositions by Sobolev et al. (2007): Enni, Sydri-Raudamelur and Ydri-Raudamelur. Due to these SVZ olivine data already existing, we sampled only one SVZ lava, Berserkjahraun (Fig. 1, Table 1). Berserkjahraun is one of the most primitive of SVZ lavas (Peate et al. 2010), erupted within the Ljósufjöll volcanic system, and inferred to be younger than 4000 a in age (Jóhannesson 1994). Our sample of Berserkjahraun lava has $Fo_{83.2–90.1}$ olivines.

Our SEVZ sample set includes olivine macrocrysts from three samples from Eyjafjallajökull volcanic system and one sample from Vestmannaeyjar volcanic system (Fig. 1, Table 1). Brattaskjól and Hvammsmúli samples are from macrocryst-rich transitional basalts (often referred to as ankaramites) from the southern slope of the volcano. Hvammsmúli is 600 ka in age (Wiese 1992), a 45 m thick outcrop that has been interpreted as a remnant of a lava lake (Loughlin 1995), whereas Brattaskjól is a less studied macrocryst-rich basalt 4 km east of Hvammsmúli. Our Hvammsmúli and Brattaskjól samples have up to $Fo_{89.8}$ and $Fo_{89.2}$ olivines, respectively.

Our "Eyjafjallajökull 2010" sample comprises forsteritic olivines from tephra of the Eyjafjallajökull 2010 eruption. This eruption was a mixed eruption of benmoreite and basalt, which carried olivine with diverse compositions ($Fo_{74–87}$). The 2010 summit eruption followed an effusive flank eruption on the Fimmvörðuháls pass, and it was the intrusion of Fimmvörðuháls parental magma into a silicic magma chamber that ignited the summit eruption (Sigmarsson et al. 2011). The olivine crystals of Fimmvörðuháls have been extensively studied (Sigmarsson et al. 2011; Viccaro et al. 2016; Pankhurst et al. 2018), and due to the co-genetic nature of Fimmvörðuháls basalt and Eyjafjallajökull 2010 tephra, they likely carry similar olivine macrocrysts.

Our olivine samples from Vestmannaeyjar were collected from the Stórhöfði lava flow field at the southern tip of Heimaey Island. According to Jakobsson (1968, 1979), Stórhöfði lava erupted during the Holocene and is slightly

older than 5470 ± 160 years in age (Mattsson and Höskuldsson 2003). It is the most primitive lava flow field on Heimaey, compositionally similar to the Surtsey 1963–1967 eruption (Mattsson and Oskarsson 2005), and it has up to Fo_{89} olivines. The Stórhöfði sample examined in this study is from a tube-fed lava flow related to a late phase of the eruption (Mattsson and Oskarsson 2005).

Methods

Electron probe microanalysis

The microprobe analyses of major and trace element compositions of olivine crystals were conducted at the Institute of Earth Sciences, University of Iceland using the JEOL JXA-8230 electron microprobe. Olivine macrocrysts were hand-picked from crushed and sieved (Ø = 0.1–4.0 mm) rock samples and mounted in 1-inch epoxy molds or glass slides, except for the Mosfellsheiði sample, for which olivines were analyzed directly from 1-inch glass slides made of polished rock. Polished sample surfaces were cleaned with ethanol and carbon coated before the electron probe and laser ablation analyses. For the high-precision trace element analyses of olivine cores, we utilized a modified version of the high-probe current protocol by Batanova et al. (2015) with an acceleration voltage of 20 kV and 500 nA beam current. These analyses were focused on forsteritic olivines using low brightness of BSE images as an indicator of high Mg content, and the analyses targeted the geometric, compositionally homogenous, center of the olivine crystals. The resulting instrumental precisions for Ni and Mn are 0.52% and 0.48% relative standard deviations, respectively. When measuring traverses across olivine zonation, we used shorter analysis time, 15 kV accelerating voltage and 20 nA probe current. This setup delivers precise Fo measurements (~ 0.5% standard error) but relatively low precision on trace elements, e.g. an average 6.5% standard error for Ni. Detailed information of analytical conditions and standards are given in Supplementary Material.

LA–ICP–MS analysis

LA–ICP–MS analyses were carried out at the Department of Geosciences and Geography, University of Helsinki using a Coherent GeoLas Pro MV 193 nm laser ablation system connected to an Agilent 7900 s quadrupole ICP–MS equipped with high-sensitivity ion lens configuration and Pt interface cones. The following isotopes were included in the measurement program: ^{7}Li, ^{23}Na, ^{24}Mg, ^{25}Mg, ^{27}Al, ^{29}Si, ^{43}Ca, ^{31}P, ^{43}Ca, ^{44}Ca, ^{45}Sc, ^{49}Ti, ^{51}V, ^{52}Cr, ^{55}Mn, ^{56}Fe, ^{57}Fe, ^{59}Co, ^{60}Ni, ^{62}Ni, ^{63}Cu, ^{66}Zn, ^{85}Rb, ^{88}Sr, ^{137}Ba. The olivine macrocrysts were ablated up to three times at the center of the crystals with a spot size of 44 µm and laser energy densities of 7 J/cm^2. Sample measurements were bracketed by analyses of reference materials NIST SRM 610 (Spandler et al. 2011) and GSE 1G (Jochum et al. 2005) at fluences of 10 J/cm^2. External standardization using GSE 1G synthetic basalt glass yielded better reproduction of EPMA compositional data than NIST SRM 610, and therefore, all data reported here were externally standardized against GSE 1G. Data reduction was carried out using the SILLS software package (Guillong et al. 2008). To avoid problems arising from Fe–Mg zoning in some olivine grains and the different sampling spot sizes of LA–ICP–MS and EPMA, internal standardization was done using Si concentrations as determined by EPMA. Further information on the analytical procedure and complete summary of instrumental parameters is given in the Supplementary Material.

Results

Compositional zonation in olivine

Olivine crystals in the analyzed samples vary in size (0.3–3.4 mm in diameter) and compositional zoning (Fig. 2). The largest crystals analyzed are from Hvammsmúli (0.5–3.4 mm), followed by Mosfellsheiði (0.5–2.5 mm), Brattaskjól (0.5–2.4 mm), Kistufell (0.3–2.3 mm), Háleyjabunga (0.5–2.2 mm), Berserkjahraun (0.6–2.2 mm), Eyjafjallajökull 2010 (0.5–2.0 mm), and Stórhöfði (0.4–1.3 mm). Mg–Fe compositional zoning rims are very thin (< 20 µm), or absent, in olivines from Háleyjabunga (Fig. 2a) and Kistufell. $Fo_{>86}$ olivine crystals from Brattaskjól have thin (up to 120 µm) normally zoned rims (i.e. Fe increases towards the edge; Fig. 2b), whereas reverse zoning (i.e. Mg increases towards the edge) is present in $Fo_{<86}$ olivines. Mg–Fe zoned rims in analyzed olivines from the Eyjafjallajökull 2010 sample are dominantly less than 100 µm in thickness and normally zoned. Moderately thick, 100–200 µm normally zoned rims characterizes the Stórhöfði and Berserkjahraun olivines. Mosfellsheiði and Hvammsmúli olivine macrocrysts have the broadest Mg–Fe zoned rims, up to 220 µm and 700 µm (Fig. 2c) in thickness, respectively.

We analyzed the zoning patterns along rim-to-core traverses in olivines from Hvammsmúli, Brattaskjól and Mosfellsheiði. Nearly all of the analyses of Hvammsmúli (19/19), Brattaskjól (10/12) and Mosfellsheiði (3/3) revealed decoupling of Fo and Ni in the Mg–Fe zoned parts of the crystals (Fig. 3), a phenomenon earlier reported by Lynn et al. (2017) from Hawaiian olivines. In Hvammsmúli olivine 'Pos–1a_Ol1', the Ni content becomes constant 190 µm from the crystal edge, whereas Mg–Fe zonation extends 520 µm from the crystal edge to core (Fig. 3).

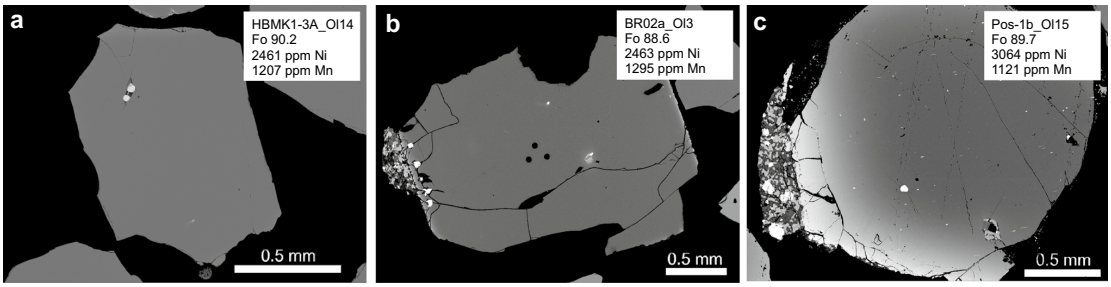

Fig. 2 Three olivine macrocrysts mounted in epoxy resin and selected to display difference in breadth of Mg–Fe compositional zoning between sampling locations **a** Háleyjabunga olivine (no.14) with thinner than 20 µm Mg–Fe zoning. **b** Brattaskjól olivine (no. 3) with a 90 µm thick Mg–Fe zoned rim. The three dots at the center are laser ablation pits. **c** Hvammsmúli olivine (no. 15) with a thick, 700 µm broad, Mg–Fe zoned rim

The broadest Mg–Fe zoning analyzed from Hvammsmúli olivines is 700 µm thick from rim to core (olivine Pos-1b_Ol15, Fig. 2c), while Ni zoning only extends ~500 µm from the rim (Fig. 2c). Zoning patterns in normally zoned Mosfellsheiði and Brattaskjól olivines are variable and thinner. Ni zonation extends 30–180 µm and 20–100 µm from the crystal edge towards the crystal cores for Mosfellsheiði and Brattaskjól olivines, respectively, while the width of the Mg–Fe zoned rims varies in the range 120–220 µm in Mosfellsheiði and 50–100 µm in Brattaskjól.

Major and trace elements in olivine

Major and trace element composition in the olivine macrocrysts examined is illustrated in Figs. 4 and 5, and the full dataset is included in the Supplementary Material. Olivine data from Kistufell and Háleyjabunga are found consistent with earlier analyses acquired by Sobolev et al. (2007) and Neave et al. (2018) (see Supplementary Material). The lowest Ni and highest Mn relative to Fo content were measured in olivines from Háleyjabunga and Berserkjahraun. Olivines from these two sampling locations define continuous linear trends on Mn vs. Fo and Ni vs. Fo plots (Fig. 4) and, at Fo_{90}, both have ~2500 ppm Ni and ~1200 ppm Mn. Kistufell and Mosfellsheiði olivine macrocrysts have higher Ni and lower Mn, and define a single trend in the Mn-Fo space (Fig. 4a). Kistufell has primitive $Fo_{88.15}$ olivines, whereas Mosfellsheiði olivines are relatively evolved ($Fo_{<86}$).

Compared to olivines from the rift-zones and SVZ, the SEVZ olivine macrocrysts have higher Ni and lower Mn contents at a given Fo content (Fig. 4). Values of Fo, Ni, Mn and Ca are similar in olivines from Hvammsmúli and Brattaskjól, although Hvammsmúli olivine are somewhat more forsteritic and have the highest Ni and lowest Mn (3536 ppm Ni and 1086 ppm Mn as compared to 3105 ppm Ni and 1189 ppm Mn in Brattaskjól). These two localities are combined for clarity as "Eyjafjallajökull lavas" in Fig. 4

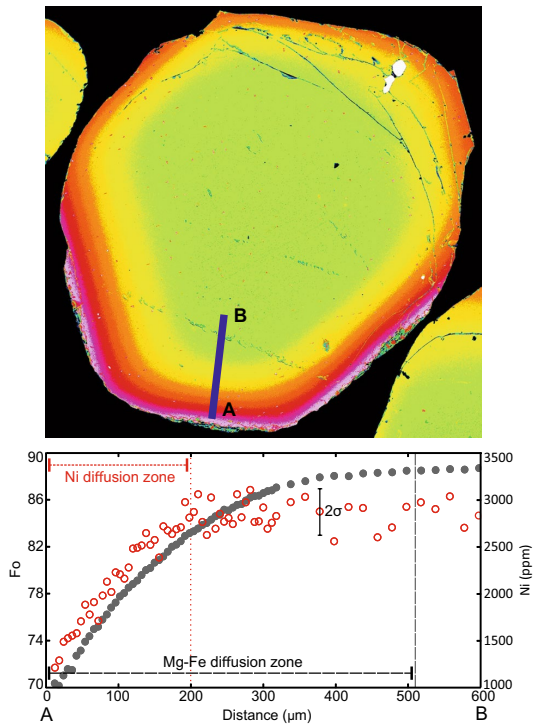

Fig. 3 Traverse across the zoning of Hvammsmúli olivine macrocryst (Pos-1a_Ol1). Location of the traverse shown on the upper false color olivine image, where yellow–green shades represent $Fo_{>80}$ olivine, and red–purple shades more ferrous ($Fo_{<80}$) compositions. In the lower graph, Fo and Ni variation at the edge segment (**a** through **b**) is shown. Near crystal edges, depressed Fo content ("Mg–Fe diffusion zone") extends farther towards the crystal core than lowered Ni ("Ni diffusion zone"). Average 2σ analytical error for Ni analyses is shown, while the propagated standard error in Fo content is approximately the size of the symbol

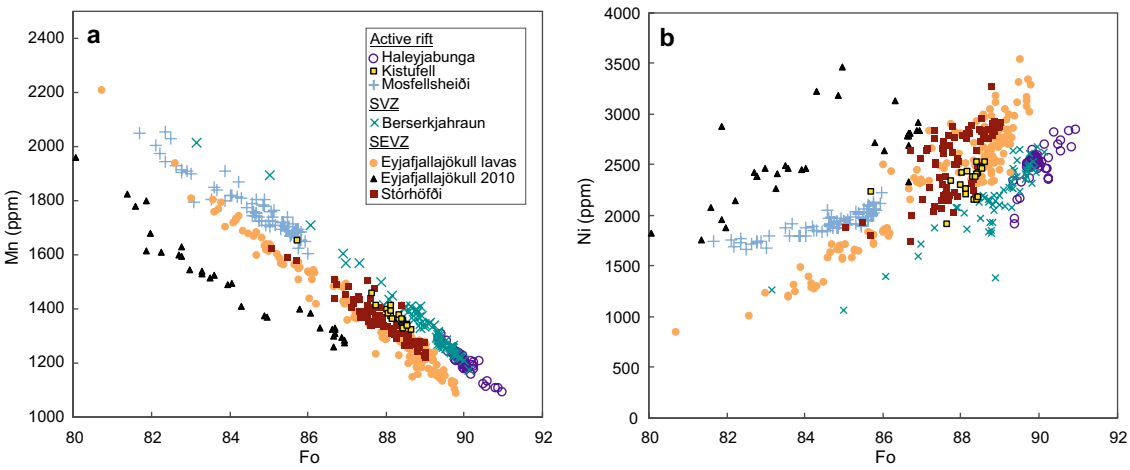

Fig. 4 **a** Mn and **b** Ni contents as a function of Fo content in olivine. Analytical error is equal or smaller than the symbol size

(compare to Fig. 8). In these lavas, there is a large trace element variability in the high-Fo primitive olivines compared to the more evolved. $Fo_{88.3–89.5}$ olivines have 1σ variations of ± 242 ppm for Ni, ± 50 ppm for Mn and ± 272 ppm for Ca in comparison to, e.g., $Fo_{85.0–86.2}$ olivines with 1σ of ± 89 ppm for Ni, ± 33 ppm for Mn and ± 93 ppm for Ca. Olivines with the lowest Ni and highest Mn in the $Fo_{88.3–89.5}$ population resemble Kistufell olivines (2350 ppm Ni and 1340 ppm Mn in Kistufell; Fig. 4), whereas the high-Ni olivines have 3360 ppm Ni and 1130 ppm Mn in average. Similarly, primitive olivines from Stórhöfði exhibit relatively large variability in trace element contents, and Eyjafjallajökull lavas and Stórhöfði form a unified linear array in the Mn vs. Fo diagram (Fig. 4). Olivine macrocrysts from the Eyjafjallajökull 2010 summit eruption have distinctively low Mn (Fig. 4a) and high Ni (Fig. 4b) in relation to the Fo content. The highest Ni is 3455 ppm in Fo_{85} olivine, whereas the more primitive olivines nearing Fo_{87} have more modest 2800–2920 ppm Ni. In addition, Ca contents in the Eyjafjallajökull 2010 olivines are low (1523 ppm on average).

Selected olivine macrocrysts from Hvammsmúli, Brattaskjól, Kistufell and Háleyjabunga were also analyzed with LA–ICP–MS for concentrations of Li, Na, Al, P, Ca, Sc, Ti, V, Cr, Mn, Co, Ni, Cu and Zn. At a given Fo, SEVZ olivines (Hvammsmúli and Brattaskjól) have lower Sc, and higher Li, Ti, Cr, Cu, and Zn, than Háleyjabunga (Fig. 5). The separate trends of SEVZ and Háleyjabunga olivines are outside of the analytical uncertainty; however, the compositions of Kistufell olivine macrocrysts overlaps the complete compositional variability detected in many trace elements (Sc, Ti, V and Al; Fig. 5). There is no significant difference in Co content, at a given Fo, between the locations. Brattaskjól olivine macrocrysts stand out with elevated Cr and Na in relation to the other samples. Our analyses of Háleyjabunga olivines are in agreement with earlier measurements by Neave et al. (2018), although our analyses have marginally higher Co contents. In turn, our SEVZ olivines resemble Neave et al. (2018) Stapafell olivines, with the exception that SEVZ olivines have higher Ti, Zn and Cu contents (Fig. 5).

Discussion

Ni, Mn and Ca in Iceland olivine macrocryst record

The major and trace element composition of Háleyjabunga and Berserkjahraun olivine macrocrysts resembles MORB olivines with low Ni and high Mn contents, and are compatible with the Herzberg (2011) model of olivine crystallizing from peridotite-derived melts and their derivate melts along Liquid Line of Descent (LLD, Fig. 6) at low pressure. Kistufell and Mosfellsheiði olivines, although richer in Ni and lower in Mn, are also consistent with peridotite melting, as long as melt mixing is allowed (red mixing lines in Fig. 6b). Mixing of primary and fractionated magmas can slightly elevate Ni in olivine relative to its Fo content (Herzberg et al. 2016). Ni contents in Mosfellsheiði olivines do not change over a range of Fo content (Fig. 6a), which may indicate cotectic crystallization of Ol + Plg + Cpx. Ca content in Háleyjabunga, Berserkjahraun, Kistufell and Mosfellsheiði olivine is compatible to Herzberg (2011) model of olivine crystallization from a peridotite source, except for a few Berserkjahraun olivines (Fig. 6c). In essence, the SVZ and rift-zone olivines in our dataset conform with lherzolite-sourced partial melts and the previous olivine data

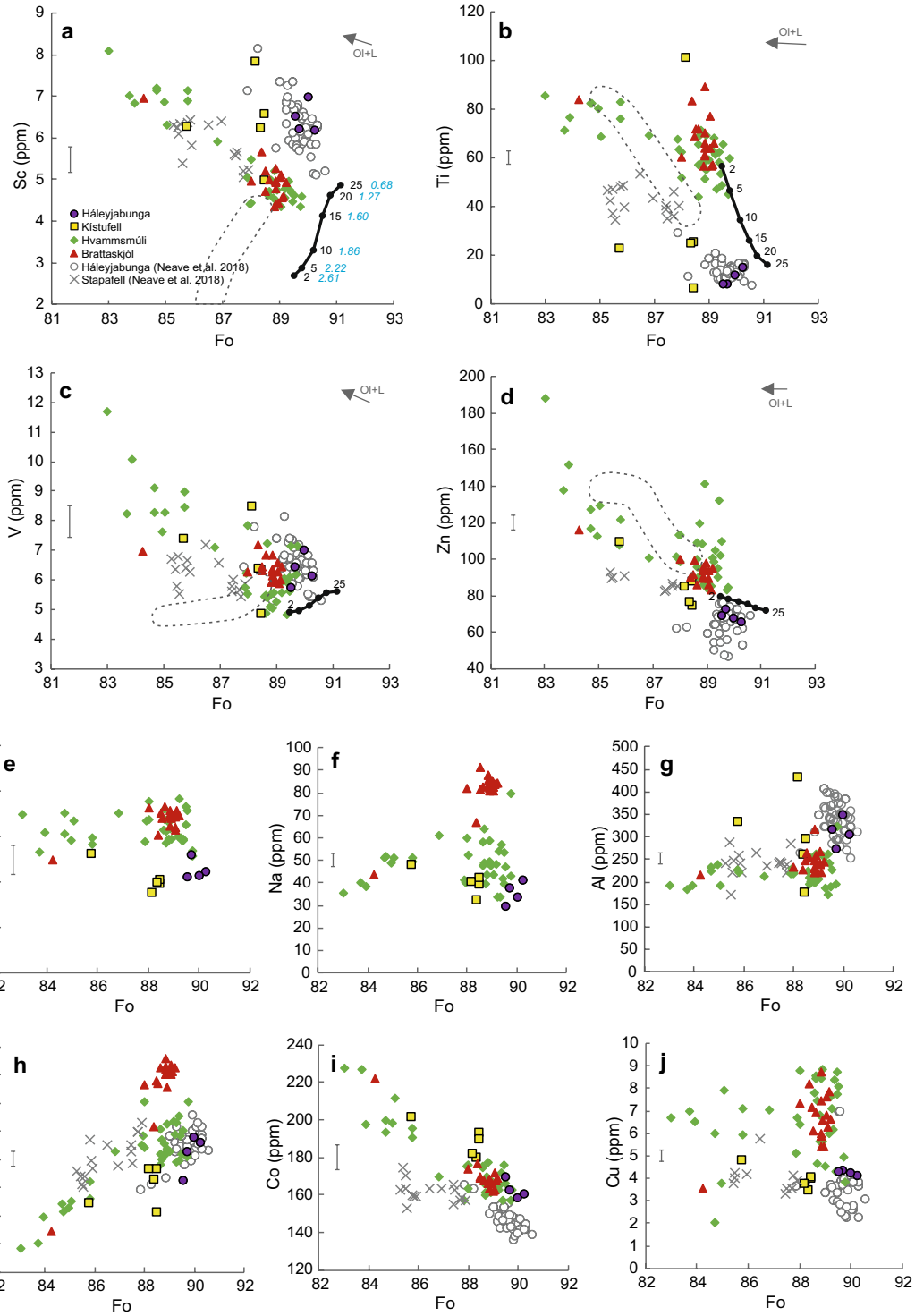
a
Sc (ppm)
Fo
Ol+L
Háleyjabunga
Kístufell
Hvammsmúli
Brattaskjól
Háleyjabunga (Neave et al. 2018)
Stapafell (Neave et al. 2018)
25 0.68
20 1.27
15 1.60
10 1.86
5 2.22
2 2.61
b
Ti (ppm)
c
V (ppm)
d
Zn (ppm)
e
Li (ppm)
f
Na (ppm)
g
Al (ppm)
h
Cr (ppm)
i
Co (ppm)
j
Cu (ppm)

◂**Fig. 5** **a–j** Sc, Ti V, Zn, Li, Na, Al, Cr, Co and Cu contents of Háleyjabunga, Stapafell, Kistufell, Hvammsmúli and Brattaskjól olivines. Compositions of model olivines crystallizing from accumulated near-fractional melts of KLB-1 mantle lherzolite (Hirose and Kushiro 1993) are indicated by the black line (cf. Sect. 5.5 for model details). Stippled field outlines the model olivine compositions in equilibrium with F5–40% melts of modally enriched KG2 peridotite (Kogiso et al. 1998). Labels in black and blue correspond to the degree of partial melting in percent (F%) and melt derivation pressures in GPa, respectively. Grey arrow marks the compositional vector produced by fractional crystallization of olivine; however, assumption of olivine-only crystallization has been shown true only for Háleyjabunga (Neave et al. 2018). Average instrumental 2σ errors are indicated by grey bars for the trace elements, whereas errors in Fo are smaller than the symbols used. Olivine Fo content is taken from EPMA analyses, whereas all trace element data is from LA-ICP-MS analyses. Háleyjabunga and Stapafell olivine compositions from Neave et al. (2018) are included for comparison

(Shorttle and Maclennan 2011; Herzberg et al. 2016; Neave et al. 2018).

Some olivines from Eyjafjallajökull and Vestmannaeyjar volcanic systems at SEVZ, however, have higher Ni contents and Fe/Mn ratios than previously published from Iceland (Fig. 6a, b). High Fe/Mn and Ni correlate in the high-Fo SEVZ olivine macrocrysts, and some of the high-Ni and high-Fe/Mn olivines, especially from the Eyjafjallajökull 2010 tephra, have low Ca (Fig. 6c). Many of the SEVZ olivines are outside the compositional range expected to crystallize from peridotite-derived melts as defined by Herzberg (2011) and may imply melting of an olivine-free mantle source (Sobolev et al. 2005) or relatively deep mantle melting combined with shallow olivine crystallization (Matzen et al. 2013, 2017a, b).

Trace elements concentrations in olivine couple strongly with Fo content. Thus, meaningful comparison of olivine compositions from different localities is achieved by normalizing the trace element contents by FeO or MgO, and by limiting the comparison to high-Fo olivines. In Fig. 7, we compare high-precision $Fo_{>86}$ olivine compositional data from SEVZ and other localities in Iceland (Sobolev et al. 2007, and this study) by utilizing Kernel density estimation (Green et al. 1988) of the probability density distribution of olivine compositions. Although SEVZ olivine compositions overlap with olivine from elsewhere in Iceland (Rift-zones and SVZ), Fig. 7 exhibits clearly how SEVZ has higher Ni and lower Mn in relation to olivine Fo. The Iceland rift-zone and SVZ olivine Ni data is somewhat bimodal, with two Ni(Mg/Fe)/100 probability density peaks at ~ 0.6 and ~ 0.7. This is not an artefact of combining our and Sobolev et al. (2007) datasets, but the result of elevated Ni in some Icelandic olivine. Herzberg et al. (2016) explained the elevated Ni in some Iceland olivine by mixing of near-primary and evolved melts derived from the same initially low-Ni, high-Mn peridotite sourced partial melt (see fig. 7 in Herzberg et al. 2016). The bimodality in SEVZ data (Fig. 7b) is solely produced by the Eyjafjallajökull 2010 olivines that have high Fe/Mn.

Indications of melt mixing

The SEVZ high-Fo olivines exhibit large variability in Ni, Mn and Ca contents, which decreases with decreasing Fo (Fig. 6). This is most evident in Brattaskjól and Hvammsmúli olivines, with $Fo_{<88.2}$ grains conforming to a crystal line of descent at low pressure and $Fo_{88.3–89.5}$ olivines exhibiting high variability in trace element contents (Fig. 8). In this high-Fo olivine population, there is an inverse correlation in Ni and Mn ($R^2 = 0.498$), and Ni and Ca ($R^2 = 0.486$). We interpret this compositional characteristic by mixing of near-primary mantle melts with initially varying Ni, Mn, and Ca.

The Hvammsmúli and Brattaskjól $Fo_{>88.2}$ olivines may initially have had variable Fo contents, which may have been later suppressed by diffusive re-equilibration with a carrier melt during crustal storage (Costa and Morgan 2010). During this process, variation in some trace elements (e.g. Ca) could have been retained due to their slower diffusion compared to Mg–Fe (e.g. Dohmen et al. 2007). Therefore, in theory, the high variability in trace element compositions in similar Fo olivines in Hvammsmúli and Brattaskjól could be a consequence of this incomplete re-equilibration process. This model is, however, hampered by the similar diffusion rates of Mn and Mg–Fe (Dohmen et al. 2007). Mn concentrations should have been similarly suppressed during diffusive re-equilibration as Fo contents, and we do not see this in the data (Fig. 8). In addition, the detected variation in Ca in olivines is so large (~ 1100 ppm, Figs. 6 and 8b), that producing it by olivine fractionation is improbable. Due to this reasoning, we favor mixing of two melts with significantly different Ca, Mn and Ni contents as the explanation for the high variability in the SEVZ olivine trace element contents. For Brattaskjól and Hvammsmúli, the higher Fo mixing end member has high Ni and relatively low Mn and Ca, whereas the more evolved member has lower Ni and higher Mn and Ca (Fig. 8).

High compositional variability is typical for high-Fo olivine-hosted melt inclusions of Icelandic magmas (Maclennan 2008a, b; Neave et al. 2013). This variability in the melt inclusion record (e.g. highly varying La/Yb) decreases as olivines become more evolved (ferrous), and the average composition of the olivine-hosted melt inclusions approaches the composition of the host magma. Maclennan (2008a) concluded that this phenomenon is consequential to mixing and homogenization of diverse mantle melts in the mid–lower crust. The major and trace element trends in Brattaskjól and Hvammsmúli olivine populations may indicate the same phenomenon: mixing of mantle melts derived from different depths and different

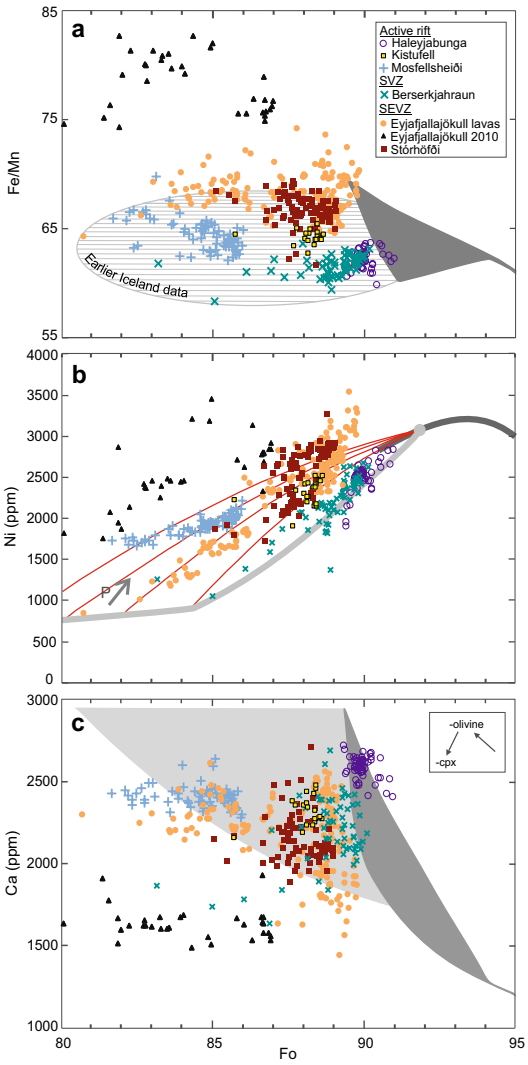

Fig. 6 Fe/Mn, Ni and Ca variation against Fo content of olivine crystals. Model olivine compositions adopted from Herzberg (2011) and Herzberg et al. (2016). "Eyjafjallajökull lavas" refer to the adjacent Hvammsmúli and Brattaskjól sampling locations. Higher Fe/Mn, Ni, and larger compositional variability at a given Fo content are evident for SEVZ magmas. **a** Olivine compositions in equilibrium with partial melts of peridotite source with 0.13% MnO marked with a gray field. Lined area defines the range of previous Iceland olivine data from Sobolev et al. (2007) and Neave et al. (2018). Olivine dominated fractional crystallization or mixing of basaltic magmas does not substantially change Fe/Mn in olivines. **b** The dark grey curve defines model olivine crystallizing from partial melts of peridotite (1964 ppm Ni) and the light grey curve describes olivine crystallizing along Liquid Line of Descent (LLD, primitive melt with 17.6% MgO). The LLD is calculated for 1 atm pressure; increase in pressure would hasten the onset of Cpx crystallization (arrow labelled 'P'). Red curves are olivine compositions that would crystallize from magmas that are mixtures of primary magma and derivate magmas along the LLD. **c** Dark grey field is model olivine of a peridotite source primary magma with 3.45 wt% CaO and 8–38 wt% MgO. The light grey area resembles model olivine crystallizing from derivate magmas with 8–20 wt% MgO. Analytical error is smaller than the symbol size

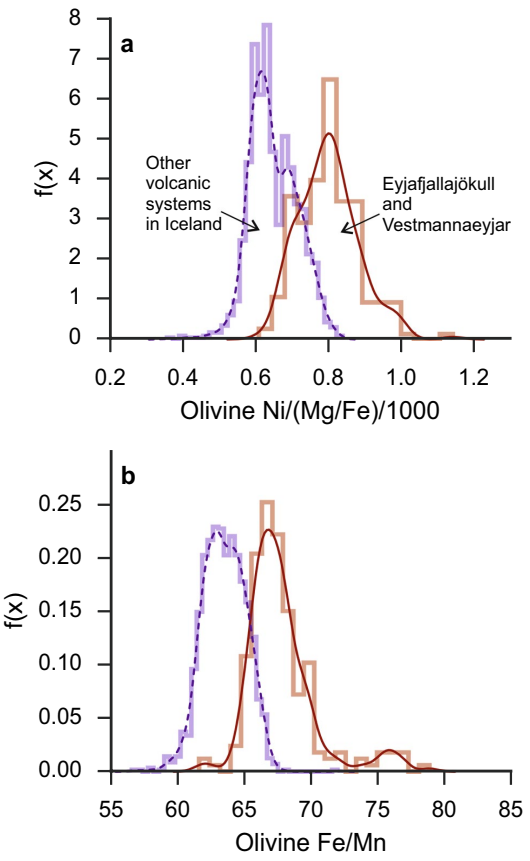

Fig. 7 $Fo_{>86}$ olivine trace element compositions from Sobolev et al. (2007) and this paper plotted as probability density against **a** olivine Ni/(Fe/Mg)/1000, **b** Olivine Fe/Mn. Dark lines are the Kernel Density Estimates of the data, and paler shades show the underlying histograms. SEVZ olivine data illustrated with red solid line and all other Iceland olivine compositions in violet stippled line. Higher values can be seen to represent higher contribution of pyroxenite mantle (e.g. Sobolev et al. 2007) or higher temperature difference between mantle melting and olivine crystallization (Matzen et al. 2013, 2017a, b)

rock-types from the mantle melting column. Furthermore, the variability in Brattaskjól and Hvammsmúli olivine trace element compositions indicates that the $Fo_{88.2–89.6}$ olivine population has had sufficiently short residence time in the magmatic environment not to be completely homogenized by diffusive re-equilibration.

High-P fractionation of clinopyroxene

Early fractionation of clinopyroxene has been proposed to explain elevated Ni and Fe/Mn and low Ca in olivines in some of the lavas of the North Atlantic Igneous Province

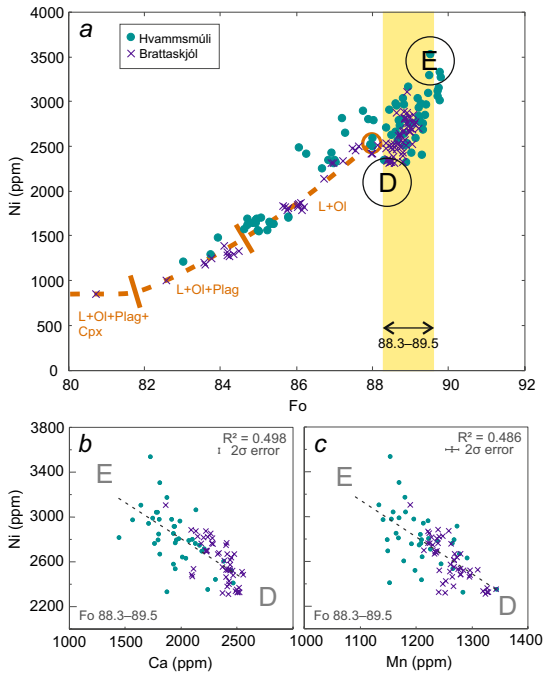

Fig. 8 **a** The observed steep Fo vs Ni trend of the Eyjafjallajökull transitional basalts (Hvammsmúli and Brattaskjól), interpreted as a mixing trend of two different mantle melts, one with high Ni (denoted with 'E' for enriched in Ni) and other with low Ni ('D' for depleted in Ni). The orange stippled line defines model olivine compositions that crystallize along Liquid Line of Descent (LLD) from a melt with equilibrium olivine composition 2500 ppm Ni at Fo_{88} (orange circle). These model olivine compositions have been calculated using the Beattie et al. (1991) model of olivine-liquid Ni partitioning and Þeistareykir initial melt composition (the same as used for the model olivines crystallizing along LLD in Fig. 6) with added 200 ppm Ni. The Þeistareykir initial melt composition was calculated with PRIMELT3 MEGA.xlsm (Herzberg and Asimow 2015). The yellow field marks the Fo range of the mixing trend and the olivine shown in the subplots **b** and **c**. In subplot **b** Ni vs Ca and **c** Ni vs Mn in $Fo_{88.3–89.5}$ olivine

(Hole 2018). Also, particular geochemical trends in Vestmannaeyjar lavas in SEVZ, specifically decreasing CaO/Al_2O_3 and Sc/Y with lowering MgO, have been explained by high-P (0.6–1.0 GPa) clinopyroxene crystallization (Furman et al. 1991; Mattsson and Oskarsson 2005). Against this backdrop, and considering that we assume olivine-dominated fractional crystallization for the Iceland magmas (Fig. 6), it is important to evaluate whether high-P clinopyroxene crystallization may have influenced the SEVZ olivine record.

The stability field of clinopyroxene expands at the expense of olivine at high P and clinopyroxene becomes a liquidus phase in progressively more primitive melts (O'Hara 1968); clinopyroxene crystallization can thus commence in near-primary mantle melts at high pressures. Crystallization of Ca-rich clinopyroxene lowers Ca and elevates Fe/Mn in the melt, and olivine crystallizing along with clinopyroxene may, therefore, be imprinted by higher Fe/Mn (Herzberg et al. 2013) and lower Ca (Hole 2018) than olivine crystallizing in the absence of clinopyroxene. Furthermore, Ni is not as compatible in clinopyroxene as in olivine, and therefore, the Ni content of mafic magmas can stay relatively elevated if clinopyroxene crystallization is initiated early in the crystallization sequence (Hole 2018).

It is unlikely that high-P fractionation of clinopyroxene could have produced the high Ni and low Mn contents in $Fo_{>88}$ olivines in Brattaskjól, Hvammsmúli and Stórhöfði, as clinopyroxene fractionation does not enrich melts in Ni, and thus cannot elevate Ni in olivines above the initial mantle-derived values. In addition, the trends of Ni and Ca against Fo content in olivines are not suggestive of clinopyroxene fractionation (i.e. steep depletion in Ni and enrichment in Ca in lower-Fo olivine, Fig. 6) for these localities. Olivine macrocrysts from the Eyjafjallajökull 2010 eruption tephra, however, may have been affected, as they are relatively evolved ($Fo_{<86.9}$), very poor in Ca and Mn, and show an increase in Fe/Mn (Fig. 6a) at $Fo_{82–85}$. Moreover, the relatively flat Ni versus Fo trend is suggestive of cotectic crystallization of olivine + clinopyroxene + plagioclase (Fig. 6b). These trace element characteristics comply with fractionation of clinopyroxene and olivine at high pressures, and thus the highest Fe/Mn values acquired from Eyjafjallajökull 2010 olivines (Figs. 6a and 7b) may have been affected by the early initiation of clinopyroxene crystallization.

Ni/Fo-decoupling in zoned olivine macrocrysts

Decoupled Fe–Mg and Ni in olivine rims likely reflects faster diffusion of Fe–Mg than Ni during re-equilibration of olivine and carrier melt (Lynn et al. 2017; Neave et al. 2018). We observed this decoupling in nearly all Hvammsmúli, Mosfellsheiði and Brattaskjól olivines. Considering the maximum thickness of olivine zonation in these localities, this phenomenon may have affected Ni/Fo ratio (by lowering Fo in relation to constant Ni) in crystal cores of Hvammsmúli olivines smaller than 1.4 mm, and Mosfellsheiði and Brattaskjól olivines smaller than 0.5 mm and 0.25 mm in diameter, respectively. Luckily, these locations host large olivine macrocrysts; therefore, only a few (potentially 13 out of 79) olivine core analyses of Hvammsmúli and none of the olivine core analyses of Mosfellsheiði or Brattaskjól may have been affected. In general, the Iceland olivine macrocryst record is dominated by large homogenous cores with thin zones of diffusive re-equilibration at crystal rims (e.g.

Thomson and Maclennan 2013). Hence, accidental analyses of Fe–Mg zoned olivine rims (with non-equilibrium Ni/Fo ratio) are improbable and unlikely to affect the current Iceland olivine trace element record (Shorttle and Maclennan 2011; Sobolev et al. 2007; Neave et al. 2018; and this study) to any significant degree.

Sc, Ti, V and Zn and their partitioning in mantle melting

In addition to the apparent enrichment in Ni coupled with lower Mn and Ca contents, SEVZ olivines have different Li, Sc, Ti, V, Zn and Cu contents in comparison to Háleyjabunga olivines (Fig. 5). This could be solely consequential to the greater depth and lower degree of mantle melting (*F*) at SEVZ, and it is uncertain, whether variation in the mantle source can be discerned based on these trace elements. To inspect this, we modelled partitioning of Sc, Ti, V and Zn during adiabatic near-fractional melting of KLB-1 lherzolite (Hirose and Kushiro 1993) at 1480 °C potential temperature (Matthews et al. 2016) and 0.5–4.0 GPa. In addition, we ran a similar melting model for the KG2 olivine-bearing pyroxenite–peridotite hybrid (Kogiso et al. 1998). Sc, Ti, V and Zn were chosen, because their partitioning has been determined at high-P conditions and sufficient partitioning coefficients were available (Davis et al. 2013; Laubier et al. 2014). Cu and Li were not modelled as their partitioning is yet poorly constrained, and since they are moderately incompatible to incompatible elements in mantle melting, their enrichment in SEVZ olivines (Fig. 5) likely reflects lower *F*, not variation in mantle mode (Ryan and Langmuir 1987; Lee et al. 2012). Al-depletion in SEVZ olivines in comparison to Háleyjabunga olivines, in turn, is likely consequential to higher Fo of Háleyjabunga olivines and the Mg-dependent partitioning of Al (Herzberg and O'Hara 2002).

The modelling of mantle melting was done with the pMELTS software (Ghiorso et al. 2002) with the ALPHAMELTS 1.8. front end (Smith and Asimow 2005). We used the correct version of pMELTS garnet model (Berman and Koziol 1991), and did not include Na_2O, K_2O, Cr_2O_3 and MnO into the initial mantle compositions. pMELTS has not been calibrated for MnO (Ghiorso et al. 2002), Cr_2O_3 was not included to avoid over-stabilization of spinel (Asimow et al. 1995), and Na_2O and K_2O were omitted to facilitate reliable estimation of the solidus (Lambart et al. 2012, 2016; Jennings et al. 2017). All models were done without imposed constrains on fO_2, although $fO_2 = FQM - 1$ was used to set Fe^{2+}/Fe^{3+} for the initial state. A 0.5 wt% threshold of melt extraction was used in all models, and a simple 1D melt aggregation column was assumed when assessing the composition of accumulated near-fractional partial melts at various pressures. After modelling mantle melting, we calculated the Fo and trace element content of olivine in equilibrium with the model mantle melts at 1 atm utilizing the parameterization of Herzberg and O'Hara (2002) and appropriate partitioning coefficients. The Supplementary Material provides the complete model conditions, initial mantle source compositions and partitioning coefficients.

Modally enriched mantle components, such as KG2, are thought to reside in the sub-Icelandic mantle as slivers in a more refractory matrix (Shorttle et al. 2014). Hence, our model melts of a one-component near-fractional mantle melting of KG2 do not fully suffice as an analogy for potential enriched Iceland melts. We opted for this simple setup, as developing a complex multi-component melting model for the sub-Icelandic mantle was not the aim of this study (cf. Shorttle and Maclennan 2011; Rudge et al. 2013; Shorttle et al. 2014; Lambart 2017 for existing parameterizations). The model olivine compositions of the KLB-1, and especially the KG2, partial melts are mainly illustrative and restricted by the limitations of pMELTS (cf. Rudge et al. 2013 and the Supplementary Material). Fo content in the KG2 model olivines should be treated with caution, as pMELTS performs poorly when calculating major element compositions in partial melts of modally enriched mantle lithologies (e.g. Lambart et al. 2016). The model olivine compositions are, however, useful for a qualitative estimation of whether typical KLB-1 lherzolite can explain the detected trace element variability in olivines, or whether lithological variation in the source is suggested.

The model olivine compositions crystallizing from KLB-1 and KG2 partial melts are shown in Fig. 5 and given in the Supplementary Material. The KLB-1 solidus is crossed at 3.2 GPa in the garnet stability field and garnet is in the residue until the spinel-garnet transition at 1.77 GPa. Spinel disappears from the residue at 1.63 GPa. The large stability range of garnet in comparison to spinel reflects limitations in the pMELTS garnet model and is partly due to omitting Cr_2O_3 from the calculations. Melt aggregation occurs over a large P-interval with a melt-fraction of 2% at 2.61 GPa, 5% at 2.22 GPa, 10% at 1.86 GPa, 15% at 1.60 GPa, 20% at 1.27 GPa and 25% at 0.68 GPa (Fig. 5a). According to the pMELTS model, the KG2 mantle is already 5% molten at 4 GPa, and this melt portion was handled as an isobaric batch melting at 4.00 GPa. Its melt fraction increases to 10% at 2.11 GPa, 15% at 1.78 GPa, 20% at 1.47 GPa, 25% at 1.30 GPa, 30% at 1.15 GPa, 40% at 0.99 GPa and 45% at 0.85 GPa. The accumulated partial melts are ferric, which manifests as low Fo content of the model olivines (Fig. 5).

The Sc, Ti, and V concentrations in the analyzed olivine crystals conform with model olivines crystallizing from partial melts of lherzolite mantle (KLB-1). Háleyjabunga olivines show compatibility with a high-degree melt of a spinel lherzolite, whereas Brattaskjól and Hvammsmúli

olivines seem to have crystallized from accumulated low-degree melts of mixed spinel and garnet lherzolite source (Fig. 5). Lower Sc in SEVZ olivines can be explained by greater depth of melting (Fig. 5a, higher D_{Sc} in garnet lherzolite compared to spinel lherzolite), whereas high Ti in SEVZ olivines is compatible with the lower F expected in off-rift setting (Fig. 5b). Differences in V can be also attributed to greater melting depth beneath SEVZ (Fig. 5c), but due to the strong dependency of V partitioning on fO_2 (Canil 1997; Laubier et al. 2014), the lower V in olivines may also reflect more oxidized nature of the SEVZ magmas. KG2-sourced model olivines have comparable Sc, Ti and V contents to those of KLB-1, although similar Sc and Ti values are reached at higher melt fractions (Fig. 5a–c).

Our KLB-1 lherzolite melting model does not explain the elevated Zn in SEVZ olivines, as Zn content is rather insusceptible to melting degree and melt derivation depth. In turn, KG2 model olivines have high Zn in comparison to KLB-1 melts (Fig. 5d), and thus the high Zn in SEVZ olivines may indicate the contribution of a modally (more pyroxene, less olivine) or compositionally (elevated Zn) enriched source in the mantle melting. Elevated Zn/Fe is a known property of many OIB magmas and has been proposed to indicate olivine-free pyroxenite in the mantle source (Le Roux et al. 2010, 2011). Alternatively, the lower Fo content in SEVZ olivines compared to Háleyjabunga, potentially implying a more differentiated host melt, may also contribute to the apparent Zn-enrichment in the SEVZ olivines. The olivine-liquid partitioning of Zn during fractional crystallization of basalts is yet inadequately constrained.

In essence, although Sc, Ti and V contents of the SEVZ olivines conform to olivine crystallizing from partial melts of KLB-1 lherzolite, the Zn enrichment may indicate that some enriched lithologies partake in melting in the mantle below. KG2-like peridotite–pyroxenite hybrid could be a good candidate for a potential enriched mantle lithology below Iceland, as it produces magmas with high-Fe/low-Ca (Shorttle et al. 2014) and, according to our analysis, does not significantly modify Sc, V, and Ti in olivines compared to 'normal lherzolite' values.

Origin of the SEVZ olivine signature

High Fe/Mn and Ni, and low Ca in olivine are attributes of olivine crystallized from a partial melt of olivine-free pyroxenite mantle (Sobolev et al. 2007). Following this rationale, the strongest affinity to 'pyroxenite source' is shown by the Eyjafjallajökull 2010 olivine macrocrysts, but also the other SEVZ samples show partial contribution of olivine-free source (Fig. 7). The highest-Ni Hvammsmúli, Brattaskjól and Stórhöfði olivines in SEVZ are comparable to, e.g., the ~ 70 Ma Quepos Terrane olivine from magmas of the Galapagos plume, for which olivine-free pyroxenite mantle source has been inferred (Trela et al. 2015). The parametrization of Gurenko et al. (2010):

$$X_{px} = 6.705 \times 10^{-4} \times \mathrm{Ni(ppm)} \times \frac{\mathrm{FeO}}{\mathrm{MgO}} - 1.332 \times 10^{-2} \times \frac{\mathrm{Mn(ppm)}}{\mathrm{FeO}} + 1.524, \quad (1)$$

implies 44–52 wt% and 64–77 wt% contribution of olivine-free pyroxenite-derived melt (X_{px}) to the parental melt of Hvammsmúli high-Ni (> 3000 ppm) and Eyjafjallajökull 2010 olivine macrocrysts, respectively.

Recent thermodynamic modelling suggests that the silicic melts of olivine-free pyroxenite are prone to react with the surrounding peridotite, and thus less likely to preserve their coherence and compositional signature and eventually crystallize olivine in the crust (Lambart 2017). In addition, as the concentrations of the transitional elements in the SEVZ olivines are compatible with a garnet lherzolite mantle source, large input from olivine-free source seems unlikely. Although some of the SEVZ olivines were found to be Zn-enriched, this does not necessarily argue for olivine-free source, as Zn-enrichment is also expected in partial melts of enriched olivine-bearing mantle types (e.g. KG2). Furthermore, the lower Ca in olivines does not indicate the absence of olivine in the mantle source either but may imply lower degree of mantle melting and source enrichment in clinopyroxene or garnet.

As large-scale contribution of magmas directly derived from olivine-free mantle (Px-1 or similar, Sobolev et al. 2007) seems unlikely for SEVZ magmatism, we proceed on deciphering the SEVZ olivines by means of relatively deep melting of olivine-bearing mantle. Also, even if the mantle signature in the SEVZ olivines was due to contribution of melts from olivine-free pyroxenite source, the mantle melting would occur deep anyhow, due to the lower solidus temperature and greater fusibility of olivine-free pyroxenite in comparison to common mantle peridotite (Lambart et al. 2016).

$D_{Ni}^{ol/liq}$ and $D_{Mn}^{ol/liq}$ are, directly (the former) and indirectly (the latter), temperature dependent (Matzen et al. 2013, 2017a, b), and elevated Ni and Mn in olivine can thus be related to the temperature difference between mantle melting and olivine crystallization ($-\Delta T_{m\text{-}c}$). The ratio between NiO in crystallizing equilibrium olivine ($NiO^{ol}@T_c$) and NiO content in olivine in the mantle ($NiO^{ol}@T_m$) relates to the temperature of olivine crystallization (T_c) and mantle melting (T_m) as follows (Matzen et al. 2017a):

$$\frac{\mathrm{NiO^{Ol}}@T_c}{\mathrm{NiO^{Ol}}@T_m} = \exp\frac{-\Delta_{r(1)}H^{\circ}_{T_{ref},P_{ref}}}{R}\left(\frac{1}{T_c} - \frac{1}{T_m}\right), \quad (2)$$

where $-\Delta_{r(1)}H^{\circ}_{T_{ref},P_{ref}}/R$ is the temperature dependency of $D^{ol/liq}_{Ni}$ (K), T_c and T_m are in Kelvin and NiO^{ol} in weight units. This can be rearranged for the temperature difference between mantle equilibration and olivine crystallization (ΔT_{m-c}):

$$\Delta T_{m-c} = \frac{-\ln \frac{NiO^{Ol}@T_c}{NiO^{Ol}@T_m}}{\left(-\Delta_{r(1)}H^{\circ}_{T_{ref},P_{ref}}/R\right)} + \frac{1}{T_c}^{-1} - T_c. \quad (3)$$

This equation allows estimation of the temperature at which the parental melt of the Ni-rich SEVZ olivine grains last equilibrated with the mantle. For the calculation, we used 0.43 wt% NiO for $NiO^{ol}@T_c$, the same amount as in the five most Ni-rich SEVZ $Fo_{>88.3}$ olivines, 2975 ppm Ni in mantle olivine ($NiO^{ol}@T_m$), as in Herzberg et al. (2016), 4505 ± 196 K for the temperature dependency of Ni-partitioning ($-\Delta_{r(1)}H^{\circ}_{T_{ref},P_{ref}}/R$; Matzen et al. 2017a), and 1316 °C for near surface olivine crystallization temperature (T_c). The last is an average of published $Fo_{>88.3}$ olivine crystallization temperatures from Holocene Icelandic lavas determined using olivine-spinel aluminum exchange thermometry (Matthews et al. 2016; Spice et al. 2016). It is to be noted that the selection of T_c has only minor effect on the calculated ΔT_{m-c} within reasonable values (e.g. 1266–1447 °C), but the formalization is susceptible to uncertainty regarding Ni in mantle olivine (Matzen et al. 2017a).

With these parameters, Eq. 3 gives 75 ± 3 °C for the $-\Delta T_{m-c}$, i.e. it indicates mantle-melt equilibration at 75 ± 3 °C higher T than the T of olivine crystallization. Using the slope of the olivine-saturated liquidus (55 °C/GPa, Sugawara 2000), ΔT_{m-c} corresponds to 1.36 ± 0.06 GPa ΔP. If we assume olivine crystallization at surface (at 1 atm) and 3100 kg/m^3 average density for crust and refractory uppermost mantle, this pressure corresponds to ~45 km final mantle melting depth. This must be considered as the absolute minimum value for the inferred depth of melt equilibration in the mantle (final melting depth), as primitive olivine macrocrysts of Hvammsmúli and Stórhöfði likely crystallized at considerable pressure and depth, not at the surface. Crystallization pressures up to 0.6–1.0 GPa for Vestmannaeyjar and Eyjafjallajökull magmas have been proposed (Jakobsson et al. 1973; Furman et al. 1991; Sigmarsson 1996; Keiding and Sigmarsson 2012). If these pressures of olivine crystallization are considered and correspondingly elevated T_c's are used (1349–1371 °C), final melting pressures of 2.0–2.5 GPa (i.e. depths of 66–81 km) are indicated. These pressures are close to the inferred pressure of spinel-garnet phase transition for KLB-1 lherzolite mantle (2.14–2.17 GPa, Jennings and Holland 2015).

Our estimation of final mantle-melt equilibration at > 45 km depth is considerably deeper than the crustal thickness at SEVZ (Darbyshire et al. 2000; Fedorova et al. 2005; Jenkins et al. 2018), but in line with the depth of the lithosphere–asthenosphere boundary (LAB) according to glacial isostatic adjustment studies (Árnadóttir et al. 2009; Barnhoorn et al. 2011). However, there is considerable uncertainty regarding the LAB in Iceland, with resent estimates of ridge centered lithospheric thicknesses varying in 10–60 km range (Pagli et al. 2007; Bjarnason and Schmeling 2009; Barnhoorn et al. 2011; Rychert et al. 2018). We do not view the olivine compositions as a direct proxy for LAB depth (as done in, e.g. Matzen et al. 2017a), but consider the SEVZ high-Ni olivines as the crystallization products of deep accumulated melts that avoided mixing and equilibration at the top of the melting column in the mantle (which may or may not correspond to LAB). This view is supported by (1) the previously discussed mantle melt mixing trend in Brattaskjól and Hvammsmúli olivine populations, where the high-Ni olivines represent a deep endmember in the presence of apparent shallower mantle melt; and (2) the likelihood of mantle-melt equilibration pressures greater than 2 GPa supported by the evidence for deep olivine crystallization and "garnet signature" (low Sc) in olivine crystals. Essentially, the SEVZ high-Ni/low-Mn olivines are an indication of the survival of mantle melts from the deep parts of the mantle-melting column to the *T*–*P*-conditions of olivine crystallization.

What makes SEVZ special?

High-Ni, low-Mn olivines seem to be characteristic for SEVZ but absent in SVZ and the rift-zone magmas. This is noteworthy, especially regarding the trace element enriched SVZ lavas (e.g. Berserkjahraun), which, alike SEVZ lavas, have compositional and isotopic characteristics arguing in favor of melt extraction from relatively deep in the mantle (e.g. Kokfelt et al. 2006). Why the apparent signature of deep mantle melting in olivines at SEVZ in particular?

It is likely that deep mantle melts are in fact ubiquitous in all rift-zones and off-rift zones in Iceland, but they are usually diluted by melt mixing in the mantle or mid–lower-crust (Maclennan 2008a; Neave et al. 2013). Although magmas originating from deep portions of the mantle can erupt at the rift zones (as indicated by trace element enriched lavas like Stapafell and Gaesafjöll, Shorttle and Maclennan 2011), survival of deep melts is most likely to occur at off-rift settings, like at SEVZ, where the degree of mantle melting is low (Kokfelt et al. 2006). Furthermore, as magmatism at SEVZ is a relatively recent phenomenon (younger than 3 Ma, Martin et al. 2011), the underlying mantle may have not yet been depleted of the most fusible lithologies (e.g. KG2), which further biases the melt production to increased depth. Sufficiently refractory shallow mantle (e.g. harzburgite, Shorttle

et al. 2014) and effective vertical melt transport could also inhibit melt mixing in the mantle and promote magma derivation from depth. Channelized melt transport (Spiegelman and Kelemen 2003; Weatherley and Katz 2012; Rudge et al. 2013), in contrast to melt extraction by diffuse (equilibrium) porous flow (Lundstrom et al. 1995; Niu 1997; Dijkstra et al. 2003), may be the required melt transfer mechanism for survival of deep mantle melts and potentially important in the mantle below SEVZ.

The nature of the crustal magma plumbing systems beneath Eyjafjallajökull and Vestmannaeyjar is also likely to contribute to the crystallization, and survival, of high-Ni/low-Mn olivine macrocrysts. Even if a parcel of deep mantle melt were to keep its coherency during transit through the mantle and manage to crystallize equilibrium olivine in the crust (with high-Ni, low-Mn), this olivine would need to be erupted relatively fast to avoid re-equilibration with accumulated magmas with diverse composition during storage in the crust or uppermost mantle. Olivine macrocrysts in Iceland are rarely in equilibrium with their carrier melts, and are prone to be modified by diffusive re-equilibration (Thomson and Maclennan 2013). For example, if the Hvammsmúli and Brattaskjól olivine population (Fig. 8) had resided in a magma reservoir for extended time, the compositional signature of deep origin would have been erased. The originally heterogeneous olivine cargo (high variability in Ni, Mn and Ca in high-Fo olivines; Fig. 8) would have re-equilibrated diffusively with itself and the carrier magma, suppressing extremes in Ni, Mn and Ca. In the end, homogenized olivine population would have only modest enrichment in Fe/Mn and "Kistufell-like" Ni and Ca (Fig. 6) and the original subpopulation of high-Ni olivines might only be identifiable from olivine-hosted melt inclusions or slowly diffusing trace elements.

There are indications of short-lived and poorly developed deep magma storage systems below Eyjafjallajökull and Vestmannaeyjar. U-series disequilibria (Sigmarsson 1996) and absence of equilibrium phenocryst assemblages (Mattsson and Oskarsson 2005) in Vestmannaeyjar lavas suggest rapid differentiation within a deep and cold crust and short magmatic residence times. Furthermore, deep seismicity prior to and during the Eyjafjallajökull 2010 eruption suggests near-direct magma derivation from the mantle (Tarasewicz et al. 2012). Relatively fast transport of mantle melts limits crystal–melt equilibration and magma mixing, promoting survival of compositional extremes in the mineral cargo. Rather little is known about the lower-crustal magma storage zones in SVZ, but the maturity of SVZ volcanism could hint at well-established magma reservoirs. SVZ low-degree primitive magmas may reside in the deep crust (or shallow mantle) long enough that magmas aggregated from different depths in the mantle melting column are better mixed and equilibrated. This limits compositional variability in populations of primitive olivine, and suppresses a potential "deep melting signature" (high-Ni/low-Mn in olivines).

Conclusion

In each of the sampling locations, major and trace element trends in olivine populations reflect events of fractional crystallization, magma mixing and diffusive re-equilibration. Two Eyjafjallajökull transitional basalts also show large variability in the Ni, Mn and Ca contents of primitive $Fo_{88.2–89.6}$ olivines, which we consider as a mixing trend of melts equilibrated at different levels in the mantle. Eyjafjallajökull and Vestmannaeyjar volcanic systems in SEVZ have anomalous (high-Ni and Fe/Mn-enriched) olivines compared to previously published olivine data from Iceland. These olivine macrocrysts likely crystallized from magmas that equilibrated with the mantle at relatively high temperatures and pressures, at depths of > 45 km and possibly as deep as 66–81 km near the spinel-garnet peridotite transition. The evidence for deep mantle melts that avoided mixing and kept their coherency while migrating up through the upper mantle and the crust is an indication of effective vertical magma transport below SEVZ.

Acknowledgements Open access funding provided by University of Helsinki including Helsinki University Central Hospital. We thank Matthew Pankhurst and Sæmundur Ari Halldórsson for providing the Eyjafjallajökull 2010 and Berserkjahraun samples, respectively. Maren Kahl is thanked for discussions and Atli Hjartarson for skillfully preparing the samples for microprobe and LA–ICP–MS analyses. Comments from two anonymous reviewers improved the manuscript. This work was funded by the Nordic Volcanological Center, Icelandic Research Fund doctoral student Grant (185267-051) and Landsvirkjun geothermal research grant.

References

Allègre CJ, Turcotte DL (1986) Implications of a two-component marble-cake mantle. Nature. https://doi.org/10.1038/323123a0

Árnadóttir T, Lund B, Jiang W et al (2009) Glacial rebound and plate spreading: results from the first countrywide GPS observations in Iceland. Geophys J Int 177:691–716. https://doi.org/10.1111/j.1365-246X.2008.04059.x

Asimow PD, Hirschmann MM, Ghiorso MS et al (1995) The effect of pressure-induced solid-solid phase transitions on decompression melting of the mantle. Geochim Cosmochim Acta 59:4489–4506. https://doi.org/10.1016/0016-7037(95)00252-U

Balta JB, Asimow PD, Mosenfelder JL (2011) Manganese partitioning during hydrous melting of peridotite. Geochim Cosmochim Acta 75:5819–5833. https://doi.org/10.1016/j.gca.2011.05.026

Barnhoorn A, van der Wal W, Drury MR (2011) Upper mantle viscosity and lithospheric thickness under Iceland. J Geodyn 52:260–270. https://doi.org/10.1016/j.jog.2011.01.002

Batanova VG, Sobolev AV, Kuzmin DV (2015) Trace element analysis of olivine: high precision analytical method for JEOL JXA-8230 electron probe microanalyser. Chem Geol 419:149–157. https://doi.org/10.1016/j.chemgeo.2015.10.042

Beattie P, Ford C, Russell D (1991) Partition coefficients for olivine-melt and ortho-pyroxene-melt systems. Contrib Miner Pet 109:212–224. https://doi.org/10.1007/bf00306480

Berman RG, Koziol AM (1991) Ternary excess properties of grossular-pyrope-almandine garnet and their influence in geothermobarometry. Am Mineral 76:1223–1231

Bjarnason IT, Schmeling H (2009) The lithosphere and asthenosphere of the Iceland hotspot from surface waves. Geophys J Int. https://doi.org/10.1111/j.1365-246X.2009.04155.x

Breddam K (2002) Kistufell: primitive melt from the Iceland mantle plume. J Petrol 43:345–373. https://doi.org/10.1093/petrology/43.2.345

Breddam K, Kurz MD, Storey M (2000) Mapping out the conduit of the Iceland mantle plume with helium isotopes. Earth Planet Sci Lett 176:45–55. https://doi.org/10.1016/S0012-821X(99)00313-1

Brown EL, Lesher CE (2014) North Atlantic magmatism controlled by temperature, mantle composition and buoyancy. Nat Geosci 7:820–824. https://doi.org/10.1038/ngeo2264

Canil D (1997) Vanadium partitioning and the oxidation state of Archaean komatiite magmas. Nature 389:842–845. https://doi.org/10.1038/39860

Chauvel C, Hémond C (2000) Melting of a complete section of recycled oceanic crust: trace element and Pb isotopic evidence from Iceland. Geochem Geophys Geosyst 1:1–22. https://doi.org/10.1029/1999GC000002

Chauvel C, Lewin E, Carpentier M et al (2008) Role of recycled oceanic basalt and sediment in generating the Hf-Nd mantle array. Nat Geosci. https://doi.org/10.1038/ngeo.2007.51

Costa F, Morgan D (2010) Time constraints from chemical equilibration in magmatic crystals. Timescales of magmatic processes: from core to atmosphere. Wiley, Chichester, pp 125–159

Darbyshire FA, White RS, Priestley KF (2000) Structure of the crust and uppermost mantle of Iceland from a combined seismic and gravity study. Earth Planet Sci Lett 181:409–428. https://doi.org/10.1016/S0012-821X(00)00206-5

Davis FA, Humayun M, Hirschmann MM, Cooper RS (2013) Experimentally determined mineral/melt partitioning of first-row transition elements (FRTE) during partial melting of peridotite at 3 GPa. Geochim Cosmochim Acta 104:232–260. https://doi.org/10.1016/j.gca.2012.11.009

Dijkstra AH, Barth MG, Drury MR et al (2003) Diffuse porous melt flow and melt-rock reaction in the mantle lithosphere at a slow-spreading ridge: a structural petrology and LA–ICP–MS study of the Othris Peridotite Massif (Greece). Geochem Geophys Geosyst. https://doi.org/10.1029/2001GC000278

Dohmen R, Becker HW, Chakraborty S (2007) Fe-Mg diffusion in olivine I: experimental determination between 700 and 1200 °C as a function of composition, crystal orientation and oxygen fugacity. Phys Chem Miner 34:389–407. https://doi.org/10.1007/s00269-007-0157-7

Fedorova T, Jacoby WR, Wallner H (2005) Crust-mantle transition and Moho model for Iceland and surroundings from seismic, topography, and gravity data. Tectonophysics 396:119–140. https://doi.org/10.1016/j.tecto.2004.11.004

Fitton J, Saunders A, Norry M et al (1997) Thermal and chemical structure of the Iceland plume. Earth Planet Sci Lett Planet Sci Lett 153:197–208. https://doi.org/10.1016/S0012-821X(97)00170-2

Fitton JG, Saunders AD, Kempton PD, Hardarson BS (2003) Does depleted mantle form an intrinsic part of the Iceland plume? Geochem Geophys Geosyst. https://doi.org/10.1029/2002GC000424

Furman T, Frey FA, Park KH (1991) Chemical constraints on the petrogenesis of mildly alkaline lavas from Vestmannaeyjar, Iceland: the Eldfell (1973) and Surtsey (1963–1967) eruptions. Contrib Mineral Petrol 109:19–37. https://doi.org/10.1007/BF00687198

Ghiorso MS, Hirschmann MM, Reiners PW, Kress VC (2002) The pMELTS: a revision of MELTS for improved calculation of phase relations and major element partitioning related to partial melting of the mantle to 3 GPa. Geochem Geophys Geosyst 3:1–35. https://doi.org/10.1029/2001GC000217

Green DH, Ringwood AE (1963) Mineral assemblages in a model mantle composition. J Geophys Res. https://doi.org/10.1029/JZ068i003p00937

Green PJ, Seheult AH, Silverman BW (1988) Density estimation for statistics and data analysis. Appl Stat 37:120. https://doi.org/10.2307/2347507

Guillong M, Meier DL, Allan MM et al (2008) SILLS: a Matlab-based program for the reduction of laser ablation ICP–MS data of homogeneous materials and inclusions. Mineral Assoc Can Short Course 40:328–333

Gurenko AA, Hoernle KA, Sobolev AV et al (2010) Source components of the Gran Canaria (Canary Islands) shield stage magmas: evidence from olivine composition and Sr–Nd–Pb isotopes. Contrib Mineral Petrol 159:689–702. https://doi.org/10.1007/s00410-009-0448-8

Hardarson BS, Fitton JG, Ellam RM, Pringle MS (1997) Rift relocation—a geochemical and geochronological investigation of a palaeo-rift in northwest Iceland. Earth Planet Sci Lett 153:181–196. https://doi.org/10.1016/S0012-821X(97)00145-3

Hauri EH (1996) Major-element variability in the Hawaiian mantle plume. Nature 382:415–419. https://doi.org/10.1038/382415a0

Heinonen JS, Fusswinkel T (2017) High Ni and low Mn/Fe in olivine phenocrysts of the Karoo meimechites do not reflect pyroxenitic mantle sources. Chem Geol 467:134–142. https://doi.org/10.1016/j.chemgeo.2017.08.002

Hemond C, Arndt NT, Lichtenstein U et al (1993) The heterogeneous Iceland plume: Nd-Sr-O isotopes and trace element constraints. J Geophys Res 98:15833. https://doi.org/10.1029/93JB01093

Herzberg C (2011) Identification of source lithology in the Hawaiian and Canary islands: implications for origins. J Petrol 52:113–146. https://doi.org/10.1093/petrology/egq075

Herzberg CT, Asimow PD (2015) PRIMELT3 MEGA.XLSM software for primarymagma calculation: peridotite primarymagma MgO contents fromthe liquidus to the solidus. Geochem Geophys Geosyst 16:563–578. https://doi.org/10.1002/2014GC005631.Received

Herzberg C, O'Hara MJ (2002) Plume-associated ultramafic magmas of phanerozoic age. J Petrol 43:1857–1883. https://doi.org/10.1093/petrology/43.10.1857

Herzberg C, Asimow PD, Ionov DA et al (2013) Nickel and helium evidence for melt above the core-mantle boundary. Nature 493:393–397. https://doi.org/10.1038/nature11771

Herzberg C, Cabral RA, Jackson MG et al (2014) Phantom Archean crust in Mangaia hotspot lavas and the meaning of heterogeneous mantle. Earth Planet Sci Lett 396:97–106. https://doi.org/10.1016/j.epsl.2014.03.065

Herzberg CT, Vidito C, Starkey NA et al (2016) Nickel-cobalt contents of olivine record origins of mantle peridotite and related rocks. Am Mineral 101:1952–1966. https://doi.org/10.2138/am-2016-5538

Hirose K, Kushiro I (1993) Partial melting of dry peridotites at high pressures: determination of compositions of melts segregated from peridotite using aggregates of diamond. Earth Planet Sci

Lett 114:477–489. https://doi.org/10.1016/0012-821X(93)90077-M
Hofmann AW, White WM (1982) Mantle plumes from ancient oceanic crust. Earth Planet Sci Lett 57:421–436. https://doi.org/10.1016/0012-821X(82)90161-3
Hole MJ (2018) Mineralogical and geochemical evidence for polybaric fractional crystallization of continental flood basalts and implications for identification of peridotite and pyroxenite source lithologies. Earth-Sci Rev 176:51–67. https://doi.org/10.1016/j.earscirev.2017.09.014
Jakobsson SP (1968) The geology and petrography of the Vestmann Islands: a preliminary report. Surtsey Res Prog Rep 4:113–129
Jakobsson SP (1972) Chemistry and distribution pattern of recent basaltic rocks in Iceland. Lithos 5:365–386. https://doi.org/10.1016/0024-4937(72)90090-4
Jakobsson SP (1979) Petrology of recent basalts of the Eastern Volcanic zone. Acta Nat alia Islandica, Iceland
Jakobsson SP, Pedersen AK, Rönsbo JG, Melchior Larsen L (1973) Petrology of mugearite-hawaiite: early extrusives in the 1973 Heimaey eruption, Iceland. Lithos 6:203–214. https://doi.org/10.1016/0024-4937(73)90065-0
Jakobsson SP, Jonasson K, Sigurdsson IA (2008) The three igneous rock series of Iceland. Jökull 58:117–138
Jenkins J, Maclennan J, Green RG et al (2018) Crustal formation on a spreading ridge above a mantle plume: receiver function imaging of the Icelandic crust. J Geophys Res Solid Earth 123:5190–5208. https://doi.org/10.1029/2017JB015121
Jennings ES, Holland TJB (2015) A simple thermodynamic model for melting of peridotite in the system NCFMASOCr. J Petrol 56:869–892. https://doi.org/10.1093/petrology/egv020
Jennings ES, Gibson SA, Maclennan J, Heinonen JS (2017) Deep mixing of mantle melts beneath continental flood basalt provinces: constraints from olivine-hosted melt inclusions in primitive magmas. Geochim Cosmochim Acta 196:36–57. https://doi.org/10.1016/j.gca.2016.09.015
Jochum KP, Nohl U, Herwig K et al (2005) GeoReM: a new geochemical database for reference materials and isotopic standards. Geostand Geoanal Res 29:333–338. https://doi.org/10.1111/j.1751-908X.2005.tb00904.x
Jóhannesson H (1994) Geological map of Iceland, sheet 2, 1:250 000. West-Iceland, 2nd edn. Icelandic Meseum of Natural History and Iceland Geodetic Survey, Reykjavik
Keiding JK, Sigmarsson O (2012) Geothermobarometry of the 2010 Eyjafjallajökull eruption: new constraints on Icelandic magma plumbing systems. J Geophys Res Solid Earth 117:1–15. https://doi.org/10.1029/2011JB008829
Kogiso T, Hirose K, Takahashi E (1998) Melting experiments on homogeneous mixtures of peridotite and basalt: application to the genesis of ocean island basalts. Earth Planet Sci Lett 162:45–61. https://doi.org/10.1016/S0012-821X(98)00156-3
Kokfelt TF, Hoernle K, Hauff F et al (2006) Combined trace element and Pb–Nd–Sr–O isotope evidence for recycled oceanic crust (upper and lower) in the Iceland mantle plume. J Petrol 47:1705–1749. https://doi.org/10.1093/petrology/egl025
Lambart S (2017) No direct contribution of recycled crust in Icelandic basalts. Geochem Perspect Lett. https://doi.org/10.7185/geochemlet.1728
Lambart S, Laporte D, Provost A, Schiano P (2012) Fate of pyroxenite-derived melts in the peridotitic mantle: thermodynamic and experimental constraints. J Petrol 53:451–476. https://doi.org/10.1093/petrology/egr068
Lambart S, Baker MB, Stolper EM (2016) The role of pyroxenite in basalt genesis: melt-PX, a melting parameterization for mantle pyroxenites between 0.9 and 5 GPa. J Geophys Res Solid Earth 121:5708–5735. https://doi.org/10.1002/2015JB012762
Laubier M, Grove TL, Langmuir CH et al (2014) Trace element mineral/melt partitioning for basaltic and basaltic andesitic melts: an experimental and laser ICP-MS study with application to the oxidation state of mantle source regions. Earth Planet Sci Lett 392:265–278. https://doi.org/10.1016/j.epsl.2014.01.053
Le Roux V, Lee CT, Turner SJ (2010) Zn/Fe systematics in mafic and ultramafic systems: implications for detecting major element heterogeneities in the Earth's mantle. Geochim Cosmochim Acta 74:2779–2796. https://doi.org/10.1016/j.gca.2010.02.004
Le Roux V, Dasgupta R, Lee CT (2011) Mineralogical heterogeneities in the Earth's mantle: constraints from Mn Co, Ni and Zn partitioning during partial melting. Earth Planet Sci Lett 307:395–408. https://doi.org/10.1016/j.epsl.2011.05.014
Lee CT, Luffi P, Chin EJ et al (2012) Copper systematics in arc magmas and implications for crust-mantle differentiation. Science 336:64–68. https://doi.org/10.1126/science.1217313
Li C, Ripley EM (2010) The relative effects of composition and temperature on olivine-liquid Ni partitioning: statistical deconvolution and implications for petrologic modeling. Chem Geol 275:99–104. https://doi.org/10.1016/j.chemgeo.2010.05.001
Loughlin SC (1995) The evolution of the Eyjafjöll volcanic system, southern Iceland. Ph.D. thesis, p 319, University of Durham, Durham, UK
Lundstrom CC, Gill J, Williams Q, Perfit MR (1995) Mantle melting and basalt extraction by equilibrium porous flow. Science 270:1958–1961. https://doi.org/10.1126/science.270.5244.1958
Lynn KJ, Shea T, Garcia MO (2017) Nickel variability in Hawaiian olivine: evaluating the relative contributions from mantle and crustal processes. Am Mineral 102:507–518. https://doi.org/10.2138/am-2017-5763
Maclennan J (2008a) Concurrent mixing and cooling of melts under Iceland. J Petrol 49:1931–1953. https://doi.org/10.1093/petrology/egn052
Maclennan J (2008b) Lead isotope variability in olivine-hosted melt inclusions from Iceland. Geochim Cosmochim Acta 72:4159–4176. https://doi.org/10.1016/j.gca.2008.05.034
Martin E, Paquette JL, Bosse V et al (2011) Geodynamics of rift–plume interaction in Iceland as constrained by new 40Ar/39Ar and in situ U-Pb zircon ages. Earth Planet Sci Lett 311:28–38. https://doi.org/10.1016/j.epsl.2011.08.036
Matthews S, Shorttle O, Maclennan J (2016) The temperature of the Icelandic mantle from olivine-spinel aluminum exchange thermometry. Geochem Geophys Geosyst. https://doi.org/10.1002/2016GC006497
Mattsson H, Höskuldsson Á (2003) Geology of the Heimaey volcanic centre, south Iceland: early evolution of a central volcano in a propagating rift? J Volcanol Geotherm Res 127:55–71. https://doi.org/10.1016/S0377-0273(03)00178-1
Mattsson HB, Oskarsson N (2005) Petrogenesis of alkaline basalts at the tip of a propagating rift: evidence from the Heimaey volcanic centre, south Iceland. J Volcanol Geotherm Res 147:245–267. https://doi.org/10.1016/j.jvolgeores.2005.04.004
Matzen AK, Baker MB, Beckett JR, Stolper EM (2013) The temperature and pressure dependence of nickel partitioning between olivine and silicate melt. J Petrol 54:2521–2545. https://doi.org/10.1093/petrology/egt055
Matzen AK, Baker MB, Beckett JR et al (2017a) The effect of liquid composition on the partitioning of Ni between olivine and silicate melt. Contrib Mineral Petrol 172:3. https://doi.org/10.1007/s00410-016-1319-8
Matzen AK, Wood BJ, Baker MB, Stolper EM (2017b) The roles of pyroxenite and peridotite in the mantle sources of oceanic basalts. Nat Geosci 10:530–535. https://doi.org/10.1038/ngeo2968
Neave DA, Passmore E, Maclennan J et al (2013) Crystal–melt relationships and the record of deep mixing and crystallization in the

ad 1783 laki eruption, Iceland. J Petrol 54:1661–1690. https://doi.org/10.1093/petrology/egt027
Neave DA, Shorttle O, Oeser M et al (2018) Mantle-derived trace element variability in olivines and their melt inclusions. Earth Planet Sci Lett 483:90–104. https://doi.org/10.1016/j.epsl.2017.12.014
Niu Y (1997) Mantle melting and melt extraction processes beneath ocean ridges: evidence from abyssal peridotites. J Petrol 38:1047–1074. https://doi.org/10.1093/petroj/38.8.1047
Niu Y, Wilson M, Humphreys ER, O'Hara MJ (2011) The origin of intra-plate ocean island basalts (OIB): the lid effect and its geodynamic implications. J Petrol 52:1443–1468. https://doi.org/10.1093/petrology/egr030
O'Hara MJ (1968) The bearing of phase equilibria studies in synthetic and natural systems on the origin and evolution of basic and ultrabasic rocks. Earth-Sci Rev. https://doi.org/10.1016/0012-8252(68)90147-5
Pagli C, Sigmundsson F, Lund B et al (2007) Glacio-isostatic deformation around the Vatnajökull ice cap, Iceland, induced by recent climate warming: GPS observations and finite element modeling. J Geophys Res Solid Earth 112:1–12. https://doi.org/10.1029/2006JB004421
Pankhurst MJ, Morgan DJ, Thordarson T, Loughlin SC (2018) Magmatic crystal records in time, space, and process, causatively linked with volcanic unrest. Earth Planet Sci Lett 493:231–241. https://doi.org/10.1016/j.epsl.2018.04.025
Peate DW, Baker JA, Jakobsson SP et al (2009) Historic magmatism on the Reykjanes Peninsula, Iceland: a snap-shot of melt generation at a ridge segment. Contrib Mineral Petrol 157:359–382. https://doi.org/10.1007/s00410-008-0339-4
Peate DW, Breddam K, Baker JA et al (2010) Compositional characteristics and spatial distribution of enriched Icelandic mantle components. J Petrol 51:1447–1475. https://doi.org/10.1093/petrology/egq025
Putirka K, Ryerson FJ, Perfit M, Ridley WI (2011) Mineralogy and composition of the oceanic mantle. J Petrol 52:279–313. https://doi.org/10.1093/petrology/egq080
Putirka K, Tao Y, Hari KR et al (2018) The mantle source of thermal plumes: trace and minor elements in olivine and major oxides of primitive liquids (and why the olivine compositions don't matter). Am Mineral 103:1253–1270. https://doi.org/10.2138/am-2018-6192
Rudge JF, Maclennan J, Stracke A (2013) The geochemical consequences of mixing melts from a heterogeneous mantle. Geochim Cosmochim Acta 114:112–143. https://doi.org/10.1016/j.gca.2013.03.042
Ryan JG, Langmuir CH (1987) The systematics of lithium abundances in young volcanic rocks. Geochim Cosmochim Acta 51:1727–1741. https://doi.org/10.1016/0016-7037(87)90351-6
Rychert CA, Harmon N, Armitage JJ (2018) Seismic imaging of thickened lithosphere resulting from plume pulsing beneath Iceland. Geochem Geophys Geosyst 19:1789–1799. https://doi.org/10.1029/2018GC007501
Sæmundsson K (1979) Outline of the geology of Iceland. Jökull 29:11–28
Sæmundsson K (1995) Svartsengi geological map (bedrock) 1:25,000. Orkustofnun, Hitaveita Sudurnesja and Landmaelingar Islands, Reykjavik
Sæmundsson K, Jóhannesson H, Hjartarson Á et al (2010) Geological map of Southewest Iceland. Icel Geosurv 1:100000
Shorttle O, Maclennan J (2011) Compositional trends of Icelandic basalts: implications for short-length scale lithological heterogeneity in mantle plumes. Geochem Geophys Geosyst. https://doi.org/10.1029/2011GC003748
Shorttle O, Maclennan J, Lambart S (2014) Quantifying lithological variability in the mantle. Earth Planet Sci Lett 395:24–40. https://doi.org/10.1016/j.epsl.2014.03.040
Sigmarsson O (1996) Short magma chamber residence time at an Icelandic volcano inferred from U-series disequilibria. Nature 382:440–442. https://doi.org/10.1038/382440a0
Sigmarsson O, Vlastelic I, Andreasen R et al (2011) Remobilization of silicic intrusion by mafic magmas during the 2010 Eyjafjallajökull eruption. Solid Earth 2:271–281. https://doi.org/10.5194/se-2-271-2011
Smith PM, Asimow PD (2005) Adiabat-1ph: a new public front-end to the MELTS, pMELTS, and pHMELTS models. Geochem Geophys Geosyst 6:1–8. https://doi.org/10.1029/2004GC000816
Sobolev AV, Hofmann AW, Sobolev SV, Nikogosian IK (2005) An olivine-free mantle source of Hawaiian shield basalts. Nature 434:590–597. https://doi.org/10.1038/nature03411
Sobolev AV, Hofmann AW, Kuzmin DV et al (2007) The amount of recycled crust in sources of mantle-derived melts. Science 316:412–417. https://doi.org/10.1126/science.1138113
Sobolev AV, Hofmann AW, Brügmann G et al (2008) A quantitative link between recycling and osmium isotopes. Science 321:536. https://doi.org/10.1126/science.1158452
Spandler C, Pettke T, Rubatto D (2011) Internal and external fluid sources for eclogite-facies veins in the Monviso Meta-ophiolite, Western Alps: implications for fluid flow in subduction zones. J Petrol 52:1207–1236. https://doi.org/10.1093/petrology/egr025
Spice HE, Fitton JG, Kirstein LA (2016) Temperature fluctuation of the Iceland mantle plume through time. Geochem Geophys Geosyst. https://doi.org/10.1002/2015GC006059
Spiegelman M, Kelemen PB (2003) Extreme chemical variability as a consequence of channelized melt transport. Geochem Geophys Geosyst. https://doi.org/10.1029/2002GC000336
Sugawara T (2000) Empirical relationships between temperature, pressure, and MgO content in olivine and pyroxene saturated liquid. J Geophys Res 105:8457. https://doi.org/10.1029/2000JB900010
Tarasewicz J, Brandsdóttir B, White RS et al (2012) Using microearthquakes to track repeated magma intrusions beneath the Eyjafjallajökull stratovolcano, Iceland. J Geophys Res Solid Earth 117:1–13. https://doi.org/10.1029/2011JB008751
Thirlwall MF, Gee MAM, Taylor RN, Murton BJ (2004) Mantle components in Iceland and adjacent ridges investigated using double-spike Pb isotope ratios. Geochim Cosmochim Acta 68:361–386. https://doi.org/10.1016/S0016-7037(03)00424-1
Thirlwall MF, Gee MAM, Lowry D et al (2006) Low δ18O in the Icelandic mantle and its origins: evidence from Reykjanes Ridge and Icelandic lavas. Geochim Cosmochim Acta 70:993–1019. https://doi.org/10.1016/j.gca.2005.09.008
Thomson A, Maclennan J (2013) The distribution of olivine compositions in icelandic basalts and picrites. J Petrol 54:745–768. https://doi.org/10.1093/petrology/egs083
Thordarson T, Larsen G (2007) Volcanism in Iceland in historical time: volcano types, eruption styles and eruptive history. J Geodyn 43:118–152. https://doi.org/10.1016/j.jog.2006.09.005
Trela J, Vidito C, Gazel E et al (2015) Recycled crust in the galápagos plume source at 70 ma: implications for plume evolution. Earth Planet Sci Lett 425:268–277. https://doi.org/10.1016/j.epsl.2015.05.036
Viccaro M, Giuffrida M, Nicotra E, Cristofolini R (2016) Timescales of magma storage and migration recorded by olivine crystals in basalts of the March–April 2010 eruption at Eyjafjallajökull volcano, Iceland. Am Mineral 101:222–230. https://doi.org/10.2138/am-2016-5365
Wang Z, Gaetani GA (2008) Partitioning of Ni between olivine and siliceous eclogite partial melt: experimental constraints on

the mantle source of Hawaiian basalts. Contrib Mineral Petrol 156:661–678. https://doi.org/10.1007/s00410-008-0308-y
Weatherley SM, Katz RF (2012) Melting and channelized magmatic flow in chemically heterogeneous, upwelling mantle. Geochem Geophys Geosyst. https://doi.org/10.1029/2011GC003989
Wiese PK (1992) Geochemistry and geochronology of the Eyjafjoll volcanic system. Unpublished MSc Thesis, University of Oregon
Wolfe CJ, Bjarnason IT, VanDecar JC, Solomon SC (1997) Seismic structure of the Iceland mantle plume. Nature 385:245–247. https://doi.org/10.1038/385245a0

Paper II

Nikkola P., Bali E., Kahl M., Quinten H. A. van der Meer, Rämö O.T., Guðfinnsson G.H., Thordarson T. 2019. *Mid-crustal storage and crystallization of Eyjafjallajökull ankaramites, South Iceland.* Jökull 69: 77–96.

Mid-crustal storage and crystallization of Eyjafjallajökull ankaramites, South Iceland

Paavo Nikkola[1,2,*], Enikő Bali[2,3], Maren Kahl[4], Quinten H. A. van der Meer[2], O. Tapani Rämö[1], Guðmundur H. Guðfinnsson[2], and Thorvaldur Thordarson[3]

[1]*Department of Geosciences and Geography, Geology and Geophysics Research Group, P.O. Box 64, FI-00014 University of Helsinki, Finland*

[2]*Nordic Volcanological Center, Institute of Earth Sciences, University of Iceland, Sturlugata 7, 101 Reykjavík, Iceland*

[3]*Faculty of Earth Sciences, University of Iceland, Sturlugata 7, 101 Reykjavík, Iceland*

[4]*Institut für Geowissenschaften, Universität Heidelberg, Im Neuenheimer Feld 234-236, 69120 Heidelberg, Germany*

[*]*Correspondence: paavo.nikkola@helsinki.fi*

Abstract — *Our understanding of the long-term intrusive and eruptive behaviour of volcanic systems is hampered by a relatively short period of direct observation. To probe the conditions of crustal magma storage below South Iceland, we have analysed compositions of minerals, mineral zoning patterns, and melt inclusions from two Eyjafjallajökull ankaramites located at Brattaskjól and Hvammsmúli. These two units are rich in compositionally diverse macrocrysts, including the most magnesian olivine (Fo_{88-90}) and clinopyroxene ($Mg\#_{cpx}$ 89.8) known from Eyjafjallajökull. Olivine-hosted spinel inclusions have high $Cr\#_{spl}$ (52–80) and TiO_2 (1–3 wt%) and low Al_2O_3 (8–22 wt%) compared to typical Icelandic chromian spinel. The spinel-olivine oxybarometer implies a moderate oxygen fugacity of $\Delta logFMQ$ 0–0.5 at the time of crystallization, and clinopyroxene-liquid thermobarometry crystallization at mid-crustal pressures (1.7–4.2 kbar, 3.0±1.4 kbar on average) at 1120–1195°C. Liquid-only thermometry for melt inclusions with $Mg\#_{melt}$ 56.1–68.5 and olivine-liquid thermometry for olivine macrocrysts with $Fo_{80.7-88.9}$ yield crystallization temperatures of 1155–1222°C and 1136–1213°C, respectively. Diffusion modelling of compositional zonations in the Brattaskjól olivine grains imply that the Brattaskjól macrocrysts were mobilized and transported to the surface from their mid-crustal storage within a few weeks (at most in 9–37 days). Trends in clinopyroxene macrocryst compositions and the scarcity of plagioclase indicate that the mid-crustal cotectic assemblage was olivine and clinopyroxene, with plagioclase joining the fractionating mineral assemblage later. In all, the crystal cargoes in the Brattaskjól and Hvammsmúli ankaramites are composed of agitated wehrlitic or plagioclase wehrlitic crystal mushes that crystallized over a large temperature interval at mid-crustal depths.*

INTRODUCTION

In South Iceland, at the southern tip of the Eastern Volcanic Zone (SEVZ), magmatism occurs outside the main zone of plate spreading in three volcanic systems: Eyjafjallajökull, Katla, and Vestmannaeyjar. The SEVZ is the most recently activated volcanic zone in Iceland (younger than 3 Ma; Martin *et al.*, 2011), where mantle-derived magmas intrude relatively cold oceanic crust (Flóvenz and Saemundsson, 1993). Magma batches fractionate comparatively fast under these conditions, as indicated by U-series disequilibria (Sigmarsson, 1996) and the absence of equilibrium phenocryst assemblages (Mattsson and Oskarsson, 2005) in erupted lavas. In Vestmannaeyjar, the mantle-derived melts have been envisioned to evolve in the crust in isolated, small magma reservoirs over a large depth range (Furman *et al.*, 1991; Mattsson and Oskarsson, 2005). Seismic, geodetic and petrogenetic studies of the Eyjafjallajökull 2010 eruption have highlighted a multi-tier volcanic plumb-

ing system beneath the volcano, and near-direct vertical magma transport from mantle depths (Sigmundsson *et al.*, 2010; Sigmarsson *et al.*, 2011; Keiding and Sigmarsson, 2012; Tarasewicz *et al.*, 2012a,b; Laeger *et al.*, 2017).

Regardless of the advances above, our understanding of crustal storage and evolution of magmas in SEVZ is inadequate, with our best inferences relying on the 2010 Eyjafjallajökull eruption alone. Analysis of minerals with pressure- and temperature-sensitive compositions offers a way forward, as it allows us to make inferences on the conditions of magma differentiation in the SEVZ crust. In this paper, we present major element data on olivine, clinopyroxene, spinel, and melt inclusions from the most primitive Eyjafjallajökull volcanic units: the Brattaskjól and Hvammsmúli ankaramites. We show that these two ankaramites host primitive olivine and clinopyroxene macrocrysts as well as chromian spinel that is the most Cr- and Ti-rich reported from Iceland. On the basis of thermobarometric calculations and diffusion modelling, we suggest that these crystals were derived from agitated and disaggregated mid-crustal (10.7±5 km) wehrlitic or plagioclase wehrlitic crystal mushes and that they ascended from these depths in a carrier magma within a few weeks only.

EYJAFJALLAJÖKULL VOLCANIC SYSTEM

Eyjafjallajökull (Figure 1) is a glacier-covered, moderately active volcano that has acted as a locus of magmatism for over 0.78 Ma (Kristjánsson *et al.*, 1988). Typical of off-rift volcanic systems in Iceland, Eyjafjallajökull magmas are enriched in K_2O and Na_2O compared to axial rift magmas (Jakobsson, 1972; Hémond *et al.*, 1993) and show trace element and isotopic signatures of "enriched" mantle source (e.g., elevated $^{206}Pb/^{204}Pb$ in comparison to MORB) (Peate *et al.*, 2010). These characteristics are most often attributed to low-degree melting of incompatible trace element rich and mineralogically distinct mantle source compared to the depleted source of common MORB (Chauvel and Hémond, 2000; Kokfelt *et al.*, 2006).

Observations of the Eyjafjallajökull 2010 eruption build a strong case for a trans-crustal magma plumbing system beneath the volcano, with defined magma intrusions in the brittle upper crust (<10–12 km depth, Hjaltadóttir *et al.* 2009) underlain by poorly constrained magma storage zones in ductile crust and upper mantle (Sigmundsson *et al.*, 2010; Sigmarsson *et al.*, 2011; Keiding and Sigmarsson, 2012; Tarasewicz *et al.*, 2012a, b). Although Eyjafjallajökull has a shallow silicic magma intrusion at 5 km depth (Sigmarsson *et al.*, 2011), and intrusions of magma into the shallow crust (e.g., 5 km beneath the eastern flank of the volcano; Sigmundsson *et al.*, 2010) predated the eruption, the Eyjafjallajökull 2010 eruption was fed by magma from considerable depths. During the first weeks of the eruption, seismicity was focused on the brittle crust (<10 km), suggesting a mid-crustal magma source. However, later a downward propagation of earthquakes down to ∼30 km below the surface was detected, with distinct seismic clusters at depths of ∼19 km and ∼25 km, potentially reflecting depressurization of two or more 1–10 km^3 intrusions at these depths (Tarasewicz *et al.*, 2012b, a). This suggests that the eruption tapped magma from the mantle (from depths greater than ∼22 km; Brandsdóttir and Menke, 2008). Exhaustion of the mid-crustal reservoirs and deep tapping of magmas supports views of SEVZ as an embryonic rift segment (e.g., Mattsson and Oskarsson, 2005), where crustal magma storage zones are still small and maybe ephemeral (Sigmarsson, 1996) in comparison to active rift zones with hotter crust (Flóvenz and Saemundsson, 1993) and presumably larger crustal magma reservoirs.

SAMPLES

The volcanic units sampled for this study, Brattaskjól and Hvammsmúli (Figure 1), are the most primitive volcanic units of the Eyjafjallajökull volcano described so far (Loughlin, 1995). Both are partly eroded outcrops on the southern slope of Eyjafjallajökull and seemingly subaerial in character (Loughlin, 1995), although a shallow intrusive origin for Hvammsmúli has also been suggested (Steinthórsson, 1964). We follow the established practise (e.g., Steinthórsson, 1964; Loughlin, 1995) and refer to

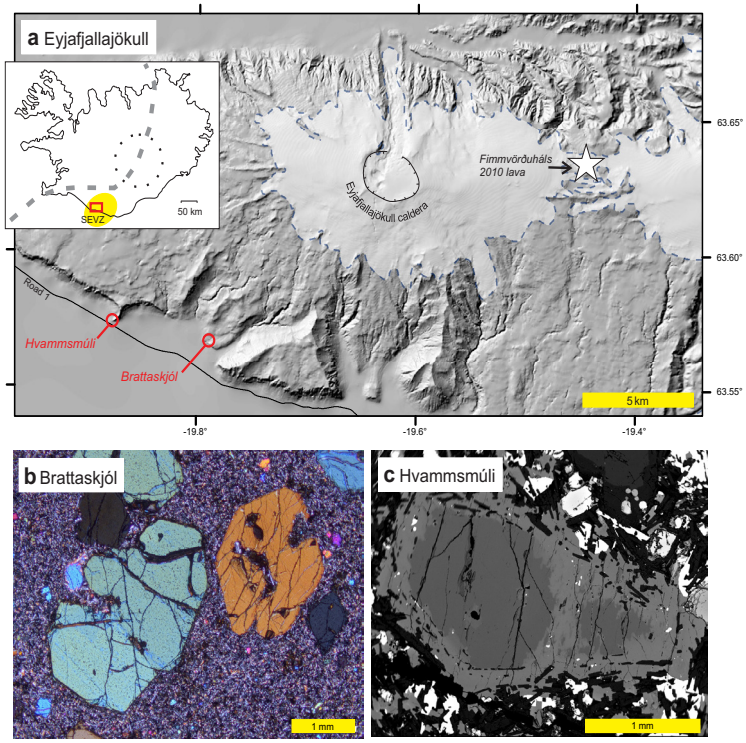

Figure 1. a) Map of the Eyjafjallajökull volcano with sampled locations and the 2010 Fimmvörðuháls lava flow field. Inset shows map location (red rectangle) and the southern tip of the Eastern Volcanic Zone (SEVZ) in yellow. The active plate boundary and the locus of the Iceland mantle plume (Wolfe *et al.*, 1997) are marked with grey and black stippled lines, respectively. b) Photomicrograph (in cross-polarized light) showing the texture of the Brattaskjól ankaramite sample. The large crystal on the left is olivine (3rd order blue interference colour) and the large crystal on the right (1st order orange) is augite. c) Backscattered electron image of an augite crystal in a Hvammsmúli ankaramite sample. – *a) Kort af Eyjafjallajökulseldstöðinni sem sýnir sýnastaði og staðsetningu hraunsins sem myndaðist í gosi á Fimmvörðuhálsi árið 2010. Innfellda myndin sýnir staðsetningu kortsins (rauður ferhyrningur) og suðurenda eystra gosbeltisins (SEVZ) með gulum lit. Virku flekamótin eru merkt með gráum strikalínum og útlínur möttulstróksins (Wolfe o.fl., 1997) með svörtum strikalínum. b) Smásjárljósmynd (tvískautað ljós) sem sýnir textúr í ankaramítsýni frá Brattaskjóli. Stóri kristallinn til vinstri er ólivín (blár bylgjuvíxllitur af þriðju röð) og stóri kristallinn hægra megin er ágít (gulur litur af fyrstu röð). c) Endurkastsrafeindamynd af ágítkristal í ankaramítsýni frá Hvammsmúla.*

these outcrops as ankaramites. These ankaramites are highly porphyritic with abundant (∼30 vol%, see Steinthórsson, 1964) olivine and clinopyroxene macrocrysts in near equal amounts. Hvammsmúli also has minor amounts of plagioclase macrocrysts, not observed in Brattaskjól. As macrocrysts, we consider crystals that are >0.3 mm in length and precede groundmass minerals. Hvammsmúli has been dated to 587±31 ka (Wiese, 1992), but the exact age of Brattaskjól is unknown. An age of 500–720 ka for Brattaskjól is probable, however, judging from its stratigraphic position (Loughlin, 1995) and normal magnetic polarity.

The Brattaskjól olivine and clinopyroxene macrocrysts are often embayed and have thin compositionally zoned rims in contact with fine-grained groundmass mineralogy (Figure 1b). In Hvammsmúli samples, conversely, the groundmass is coarse and olivine and clinopyroxene macrocrysts have broad compositionally zoned rims that commonly enclose groundmass plagioclase near the macrocryst edges (Figure 1c). In addition to the zonation near crystal edges, clinopyroxene macrocrysts in both localities exhibit complex oscillatory and convolute zoning, while sector zoning was not identified.

The Brattaskjól olivine macrocrysts are commonly devoid of spinel and melt inclusions. When present, the Brattaskjól melt inclusions are found in the cores of the crystals as primary or pseudosecondary inclusions (following the nomenclature of Roedder, 1984). Their size varies between 20 and 250 μm and they are partially crystallized, containing dominantly clinopyroxene daughter minerals, silicate glass and a large bubble phase. These inclusions may also contain opaque phases, which are generally accidentally trapped spinel crystals. Spinel and melt inclusions are more common in the Hvammsmúli samples, and some Hvammsmúli olivines have small (usually <1 μm) oxide exsolutions. The textural appearance of melt inclusions is similar to those observed in olivine grains from Brattaskjól. These inclusions contain abundant clinopyroxene, minor orthopyroxene, ilmenite and spinel daughter minerals, a vapour phase and interstitial silicate glass (see Björnsson, 2019). In backscattered electron images, we commonly observe a bright Fe-rich diffusion halo in olivine around the melt inclusions in Hvamsmmúli samples. This halo is missing around Brattaskjól melt inclusions.

ANALYTICAL AND EXPERIMENTAL METHODS

Melt inclusion homogenization experiments

As melt inclusions from both localities were partially crystalline, we tried to homogenize them. Handpicked olivine crystals were placed in a graphite crucible and mixed with graphite powder in order to avoid oxidation during the heating experiments. We carried out three sets of experiments at temperatures of 1200, 1220 and 1240°C. The precision of the temperature reading, calibrated to the melting points of Au, Ag and NaCl, was ±5°C. Crucibles were placed in the high-temperature oven at the target temperature and kept there for 5 minutes. After 5 minutes, the samples were quenched in room temperature water. Olivine was recovered after quenching and mounted in epoxy. Melt inclusions were exposed by manual polishing and inspected under the polarizing microscope. More than 90% of the melt inclusions from Brattaskjól were homogenized at 1200±5°C, and all of them at 1220°C. By contrast, a few crystals were observed in Hvammsmúli melt inclusions even after heating to 1240°C.

Electron microprobe analysis

We separated olivine and clinopyroxene macrocrysts from crushed and sieved (Ø = 0.1–4.0 mm) rock samples and determined their major and minor element compositions using a JEOL JXA-8230 electron microprobe at the University of Iceland. Clinopyroxene was analysed in a thin section made from the Hvammsmúli sample. In total, we analysed 192 olivine and 51 clinopyroxene crystals for their core compositions, 38 spinel and 21 melt inclusions in olivine, and 47 concentration profiles (with 4–10 μm spacing between analysis spots) across olivine zonation. Acceleration voltage and a beam current of 15 keV and 20 nA, respectively, were used for analysis of clinopyroxene, spinel and olivine zonation, whereas 10 nA beam current was used for analyses of melt inclusions. For the high-precision trace element analyses of olivine cores, we used a modified version of the analysis protocol by Batanova *et al.* (2015) with acceleration voltage of 20 keV and a high beam current of 500 nA (see Nikkola *et al.*, 2019; for details). Crystals of known composition were analysed to check for instrumental drift. The mineral and melt compositions are available from the authors on request.

EBSD analysis

Crystallographic orientations of olivine macrocrysts were resolved with electron backscatter diffraction (EBSD, Prior *et al.*, 1999) using FEI Quanta SEM at the University of Leeds (UK). The EBSD analyses were performed to constrain the crystallographic

directions with respect to the micro-analytical traverses. This is essential for diffusion modelling of olivine, as the diffusivity of elements (e.g., Fe-Mg or Ni) in olivine is anisotropic, with diffusion along the crystallographic c-axis being six times faster than along the a- or b-axes (e.g. Dohmen and Chakraborty, 2007; Dohmen *et al.*, 2007). Following the procedure of Kahl *et al.* (2017), we acquired orientation maps consisting of hundreds of EBSD point determinations for a total of 46 olivine grains from Brattaskjól and Hvammsmúli. We used the HKL CHANNEL 5 EBSD post-processing software to extract hundreds of orientation measurements from individual crystals. The EBSD Euler angles were converted into plunges and trends of the a-, b- and c-axes of the analysed olivines using an Excel sheet provided by Dr. D. Morgan (University of Leeds). Finally, the angular relations between the crystals a-, b- and c-directions and the micro-analytical traverses were acquired using the Stereo32 software developed at the Ruhr-Universität Bochum.

MINERAL AND MELT COMPOSITIONS

Olivine

The Brattaskjól and Hvammsmúli olivine macrocryst cores show substantial, yet similar, compositional variability in terms of Fo (Fo_{81-90}) and minor elements (e.g., Ni, Figure 2a). Both have a population of Fo_{88-90} olivine cores showing a large minor element variability (Ni, Mn, Ca). Minor element variation in $Fo_{<86}$ olivine cores, at a given Fo content, is less pronounced (see Nikkola *et al.*, 2019).

All Brattaskjól olivine macrocrysts (n=22) analysed for their compositional zonation have thin (<100 μm) Fe-Mg zonation around homogenous cores. Interestingly, olivine grains with $Fo_{>85.7}$ cores (n=15) are normally zoned (Fo decreases towards crystal edges), whereas olivine grains with $Fo_{<84.4}$ cores have complex reverse zoned rims (n=7, high-Fo bands near crystal edges, Figure 2d).

The Fo zonation in normally zoned Brattaskjól olivines exhibits changes in slope (Figure 2b) and steps (Figure 2c), and as such does not follow the steady decrease in Fo towards crystal boundaries typical of diffusion under steady-state conditions (Costa *et al.*, 2008). The outermost parts of the olivine crystals have the steepest decrease in Fo (B1 and C1 in Figure 2b and 2c), followed by an inner rim section with a shallower gradient in the change of Fo (B2 and C2 in Figure 2b and 2c). These olivine grains also commonly exhibit high-Fo "shoulders", with an approximate composition of $Fo_{89.2}$, near the outer edges of the otherwise homogenous crystal cores (B3 in Figure 2b). The complexly reverse zoned Brattaskjól olivine crystals with homogenous $Fo_{80.9-84.4}$ cores have ~10–30 μm thick $Fo_{83.1-85.4}$ bands near crystal edges (Figure 2d). The outermost edges of the crystals have the lowest and very variable Fo contents ranging from $Fo_{73.5}$ to $Fo_{82.8}$. Typically, the high-Fo bands near the crystal edges have relatively broad diffuse boundaries towards the crystal interior in comparison to the steep decrease in Fo towards the outer edge of the crystals (Figure 2d).

Unlike the Brattaskjól olivine macrocrysts, all Hvammsmúli olivine macrocrysts show broad (up to 700 μm) normal zoning, irrespective of the Fo content in olivine cores (Figure 2e). Some olivine grains also exhibit a two-fold division in the Fo zoning pattern (Figure 2e). In these olivine crystals, the Fo zonation pattern in the outermost 200 μm of the crystal has a concave slope (E1), which is indicative of growth-dominated zoning, followed by up to 500 μm convex slope (E2), more typical to diffusive re-equilibration.

Spinel inclusions in olivine

Spinel inclusions in the Brattaskjól (n = 16) and Hvammsmúli olivine macrocrysts (n = 22) have $Mg\#_{spl}$ ($Mg\#_{spl}$ = cation fraction $100Mg/(Mg+Fe^{2+})$) of 38–66, Cr# (Cr# = cation fraction 100Cr/(Cr+Al)) of 52–80, Fe^{3+}/Fe_{tot} of 0.15–0.35, 1–3 wt% TiO_2, and 8–22 wt% Al_2O_3 (Figure 3). The spinel inclusions in Brattaskjól olivine grains have somewhat higher mean Cr# and Fe^{3+}/Fe_{tot} than in the Hvammsmúli olivine grains, although their compositions do overlap. In addition, variation in Al_2O_3 is less in the Brattaskjól spinels (10–16 wt% Al_2O_3). In the Hvammsmúli samples, spinel is also found in olivine-hosted melt inclusions; these have a distinct composition with relatively high (>55 wt%) Al_2O_3 (Björnsson, 2019).

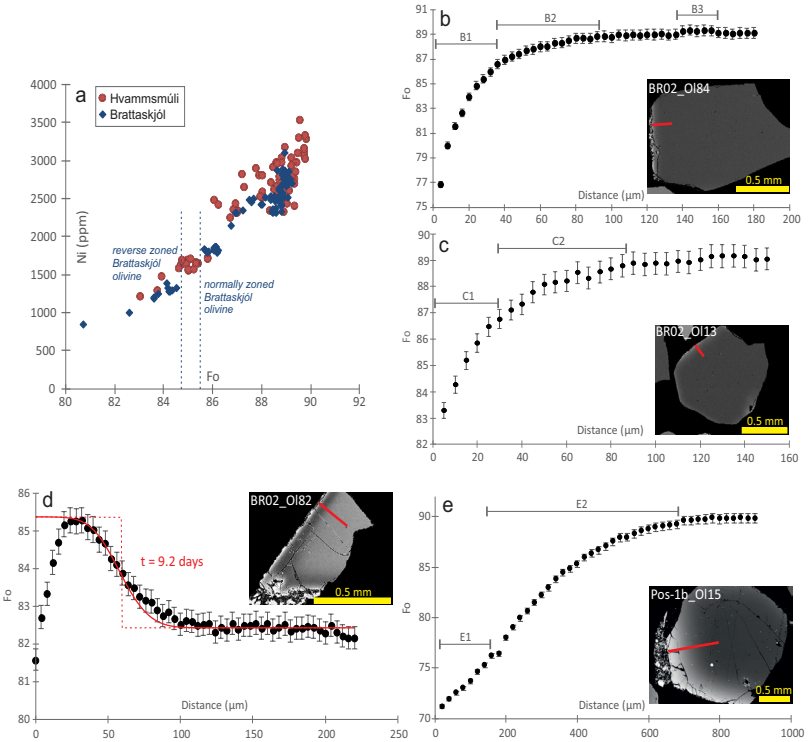

Figure 2. a) Ni (ppm) vs. forsterite (Fo = cation fraction 100Mg/(Mg+Fe)) plot of Brattaskjól and Hvammsmúli olivine core compositions; data from Nikkola *et al.* (2019). Brattaskjól olivines with core compositions up to $Fo_{84.4}$ have complex reverse zonation, whereas olivines with $Fo_{>85.7}$ core compositions are always normally zoned. All Hvammsmúli olivines are normally zoned. b-e) Compilation of micro-analytical traverses across compositionally zoned olivine macrocrysts displaying different zoning patterns (e.g., normal vs. complex reverse). Locations of the traverses are shown with red lines in the backscatter electron images. Olivine macrocrysts BR02_Ol84 (b), BR02_Ol13 (c) and Pos-1b_Ol5 (e) are normally zoned with decreasing Fo towards outermost rims. Zonation sections B1, B2, B3, C1, C2, E1 and E2 are discussed in the text. Brattaskjól olivine BR02_Ol82 (d) is complex reverse zoned, with a band of high Fo near the crystal rim in comparison to Fo in the olivine core. Complex reverse zoned olivine grains like these were used for diffusion modelling. The red stippled line is the initial diffusion model and the red curve is the model zonation after 9.2 days of diffusion. – *a) Ni (ppm) sem fall af forsterítinnihaldi (Fo = katjónahlutfallið 100Mg/(Mg+Fe)) í kjörnum ólivíns frá Brattaskjóli og Hvammsmúla; gögnin eru frá Nikkola o.fl. (2019). Ólivín í Brattaskjóli með kjarnasamsetningu allt up í* $Fo_{84,4}$ *er með flókna öfuga beltun en ólivín með* $Fo_{>85,7}$ *kjarnasamsetningu er alltaf með reglulega beltun (e. normal zoning). Allt ólivín frá Hvammsmúla er með reglulega beltun. b-e) Dæmi um örgreiningalínur yfir beltaða ólivíndíla með mismunandi gerðir beltunar (þ.e. reglulega og flókna öfuga beltun). Staðsetning línanna er gefin til kynna með rauðum línum á rafeindasmásjármyndunum. Ólivíndílarnir BR02_Ol84 (b), BR02_Ol13 (c) og Pos-1b_Ol5 (e) eru með reglulega beltun þar sem kjarninn hefur hátt Fo-gildi sem síðan lækkar í átt að kristalrimanum. Í greininni er rætt um þá hluta beltunar sem merktir eru B1, B2, B3, C1, C2, E1 og E2. Ólivín frá Brattaskjóli merkt BR02_Ol82 (d) er með flókna öfuga beltun, þar sem belti næst kristalrimanum er með hátt Fo-gildi í samanburði við kjarna kristalsins. Ólivíndílar sem þessi voru notaðir við líkanreikinga á efnasveimi. Brotna rauða línan gefur til kynna efnasamsetningu dílsins við upphaf líkanreikningsins en heila rauða lína sýnir útreiknaða beltun eftir 9,2 daga af efnasveimi.*

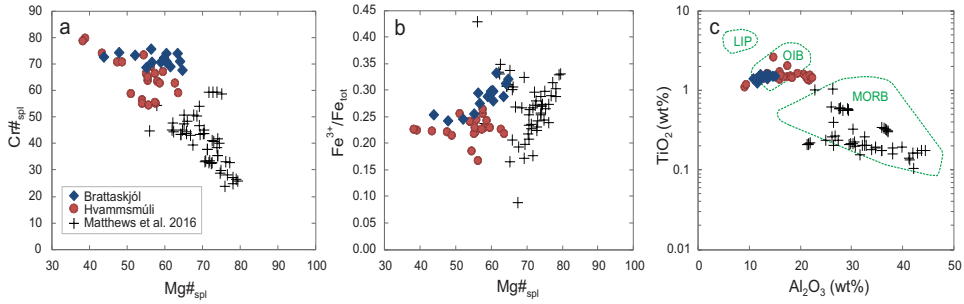

Figure 3. a) Cr number (Cr#$_{spl}$ = cation fraction 100Cr/(Cr+Al)) against Mg number (Mg#$_{spl}$ = cation fraction 100Mg/(Mg+Fe^{2+})) in spinel. 2σ analytical error is smaller or equal to the symbol size. b) The ratio of ferric iron to total iron (Fe^{3+}/Fe$_{tot}$) vs. Mg# in spinel. The amount of Fe^{3+} is calculated based on stoichiometry. c) Spinel TiO_2 vs. Al_2O_3 diagram; spinel discrimination fields are after Kamenetsky (2001). Spinel compositions from the Northern Rift Zone of Iceland (Matthews *et al.*, 2016) are shown for comparison (black crosses). – *a) Cr-tala (Cr#$_{spl}$ = katjónahlutfallið 100Cr/(Cr+Al)) sem fall af Mg-tölu (Mg#$_{spl}$ = katjónahlutfallið 100Mg/(Mg+Fe^{2+}2)) spínils. 2σ óvissa í efnagreiningum er minni eða jafnstór og sýnatáknin. b) Hlutfall ferríjónar af heildarmagni járns (Fe^{3+}/Fe$_{tot}$) á móti Mg# spínils. Magn Fe^{3+} er reiknað út frá efnaformúlu spínils. c) Styrkur TiO_2 á móti styrk Al_2O_3 í spínli; aðgreiningarsvæði fyrir spínil eru frá Kamenetsky (2001). Efnasamsetningar spínils frá Norðurgosbelti (Matthews o.fl., 2016) eru sýndar til samanburðar (svartir krossar).*

Table 1. Representative melt inclusion (MI) compositions* (in wt%) from Brattaskjól and Hvammsmúli olivine macrocrysts. All melt inclusions from Brattaskjól reported here were homogenized at 1200°C. – *Dæmigerðar efnasamsetningar (% af massa) bráðarinnlyksna (MI) í ólivíndílum frá Brattaskjóli og Hvammsmúla. Allar bráðarinnlyksur frá Brattaskjóli sem rætt er um í greininni voru gerðar einsleitar með því að bræða þær við 1200°C.*

	SiO_2	TiO_2	Al_2O_3	FeO_{tot}	MnO	MgO	CaO	Na_2O	K_2O	P_2O_5	SO_3	Cl	Total	PEC%[a]	Mg#[b]	Fo[c]	Type[d]
Brattaskjól																	
Ol14_mi1_2	46.39	2.54	15.11	11.21	0.16	8.82	12.27	2.36	0.44	0.30	0.32	0.03	99.9	–	60.9	80.9	alk. bas.
Ol17_mi1	46.99	2.31	16.11	9.75	0.16	7.99	13.28	2.24	0.53	0.34	0.27	0.03	100.0	–	61.9	82.4	alk. bas.
Ol10_mi1	45.60	2.69	15.71	10.27	0.17	8.91	13.31	2.23	0.43	0.36	0.30	0.02	100.0	–	63.2	82.9	alk. bas.
Ol7_mi1	46.33	2.32	15.55	9.72	0.16	9.09	12.91	2.25	0.53	0.45	0.29	0.04	99.6	–	65.0	83.0	alk. bas.
Ol25_mi1_2	48.02	2.07	15.25	8.27	0.12	8.87	14.19	2.29	0.44	0.28	0.25	0.02	100.0	–	68.0	86.0	alk. bas.
Ol33_mi1	47.81	2.27	16.06	7.84	0.12	8.60	14.21	2.46	0.40	0.21	0.20	0.03	100.2	–	68.5	87.0	alk. bas.
Ol11_mi1	49.31	2.87	13.46	7.60	0.11	9.06	13.60	2.34	0.64	0.58	0.21	0.03	99.8	–	70.2	87.9	ol. tho.
Ol1_mi1_2	48.58	3.56	12.97	7.29	0.15	9.96	15.79	0.89	0.18	0.24	0.03	0.00	99.6	–	73.0	88.6	tho.
Ol9_mi1	47.27	2.44	16.29	9.56	0.17	6.25	13.28	2.68	0.53	0.32	–	–	98.8	6.7	56.4	81.6	alk. bas.
Ol9_mi2_2	46.86	2.54	16.56	9.57	0.11	6.17	13.44	2.73	0.49	0.27	–	–	98.7	9.5	56.1	81.6	alk. bas.
Ol23_mi2_2	51.11	2.65	15.10	6.27	0.13	6.98	14.62	2.14	0.28	0.14	–	–	99.4	3.9	68.8	87.9	tho.
Ol29_mi1	53.91	2.31	14.69	5.86	0.15	7.46	12.88	1.76	0.38	0.06	–	–	99.4	-0.6	71.6	88.7	bas. and.
Hvammsmúli																	
Ol3_mi1_1160_3	49.48	2.40	14.37	6.25	0.11	7.63	11.87	3.62	0.96	1.64	0.10	0.06	98.5	not calc.	70.7	79.6	alk. bas.
Ol1_mi1_1200_1	47.94	3.35	13.71	6.18	0.09	8.38	13.86	3.26	0.76	0.52	0.07	0.04	98.2	not calc.	72.9	85.6	alk. bas.

Compositions in wt%. [a]PEC% = percentage of post-entrapment olivine crystallization in MI

[b]Mg# = 100Mg/(Mg+0.9Fe$_{tot}$) [c]Fo = forsterite content (100Mg/(Mg+Fe^{2+})) in host olivine

[d]MI type according to normative mineralogy

Melt inclusions in olivine

Representative compositions of melt inclusions in the Brattaskjól and Hvammsmúli olivine macrocrysts are shown in Table 1. At Brattaskjól, the melt inclusions in $Fo_{<80.9-87.0}$ olivine macrocrysts correspond to mildly alkaline basalt (1–3 wt% normative nepheline) with $Mg\#_{melt}$ ($Mg\#_{melt}$ = molar $100Mg/(Mg+0.9Fe_{tot})$) of 56.1–68.5, whereas the four melt inclusions in more primitive $Fo_{87.9-88.6}$ olivines are silica saturated with low FeO_{tot} and $Mg\#_{melt}$ of 68.8–73.0. Most of the homogenized Brattaskjól melt inclusions are in equilibrium with their host olivine (Kd^{Mg-Fe}_{Ol-Liq} = 0.30±0.3, Toplis 2005) and do not require post-entrapment crystallization (PEC) correction. For those melt inclusions that require it, a PEC correction of 1–6 wt% was made using the Petrolog software of Danyushevsky and Pletchov (2011). For these calculations, FeO* (FeO content before post-entrapment crystallisation and diffusion) of the melt inclusions was derived from the relationship of Fo in olivine and FeO in melt in suitable Eyjafjallajökull magmas (this study and Moune *et al.*, 2012). The melt inclusions in olivines from Hvammsmúli often exhibit crystals, even after heating to 1240°C, and it was thus not possible to perform proper PEC and diffusion correction for them. In addition, all Hvammsmúli melt inclusions have so low FeO_{tot} in relation to their high $Mg\#_{melt}$ that they are unlikely to represent any reasonable near-primary parental melt. Most likely, these melt inclusions have been modified by post-entrapment olivine crystallization and solid-state diffusion of elements from their host olivine (see Danyushevsky *et al.*, 2000). For additional Hvammsmúli melt inclusion data, see Björnsson (2019).

Clinopyroxene

Clinopyroxene macrocrysts in the Brattaskjól (n=31) and Hvammsmúli (n=20) ankaramites have similar core compositions of Ca-rich augite, although only in the case of Brattaskjól, a subpopulation of magnesium-rich ($Mg\#_{cpx}$ 89.7–89.8; $Mg\#_{cpx}$ = cation fraction $Mg/(Mg+Fe_{tot})$ clinopyroxene was identified (Figure 4). Interestingly, as the clinopyroxene macrocrysts become more ferrous ($Mg\#_{cpx}$ decreases), CaO and Al_2O_3 contents gradually increase until $Mg\#_{cpx}$ 84.5, followed by a decrease in these oxides in more evolved clinopyroxene crystals (Figure 4c and d). The enrichment in CaO and Al_2O_3, together with simultaneous decrease in SiO_2 and no variation in Na_2O, points to an increase in the Ca-Tschermak (CaTs) component (Figure 4b). The variation in Na_2O is low, hence jadeite (Jd) component is unchanged against $Mg\#_{cpx}$ in clinopyroxene cores (Figure 4e). In contrast, TiO_2 shows negative (Figure 4f) and Cr_2O_3 positive correlation with $Mg\#_{cpx}$. Compared to clinopyroxene cores, the rims are typically richer in the ferrosilite (Fs) component and TiO_2 and have lower Mg#, Jd, CaTs (Figure 4) and Cr_2O_3.

Figure 4. – *Efnasamsetningar klínópýroxendíla í ankaramíti frá Brattaskjóli og Hvammsmúla. Samsetningar kjarna eru meðaltal þriggja efnagreininga á hverjum kjarna, en samsetningar kristalrima meðaltal tveggja til þriggja greininga gerðar nærri rimanum. Klínópýroxendílarnir hafa óðul með breytilega samsetningu og þessi breytileiki í samsetningu einstakra klínópýroxenkristalla er gefinn til kynna með fylltu gráu ferningunum (óbirt gögn). Svörtu örvarnar gefa til kynna áætluð áhrif af kristaldiffrun ólivíns (ol), Ca-ágíts (cpx) og plagíóklass (plg), þar sem gert er ráð fyrir að* Kd^{Mg-Fe}_{Ol-Liq} *= 0.30,* $Kd^{Mg-Fe}_{Cpx-Liq}$ *= 0.27,* D^{Ca}_{Ol-Liq} *= 0,* $D^{Ca}_{Cpx-Liq}$ *= 1.7,* D^{Al}_{Ol-Liq} *= 0 og* $D^{Al}_{Cpx-Liq}$ *= 0.15–0.25 (0,005 aukning þegar hvert mól% er fjarlægt úr bráðinni til að líkja eftir hitaháðum áhrifum á dreifingu Al milli bráðar og klínópyroxens). Kristaldiffrun plagíóklass minnkar styrk CaO og* Al_2O_3 *í bráðinni en hefur ekki áhrif á Mg-tölu ((*$Mg\#_{cpx}$ *= katjónahlutfallið 100Fe/(Fe+Mg)). Brotna örin er vektor sem sýnir áhrif diffrunar ólivíns og klínópýroxens í jöfnu hlutfalli. a) Klínópýroxenfjórhliðungur; Di = díopsíð, Hd = hedenbergít, En = enstatít, Wo = wollastonít, Fs = ferrósilít; b) Ca-tschermak's (CaTs) kristalþáttur á móti* $Mg\#_{cpx}$*; c) CaO á móti* $Mg\#_{cpx}$*; d)* Al_2O_3 *á móti* $Mg\#_{cpx}$*; e) Jaðeít (Jd) kristalþáttur á móti* $Mg\#_{cpx}$*; d)* TiO_2 *á móti* $Mg\#_{cpx}$*.*

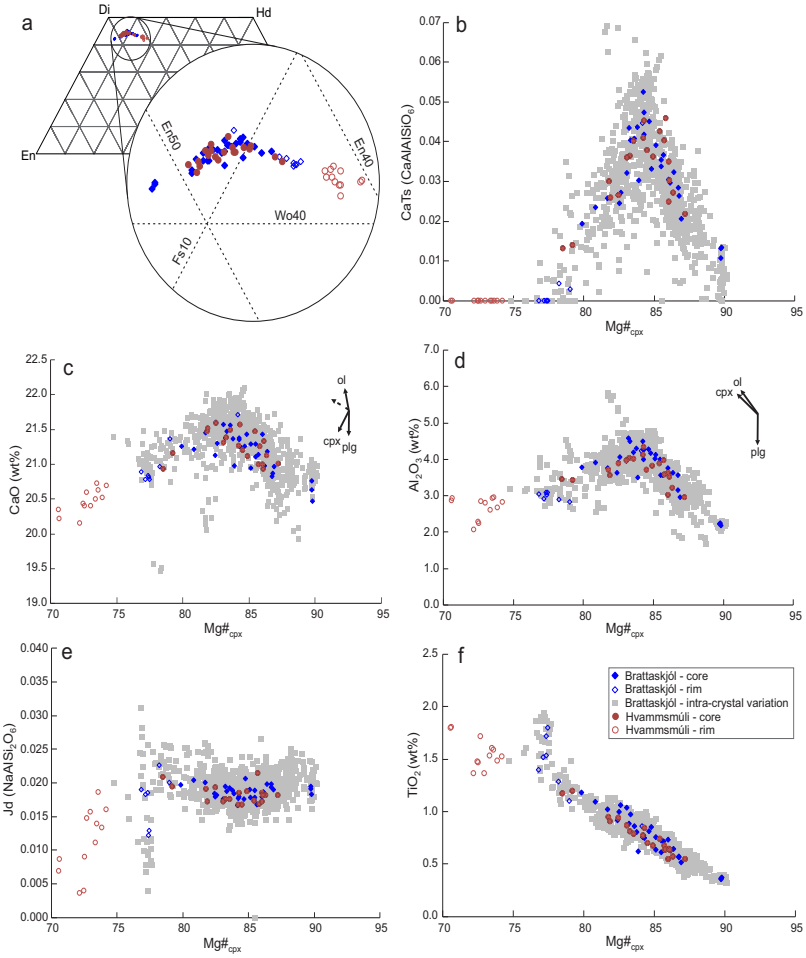

Figure 4. Clinopyroxene macrocryst compositions from the Brattaskjól and Hvammsmúli ankaramites. The core compositions are average compositions determined by three analyses from each clinopyroxene core, whereas the crystal rim compositions are averages of two to three analyses from near the crystal rims. The clinopyroxene macrocrysts include compositionally variable domains and this intra-clinopyroxene variability in all the studied crystals is illustrated with grey squares (unpublished data). Black arrows are approximated compositional vectors of olivine (ol), Ca-augite (cpx) and plagioclase (plg) fractionation, calculated assuming Kd^{Mg-Fe}_{Ol-Liq} = 0.30, $Kd^{Mg-Fe}_{Cpx-Liq}$ = 0.27, D^{Ca}_{Ol-Liq} = 0, $D^{Ca}_{Cpx-Liq}$ = 1.7, D^{Al}_{Ol-Liq} = 0 and $D^{Al}_{Cpx-Liq}$ = 0.15–0.25 (.005 increase with every mol% removed from melt to simulate the T-dependent partitioning of Al in clinopyroxene). Plg fractionation lowers CaO and Al_2O_3 but does not affect Mg number ($Mg\#_{cpx}$ = cation ratio Fe/(Fe+Mg)). Stippled arrow is the compositional vector of ol + cpx fractionation in equal proportions. a) Clinopyroxene quadrilateral; Di = Diopside, Hd = Hedenbergite, En = Enstatite, Wo = Wollastonite, Fs = Ferrosilite; b) Ca-Tschermak's (CaTs) component vs. $Mg\#_{cpx}$; c) CaO vs. $Mg\#_{cpx}$; d) Al_2O_3 vs. $Mg\#_{cpx}$; e) Jadeite (Jd) component vs $Mg\#_{cpx}$; d) TiO_2 vs. $Mg\#_{cpx}$.

DISCUSSION

Oxygen fugacity, pressure and temperature estimates

We used olivine-spinel pairs to determine oxygen fugacity (fO_2) during olivine crystallization using the most recent calibration (Nikolaev *et al.*, 2016) of the Ballhaus-Berry-Green olivine-orthopyroxene-spinel oxybarometer (Ballhaus *et al.*, 1991; Beattie, 1993). Depending on the size of the spinel grains, up to three EPMA analyses were performed, with two to three analyses from the host olivine at least $\sim$75 μm from the spinel and along the same growth zone of the olivine grain. Assuming spinel-olivine co-crystallization at 3.0 kbar and 1230°C, these calculations yielded $\Delta \log fO_2$(FMQ) values of 0.1$\pm$0.5 and 0.5$\pm$0.5 for Hvammsmúli and Brattaskjól, respectively (Figure 5a). This is in line with earlier estimates of the magma oxidation state at Vestmannaeyjar (Steinthorsson 1972; Gerlach, 1980; Schipper and Moussallam, 2017) and in the Eastern Volcanic Zone of Iceland (Hartley *et al.*, 2017).

We utilized clinopyroxene-liquid thermobarometry to estimate the temperature and pressure of clinopyroxene crystallization. This was done using the thermometer of Putirka (2008), coupled with the newly calibrated barometer of Neave and Putirka (2017). The thermobarometric calculations were carried out with an Excel workbook of Neave *et al.* (2019a) and by pairing the average clinopyroxene macrocryst core compositions with basaltic Eyjafjallajökull melt compositions from this study (Table 1) and the datasets of Loughlin (1995) and Moune *et al.* (2012). First, putative melt compositions for individual clinopyroxene crystals were selected on the basis of Fe-Mg equilibrium, assuming $Kd^{Mg-Fe}_{Cpx-Liq}$ = 0.27$\pm$0.6, 1 wt% H_2O, and $Fe^{2+}/\sum$Fe = 0.82 in accordance with fO_2 = FMQ+0.3 (Kress and Carmichael, 1991). Crystallization pressures and temperatures for these putative clinopyroxene-melt pairs were solved using the Eq. 1 barometer of Neave and Putirka (2017), coupled with Eq. 33 thermometer of Putirka (2008) and by iteratively using an output of one model as an input to another. Then, we filtered these "pseudo" P-T results by only accepting the clinopyroxene-melts pairs that are in multi-component equilibrium following a method resembling that of Neave *et al.* (2019a). Firstly, suitable clinopyroxene-melt pairs had to be within $\pm$10% Fe-Mg equilibrium in accordance to Eq. 35 in Putirka (2008). Secondly, the measured and predicted CaTs-, EnFs- and DiHd-components in clinopyroxene had to agree within the 1SEE precision, $\pm$0.03 for CaTs, $\pm$0.05 for EnFs and $\pm$0.06 for DiHd (mol fractions), of modelling equilibrium clinopyroxene components from the paired melts (Putirka, 1999; Mollo *et al.*, 2013). Thirdly, we only accepted P-T estimates from the clinopyroxene-melt pairs that deviated less than $\pm$40% from Ti equilibrium according to the model of Hill *et al.* (2011). If multiple melt compositions were in equilibrium with a single clinopyroxene after this extensive equilibrium filtering, the P-T estimates were most often within the methods 1SEE precision ($\pm$1.4 kbar and $\pm$28°C; Neave and Putirka, 2017; see Figure 5), and a mean of the calculated P and T was assigned for the clinopyroxene crystal. Suitable equilibrium liquids were found for nearly all clinopyroxene grains with the exception of the most magnesian (Mg#$_{cpx}$ 89.7–89.8) clinopyroxene macrocrysts indentified from Brattaskjól.

Clinopyroxene thermobarometry reveals similar crystallization temperatures and pressures for the Brattaskjól and Hvammsmúli ankaramites (Figure 5b and c). Model temperatures correlate with Mg#, such that the most primitive clinopyroxene macrocryst with Mg#$_{cpx}$>86 record 1190°C and the most evolved Mg#$_{cpx}$<81 clinopyroxene crystal records 1120°C (Figure 5b). All P estimates (1.7–4.2 kbar) are within the methods precision ($\pm$1.4 kbar, Neave and Putirka, 2017) and average at 3.0 kbar, although there is a trend of increasing P as a function of Mg#$_{cpx}$ (Figure 5b). This P and Mg#$_{cpx}$ correlation is partly related to, but not fully explained by, the T dependency of the barometer. The Brattaskjól olivine-hosted melt inclusion with the lowest Mg#$_{melt}$ (Ol14_mi1_2, see Table 1) was found to be a suitable equilibrium liquid for thirteen Mg#$_{cpx}$ 84.9–86.9 clinopyroxenes, implying crystallization conditions of 1178°C and 3.7 kbar for these crystals. These are similar to the mean crystallization T and P of 1182°C and 3.5 kbar derived for similar Mg#$_{cpx}$ 84.9–86.9 clinopyroxene

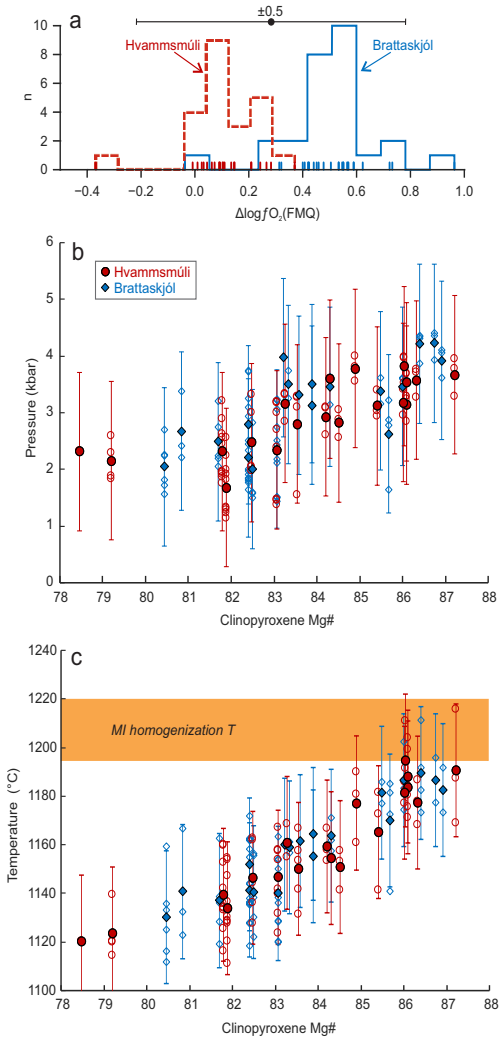

Figure 5. a) Olivine-spinel oxygen fugacity histograms for Hvammsmúli and Brattaskjól samples. b) Jd-in-clinopyroxene crystallization pressures vs. clinopyroxene Mg number ($Mg\#_{cpx}$). The solid symbols are mean values for individual clinopyroxene grains and the hollow symbols represent values from all clinopyroxene-melt equilibrium pairs (potentially multiple P and T determinations for individual clinopyroxene crystals, see discussion). Error bars (±1.4 kbar) correspond to the 1SEE calibration error of the barometer. c) Crystallization temperatures estimated using clinopyroxe-liquid thermometry vs. clinopyroxene Mg#. The solid and hollow symbols as in (b), and the orange bar shows homogenization temperatures of olivine-hosted melt inclusions (MI) from Brattaskjól. Error bars (±28°C) correspond to the 1SEE calibration error of the thermometer (Neave and Putirka, 2017). – *a) Stuðlarit sem sýnir hlutþrýsting súrefnis sem var ákvarðaður út frá ólivín-spíniljafnvægi í sýnum frá Hvammsmúla og Brattaskjóli. b) Kristöllunarþrýstingur reiknaður út frá magni jaðeitkristalþátts í klínópýroxeni á móti Mg-tölu klínópýroxens ($Mg\#_{cpx}$). Fylltu táknin eru meðalgildi fyrir einstök klínópýroxenkorn og ófylltu táknin eru gildi fyrir öll jafnvægispör af klínópýroxen og bráð (í sumum tilfellum fleiri en ein ákvörðun þrýstings og hitastigs fyrir einstakan klínópýroxenkristal, sjá texta). Óvissustikurnar (±1,4 kbar) eru 1SEE kvörðunaróvissa þrýstingsmælisins. c) Kristöllunarhiti áætlaður með klínópýroxen-bráðarhitamæli á móti Mg# klínópýroxens. Fylltu og ófylltu táknin eins og á (b), og gula röndin gefur til kynna hitastig þegar bráðarinnlyksur (MI) í ólivíni frá Brattaskjóli voru gerðar einsleitar. Óvissustikurnar (±28°C) eru 1SEE kvörðunaróvissa hitamælisins (Neave og Putirka, 2017).*

when pairing them with the complete Eyjafjallajökull melt dataset. This strengthens the case for using the method of pairing clinopyroxene to temporally unrelated magmas from the same volcanic system (such as Eyjafjallajökull in our case) using sufficiently robust filtering criteria of chemical equilibrium (see Neave *et al.*, 2019a).

Complementary to the clinopyroxene-liquid P-T estimates, we used olivine-liquid (Putirka *et al.*, 2007) and liquid-only (Putirka, 2008) thermometry to establish the olivine crystallization temperature. Olivine-liquid thermometry according to Eq. 4 in Putirka *et al.* (2007) gives olivine-crystallization temperatures of 1136–1213°C for $Fo_{80.7-88.9}$ olivine

from Brattaskjól and Hvammsmúli. For these calculations, we paired the alkali basaltic Brattaskjól melt inclusions (Table 1) with high-precision Brattaskjól and Hvammsmúli olivine core compositions (n=160, Figure 2a) given that they were in Fe-Mg equilibrium (Kd^{Mg-Fe}_{Ol-Liq}=0.30±0.3; Toplis, 2005) with the melt inclusions, and assumed 1 wt% H_2O in the melt (Moune *et al.*, 2012). The liquid-only model temperatures for Brattaskjól alkali basalt melt inclusions (with $Mg\#_{melt}$ 56–69, Table 1), in accordance with Eq. 15 in Putirka (2008) and assuming 1 wt% H_2O in melt, are 1155–1222°C. The melt inclusions in $Fo_{87.9-88.6}$ Brattaskjól and all Hvammsmúli olivine grains were not utilized for thermobarometric purposes, as their low FeO_{tot} contents suggest modification by post-entrapment solid-state diffusion.

The thermobarometric calculations indicate that the macrocrysts in the Brattaskjól and Hvammsmúli ankaramites crystallized at 3±1.4 kbar and over a ≥100°C temperature window. Assuming oceanic crustal density of 2860 kg/m^3 (Carlson and Herrick, 1990), the 3±1.4 kbar crystallization pressure of the studied clinopyroxene crystals corresponds to a depth of 10.7±5 km. This depth overlaps with the proposed depth of the brittle-ductile transition below Eyjafjallajökull (Hjaltadóttir *et al.*, 2009) and is a typical pre-eruption residence depth of basaltic magmas in Iceland (Neave and Putirka, 2017). However, considering the high $Mg\#_{cpx}$ (up to $Mg\#_{87}$) values of the clinopyroxene crystals, the obtained mid-crustal crystallization depth is noteworthy. Due to their primitive character (magnesian whole-rock and macrocryst compositions), the Eyjafjallajökull ankaramites have been envisioned to represent magmas from the deep crust or shallow mantle (e.g., Loughlin, 1995). This, however, is not the case for the majority of the clinopyroxene grains in the Brattaskjól and Hvammsmúli ankaramites, the only potential exception being the primitive clinopyroxene crystals with $Mg\#_{cpx}$ 89.7–89.8 for which crystallization pressures were not determined because of the lack of suitable equilibrium liquids.

Significance of olivine-hosted spinel inclusions

The spinel inclusions in the Brattaskjól and Hvammsmúli olivine macrocrysts have higher Cr# and TiO_2 than hitherto published for chromian spinels from Iceland (Thy, 1983; Sigurdsson *et al.*, 2000; Matthews *et al.*, 2016; Spice *et al.*, 2016) and their Al_2O_3 content is low (Figure 3). According to Kamenetsky (2001), spinel TiO_2 and Al_2O_3 correlate well with the host-magma composition; therefore, spinel compositions likely reflect the nature of the parental magma. We have a poor control on the magma at depth from which these spinels crystallized, yet Eyjafjallajökull magmas are generally mildly alkaline with relatively low Al_2O_3 and high TiO_2. Spinels with high Cr# and TiO_2 and low Al_2O_3 are typical for oceanic (OIB) and Large Igneous Province (LIP) basalts, in contrast to mid-ocean ridge basalts (MORB). In the classification of Kamenetsky (2001), the Brattaskjól and Hvammsmúli spinels plot in the OIB field (Figure 3c). The high TiO_2 content in these spinels also discriminates them from mantle-derived spinels that typically have <0.2 wt% TiO_2 (Kamenetsky, 2001). The Al_2O_3-poor and TiO_2-enriched nature of the spinels suggests that the parental melts of the ankaramites were produced by low-degree melting of deep and enriched mantle sources, in accordance with the olivine minor and trace element chemistry (see Nikkola *et al.*, 2019).

Insights into magmatic time scales from olivine zonation

The wide compositional zonation in the Hvammsmúli olivine macrocrysts, coarse groundmass, and the fact that both clinopyroxene and olivine macrocrysts enclose groundmass minerals around them (Figure 1c) indicate an extended cooling and crystallization history for the Hvammsmúli ankaramite. In addition, the low FeO and MgO contents in the Hvammsmúli melt inclusions suggest transfer of these elements to olivine by post-entrapment solid-state diffusion during an extended stay of the olivine crystals at magmatic conditions. According to Loughlin (1995), the Hvammsmúli ankaramite outcrop is likely an eroded lava lake, which is consistent with the diffusive re-equilibration of melt inclusions and the wide compositional zonation in olivine macrocryst. It is possible that the bulk of the diffusive re-equilibration in Hvammsmúli macrocrysts took place when they resided in the postulated lava lake.

Regarding the Brattaskjól olivine zonation, the most plausible explanation for the detected steps and changes in the slope of the Fe-Mg zoning patterns in the $Fo_{>85.4}$ olivine grains (Figure 2b) is a combination of solid-state diffusion and episodes of olivine growth from an evolving host liquid. The rim-growth events in the normally zoned olivine macrocrysts may have been caused by step-like ascent of the olivine-carrying host liquid, episodic changes in the host-liquid composition, infiltration of liquid into the system (i.e., magma mixing), or related to movement of olivine macrocrysts within a magmatic system with temperature gradients (see Pankhurst *et al.*, 2018).

The high-Fo bands in the rims of the complex reverse zoned Brattaskjól olivine macrocrysts indicate mixing between an olivine rim forming primitive melt and the more evolved olivine cores with $Fo_{80-84.4}$. Below, we refer to these high-Fo bands in the olivine macrocryst rims as 'mixing plateaus'. Although the Fo content in the mixing plateaus varies, three olivine crystals show mixing plateaus with $Fo_{85.4}$ composition (Figure 6a, b and d), and the lowest Fo mixing plateaus are in-fact not compositional plateaus but appear as sharp high-Fo tips in the analytical traverses (Figure 6c and e). This, along with the fact that all $Fo_{<84.4}$ olivine macrocrysts have complex reverse zoned rims, implies that all the mixing plateaus near olivine rims may have had an original composition of $Fo_{85.4}$ and the Fo content in some of the mixing plateaus has later degreased in response to partial diffusive equilibration with the carrier melt.

We suggest that these $Fo_{85.4}$ mixing plateaus formed during a magmatic recharge event in which a melt (with $Mg\#_{melt}$ of ∼63 in equilibrium with $Fo_{85.4}$ olivine; Toplis, 2005) intruded an olivine-bearing crystal mush. We propose this "magma-recharge model" as (i) it offers a simple explanation why the $Fo_{<84.4}$ olivine grains are consistently reverse zoned, (ii) the large amount (∼30 vol%) of compositionally variable macrocrysts in the Brattaskjól ankaramite suggests a cumulative origin for the macrocrysts, and (iii) mixing of magmas and crystal mushes is common in Icelandic magmatic systems (Halldorsson *et al.*, 2008; Neave *et al.*, 2013; Halldórsson *et al.*, 2018). In particular, the consistent change from complex reverse to normally zoned olivine at $Fo_{84.4-85.4}$ (Figure 2a), and the varying offset in Fo content (1–3 mol%) between mixing plateaus and crystal cores, support a magma-recharge origin for the complex reverse zonation in olivine macrocrysts. Alternatively, the complex reverse zoned olivine macrocrysts could have been formed during their movement in a crustal intrusion with temperature gradients (cf. Pankhurst *et al.*, 2018). Considering the low number of analysed crystals, our data cannot disprove, but neither particularly support, this mode of formation.

Assuming that our hypothesis of the magma recharge origin for the complex reverse zoned crystals is valid, we can utilize diffusion modelling (Costa *et al.*, 2008; Zhang and Cherniak, 2010) of the chemical re-equilibration in the Fe-Mg profiles (e.g., Figure 2d) to constrain the time frame within which the Brattaskjól complex reverse zoned olivines cooled after the recharge event. We did this by using the finite difference diffusion code of Kahl *et al.* (2015) that follows the procedures outlined in Costa and Chakraborty (2004) and Costa *et al.* (2008), with Fe-Mg inter-diffusion coefficients of Dohmen *et al.* (2007) and Dohmen and Chakrabortny (2007). As the pre-diffusion initial state in our model crystals, we assumed the measured Fo contents in olivine cores, and a variably thick (9–26 μm) $Fo_{85.4}$ mixing plateau for the olivine crystals (stippled lines in Figure 6). We only modelled the time of diffusive re-equilibration between the mixing plateau and olivine-core, not between the mixing plateau and the outer crystal rim, because the outermost rims have likely been formed, at least partly, by crystallization from cooling and evolving host-magma after the magma recharge, not by solid-state diffusive re-equilibriation. Some late-stage crystallization in the outermost macrocryst rims is to be expected considering the crystalline groundmass (Figure 1b) and as the macrocrysts are hosted by a comparatively slowly cooled lava.

In diffusion modelling, we used a fO_2 of FMQ+0.5, temperature of 1170°C and pressure of 3.0 kbar, corresponding to the mean conditions of clinopyroxene crystallization in the Brattaskjól ankaramite (Figure 5). Varying the fO_2 and pressure has only a minor effect on the model results (e.g.,

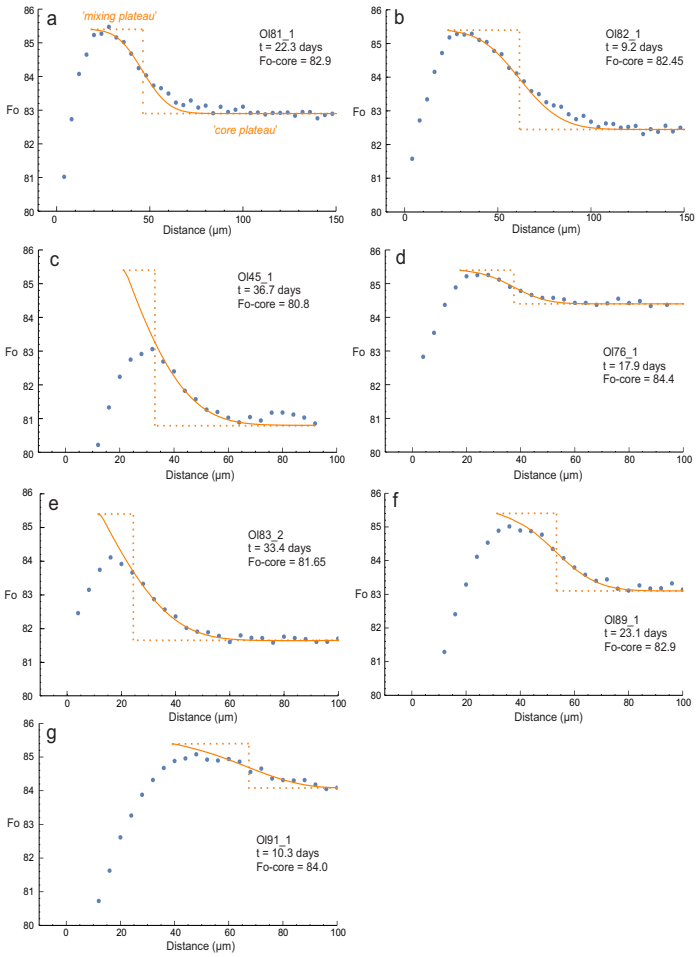

Figure 6. a-g)Fe-Mg zonation in the seven complex reverse zoned olivine macrocrysts used for diffusion modelling. The blue dots show the measured forsterite (Fo) content near the olivine rims, the orange stippled line is the assumed initial olivine composition, and the orange curve is the calculated end result of diffusive re-equilibration after time (t). – *a-g) Fe-Mg-beltun í sjö ólivíndílum með flókna öfuga beltun og notaðir voru við líkanreikninga efnasveimis. Bláu punktarnir sýna mælt forsterítgildi (Fo) nærri rimum ólivíns. Gula brotalínan á hverri mynd er áætluð samsetning ólivíns í upphafi líkanreiknings og heila gula línan er reiknuð samsetning af völdum efnasveimis eftir tíma t.*

Kahl *et al.*, 2015); however, the timescales are sensitive to the selected model temperature. Considering the primitive nature of the Brattaskjól ankaramite, we surmise that 1170°C is fair, although conservative (potentially low) estimate of the diffusion T (see Figure 5). We prefer a lower model temperature to avoid underestimating the diffusion time scales, because, irrespective of the model conditions, the resulting diffusion timescales are the maximum time scales of subsurface storage and ascent (after magmatic recharge) as the crystals are hosted by a lava flow. Lava flow fields insulate themselves effectively (e.g., Hon *et al.*, 1994; Self *et al.*, 1998; Harris and Rowland, 2009) and hence lava-hosted olivine crystals may remain at high but gradually decreasing temperature for weeks to months after eruption. We cannot separate diffusion in a lava flow/lava lake and diffusion occurring at depth during subsurface ascent; this is the caveat of working with crystalline lava samples instead of tephra.

The diffusion modelling gives diffusion time scales in the range 9–37 days (Figure 6). This time frame does not reflect the speed of the ankaramite magma ascent directly, because of the unknown olivine residence time in the lava and the fact that the timing of the magmatic recharge (forming the reverse zoned high-Fo rims) does not necessarily coincide with the beginning of the magma ascent. The magmatic recharge to the crystal mush did not necessarily act as the eruption trigger and may have occurred considerably earlier than agitation and upheaval of the olivine (and clinopyroxene) crystals (see Rae *et al.*, 2016). Nevertheless, as the unknown time of diffusion at the surface and the potential time-delay between magmatic recharge and crystal lift both lengthen the diffusion time, our 9–37-day estimate for diffusive re-equilibration can be viewed as a likely maximum time that elapsed from crystal mush disaggregation to eruption. The 9–37-day range may reflect varying olivine residence times in a magma ascent conduit or surficial lava-feeding system after the magmatic recharge event, or be due to olivine sectioning and anisotropy effects (Shea *et al.*, 2015).

Moderate-pressure co-crystallization of primitive clinopyroxene and olivine

The Brattaskjól and Hvammsmúli ankaramites have abundant olivine and clinopyroxene macrocrysts and only minor plagioclase macrocrysts, $Mg\#_{cpx}$ of clinopyroxene being as high as 90. This and the compositional variation in clinopyroxene cores suggest olivine- and clinopyroxene-dominated fractionation and a late arrival of plagioclase on the liquidus. Specifically, Ca and Al enrichment with decreasing magnesium number in clinopyroxene grains with $Mg\#_{cpx}$ 84.5–90.0 suggests fractionation of olivine and clinopyroxene in approximately equal amounts, and the decrease in Ca and Al, which indicates simultaneous plagioclase fractionation from the host melt, is only seen in clinopyroxene grains with $Mg\#_{cpx}$<84.5 (Figure 4c and d). Variation in crystallization conditions (T and P) or disequilibrium crystallization processes are unlikely to explain this compositional variation because of the unchanged Jd content in clinopyroxene cores (Figure 4e), which should be dependent on pressure, temperature and crystallization rate (e.g., Mollo *et al.*, 2010; Hammer *et al.*, 2016; Welsch *et al.*, 2016; Ubide *et al.*, 2019). Moreover, rapid disequilibrium crystallization is expected to produce anti-correlation between Ca and Al (Mollo *et al.* 2010), contrary to what is seen in our clinopyroxene data (Figures 4c and d).

MORB melts typically crystallize in the sequence of olivine (±spinel) –> olivine + plagioclase –> olivine + plagioclase + clinopyroxene, leaving behind troctolitic or gabbroic cumulates, not wehrlite cumulates, such as in the case of the Brattaskjól and Hvammsmúli ankaramites. In addition, due to the late arrival of clinopyroxene as a crystallizing phase, the most primitive clinopyroxene produced in MORB crystallization experiments typically has $Mg\#_{cpx}$ of ∼83 (Grove and Bryan, 1983; Tormey *et al.*, 1987; Yang *et al.*, 1996), not $Mg\#_{cpx}$ 90 like in Brattaskjól ankaramite. Geochemical trends indicative of clinopyroxene fractionation before plagioclase have been noted from lavas in SEVZ and other parts of Iceland (Furman *et al.*, 1991; Thy, 1991a; Maclennan *et al.*, 2001; Mattsson and Oskarsson, 2005), and some Iceland lavas do host high-Mg# clinopyroxene (up to $Mg\#_{cpx}$ 92 in Borgarhraun lava, Winpenny and Maclennan 2011). In this regard, our findings are in line with earlier studies. Anyhow, clinopyroxene fractionation from primitive SEVZ lavas has usually been regarded as indicative of high (>8 kbar) crystallization pressures near Moho or at upper mantle depths (Furman *et al.*, 1991; Thy, 1991a, b; Mattsson and Oskarsson, 2005), as the stability of clinopyroxene increases with pressure (Presnall *et al.*, 1978, 2002; Stolper, 1980). The calculated 3.0±1.4 kbar crystallization pressures for the primitive Brattaskjól and Hvammsmúli clinopyroxene macrocrysts (up to $Mg\#_{cpx}$ 87) contradicts this contention and suggest that the mildly alkaline SEVZ magmas crystallized clinopyroxene and olivine before plagioclase at depths as shallow as in the mid-crust. This inference is supported by, and is in line with, recent experimental work that shows that "enriched end-member" (Shorttle and Maclennan, 2011) Iceland tholeiite melt crystallized clinopyroxene before plagioclase at 3 kbar (Neave *et al.*, 2019b). Elevated H_2O in primitive SEVZ magmas (Thy, 1991a; Moune *et al.*, 2012) and low amounts of

plagioclase-forming elements (Ca and Al; see Neave *et al.* 2019b) are the likely factors stabilizing olivine +clinopyroxene co-crystallization in magmatic storage zones below SEVZ.

PRE-ERUPTIVE CRYSTAL STORAGE AND DIFFERENTIATION

High-Mg macrocrysts are often assumed to have crystallized deep in the Earth's crust or in the upper mantle as they represent the first crystallizing phases from mantle melts. Our data indicate mid-crustal crystallization conditions (3.0±1.4 kbar, 10.7±5 km) at a moderate oxygen fugacity for most clinopyroxene macrocrysts in the Hvammsmúli and Brattaskjól ankaramites. The degree of diffusive relaxation in Brattaskjól olivine macrocrysts indicates diffusion times in the range of 9–37 days, which we interpret as the maximum time elapsed from crystal mush disaggregation to eruption. Clinopyroxene composition trends suggest fractionation of olivine and clinopyroxene until late in the crystallization sequence, and as such, the Hvammsmúli and Brattaskjól ankaramites likely represent magmas that incorporated wehrlite or plagioclase-wehrlite crystal mushes in the mid-crust on their way to the surface. Formation of a wehrlitic cumulus assemblage by fractional crystallization at mid-crustal pressure is possible, given that the primitive parental melt is sufficiently rich in H_2O and poor in Ca and Al. Our findings are in line with the earlier propositions of olivine and clinopyroxene co-crystallization from primitive SEVZ magmas, although we propose that this occurs as shallow as in the mid-crust.

Acknowledgements

This work was funded by Nordic Volcanological Centre and Icelandic Research Fund doctoral student grant (185267-051). We thank Atli Hjartarson for the aid in sample preparation and Jussi S. Heinonen for discussions. Eero Hanski delivered a useful review of an early version of the manuscript.

ÁGRIP

Skilningur á hegðun eldfjallakerfa hvað varðar innskota- og eldgosavirkni takmarkast af því hve skammt er síðan eftirlit með eldfjöllum hófst. Til að greina hvaða skilyrði ríkja í kvikugeymum undir eldfjöllum á Suðurlandi höfum við greint efnasamsetningu steinda, beltun í steindum og efnasamsetningu bráðarinnlyksna í tveimur ankaramítmyndunum í Eyjafjöllum, sem kenndar eru við Brattaskjól og Hvammsmúla. Þessar tvær myndanir eru ríkar af dílum með fjölbreytilega samsetningu. Þar á meðal er magnesínríkasta ólivín (Fo_{88-90}) og klínópýroxen ($Mg\#_{cpx}{}_{89,8}$) sem þekkt er frá Eyjafjallajökli. Auk þess hafa spínilinnlyksur í ólivíni hátt $Cr\#_{spl}$ (52–80), hátt magn TiO_2 (1–3%) og lágt magn Al_2O_3 (8–22%) í samanburði við dæmigerða íslenska krómspínla. Spínil-ólivín súrefnisþrýstingsmælirinn gefur miðlungs háan hlutþrýsting súrefnis við kristöllun, eða ΔlogFMQ 0–0,5, og hitastigs-þrýsingsmælir byggður á efnajafnvægi klínópýroxens og bráðar gefur til kynna kristöllun við þrýsting sem ríkir í miðri jarðskorpunni (1,7–4,2 kbar, að meðaltali 3,0±1,4 kbar) og 1120–1195°C hita. Fyrir bráðarinnlyksur með $Mg\#_{melt}$ 56,1–68,5 gefur hitamælir sem byggir á samsetningu bráðar 1155–1222°C kristöllunarhita, en ólivín-bráðarhitamælir fyrir ólivín með samsetningunum $Fo_{80,7-88,9}$ gefur 1136–1213°C. Líkanreikningar á efnasveimi í beltuðu ólivíni benda til að dílar frá Brattaskjóli hafi farið af stað og flust til yfirborðs frá geymslurými í miðri skorpunni innan fárra vikna (innan 9–37 daga). Leitni í samsetningu klínópýroxendíla og það hversu sjaldgæfir plagíóklasdílar eru gefur til kynna að kótektískt fasafylki í miðskorpunni hafi verið ólivín ásamt klínópýroxeni og að plagíóklas hafi komið seinna til sögunnar. Niðurstaðan er að dílafarmur ankaramítsins í Brattaskjóli og Hvammsmúla hafi verið að uppruna kristalríkur massi í miðskorpunni með steindafylki wehrlíts og plagíóklaswehrlíts sem kristallaðist á víðu hitastigsbili og varð síðan fyrir röskun.

REFERENCES

Ballhaus, C., R. F. Berry and D. H. Green 1991. High pressure experimental calibration of the olivine-orthopyroxene-spinel oxygen geobarometer: implications for the oxidation state of the upper mantle. *Contrib. Mineral Petrol.* 107, 27–40

Batanova, V. G., A. V. Sobolevand and D. V. Kuzmin

2015. Trace element analysis of olivine: High precision analytical method for JEOL JXA-8230 electron probe microanalyser. *Chem. Geol.* 419, 149–157. https://doi.org/10.1016/j.chemgeo.2015.10.042

Beattie, P. 1993. Olivine-melt and orthopyroxene-melt equilibria. *Contrib. Mineral Petrol.* 115, 103–111. https://doi.org/10.1007/BF00712982

Björnsson, G. 2019. *High-temperature experimental study of olivine-hosted melt inclusions from Hvammsnúpur.* BSc thesis, Faculty of Earth Science, University of Iceland, 43 pp.

Brandsdóttir, B. and W. H. Menke 2008. The seismic structure of Iceland. *Jökull* 58, 17–34.

Carlson, R. L. and Herrick, C. N. 1990. Densities and porosities in the oceanic crust and their variations with depth and age. *J. Geophys. Res.* 95, 9153. https://doi.org/10.1029/JB095iB06p09153

Chauvel, C. and C. Hémond 2000. Melting of a complete section of recycled oceanic crust: Trace element and Pb isotopic evidence from Iceland. *Geochem. Geophys. Geosys.* 1, 1–22. https://doi.org/10.1029/1999GC000002

Costa, F. and S. Chakraborty 2004. Decadal time gaps between mafic intrusion and silicic eruption obtained from chemical zoning patterns in olivine. *Earth Planet. Sci. Lett.* 227, 517–530. https://doi.org/10.1016/j.epsl.2004.08.011

Costa, F., R. Dohmen and S. Chakraborty 2008. Time scales of magmatic processes from modelling the zoning patterns of crystals. *Rev. Mineral. Geochem.* 69, 545–594. https://doi.org/10.2138/rmg.2008.69.14

Danyushevsky, L. V., F. N. Della-Pasqua and S. Sokolov 2000. Re-equilibration of melt inclusions trapped by magnesian olivine phenocrysts from subduction-related magmas: Petrological implications. *Contrib. Mineral. Petrol.* 138, 68–83. https://doi.org/10.1007/PL00007664

Danyushevsky, L. V. and P. Plechov 2011. Petrolog3: Integrated software for modeling crystallization processes. *Geochem. Geophys. Geosys.* 12, 1–32. https://doi.org/10.1029/2011GC003516

Dohmen, R., H.-W. Becker and S. Chakraborty 2007. Fe-Mg diffusion in olivine I: experimental determination between 700 and 1,200°C as a function of composition, crystal orientation and oxygen fugacity. *Phys. Chem. Miner.* 34, 389–407. https://doi.org/10.1007/s00269-007-0157-7

Dohmen, R. and S. Chakraborty 2007. Fe-Mg diffusion in olivine II: point defect chemistry, change of diffusion mechanisms and a model for calculation of diffusion coefficients in natural olivine. *Phys. Chem. Miner.* 34, 409–430. https://doi.org/10.1007/s00269-007-0158-6

Flóvenz, Ó. G. and K. Saemundsson 1993. Heat flow and geothermal processes in Iceland. *Tectonophysics* 225, 123–138. https://doi.org/10.1016/0040-1951(93)90253-G

Furman, T., Frey, F. A. and Park, K. H. 1991. Chemical constraints on the petrogenesis of mildly alkaline lavas from Vestmannaeyjar, Iceland: the Eldfell (1973) and Surtsey (1963-1967) eruptions. *Contrib. Mineral Petrol.* 109, 19–37. https://doi.org/10.1007/BF00687198

Gerlach, T. M. 1980. Evaluation of volcanic gas analysis from Surtsey volcano, Iceland 1964–1967. *J. Volcanol. Geotherm. Res.* 8, 191–198. https://doi.org/10.1016/0377-0273(80)90104-3

Grove, T. L. and W. B. Bryan 1983. Fractionation of pyroxene-phyric MORB at low pressure: An experimental study. *Contrib. Mineral. Petrol.* 84, 293–309. https://doi.org/10.1007/BF01160283

Halldórsson, S. A., E. Bali, M. E. Hartley *et al.* 2018. Petrology and geochemistry of the 2014–2015 Holuhraun eruption, central Iceland: compositional and mineralogical characteristics, temporal variability and magma storage. *Contrib. Mineral. Petrol.* 173, 1–25. https://doi.org/10.1007/s00410-018-1487-9

Halldorsson, S. A., N. Oskarsson, K. Gronvold *et al.* 2008. Isotopic-heterogeneity of the Thjorsa lava-Implications for mantle sources and crustal processes within the Eastern Rift Zone, Iceland. *Chem. Geol.* 255, 305–316. https://doi.org/10.1016/j.chemgeo.2008.06.050

Hammer, J., S. Jacob, B. Welsch *et al.* 2016. Clinopyroxene in postshield Haleakala ankaramite: 1. Efficacy of thermobarometry. *Contrib. Mineral. Petrol.* 171, 1–23. https://doi.org/10.1007/s00410-015-1212-x

Harris, A. J. L. and S. K. Rowland 2009. Effusion rate controls on lava flow length and the role of heat loss: a review. In: *Studies in Volcanology: The Legacy of George Walker.* The Geological Society of London on behalf of The International Association of Volcanology and Chemistry of the Earth's Interior, 33–51.

Hartley, M. E., O. Shorttle, J. Maclennan *et al.* 2017. Olivine-hosted melt inclusions as an archive of redox heterogeneity in magmatic systems. *Earth Planet. Sci. Lett.* 479, 192–205. https://doi.org/10.1016/j.epsl.2017.09.029

Hémond, C., N. T. Arndt, U. Lichtenstein *et al.* 1993. The heterogeneous Iceland plume: Nd-Sr-O isotopes and trace element constraints. *J. Geophys. Res.* 98, 15833–15850. https://doi.org/10.1029/93JB01093

Hill, E., J. D. Blundy and B. J. Wood 2011. Clinopyroxene-melt trace element partitioning and the development of a predictive model for HFSE and Sc. *Contrib. Mineral. Petrol.* 161, 423–438. https://doi.org/10.1007/s00410-010-0540-0

Hjaltadóttir, S., K. S. Vogfjörð and R. Slunga 2009. *Seismic signs of magma pathways through the crust in the Eyjafjallajökull volcano, south Iceland.* Rep. 2009–13, Icel. Meteorol. Office, Reykjavík, 25 pp.

Hon, K., J. Kauhikau, R. Denlinger and K. Mackay 1994. Emplacement and inflation of pahoehoe sheet flows: Observations and measurements of active lava flows on Kilauea Volcano, Hawaii. *Geol. Soc. Am. Bull.* 106, 351–370. https://doi.org/10.1130/0016-7606(1994)106<0351:EAIOPS>2.3.CO;2

Jakobsson, S. P. 1972. Chemistry and distribution pattern of recent basaltic rocks in Iceland. *Lithos* 5, 365–386. https://doi.org/10.1016/0024-4937(72)90090-4

Kahl, M., S. Chakraborty, M. Pompilio and F. Costa 2015. Constraints on the nature and evolution of the magma plumbing system of Mt. Etna volcano (1991–2008) from a combined thermodynamic and kinetic modelling of the compositional record of minerals. *J. Petrol.* 56, 2025–2068. https://doi.org/10.1093/petrology/egv063

Kahl, M., M. Viccaro, T. Ubide *et al.* 2017. A branched magma feeder system during the 1669 eruption of Mt Etna: Evidence from a time-integrated study of zoned olivine phenocryst populations. *J. Petrol.* 58, 443–472. https://doi.org/10.1093/petrology/egx022

Kamenetsky, V. S. 2001. Factors controlling chemistry of magmatic spinel: an empirical study of associated olivine, Cr-spinel and melt Inclusions from primitive rocks. *J. Petrol.* 42, 655–671. https://doi.org/10.1093/petrology/42.4.655

Keiding, J. K. and O. Sigmarsson 2012. Geothermobarometry of the 2010 Eyjafjallajökull eruption: New constraints on Icelandic magma plumbing systems. *J. Geophys. Res. Solid Earth* 117, 1–15. https://doi.org/10.1029/2011JB008829

Kokfelt, T. F., K. Hoernle, F. Hauff *et al.* 2006. Combined trace element and Pb-Nd-Sr-O isotope evidence for recycled oceanic crust (upper and lower) in the Iceland mantle plume. *J. Petrol.* 47, 1705–1749. https://doi.org/10.1093/petrology/egl025

Kress, V. C. and I. S. E. Carmichael 1991. The compressibility of silicate liquids containing Fe^2O^3 and the effect of composition, temperature, oxygen fugacity and pressure on their redox states. *Contrib. Mineral. Petrol.* 108, 82–92. https://doi.org/10.1007/BF00307328

Kristjánsson, L., H. Jóhannesson, J. Eiríksson and A. I. Gudmundsson 1988. Brunhes-Matuyama paleomagnetism in three lava sections in Iceland. *Can. J. Earth Sci.* https://doi.org/10.1139/e88-024

Laeger, K., M. Petrelli, D. Andronico *et al.* 2017. High-resolution geochemistry of volcanic ash highlights complex magma dynamics during the Eyjafjallajökull 2010 eruption. *Am. Mineral.* 102, 1173–1186. https://doi.org/10.2138/am-2017-5860

Loughlin, S. C. 1995. *The evolution of the Eyjafjöll volcanic system, southern Iceland.* PhD thesis, University of Durham, UK, 319 pp.

Maclennan, J., D. McKenzie, K. Grönvold and L. Slater 2001. Crustal accretion under Northern Iceland. *Earth Planet. Sci. Lett.* 191, 295–310. https://doi.org/10.1016/S0012-821X(01)00420-4

Martin, E., J. L. Paquette, V. Bosse *et al.* 2011. Geodynamics of rift-plume interaction in Iceland as constrained by new 40Ar/39Ar and in situ U-Pb zircon ages. *Earth Planet. Sci. Lett.* 311, 28–38. https://doi.org/10.1016/j.epsl.2011.08.036

Matthews, S., O. Shorttle and J. Maclennan 2016. The temperature of the Icelandic mantle from olivine-spinel aluminum exchange thermometry. *Geochem. Geophys. Geosys.*https://doi.org/10.1002/2016GC006497

Mattsson, H. B. and N. Oskarsson 2005. Petrogenesis of alkaline basalts at the tip of a propagating rift: Evidence from the Heimaey volcanic centre, south Iceland. *J. Volcanol. Geotherm. Res.* 147, 245–267. https://doi.org/10.1016/j.jvolgeores.2005.04.004

Mollo, S., P. Del Gaudio, G. Ventura *et al.* 2010. Dependence of clinopyroxene composition on cooling rate in basaltic magmas: Implications for thermobarometry. *Lithos* 118, 302–312. https://doi.org/10.1016/j.lithos.2010.05.006

Mollo, S., K. Putirka, V. Misiti *et al.* 2013. A new test for equilibrium based on clinopyroxene-melt pairs: Clues on the solidification temperatures of Etnean alkaline melts at post-eruptive conditions. *Chem. Geol.* 352, 92–100. https://doi.org/10.1016/j.chemgeo.2013.05.026

Moune, S., O. Sigmarsson, P. Schiano *et al.* 2012. Melt inclusion constraints on the magma source of Eyjafjallajökull 2010 flank eruption. *J. Geophys. Res. Solid Earth* 117, 1–13. https://doi.org/10.1029/2011JB008718

Neave, D. A., E. Bali, G. H. Guðfinnsson *et al.* 2019a. Clinopyroxene-liquid equilibria and geothermobarometry in natural and experimental tholeiites: the 2014–2015 Holuhraun eruption, Iceland. *J. Petrol.* 60, 1653–1680. https://doi.org/10.1093/petrology/egz042

Neave, D. A., O. Namur, O. Shorttle and F. Holtz 2019b. Magmatic evolution biases basaltic records of mantle chemistry towards melts from recycled sources. *Earth Planet. Sci. Lett.* 520, 199–211. https://doi.org/10.1016/j.epsl.2019.06.003

Neave, D. A., E. Passmore, J. Maclennan *et al.* 2013. Crystal-melt relationships and the record of deep mixing and crystallization in the AD 1783 Laki eruption, Iceland. *J. Petrol.* 54, 1661–1690. https://doi.org/10.1093/petrology/egt027

Neave, D. A. and K. D. Putirka 2017. A new clinopyroxene-liquid barometer, and implications for magma storage pressures under Icelandic rift zones. *Am. Mineral.* 102, 777–794. https://doi.org/10.2138/am-2017-5968

Nikkola, P., G. H. Guðfinnsson, E. Bali *et al.* 2019. Signature of deep mantle melting in South Iceland olivine. *Contrib. Mineral. Petrol.* 174, 1–19. https://doi.org/10.1007/s00410-019-1580-8

Nikolaev, G. S., A. A. Ariskin, G. S. Barmina *et al.* 2016. Test of the Ballhaus-Berry-Green Ol-Opx-Sp oxybarometer and calibration of a new equation for estimating the redox state of melts saturated with olivine and spinel. *Geochemistry Int.* 54, 301–320. https://doi.org/10.1134/S0016702916040078

Pankhurst, M. J., D. J. Morgan, T. Thordarson and S. C. Loughlin 2018. Magmatic crystal records in time, space, and process, causatively linked with volcanic unrest. *Earth Planet. Sci. Lett.* 493, 231–241. https://doi.org/10.1016/j.epsl.2018.04.025

Peate, D. W., K. Breddam, J. A. Baker *et al.* 2010. Compositional characteristics and spatial distribution of enriched Icelandic mantle components. *J. Petrol.* 51, 1447–1475. https://doi.org/10.1093/petrology/egq025

Presnall, D. C., S. A. Dixon, J. R. Dixon *et al.* 1978. Liquidus phase relations on the join diopside-forsterite-anorthite from 1 atm to 20 kbar: Their bearing on the generation and crystallization of basaltic magma. *Contrib. Mineral. Petrol.* 66, 203–220. https://doi.org/10.1007/BF00372159

Presnall, D. C., G. H. Gudfinnsson and M. J. Walter 2002. Generation of mid-ocean ridge basalts at pressures from 1 to 7 GPa. *Geochim. Cosmochim. Acta* 66, 2073–2090. https://doi.org/10.1016/S0016-7037(02)00890-6

Prior, D. J., A. P. Boyle, F. Brenker *et al.* 1999. The application of electron backscatter diffraction and orientation contrast imaging in the SEM to textural problems in rocks. *Am. Mineral.* 84, 1741–1759. https://doi.org/10.2138/am-1999-11-1204

Putirka, K. 1999. Clinopyroxene + liquid equilibria to 100 kbar and 2450 K. *Contrib. Mineral. Petrol.* 135, 151–163. https://doi.org/10.1007/s004100050503

Putirka, K. D. 2008. Thermometers and barometers for volcanic systems. *Rev. Mineral. Geochem.* 69, 61–120. https://doi.org/10.2138/rmg.2008.69.3

Putirka, K. D., M. Perfit, F. J. Ryerson and M. G. Jackson 2007. Ambient and excess mantle temperatures, olivine thermometry, and active vs. passive upwelling. *Chem. Geol.* 241, 177–206. https://doi.org/10.1016/j.chemgeo.2007.01.014

Rae, A. S. P., M. Edmonds, J. Maclennan *et al.* 2016. Time scales of magma transport and mixing at Kīlauea Volcano, Hawai'i. *Geology* 44, 463–466. https://doi.org/10.1130/G37800.1

Roedder, E. 1984. Fluid Inclusions. *Reviews in Mineralogy* Vol. 12, Mineralogical Society of America, 644 pp.

Schipper, C. I. and Y. Moussallam 2017. Temporal redox variation in basaltic tephra from Surtsey volcano (Iceland). *Bull. Volcanol.* 79, 1–5. https://doi.org/10.1007/s00445-017-1156-2

Self, S., L. Keszthelyi and T. Thordarson 1998. The importance of pahoehoe. *Annu. Rev. Earth Planet. Sci.* 26, 81–110. https://doi.org/10.1146/annurev.earth.26.1.81

Shea, T., F. Costa, D. Krimer and J. E. Hammer 2015. Accuracy of timescales retrieved from diffusion modeling in olivine: A 3D perspective. *Am. Mineral.* 100, 2026-2042. https://doi.org/10.2138/am-2015-5163

Shorttle, O. and J. Maclennan 2011. Compositional trends of Icelandic basalts: Implications for short-length scale lithological heterogeneity in mantle plumes. *Geochem. Geophys. Geosys.* 12, Q11008. https://doi.org/10.1029/2011GC003748

Sigmarsson, O. 1996. Short magma chamber residence time at an Icelandic volcano inferred from U-series disequilibria. *Nature* 382, 440-442. https://doi.org/10.1038/382440a0

Sigmarsson, O., I. Vlastelic, R. Andreasen *et al.* 2011. Remobilization of silicic intrusion by mafic magmas during the 2010 Eyjafjallajökull eruption. *Solid Earth* 2, 271–281. https://doi.org/10.5194/se-2-271-2011

Sigmundsson, F., S. Hreinsdóttir, A. Hooper *et al.* 2010. Intrusion triggering of the 2010 Eyjafjallajökull explosive eruption. *Nature* 468, 426–430. https://doi.org/10.1038/nature09558

Sigurdsson, I. A., S. Steinthorsson and K. Grönvold 2000. Calcium-rich melt inclusions in Cr-spinels from Borgarhraun, northern Iceland. *Earth Planet. Sci. Lett.* 183, 15–26. https://doi.org/10.1016/S0012-821X(00)00269-7

Spice, H. E., J. G. Fitton and L. A. Kirstein 2016. Temperature fluctuation of the Iceland mantle plume through time. *Geochem. Geophys. Geosys.* İ7. https://doi.org/10.1002/2015GC006059

Steinthórsson, S. 1964. The ankaramites of Hvammsmuli. *Acta Nat. Islandica* 2, 1–31.

Steinthorsson, S. 1972. The opaque mineralogy of Surtsey. *Surtsey Res. Prog. Rep.* 6, 152–157.

Stolper, E. 1980. A phase diagram for mid-ocean ridge basalts: Preliminary results and implications for petrogenesis. *Contrib. Mineral. Petrol.* 74, 13–27. https://doi.org/10.1007/BF00375485

Tarasewicz, J., B. Brandsdóttir, R. S. White *et al.* 2012a. Using microearthquakes to track repeated magma intrusions beneath the Eyjafjallajökull stratovolcano, Iceland. *J. Geophys. Res. Solid Earth* 117, 1–13. https://doi.org/10.1029/2011JB008751

Tarasewicz, J., R. S. White, A. W. Woods *et al.* 2012b. Magma mobilization by downward-propagating decompression of the Eyjafjallajkull volcanic plumbing system. *Geophys. Res. Lett.* 39, 1–5. https://doi.org/10.1029/2012GL053518

Thy, P. 1983. Spinel minerals in transitional and alkali basaltic glasses from Iceland. *Contrib. Mineral. Petrol.* 83, 141–149. https://doi.org/10.1007/BF00373087

Thy, P. 1991a. High and low pressure phase equilibria of a mildly alkalic lava from the 1965 Surtsey eruption: Implications for the evolution of mildly alkalic and transitional basalts in the south-eastern propagating rift zone of Iceland. *Lithos* 26, 253–269. https://doi.org/10.1016/0024-4937(91)90032-G

Thy, P. 1991b. High and low pressure phase equilibria of a mildly alkalic lava from the 1965 Surtsey eruption: Experimental results. *Lithos* 26, 223–243. https://doi.org/10.1016/0024-4937(91)90030-O

Toplis, M. J. 2005. The thermodynamics of iron and magnesium partitioning between olivine and liquid: Criteria for assessing and predicting equilibrium in natural and experimental systems. *Contrib. Mineral. Petrol.* 149, 22–39. https://doi.org/10.1007/s00410-004-0629-4

Tormey, D. R., T. L. Grove and W. B. Bryan 1987. Experimental petrology of normal MORB near the Kane Fracture Zone: 22°–25° N, mid-Atlantic ridge. *Contrib. Mineral. Petrol.* 96, 121–139. https://doi.org/10.1007/BF00375227

Ubide, T., S. Mollo, J. Zhao *et al.* 2019. Sector-zoned clinopyroxene as a recorder of magma history, eruption triggers, and ascent rates. *Geochim. Cosmochim. Acta* 251, 265–283. https://doi.org/10.1016/j.gca.2019.02.021

Welsch, B., J. Hammer, A. Baronnet *et al.* 2016. Clinopyroxene in postshield Haleakala ankaramite: 2. Texture, compositional zoning and supersaturation in the magma. *Contrib. Mineral. Petrol.* 171, 1–19. https://doi.org/10.1007/s00410-015-1213-9

Winpenny, B. and J. Maclennan 2011. A partial record of mixing of mantle melts preserved in Icelandic phenocrysts. *J. Petrol.* 52, 1791–1812. https://doi.org/10.1093/petrology/egr031

Wiese, P. K. 1992. *Geochemistry and geochronology of the Eyjafjöll Volcanic System.* Unpubl. MSc Thesis, University of Oregon.

Wolfe, C. J., I. T. Bjarnason, J. C. VanDecar and S. C. Solomon 1997. Seismic structure of the Iceland mantle plume. *Nature* 385, 245–247. https://doi.org/10.1038/385245a0

Yang, H., R. J. Kinzler and T. L. Grove 1996. Experiments and models of anhydrous, basaltic olivine-plagioclase-augite saturated melts from 0.001 to 10 kbar. *Contrib. Mineral. Petrol.* 124, 1–18. https://doi.org/10.1007/s004100050169

Zhang, Y. and D. Cherniak 2010. Diffusion in Minerals and Melts. *Rev. Mineral. Geochem.* https://doi.org/10.2138/rmg.2010.72.2

Paper III

Nikkola P., Thordarson T., Rämö O.T., Heikkilä P. 2019. *Formation of segregation structures in Hafnarhraun pāhoehoe lobe, SW Iceland: a window into crystal–melt separation in basaltic magma.* Bulletin of Volcanology 81:70.

Bulletin of Volcanology (2019) 81:70
https://doi.org/10.1007/s00445-019-1330-9

RESEARCH ARTICLE

Formation of segregation structures in Hafnarhraun pāhoehoe lobe, SW Iceland: a window into crystal–melt separation in basaltic magma

Paavo Nikkola[1,2] · Thorvaldur Thordarson[3] · O. Tapani Rämö[1] · Pasi Heikkilä[1,4]

Received: 12 March 2019 / Accepted: 16 October 2019

Abstract

To gain insights into crystal–melt separation processes during basalt differentiation, we have studied an 8-m-thick pāhoehoe lava lobe from the Hafnarhraun lava flow field in SW Iceland. The lobe has abundant melt segregations, porous cylindrical and sheet-like structures, generally interpreted as separated residual melts of a lava lobe. We divide these melt segregations into three types based on morphology and composition: vesicle cylinders (VC), type 1 horizontal vesicle sheets (HVS1), and type 2 horizontal vesicle sheets (HVS2). Remarkably, the studied VC are not simple residual melts generated by fractional crystallization, but their composition points to removal of plagioclase from the parental lava. HVS1 resemble VC, but have fractionated more olivine (ol) + plagioclase (plg) ± augite and have lost most, if not all, of their olivine phenocrysts. HVS2 are Fe-rich and evolved, corresponding to residual melts after 50–60% fractional crystallization of the lobe. We suggest that the Hafnarhraun VC formed in a two-stage process. Firstly, VC forming residual melt and vapor detached as rising diapirs from ol+plg+melt+vapor mush near the lava base, and later, these VC diapirs accumulated ol phenocrysts and minor plg microphenocrysts in the lava core. HVS1 represent accumulations of VC to the viscous base of the solidifying upper crust of the lobe, and HVS2 formed as evolved vapor-saturated residual melts seeped into voids within the upper crust. Such vapor-aided differentiation, here documented for the Hafnarhraun lava, may also apply to shallow crustal magma storage zones, contributing to the formation of evolved basalts.

Keywords Lava flow · Basalt · Fractional crystallization · Melt segregations · Magmatic differentiation

Introduction

Magmatic differentiation by fractional crystallization is one of the key processes of igneous petrology. However, it is not adequately known how crystals separate from their coexisting melts in various magmatic systems. Various mechanisms of crystal–melt separation have been identified. These include gravitational crystal settling (Darwin 1844), liquid convection (Sparks et al. 1984), and filter pressing (Philpotts et al. 1996). It has also been suggested that exsolution of volatiles drives magmatic differentiation in shallow magma storage zones by pressing residual melts out of crystal–melt mushes (Anderson et al. 1984; Sisson and Bacon 1999; Pistone et al. 2015; Parmigiani et al. 2016). In intrusive bodies, the physical processes of crystal–melt separation have proven difficult to study (cf. Wilson 1993), as the emplacement of differentiated magmatic intrusions is often complex and may involve multiple evolutionary stages (e.g., Gibb and Henderson 1992, 2006; Menand 2011). The emplacement mechanism of

Editorial responsibility: R.J. Brown

Electronic supplementary material The online version of this article (https://doi.org/10.1007/s00445-019-1330-9) contains supplementary material, which is available to authorized users.

✉ Paavo Nikkola
paavo.nikkola@helsinki.fi

[1] Department of Geosciences and Geography, Geology and Geophysics Research Group, University of Helsinki, PO Box 64, FI-00014 Helsinki, Finland

[2] Nordic Volcanological Center, Institute of Earth Sciences, Sturlugata 7, 101 Reykjavík, Iceland

[3] Faculty of Earth Sciences, University of Iceland, Sturlugata 7, 101 Reykjavík, Iceland

[4] Geological Survey of Finland, PO Box 96, FI-02151 Espoo, Finland

Published online: 25 November 2019

pāhoehoe lavas, however, is well-documented (Self et al. 1998) owing to detailed field observations of effusive eruptions (Hon et al. 1994; Hamilton et al. 2013) and abundant research conducted on solidified pāhoehoe lavas exposed along eroded cliffs, road cuts, and quarry walls (e.g., Walker 1991; Self et al. 1996; Thordarson and Self 1998; Hartley and Thordarson 2009). A well-understood emplacement mechanism, robust control on P–T conditions of crystallization, and limited size make pāhoehoe ideal for the study of crystal–melt separation in basalts.

Emplacement of a pāhoehoe sheet lobe can be viewed through a series of steps, outlined herewith (see Hon et al. 1994; Thordarson and Self 1998; Self et al. 1998, for details). When a lobe of hot molten lava breaks out, either directly from the transport system (i.e., lava tube) or from the margins of an existing lobe, its outer surface quenches against the cold surrounding and envelopes the lobe with a viscous and stretchable skin. Given that the newly formed stiff outer layer of the lobe can withstand the pressure of the incoming magma, the lobe starts to grow by continued flow of magma into it. This growth, called lava inflation (Walker 1991), often multiplies the original lobe thickness, so that a lobe initially some decimeters thick can become several meters high (Hon et al. 1994). During inflation, the upper part of the lobe gradually solidifies towards the lobe interior. Due to the internal replenishment in hot magma and efficient insulation provided by the solid upper part of the lobe (cf. Harris and Rowland 2009), the lobe interiors may stay nearly liquid for months to years, thus providing a setting for magmatic differentiation to occur.

Solidified pāhoehoe sheet lobes typically consist of three structural units: basal crust, lava core, and upper crust (e.g., Self et al. 1996; Thordarson and Self 1998; Self et al. 1998). The borders of these units are marked by changes in vesiculation, jointing style, and crystallinity. The basal crust, next to the quenched base of the lobe, usually contains vesicular hypohyaline to hypocrystalline lava, often characterized by elongated, pipe-like vesicles (pipe-vesicle, cf. Walker 1987). The crystallinity of the basal crust gradually increases upwards until the lava transitions to massive, sparsely jointed, macrovesicle poor and holocrystalline lava core (Self et al. 1998). Above the lava core is the upper crust that is generally composed of jointed and highly vesicular (e.g., 20–35 vol% macrovesicles, Thordarson and Self 1998) lava characterized by repetitive horizontal banding of varying vesicle sizes (Self et al. 1998). The uppermost surface of the upper crust, usually few millimeters in thickness, is the quenched glassy top selvage of pāhoehoe that can exhibit "ropy" surface folding. The critical realization made from these structural units is that the lava core represents the dominantly liquid part, while the upper and basal crusts are the solidifying component of the lobe that grew in thickness during lobe emplacement (e.g., Self et al. 1996; Thordarson and Self 1998; Hartley and Thordarson 2009). The accretion of upper crust occurs through conductive cooling of the lobe and is continuous throughout the lobe emplacement (Hon et al. 1994), and hence, the upper crust can attain the thickness of several meters. In turn, the basal crust is typically thin (10–35 cm) irrespective of the height of the upper crust, which has been explained by magma flux-induced thermal–mechanical erosion next to lava base (Thordarson and Self 1998; Hartley and Thordarson 2009).

Besides the primary structural units, many pāhoehoe sheet lobes host melt segregations, which are vesicular (20–40%) and chemically distinct structures, typically interpreted as separated residual melts of the lava lobe (Anderson et al. 1984; Goff 1996; Rogan et al. 1996; Caroff et al. 2000; Stephenson et al. 2000; Martin and Sigmarsson 2007; Hartley and Thordarson 2009; Sigmarsson et al. 2009; Kuritani et al. 2010). Within the lava core, melt segregations occur as vertical vesicular cylinders, i.e., vesicle cylinders (VC) that often transect the whole lava core from the basal crust to the upper crust (Hartley and Thordarson 2009; Kuritani et al. 2010). In turn, near the top of the lava core and in the upper crust, segregations usually occur as horizontal vesicular sheets, i.e., horizontal vesicle sheets (HVS), and as fillings in large vesicles, i.e., in megavesicles (Thordarson and Self 1998). Melt segregations are typically enriched in incompatible elements relative to the lava surrounding them and thus crystallized from more evolved liquids (Goff 1996; Martin and Sigmarsson 2007; Hartley and Thordarson 2009; Sigmarsson et al. 2009), although VC with more primitive (magnesian) compositions than the host lava have also been reported (Kuritani et al. 2010).

At least three physical models have been suggested to explain the separation of residual melts and formation of VC in pāhoehoe lavas: vapor differentiation (Goff 1996), Rayleigh–Taylor instability near the base of the lava (Costa et al. 2006), and mushy convection (Fowler et al. 2014). In vapor differentiation, coalescence of bubbles near the partly crystalline base of the lobe results in the formation of proto-cylinders (Manga and Stone 1994). When these proto-cylinders begin to rise, the intercrystalline melt within the partly crystalline basal crust migrates, via gas filter-pressing (Anderson et al. 1984), towards the ascending proto-cylinders (that are regions of low pressure) and VC are formed. In the Rayleigh–Taylor instability model, VC are consequential to accumulation of vapor-enriched interstitial melt above the crystallizing base of the lava flow from which VC ascend, if sufficiently stiff and buoyant, as diapirs to the liquid lava core due to Rayleigh–Taylor instability (Costa et al. 2006). In the mushy-convection model, VC are consequential to a positive feedback between velocity and permeability in crystallizing lava (Fowler et al. 2014). Gas bubble-growth in partly crystalline lava increases local permeability (increased volume of gas and silicate melt in relation to crystals), which enhances local buoyant upward

flow (velocity). This, in turn, concentrates evolved intercrystalline melt to the loci of the flow lowering the local liquidus temperature, and as the lower liquidus temperature decreases the rate of crystallization, it enhances permeability and upward flow even further (Fowler et al. 2014). This positive feedback loop may result in VC formation.

Varying models of formation have also been proposed for HVS. Firstly, they have been interpreted as accumulations of VC at the base of the downward moving cooling front of the lava, which is equal to the base of the upper crust (Goff 1996; Thordarson and Self 1998; Stephenson et al. 2000; Hartley and Thordarson 2009; Sigmarsson et al. 2009). Secondly, they have been understood as interstitial melts that fill subhorizontal fractures in the upper lava flow (Greenough et al. 1999; Kuritani et al. 2010), comparable to the proposed formation mechanism of segregation sheets in intrusions (Marsh 2002). Thirdly, HVS formation in response to the compaction of the lava core (Philpotts et al. 1996) has been suggested.

These varying models of segregation formation imply that (i) the origin and emplacement of melt segregations in pāhoehoe are not adequately understood and (ii) segregation structures are possibly formed via several mechanisms. A quarry in the Hafnarhraun lava flow field, SW Iceland (Fig. 1), offers an outstanding site for investigation of segregations, as here a thick (7–8.5 m) pāhoehoe lava lobe that hosts abundant VC and HVS is dissected approximately parallel to its crest by the working face of the quarry. We thus use this site to describe the segregation structures in detail and compile a model of differentiation for this lava lobe. We also discuss the significance of these findings to the improved understanding of related processes of basalt differentiation in crustal magma chambers.

Geological setting

The neovolcanic rift zones of Iceland are characterized by abundant tholeiitic to olivine tholeiitic basalts erupted from fissure segments, lava shields, shield volcanoes, and stratovolcanoes (Thordarson and Larsen 2007). Pāhoehoe sheet flows

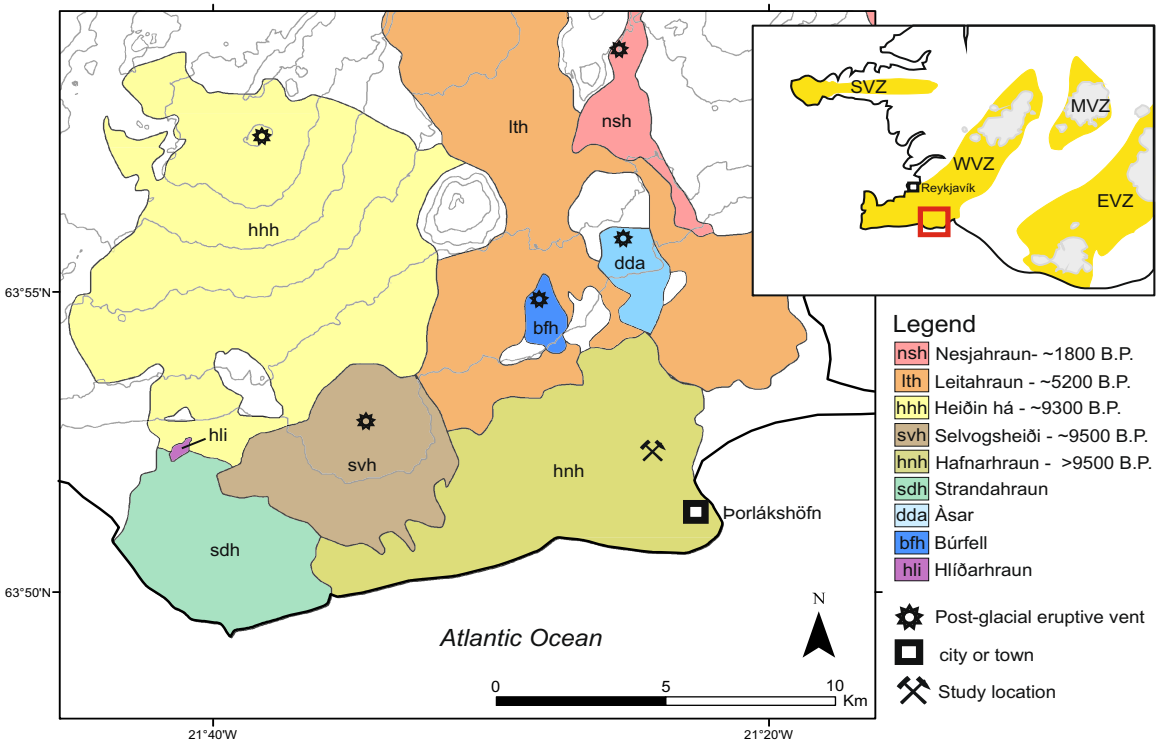

Fig. 1. Geological map of the post-glacial lava units around the Hafnarhraun lava field in SW Iceland with the location of the studied lava lobe marked. Hliðahraun, Búrfell, and Ásar are picritic; the other lava units are olivine tholeiitic basalts. Topographic contours are at 100 m intervals. Glaciers and currently active volcanic zones of Iceland are shown in inset, SVZ = Snæfellsnes Volcanic Zone, WVZ = Western Volcanic Zone, MVC = Middle Volcanic Zone, and EVZ = Eastern Volcanic Zone. Modified after Sinton et al. (2005), Eason et al. (2015), and Saemundsson et al. (2010)

are by far the dominant lava morphology but a ā lavas are found as well (e.g., Rossi 1997; Thordarson and Höskuldsson 2008; Pedersen et al. 2017). We investigated the internal structure of pāhoehoe from a quarried lava-rise plateau, topographically elevated by 3–5 m in comparison with its surroundings, at the Hafnarhraun lava flow field, Western Volcanic Zone of Iceland (Fig. 1). The outcrop segment examined is a 7–8.5-m-high quarry wall that dissects an elongated pāhoehoe lobe approximately along its crest.

The Hafnarhraun lava flow field is composed of pāhoehoe flow lobes with abundant lava tubes and tumuli. Sinton et al. (2005) defined Hafnarhraun as a separate unit from the neighboring Heiðin há and Leitahraun lava flow fields. The exact age of the Hafnarhraun is unknown, although it is clearly postglacial (younger than ~ 13 ka) and older than the neighboring Heiðin há lava flow field (Jónsson 1978), for which ^{14}C ages indicate a maximum age around 10.3 ka (Sinton et al. 2005) and ^{3}He exposure age a minimum of ~ 9.3 ka (Eason et al. 2015).

Materials and methods

Twenty-three rock samples were analyzed from the exposed section of the Hafnarhraun lava lobe. The sample set includes pieces of the upper crust (5 samples), basal crust (1 sample), VC (2 samples), HVS (9 samples), and lava core (6 samples). The lava core and the quenched top selvage of the lava flow were sampled in abundance to quantify chemical variation in the host lava outside the segregations. Two samples of the extensive lowermost HVS were taken 5 m apart to evaluate homogeneity of the unit.

The major and trace element composition of the samples was analyzed with PANalytical Axios mAX 4kW WD-XRF from glass beads at the Department of Geosciences and Geography, University of Helsinki. The rock samples were crushed to chips (2–5 mm in diameter) using an iron-jawed crusher, wet-sieved with deionized water to reach the 1–5 mm fraction, and fine-powdered with agate-mill. Glass beads were fused using a sample-flux ratio of 1:10 (0.600 g ± 1 mg sample and 6.000 g ± 1 mg Li-borate ultrapure flux: 49.5 wt% $Li_2B_4O_7$, 49.5 wt% $LiBO_2$, and 1.0 wt% LiBr). The measurement application in SuperQ 5 software was set up for minimized line-overlap issues (maximum accuracy) and calibrated with 20 basalt to granite natural rock certified reference material (CRM) standards that were prepared identically to the unknown samples. The application contained corrections for background, selected line-overlaps, and a fixed-alpha matrix correction table that was calculated for andesitic composition. A total analysis time of 2.5 h per sample was used for high precision results. Sample 33TH15 was repetitively analyzed for 20 times, which revealed standard deviations of < 0.05 wt% for major oxides (cf. Online Resource 1).

To evaluate the amount of mineral phases and vesicles in various structures within the lava lobe, 1.5 × 2.5 cm areas in six thin section samples were point counted (600 points in total) with a standard electromechanical point counter (cf. Table 1). In addition, the composition of rock-forming minerals was determined by using a JEOL JXA-8230 electron microprobe at the University of Iceland. In total, 192 spots were measured from thin sections of four samples (11TH15-G, 11TH15-D, 33TH15, and 35TH15), 75 from plagioclase, 52 from olivine, and 65 from clinopyroxene (cf. Online Resource 1). Beam current and acceleration voltage were set at 15 nA and 15 kV, respectively. An electron beam diameter of 5 μm was used for plagioclase analyses, and a focused beam when measuring clinopyroxene and olivine compositions. To check for instrumental drift, crystals of known composition were analysed in regular intervals.

To understand the formation of the segregation structures, we modelled the fractional crystallization of the host lava using COMAGMAT-5.2.2. (Ariskin 1999; Ariskin et al. 2018) software that utilizes phase equilibria to calculate phase compositions in mafic silicate melts. All calculations were performed at FMQ (the fayalite–magnetite–quartz buffer), at 1 atm crystallization conditions, and the model of Kress and Carmichael (1991) was used to calculate the activities of Fe^{3+} and Fe^{2+} species in the melt phase. We also utilized Rayleigh fractionation (Rayleigh 1896) of incompatible elements to evaluate the amount of fractional crystallization required in the host lava to generate segregations. According to Rayleigh fractionation, if an element is incompatible to crystallizing phases, its content in residual liquid (CL) is the element content in initial host lava (CH) divided by liquid fraction. Hence, the crystal fraction (FC) at the time of melt separation can be calculated as FC = 1 − (CH/CL).

Hafnarhraun pāhoehoe lobe

Internal structure

The exposed internal structure of the lava lobe resembles that of a pāhoehoe sheet lobe, i.e., the basal crust, the lava core, and the upper crust (Fig. 2a) can all be identified, although here the lava crust is unusually thick, approximately ~ 60% of the 7–8.5 m lobe thickness. In addition, the exposed lobe hosts abundant VC and HVS melt segregations.

The base of the pāhoehoe lobe, the basal surface, is quenched basaltic glass (tachylite) resting directly on an earlier pāhoehoe lobe (Fig. 2b). The basal crust is 10–20-cm-thick and contains an abundance of pipe vesicles (cf. Walker 1987). The pipe vesicles are present in clusters, and they seem to transform to VC that extend into the lava core above (Figs.

Table 1 Point counting results, vesicularity and modal mineralogy (vol%), of units within Hafnarhraun pāhoehoe lobe

	Lava core	Basal crust	VC	HVS1	HVS1	HVS2
Sample ID	11TH15-G	49TH16	11TH15-D	31TH15	33TH15	35TH15
Height (m)[a]	1.7	0	1.7	3	4.55	4.1
Porosity (%)	12	15	33	30	37	23
Ol-ph	11	6	13	5	0	0
Ol	8	4	7	5	6	0
Plg	43	21	42	46	42	33
Cpx	28	0	31	30	34	33
Oxides	5	0	3	8	9	13
Glass	5	69	3	6	9	20

[a] Sample height from the bottom of the lava flow (max 8 m)

VC vesicle cylinder, *HVS1* type 1 horizontal vesicle sheet, *HVS2* type 2 horizontal vesicle sheet, *Ol-ph* olivine phenocryst, *Ol* groundmass olivine, *Plg* plagioclase, *Cpx* clinopyroxene

2b and S-2 in Online Resource 2). The lava core is approximately 3-m-thick and comprised of massive lava with numerous VC commonly transcending the core (Figs. 2a, b and S-3 in Online Resource 2). At a height of 3 m, the VC connect to a 4–7-cm-thick HVS with a lateral extent of ~ 15 m (Fig. 2a). Above this horizon, we define the boundary between lava core and upper crust (height = ~ 3.15 m), i.e., below this level, the lava was mostly liquid when the input of fresh magma into the lobe came to halt. This is supported by the change in jointing and vesiculation in the lava and by the fact that continuous VC are nonexistent above this level. The lower 3 m of the lava crust is poorly vesicular, but contains multiple MV and HVS (Figs. 2a and S-4 in Online Resource 2). The top 2 m of the upper crust, in turn, is highly vesicular, and variations in vesicle sizes define horizontal banding, as common in pāhoehoe (Self et al. 1998). The very top of the lobe is defined by up to 1-cm-thick glassy selvage and often features well-preserved ropy domains. Jointing in the examined lava section is dominantly uneven and blocky, especially in the lava core (Fig. 2a). Systematic vertical jointing becomes less evident with depth in the lobe, being the strongest at the top 2 m of the flow, and sparse and often curved in the lava core. Maximum horizontal jointing is present in the lower parts of the upper crust (Fig. 2a).

Melt segregations in the lava core and upper crust differ from the host lava by their high vesicularity (23–33 vol%) and darker color (Fig. 2). The boundaries between the host lava and the segregations are sharp (Fig. 2c, d), whereas the vesicularity in the upper crust has a gradational boundary to the underlying lava. VC are continuous cylindrical structures that extend from the basal crust to the lowermost extensive HVS that is 3 m above the lava base. In the lowermost 0.7 m of the lava core, the VC are inclined in the direction of flow (Fig. 2b). Above this level, they are vertical and their diameter varies relative to their height in the lobe: 1 cm close to the base of the crust (Fig. 2b) and ~ 3–4 cm at 2 m height (Fig. 2c). VC can locally occupy 10–22% of the surface of the quarry wall in the lava core, but they are scarce above the lowermost HVS (i.e., above ~ 3 m), with only one discontinuous VC-like bubble trail, which was not sampled, found from the upper crust. In the upper crust, the abundant HVS are at most 3 m in lateral extent and 35 cm in height, and they often have a pod-like character with thick center and tapered edges (Figs. S-4 and S-5 in Online Resource 2). Unlike the laterally extensive lower-most HVS that is linked to the VC in the lava core, there is no visible connection between HVS in the upper crust and the underlying segregation system at least on the plane of the quarry face.

HVS within the Hafnahraun lava lobe can be divided into two types based on their petrography and whole-rock chemistry: less-evolved type 1 HVS (HVS1) and more-evolved type 2 HVS (HVS2). In outcrop, we could not distinguish these two sheet types from each other, although hand samples of HVS2 are slightly darker due to their finer, often microcrystalline, groundmass (Fig. 3f). The lowermost extensive HVS is of type 1, but otherwise, HVS1 and HVS2 are located randomly in the upper crust. Both can contain overlying megavesicles. In one instance, HVS2 (sample 34TH15-B) was found overlying HVS1 (sample 34TH15-A). We identified these two HVS from each other only during sample preparation due to the darker tone of the overlying HVS2 (Fig. S-6 in Online Resource 2).

Petrography and mineralogy

Point counting results of mineral phases in the different lithological units are shown in Table 1, and photomicrographs of the respective units are given in Fig. 3. Olivine, plagioclase, and clinopyroxene compositions in the lava lobe are illustrated in Fig. 4 and given in Online Resource 1.

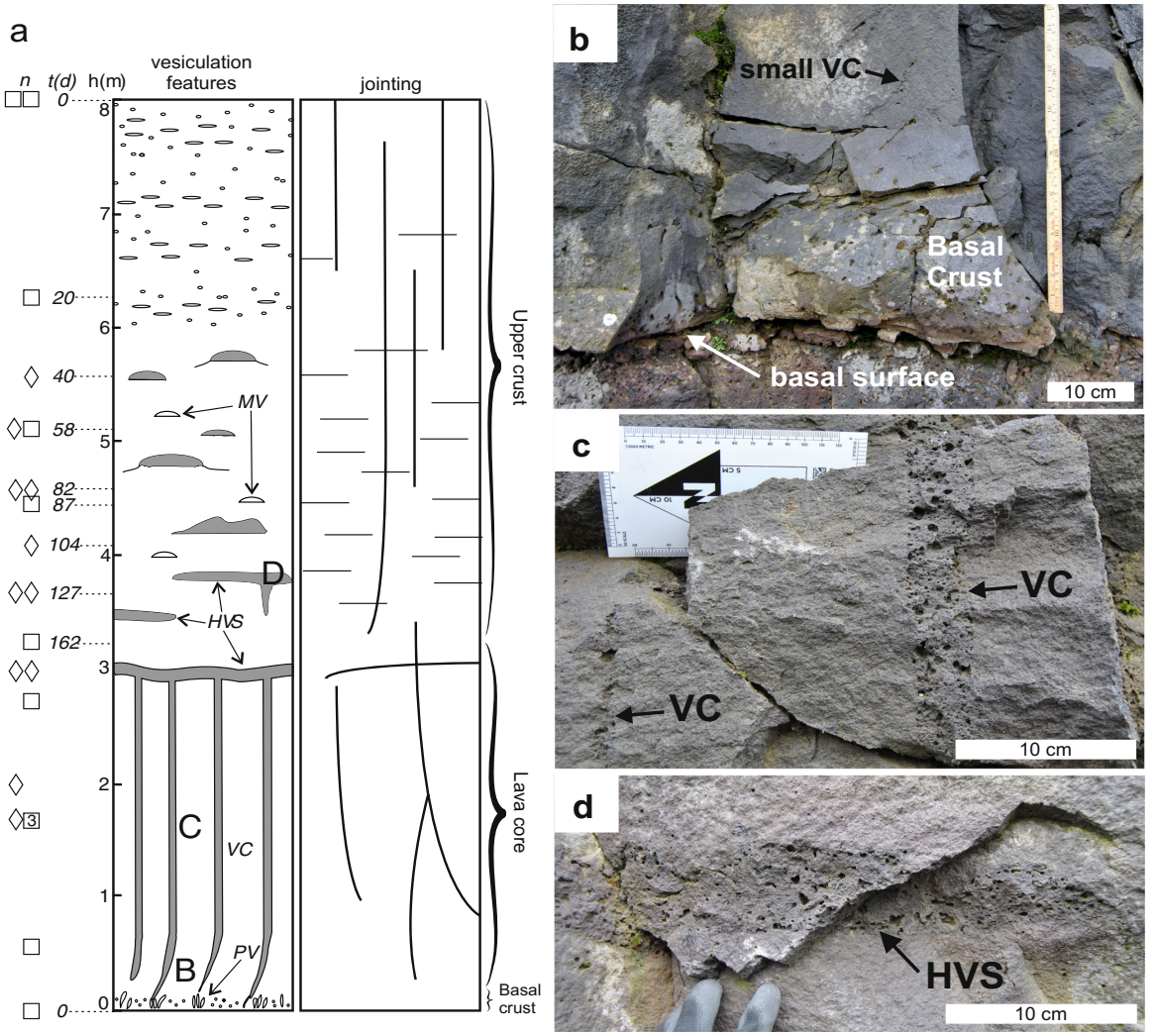

Fig. 2 **a** Simplified log of the Hafnarhraun pāhoehoe lobe. On the left side of the log, location of samples (*n*), estimated time (*t*, in days) of solidification after lobe emplacement following the Hon et al. (1994) model (see the "Discussion" section), and approximate height (*h*, in meters) from the bottom of the lava lobe are shown. Squares depict lava core and crust samples, diamonds segregation samples. Left panel gives the position of photographs **b**, **c**, and **d** and depicts vesiculation features with vesicle cylinders (VC) and horizontal vesicle sheets (HVS) marked in gray. MV and PV refer to megavesicles and pipe vesicles, respectively. Right panel shows jointing features formed during cooling and emplacement of the lava. **b** Basal crust with pipe vesicles, basal surface, and small VC. **c** Vesicle cylinders (VC). **d** Horizontal vesicle sheet (HVS)

The quenched basal selvage of the Hafnarhraun lava lobe is hypohyaline with 4 vol% olivine phenocrysts and varying amounts of 50–300-μm-long plagioclase microphenocrysts and small (sub 100 μm in diameter) vesicles in a glassy tachylite groundmass (Fig. 3a). Occasionally, olivine phenocrysts and plagioclase microphenocrysts form glomerocrysts (Fig. 3a). The average size of plagioclase microphenocrysts increases, and the groundmass becomes increasingly crystalline away from the basal contact. Plagioclase microphenocrysts do exist even at the very bottom contact of the lava, implying plagioclase crystallization before the lava flow came to halt. The vesicle size in the basal crust is also larger higher up near the lava core so that up to 1 cm vesicles are found 2 cm from the quenched basal contact.

The holocrystalline lava core contains 11 vol% olivine phenocrysts in a groundmass featuring a well-developed subophitic texture of Ca-plagioclase and augite along with groundmass olivine, ilmenite, and magnetite (Fig. 3b).

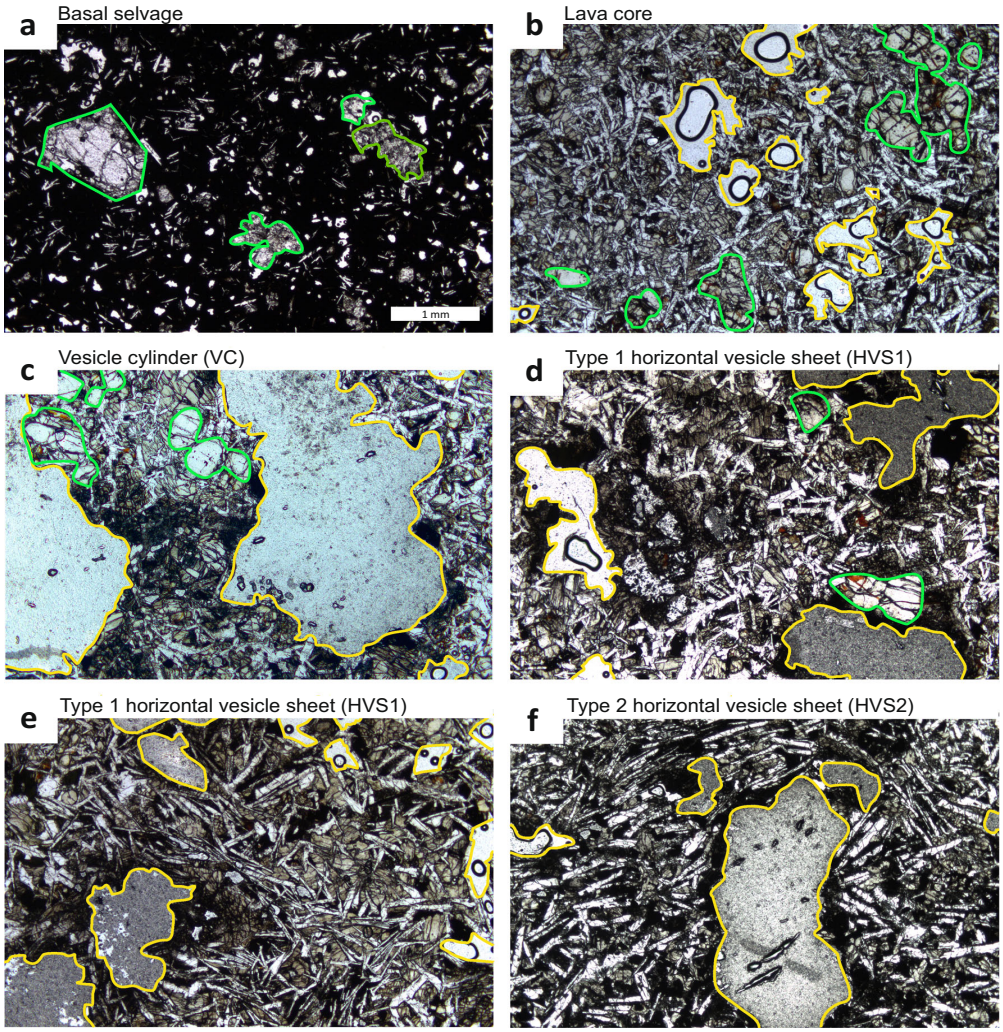

Fig. 3. Photomicrographs in plane-polarized light showing textures of units in the Hafnarhraun lava lobe. **a** Basal selvage of the basal crust (sample 49TH16). **b** Lava core (sample 11TH15-G). **c** Vesicle cylinder (VC, sample 11TH15-D). **d** Type 1 horizontal vesicle sheet (HVS1, 3 m above the base of the lava, sample 31TH15). **e** HVS1 (4.5 m above the lava base, sample 33TH15). **f** Type 2 horizontal vesicle sheet (HVS2, 4.1 m above the lava base, sample 35TH15). For clarity, olivine phenocrysts and microphenocrysts are outlined in green and vesicles in yellow (except for image "**a**" with abundant small vesicles). Scale for all panels is in panel **a**

Irregular-shaped vesicles occupy 12 vol% of the lava core and are typically 0.2–1.0 mm in diameter (Fig. 3b), although rare vesicles up to 5 mm in diameter also exist. Vesicles are commonly mantled by microcrystalline groundmass. There are also some rare (< 0.5 vol%) < 200 μm angular voids and interstitial glass pockets with small anhedral apatite and skeletal magnetite. In the lava core, phenocryst and groundmass olivine crystal cores are $Fo_{77–79}$ and $Fo_{39–69}$, respectively, in composition (Fig. 4a), the plagioclase crystal cores are $An_{65–77}$ (Fig. 4b), and augite compositions vary between $En_{38}Fs_{28}Wo_{34}$ and $En_{47}Fs_{15}Wo_{39}$ (Fig. 4c). Olivine phenocrysts commonly have variably thick $Fo_{29–72}$ rims occasionally grow to the surrounding groundmass partly enclosing tips of plagioclase laths. In all examined samples, segregations included, magnetite shows subsolidus exsolution to ilmenite forming trellis-type lamellae.

The segregations are distinguished from the lava core and crust by abundant rounded vesicles (23–33 vol%), by slightly darker color, and by larger grain size, especially evident when comparing the size of plagioclase laths (Fig. 3c, d, and e). The

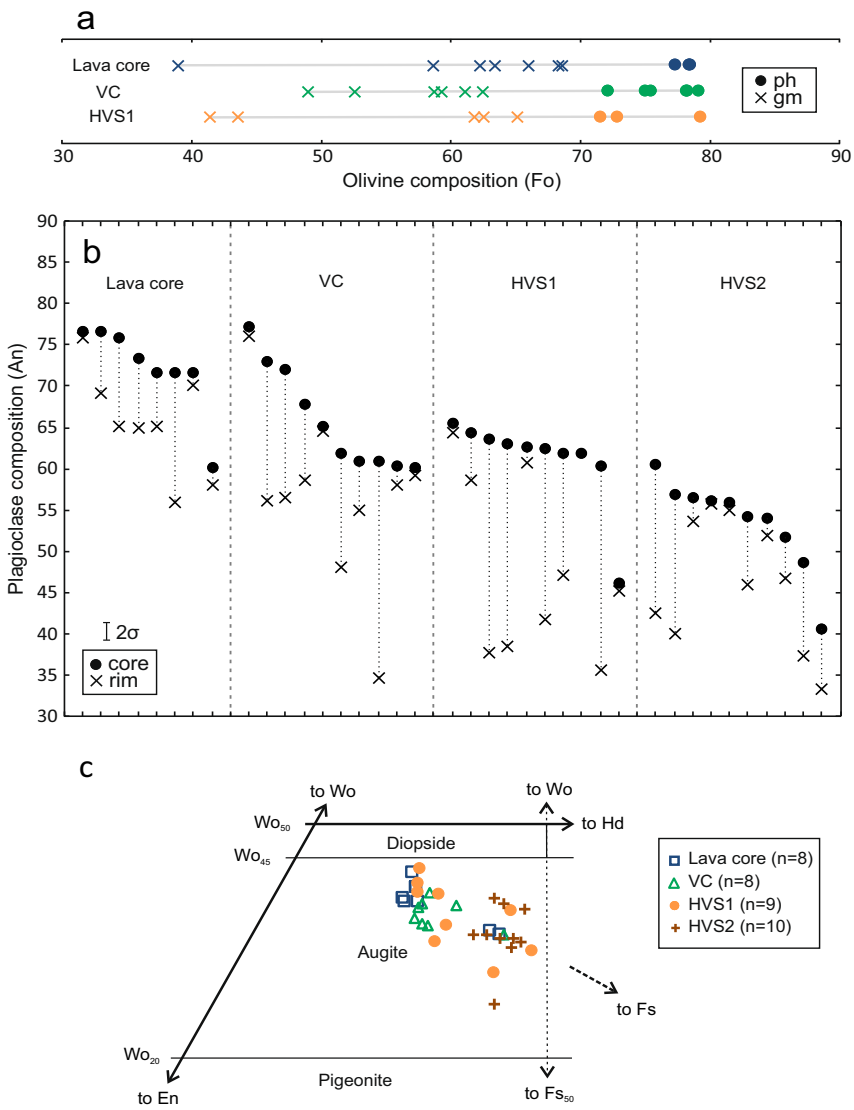

Fig. 4. **a** Variation in forsterite (Fo) content in olivine cores within the Hafnarhraun lava lobe. Phenocryst and groundmass olivine marked with circles and crosses, respectively. Propagated 2σ instrumental error is smaller than the symbol size. **b** Plagioclase composition in different units of the Hafnarhraun lava lobe. Propagated average 2σ instrumental uncertainty of An-content (approximately ± 1 cation %) is illustrated. Crystal cores and rims are marked with circles and crosses, respectively. Rim compositions were analyzed ~ 10–15 μm from the crystal edge. **c** Core compositions of augite crystals in the Hafnarhraun pāhoehoe lava shown in the pyroxene quadrilateral

mineral assemblages in VC and HVS1 are, however, almost identical to those in the lava core with subophitic Ca-plagioclase and augite, and olivine phenocrysts (Table 1, Fig. 3). The amount of olivine phenocrysts decreases from VC (13 vol%) to HVS1 (0–5 vol%). The composition of olivine, plagioclase and augite in the lava core, VC, and HVS1 overlap, although HVS1 seem to lack the most primitive calcic variety of plagioclase ($An_{76–71}$) present in the lava core and VC (Fig. 4b), and augite in HVS1 tends to be more ferrous (Fig. 4c) compared to VC and lava core.

The HVS2 are, on thin section scale, petrographically distinct in comparison with all other units in the lava lobe (Table 1, Fig. 3f). They are nearly devoid of olivine (only a few grains) and display a texture of flow-aligned plagioclase in a groundmass of augite, euhedral magnetite and ilmenite, and microcrystalline glass with skeletal magnetite (Fig. 3f). Plagioclase in HVS2 is relatively sodic ($An_{<63}$, Fig. 4b), and augite crystals in the HVS2 are distinctively Fe-rich ($Fs_{>25}$, Fig. 4c). At the contacts of HVS2 and the host lava, plagioclase laths are aligned parallel to the contact in

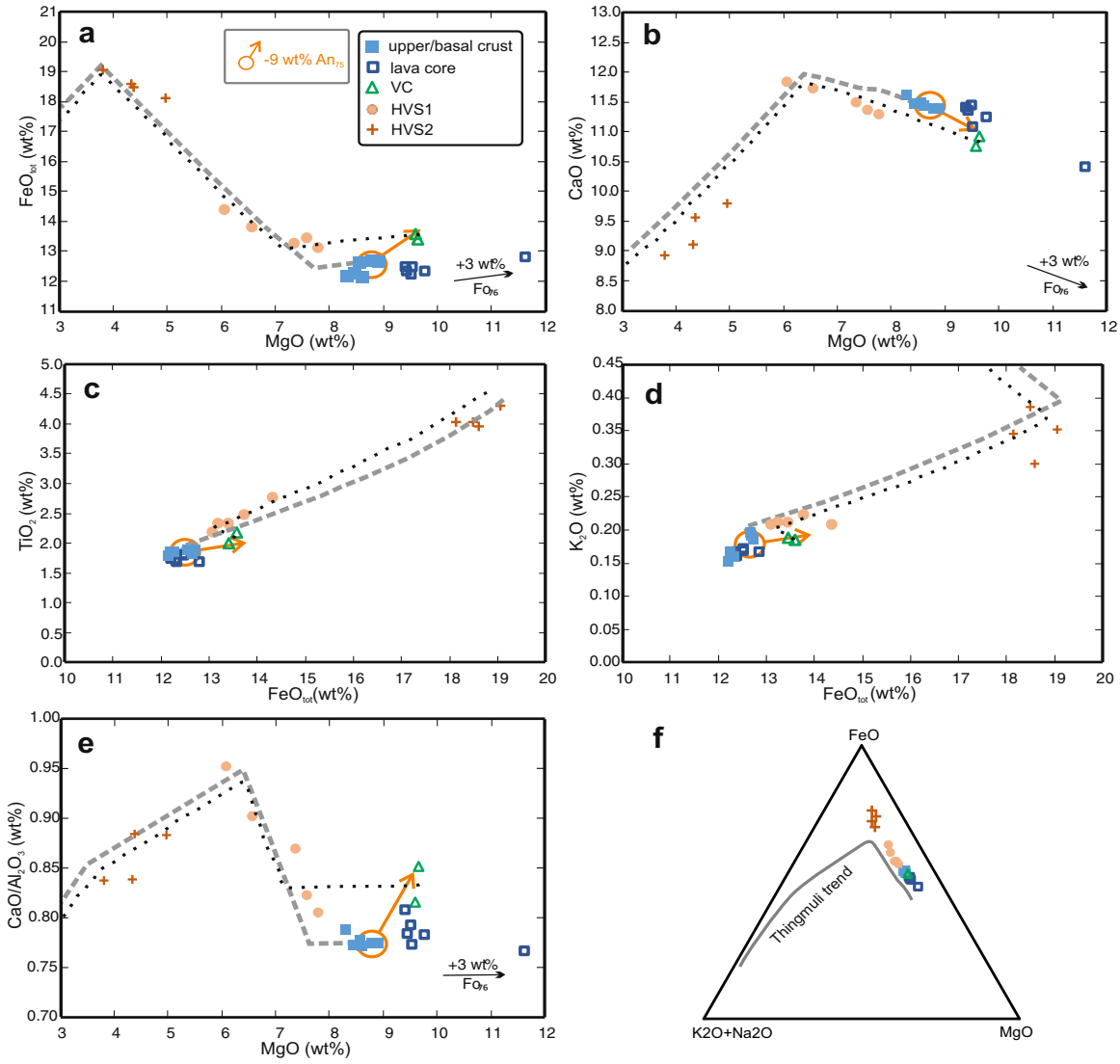

Fig. 5. Major element composition of the Hafrarhraun samples shown in MgO vs. FeO_{tot} (**a**), MgO vs. CaO (**b**), FeO_{tot} vs. TiO_2 (**c**), FeO_{tot} vs. K_2O (**d**), MgO vs. CaO/Al_2O_3 (**e**), and FeO–K_2O+Na_2O–MgO (**f**) diagrams. Instrumental errors (2σ) for the compositions and elemental ratios are smaller than or equal to the symbol size. Calculated residual liquid compositions are marked by gray dashed and black dotted lines for 1 atm fractional crystallization of "host lava" and "VC" initial compositions, respectively. The "host lava" composition corresponds to the average composition of quenched basal surface and upper crust selvage samples, whereas the "VC" composition is the average of VC analyses. Model residual liquids were calculated at 1 atm and at the fayalite-magnetite-quartz oxygen buffer. The effect of 9 wt% plagioclase (An_{75}) fractionation from host lava composition is shown by orange arrow, and the effect of 3 wt% Fo_{76} olivine addition (ol-accumulation vector) is shown by black arrow

microcrystalline matrix. The rare olivine crystals found from HVS2 in the studied thin sections were anhedral and mantled by oxide.

Whole-rock geochemistry

The whole-rock geochemical variation in the Hafnarhraun lobe is illustrated in Fig. 5 and Fig. 6, and the analytical data can be found in Table 2 and Online Resource 1. The lava core is

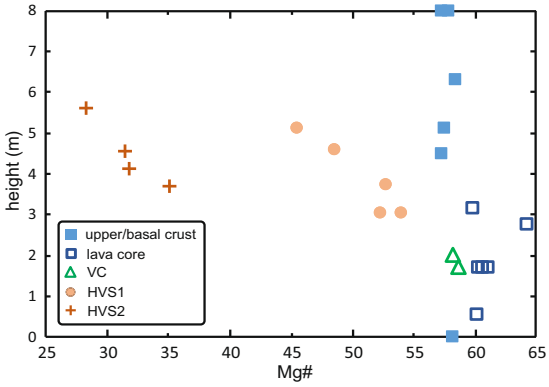

Fig. 6. Height above lava base vs. Mg# (Mg# = molar 100 × Mg/(Mg + Fe^{2+}), Fe^{2+} = 0.9Fe_{tot}) for the Hafnarhraun samples

olivine tholeiite with a magnesium number (Mg# = molar 100 × Mg/(Mg + Fe^{2+}), Fe^{2+} = 0.9Fe_{tot}) of 60–61, with one sample (42TH15) from underneath the extensive lowermost HVS with a more MgO-rich composition (Mg# = 64). The basal and upper crust samples from the top and bottom of the flow have consistently lower Mg# (57–58) than the lava core (Fig. 6).

VC show only slight compositional difference from the lava core or crust samples (Fig. 5, Table 2). Although they are somewhat richer in FeO_{tot}, TiO_2, K_2O, Na_2O, P_2O_3, and V, and poorer in Al_2O_3, CaO, and Cr compared to the lava core, their MgO content and many of the trace elements are nearly the same as in the lava core samples. From the two samples taken from VC, the stratigraphically higher of the two is slightly more ferrous and incompatible element enriched.

HVS1 have Mg# 46–54, whereas HVS2 have Mg# equal or below 35. The compositional gap between these two segregation sheet types is notable in all major elements (Fig. 5). The FeO_{tot} of the HVS1 peak at 14.3 wt%, whereas HVS2 reach 19.1 wt% FeO_{tot}. The HVS2 also have the highest concentrations of incompatible elements, notably Zr, Y, and V, and strikingly low Cr in comparison with other sample types (Table 2). Both HVS1 and HVS2 tend to have more FeO_{tot} and incompatible element upward in the lobe. This is the clearest in the variation in Mg# (Fig. 6), but can also be illustrated by plotting other elements.

Discussion

Time constraints of lava lobe formation

It is crucial to understand the temporal relationships of the units in the lava lobe. According to Hon et al. (1994), the downward solidification of pāhoehoe upper crust is progressive during lava emplacement, and hence, the final thickness of the upper crust (H_c, in meters) can be related to the emplacement time of the lobe (t, in hours) by $t = 164.8 \times H_c^2$. Based on this, the downward solidification of the Hafnarhraun upper crust took around 160 days (Fig. 2a), after which the lava core would have taken about a further month to solidify completely. Consequently, if we interpret that at least the HVS1 represent accumulations of VC to the base of the gradually solidifying upper crust (as usually done, cf. Self 1998), HVS1 higher in the crust must have formed before HVS1 lower in the crust (Fig. 2a). In addition, as the lava core is the last part of the lobe to solidify, segregations within it are the youngest.

Temporal evolution of the host lava

In the studied Hafnarhraun lava lobe, the lava core is more magnesian than the crust (Fig. 6). This compositional variation suggests more olivine in the lava core than in the crust. Addition of ~ 3 wt% of Fo_{76} olivine (the average composition of olivine phenocrysts in the lobe) to the crust delivers the composition of the lava core (olivine-accumulation vector in Fig. 5). Sample 42TH15, taken from the lava core just below the lowest extensive HVS, is particularly rich in MgO (11.7 wt%, Fig. 5), and its composition suggests ~ 10 wt% relative enrichment in olivine. Gravitational settling may have enriched the lava core in olivine phenocrysts during the lifespan of the lobe. Additionally, the lava in the lava core may have been hotter and thus richer in olivine-forming elements than the lava that formed the crust. The lava that formed the crustal selvages had probably cooled and fractionated olivine on transit from the vent. The lava core, however, represents a later phase in the effusive sequence, when lava likely moved within a well-insulated lava tube network. Because of this enhanced insulation (cf. Harris and Rowland 2009), melt in the lava core may have stayed hotter, fractionated less olivine, and remained rich in MgO.

Differentiation of segregations by fractional crystallization

To evaluate whether the melt segregations in the Hafnarhraun pāhoehoe lobe are differentiated melts produced by fractional crystallization of the lava lobe, we modeled the fractional crystallization of the lobe and composition of derivate melts along the liquid line of descent (LLD, Fig. 5) with COMAGMAT-5.2.2. (Ariskin 1999; Ariskin et al. 2018) software. As the non-fractionated initial lava composition, we used the average composition of the quenched top and bottom lava selvages (solid line in Fig. 5), referred as "host lava" herein. As discussed earlier, the chemical variability within lava core and crustal units is controlled by the amount of liquidus olivine (either as phenocrysts or in the melt), which is the first crystallizing phase. Hence, the LLD trajectory is rather indifferent to the selection of initial composition from the available crust and lava core samples. We also calculated the composition of residual melts generated in fractional

Table 2 Major oxide and trace element compositions of units within Hafnarhraun lava lobe

	QBCr	Lava core				Upper crust					QUCr	
Sample ID	49TH16	40TH15	11TH15-H	11TH15-I	11TH15-J	42TH15	43TH15	44TH15	45TH15	47TH15	51TH16	52TH16
h (m)[a]	0.00	0.55	1.70	1.70	1.70	2.75	3.15	4.45	5.10	6.30	8.00	8.00
SiO_2	48.06	47.52	47.64	47.90	47.67	47.02	47.74	48.07	48.12	47.83	47.99	47.88
TiO_2	1.85	1.78	1.67	1.73	1.70	1.68	1.80	1.85	1.85	1.79	1.87	1.88
Al_2O_3	14.69	14.34	14.48	14.44	14.35	13.58	14.14	14.76	14.86	14.85	14.70	14.78
FeO	12.64	12.49	12.33	12.22	12.32	12.81	12.49	12.21	12.29	12.15	12.68	12.63
MnO	0.20	0.21	0.20	0.20	0.20	0.21	0.21	0.20	0.20	0.20	0.20	0.20
MgO	8.90	9.53	9.44	9.50	9.78	11.63	9.41	8.30	8.44	8.61	8.78	8.55
CaO	11.39	11.08	11.35	11.45	11.23	10.41	11.41	11.62	11.46	11.45	11.39	11.48
Na_2O	2.15	2.00	2.00	2.02	2.02	1.90	2.01	1.93	1.84	1.93	2.16	2.17
K_2O	0.19	0.17	0.16	0.17	0.16	0.17	0.17	0.16	0.16	0.15	0.19	0.20
P_2O_5	0.17	0.16	0.15	0.15	0.15	0.15	0.16	0.16	0.16	0.16	0.17	0.17
Mg#	58.3	60.2	60.3	60.6	61.1	64.3	59.9	57.4	57.6	58.4	57.8	57.3
Ba	63	54	53	56	46	63	63	50	68	70	71	69
Cu	157	137	117	129	121	112	127	147	117	119	161	165
Cr	347	357	410	387	385	450	376	329	294	310	346	334
Ni	164	179	175	182	183	254	165	126	135	139	160	151
Sr	173	153	158	164	153	143	157	161	161	160	177	174
Zn	104	98	91	98	101	105	107	100	100	98	103	105
Zr	75	71	68	85	83	74	93	92	104	80	80	81
Rb	3	5	8	3	7	4	8	7	7	5	3	3
Nb	9	11	10	12	11	11	11	11	12	11	8	14
Y	26	32	39	30	34	37	38	41	38	39	27	27
V	364	346	341	353	340	322	355	376	362	358	357	364
Total	100.40	99.42	99.57	99.93	99.74	99.70	99.69	99.41	99.52	99.25	100.29	100.08

	VC		Type 1 HVS					Type 2 HVS			
Sample ID	11TH15-D	32TH15	31TH15	41TH15	34TH15-A	33TH15	25TH15	34TH15-B	35TH15	30TH15	23TH15
h (m)[a]	1.70	2.00	3.00	3.00	3.70	4.55	5.10	3.70	4.10	4.55	5.60
SiO_2	47.95	47.49	48.01	48.67	48.04	48.71	49.33	47.03	47.82	49.11	48.00
TiO_2	1.99	2.18	2.16	2.30	2.30	2.46	2.75	4.03	4.02	3.95	4.30
Al_2O_3	12.82	13.20	14.03	13.22	13.83	13.01	12.44	11.10	10.82	10.86	10.66
FeO	13.42	13.57	13.09	13.22	13.42	13.77	14.35	18.14	18.49	18.60	19.07
MnO	0.22	0.22	0.21	0.23	0.22	0.23	0.24	0.28	0.30	0.28	0.29
MgO	9.64	9.58	7.81	7.37	7.60	6.58	6.08	4.96	4.37	4.32	3.80
CaO	10.92	10.76	11.27	11.48	11.35	11.72	11.83	9.81	9.57	9.10	8.93
Na_2O	2.11	2.10	2.17	2.28	2.20	2.19	2.00	2.45	2.35	1.87	1.85
K_2O	0.19	0.18	0.21	0.21	0.21	0.22	0.21	0.35	0.39	0.30	0.35
P_2O_5	0.18	0.17	0.19	0.20	0.20	0.21	0.22	0.34	0.39	0.33	0.40
Mg#	58.7	58.3	54.2	52.5	52.9	48.6	45.6	35.1	31.9	31.5	28.3
Ba	51	62	50	79	56	61	61	76	108	63	95
Cu	127	116	177	160	150	148	179	189	212	178	241
Cr	267	286	231	169	244	189	177	37	17	23	13

Table 2 (continued)

Ni	172	179	120	96	107	61	47	37	24	30	21	
Sr	148	154	160	159	162	158	172	163	165	167	176	
Zn	105	116	109	106	116	108	125	167	176	173	183	
Zr	98	102	95	100	98	110	130	180	187	218	235	
Rb	8	6	7	4	9	10	5	8	10	6	11	
Nb	13	13	14	13	13	14	16	20	23	25	27	
Y	33	37	41	51	38	45	47	73	79	79	86	
V	408	425	408	442	444	481	524	653	555	526	497	
Total	99.57	99.60	99.30	99.32	99.51	99.25	99.61	98.65	98.68	98.88	97.81	

Measured Ce, La, and U are close to lowest limit of detection and thus not reported

QBCr quenched basal crust, *QUCr* quenched upper crust, *VC* vesicle cylinder, *HVS* horizontal vesicle sheet

[a] Sample height from the bottom of the lava flow (max 8 m)

crystallization of a VC-like initial melt, as these were the best fits for HVS1 compositions (stippled line in Fig. 5). The order of fractionating phases is olivine, olivine + plagioclase, olivine + plagioclase + augite, and olivine + plagioclase + augite + magnetite. The first modeled mineral on liquidus is Fo_{80} olivine that develops to Fo_{78} before An_{78} plagioclase is stabilized. The first modeled augite to fractionate has the composition of $En_{46}Fs_{13}Wo_{40}$. This modeled crystallization assemblage corresponds well to the observed phenocryst and groundmass mineralogy in the Hafnarhraun lava lobe (compare to Fig. 4).

The VC in Hafnarhraun are compositionally nearly similar to the lava core and crust (Fig. 5), and thus differ from the VC reported elsewhere that correspond to residual melts after 36–60% crystallization of the host lava (Rogan et al. 1996; Stephenson et al. 2000; Hartley and Thordarson 2009; Sigmarsson et al. 2009). In fact, the Hafnarhraun VC do not correspond to any likely residual melt produced by fractional crystallization of the host lava, as the expected fractionate from olivine tholeiitic magma always depletes the residual liquid in MgO (Fig. 5). However, crystallizing and removing ~ 9 wt% An_{75} plagioclase from the host lava results in a VC-like composition with relatively high MgO (9.6 wt%) and FeO (13.5 wt%), low CaO (10.8 wt%), and Al_2O_3 (13.01 wt%) along with minor enrichment in incompatible elements (Fig. 5).

The major oxide composition of HVS1 resembles that of VC that were fractionated further and lost most or all of their olivine phenocryst cargo in the process (Fig. 5, stippled line). This is consistent with the fewer olivine phenocrysts in those HVS1 that are positioned higher in the lava lobe. Depending on the initial composition (host lava or VC, solid or stippled line in Fig. 5), our fractional crystallization models produce HVS1-like residual liquids after either 17–38 wt% (host lava) or 11–23 wt% (VC) fractional crystallization. Rayleigh fractionation of TiO_2 and Zr, in turn, suggests host lava crystallinity of 13–39 wt% before segregation of the HVS1 forming residual melt.

HVS2 represent the most fractionated liquids of the analyzed section, and their composition fits that of simple residual melts of the host lava generated by fractional crystallization. The model residual melts attain HVS2-like compositions after ~ 50–60 wt% fractional crystallization from the host lava, corresponding to removal of 12–13 wt% olivine, 24–28 wt% plagioclase, and 12–17 wt% augite (Fig. 5). Correspondingly, relative enrichment in TiO_2, K_2O, and Zr in HVS2 suggests 53–57 wt%, 36–50 wt%, and 56–67 wt% crystallinity in the host lava, respectively, before residual melt segregation.

Co-genetic formation of VC and HVS1

We have shown that VC compositions in Hafnarhraun do not correspond to any expected residual melt produced by fractional crystallization of the host lava. Comparable VC that do

not represent simple differentiated liquids of the host lava have been reported earlier by Caroff et al. (2000) and Kuritani et al. (2010). Caroff et al. (2000) published segregation compositions that included a VC (TB10B) with a composition similar to its host lava. They noted that this VC is cumulative in olivine phenocrysts, but did not discuss its genesis further. Kuritani et al. (2010) reported VC enriched in both incompatible elements and MgO compared to the surrounding lava, and envisioned that these VC were formed by selective fractionation of plagioclase and pyroxene from the lava when olivine-bearing interstitial melt was extracted from partly crystalline lava core. The Hafnarhraun VC are reminiscent of those reported by Kuritani et al. (2010), as selective crystal fractionation applies as a first-order explanation for the composition of Hafnarhraun VC as well.

As we envision it, the simplest, yet probably unrealistic model to explain the composition of Hafnarhraun VC, is illustrated in Fig. 7a. In this model, olivine crystals and residual liquid are separated from a crystal mush near the lower crystallization front of the lava base, while plagioclase (9 wt%) remains in the lava base. This model of genesis, although able to reproduce the detected depletion in plagioclase bearing elements in VC, is problematic because of the indicated low crystallinity of the crystal mush during VC segregation (~ 16 wt%), and we struggle to understand how dense olivine phenocrysts were drawn to the upwelling VC while plagioclase was not. Hence, we propose an alternative model, illustrated in Fig. 7b, in which VC forming residual melt (liquid + vapor) first segregates from olivine + plagioclase + liquid + vapor

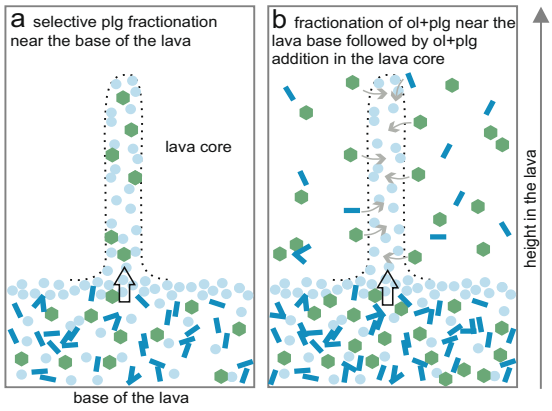

Fig. 7. Illustration of two petrogenetic models for the formation of VC. Pale blue circles are vapor bubbles, green hexagons olivine (ol), and dark blue rectangles plagioclase (plg). Bottom of the images corresponds to the lava base and top to the center parts of the lava core. **a** A model of selective derivation of olivine and vapor saturated interstitial melt from ol+plg+melt+vapor mixture near the base of the lava, i.e., plagioclase is fractionated from the host lava to form VC. **b** Our preferred model of intercrystalline melt sequestering from ol+plg+liquid+vapor mush near the lava base followed by olivine and minor plagioclase addition in the lava core

mush near the lava base and later accumulates olivine phenocrysts and plagioclase microphenocrysts in ascent in the lava core. The segregation of VC melt must have occurred after a minimum of ~ 13–16 wt% fractional crystallization of ~ 6–7 wt% olivine + ~ 7–9 wt% plagioclase near the lava base, and in this scenario, only ~ 5–6 wt% olivine phenocrysts needs to be added to the VC in the lava core to reproduce the observed VC composition. Anyhow, it is likely that the crystallinity near the lava base must have been higher (up to 25%) to allow effectively melt+vapor separation from the crystal phases (Philpotts et al. 1998). In this scenario, more olivine and variable amounts of plagioclase must have accumulated in VC while it was forming in the liquid lava core (Fig. 7b). The detected 13 vol% olivine phenocrysts in VC indicate high amount of olivine accumulation to VC in the lava core, but can also be, at least partly, attributed to the in situ growth of the olivine phenocrysts within VC.

In the two-stage model of VC formation outlined in Fig. 7b, the depletion in plagioclase bearing elements in VC reflects different levels of crystallization between the base of the lava (origin of VC) and lava core (source of entrained crystal assemblage). This model of formation is easier to conceive than selective removal of plagioclase, or selective segregation of olivine and melt from a crystal mush (e.g., Fig. 7a). In addition, the model is consistent with field evidence suggesting VC derivation from near the lava base and strongly supported by the detected high-Fo olivine phenocrysts (Table 1 and Fig. 4a) and Ca-rich plagioclase in VC (Fig. 4b), which are clear indications of crystal accumulation to VC.

Although only the lowermost HVS1 is visibly fed by the underlying VC, the petrographic and compositional similarity of VC and HVS1 suggest that all HVS1 are accumulations of VC material to the bottom of the solidifying upper crust at different stages of lava lobe development. In particular, the similar CaO depletion in HVS1 and VC in comparison with the modeled residual liquids of the host lava (Fig. 5b), and the fact that HVS1-like melts are produced by fractional crystallization of a VC-like initial composition, point to co-genetic relationship between VC and HVS1. The increasing level of differentiation in HVS1 composition higher up in the lava lobe (Fig. 6) may be consequential to lesser contamination with primitive olivine and plagioclase higher in the lobe, and preferential uprising of the residual liquid in comparison with in situ fractional crystallization assemblage in ascending VC.

Our model of two-stage formation of Hafnarhraun VC and their co-genetic relation with HVS1 requires the lava core to have been mostly liquid during VC ascent and HVS1 formation. Whatever the physical process that segregated VC at the base of the lava flow—gas-filter pressing (Anderson et al. 1984), Rayleigh–Taylor instability (Costa et al. 2006), or mushy convection (Fowler et al. 2014)—VC must have later ascended within the lava core in a manner that allowed contamination with primitive mineral phases. In addition, the lava

core must have been fairly liquid to facilitate horizontal spreading of HVS1 below the lower crystallization front of the upper crust.

Formation of HVS2

HVS2 are chemically and mineralogical distinct from VC and HVS1, and their composition suggests that they are segregated residual melts of the lava lobe. The sample 34TH15 with a HVS1-type lower and HVS2-type upper part could be seen suggestive of HVS2-like residual melt derivation from HVS1. However, expulsion of sufficient residual melt from the underlying HVS1 (34TH15-A) to make the HVS2-like upper part (34TH15-B), which is 10–30% of the total sheet volume, should have effectively depleted the underlying HVS1 of incompatible elements and we do not see this. In all, we did not locate incompatible-element-depleted layers of "solid residue" from the upper crust or lava core from which the HVS2 residual melt was removed. Hence, it is likely that the segregation of HVS2 mobilized residual melt over a relatively large area in the lava lobe and the chemical depletion related to removal of HVS2 melt was widely distributed. HVS2 likely formed at a late stage of lava flow cooling, when residual melts of the lava lobe seeped into megavesicles and other voids within the upper crust by gas-filter pressing (Anderson et al. 1984) or other mechanism. Megavesicles are very common in the top part of HVS1, and this could explain why HVS2 formed directly on the top of HVS1 in sample 34TH15.

Differentiation of Hafnarhraun pāhoehoe lobe

A model of the evolution of the Hafnarhraun lava lobe is shown in Fig. 8. During periods when lava effusion within the lobe shortly stalls or weakens, VC form in response to the separation of vapor-saturated liquids from the solidifying lava base and act as sites of material transport from the bottom to the top of the lava core. During these magmatic lulls, potentially extensive HVS1 are generated as VC-fed material accumulates beneath the lower solidification front of the upper crust (Fig. 8c). However, only a small portion of the HVS1 are preserved in the Hafnarhraun lava flow, as pulses of new magma entering the lava tube system occasionally flush the

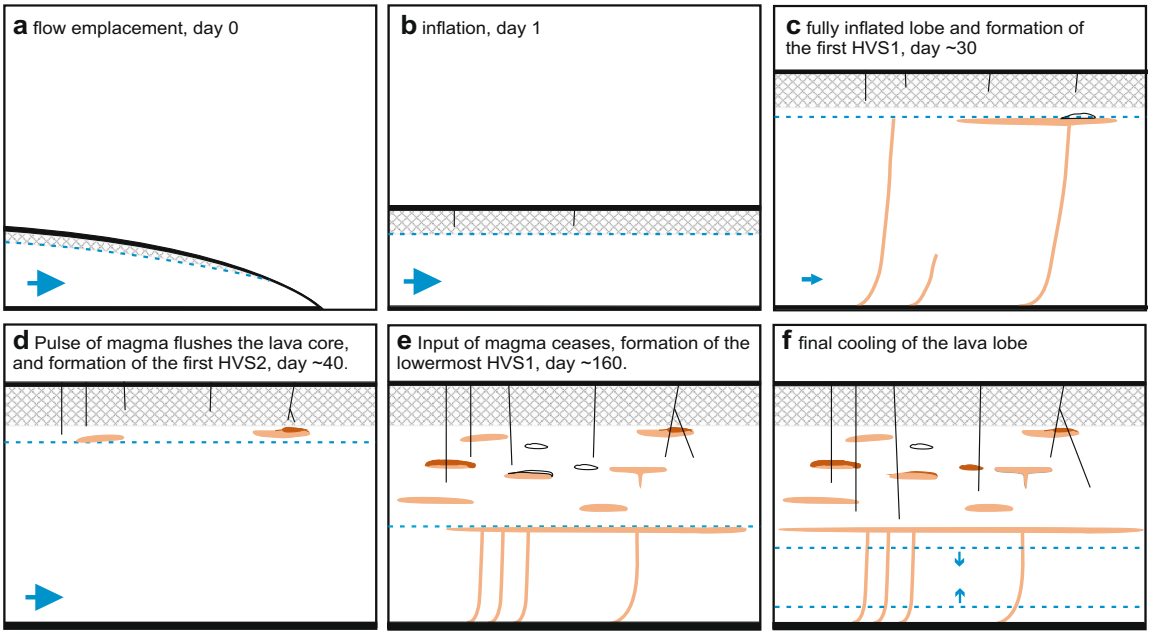

Fig. 8. Cartoon depicting the evolution of the Hafnarhraun pāhoehoe lobe from emplacement to solidification. Vesicular portion of the upper crust is marked in cross-hatching, basal zone in black, and segregation features in beige (VC and HVS1) and brown (HVS2). Megavesicles illustrated as hollow shapes in the upper crust. The blue arrow depicts the magma flow intensity and direction within the lava, and the blue stippled line marks the level of solidification front(s). Stages of development: **a** Emplacement of a lobe. **b** Lobe inflation. **c** As the input of new magma to the lobe is limited, crystallization commences near the base of the lobe and VC form. Some VC ascent to the base of the upper solidification front forming HVS1. **d** Pulse of new fresh magma to the lava lobe disturbs the formation of segregations and flushes the lava core; relicts of HVS1 segregations are preserved. Unrelated to this event, the first HVS2 is formed high in the upper crust, as highly evolved interstitial melts seep to a deflating gas pocket above HVS1. **e** After months of variable effusion rate in the lava lobe, fresh magma is no longer delivered to the system, and the lowermost extensive HVS1 is formed. **f** Final cooling and crystallization preserves VC in the lava core, and further HVS2 are formed in the upper crust

crystallizing core of the segregation features (Fig. 8d). The lowermost HVS1 remains extensive, as it forms during the final stage of lava cooling as the lava lobe becomes inactive (Fig. 8e). HVS2 form independently of VC, as vesicular residual melts seep to void spaces in the upper crust (Fig. 8d–f) in later stages of the lobe cooling. The two different mechanisms of HVS formation, now identified within a single lava flow, may explain some of the diverging observations of HVS development in earlier studies, compare, for example, Hartley and Thordarson (2009) and Kuritani et al. (2010).

Magma differentiation in crustal magma storage zones

Volatile-driven magma differentiation, at least partly analogous to segregation formation in Hafnarhraun, may take place in shallow crustal magma storage zones (e.g., chambers and sills) and has been evoked to explain silicic segregation lenses and sheets in intrusions (Carman 1994; White 2007; Zavala et al. 2011) and formation of crystal-poor FeTi-basalts (Sigmarsson et al. 2009). Andesitic to rhyolitic magmas are most likely to experience crystal–melt separation aided by volatiles due to their high volatile content and expansion during vapor exsolution (Sisson and Bacon 1999; Parmigiani et al. 2016), but also basaltic magma may be affected, at least during slow ascent in conduits and in intrusions at shallow crustal levels. Additionally, upper crustal magmas may feature vapor-aided convection (or "bubble-driven convection", cf. Cardoso and Woods 1999) that could occur in a similar manner to that observed within the Hafnarhraun lava lobe, i.e., driven by VC accommodated mass transfer from the bottom to the top of system. This vapor-aided mass movement could explain, in some cases, signs of convection in small and shallow intrusions that are not expected to undergo significant thermal convection.

We have demonstrated that the Hafnarhraun VC are not simple residual liquids of the host lava, generated by fractionation of equilibrium mineral phases, but residual liquids that have accumulated primitive olivine and plagioclase. Volcanic rocks with crystal cargoes of more primitive character than in equilibrium with the carrier melt are common (e.g., Davidson et al. 2007; Thomson and Maclennan 2013; Neave et al. 2015). Usually, these primitive crystals are thought to accumulate to evolved melts from disaggregated crystal mushes; however, in the Hafnarhraun lava lobe, VC accumulated primitive crystals from the nearly liquid portion of the lobe when VC-melts ascended through it. Although the accumulation of primitive phenocrysts to magmas often occurs in mid- to lower-crustal settings, and significant vapor is unlikely to be present at these pressures in most basaltic magmas, the Hafnarhraun VC are a novel example of crystal accumulation and basalt differentiation, applicable to at least shallow crustal settings.

Conclusions

Our work gives additional support to the concept of lava degassing as a significant differentiation mechanism in pāhoehoe lavas. We found that the Hafnarhraun VC are not simple segregated residual melts of the host lava, but rather formed in a two-stage process involving separation of vapor-saturated residual melt in the crystallizing base of the lava followed by accumulation of primitive crystals in the nearly liquid lava core. Furthermore, we suggest that the Hafnarhraun HVS formed by two different processes: (i) accumulation of VC-transported segregated material to the lower solidification front of the upper crust at the top of the lava core and (ii) later seepage of evolved and vapor-saturated melts into void spaces in the upper crust of the lava lobe. Overall, exsolution of volatiles promotes transfer of residual liquid from the bottom to the top of a crystallizing pāhoehoe lava core in thick, slow-cooling lobes. In shallow crustal levels, similar processes may drive mass transfer and crystal–melt separation in magmatic intrusions, potentially promoting crystal accumulation in segregated residual melts and leading to differentiated magma compositions not expected by fractionation of equilibrium mineral phases.

Acknowledgments The Nordic Volcanological Center funded this work 2015–2017. We thank Robert A. Askew and Leó Kristjánsson for the aid in sampling, Atli Hjartarson and Guðmundur H. Guðfinnsson for the help in sample preparation and microprobe analyses, and Richard J. Brown for the editorial handling. Comments from Kaisa Nikkilä, Scott Rowland, and anonymous reviewer significantly improved the manuscript.

Funding information Open access funding provided by University of Helsinki including Helsinki University Central Hospital.

References

Anderson AT, Swihart GH, Artioli G, Geiger CA (1984) Segregation vesicles, gas filter-pressing, and igneous differentiation. J Geol 92: 55–72. https://doi.org/10.1086/628834

Ariskin AA (1999) Phase equilibria modeling in igneous petrology: use of COMAGMAT model for simulating fractionation of ferro-basaltic magmas and the genesis of high-alumina basalt. J Volcanol Geotherm Res 90:115–162. https://doi.org/10.1016/S0377-0273(99)00022-0

Ariskin AA, Bychkov KA, Nikolaev GS, Barmina GS (2018) The COMAGMAT-5: modeling the effect of Fe-Ni sulfide immiscibility in crystallizing magmas and cumulates. J Petrol 59:283–298. https://doi.org/10.1093/petrology/egy026

Cardoso SSS, Woods AW (1999) On convection in a volatile-saturated magma. Earth Planet Sci Lett 168:301–310. https://doi.org/10.1016/S0012-821X(99)00057-6

Carman MF (1994) Mechanisms of differentiation in shallow mafic alkaline intrusions, as illustrated in the Big Bend area, western Texas. J Volcanol Geotherm Res 61:1–44. https://doi.org/10.1016/0377-0273(94)00008-5

Caroff M, Maury RC, Cotten J, Clement JP (2000) Segregation structures in vapor-differentiated basaltic flows. Bull Volcanol 62:171–187. https://doi.org/10.1007/s004450000077

Costa A, Blake S, Self S (2006) Segregation processes in vesiculating crystallizing magmas. J Volcanol Geotherm Res 153:287–300. https://doi.org/10.1016/j.jvolgeores.2005.12.006

Darwin CR (1844) Geological observations on the volcanic islands visited during the voyages of H.M.S. Beagle, with brief notices on the geology of Australia and the Cape of Good Hope, being the second part of the Voyage of the Beagle. Smith Elder & Co., London

Davidson JP, Morgan DJ, Charlier BLA et al (2007) Microsampling and isotopic analysis of igneous rocks: implications for the study of magmatic systems. Annu Rev Earth Planet Sci 35:273–311. https://doi.org/10.1146/annurev.earth.35.031306.140211

Eason DE, Sinton JM, Grönvold K, Kurz MD (2015) Effects of deglaciation on the petrology and eruptive history of the Western Volcanic Zone, Iceland. Bull Volcanol 77:47–27. https://doi.org/10.1007/s00445-015-0916-0

Fowler AC, Rust AC, Vynnycky M (2014) The formation of vesicular cylinders in pāhoehoe lava flows. Geophys Astrophys Fluid Dyn 109:1–23. https://doi.org/10.1080/03091929.2014.955799

Gibb FGF, Henderson CMB (1992) Convection and crystal settling in sills. Contrib Mineral Petrol 109:538–545. https://doi.org/10.1007/BF00306555

Gibb FGF, Henderson CMB (2006) Chemistry of the Shiant Isles Main Sill, NW Scotland, and wider implications for the petrogenesis of Mafic Sills. J Petrol 47:191–230. https://doi.org/10.1093/petrology/egi072

Goff F (1996) Vesicle cylinders in vapor-differentiated basalt flows. J Volcanol Geotherm Res 71:167–185. https://doi.org/10.1016/0377-0273(95)00073-9

Greenough JD, Lee CY, Fryer BJ (1999) Evidence for volatile-influenced differentiation in a layered alkali basalt flow, Penghu Islands, Taiwan. Bull Volcanol 60:412–424. https://doi.org/10.1007/s004450050241

Hamilton CW, Glaze LS, James MR, Baloga SM (2013) Topographic and stochastic influences on pāhoehoe lava lobe emplacement. Bull Volcanol 75:1–16. https://doi.org/10.1007/s00445-013-0756-8

Harris AJL, Rowland SK (2009) Effusion rate controls on lava flow length and the role of heat loss: a review. Spec Publ IAVCEI 33–51. https://doi.org/10.1144/IAVCEI002.3

Hartley ME, Thordarson T (2009) Melt segregations in a Columbia River Basalt lava flow: a possible mechanism for the formation of highly evolved mafic magmas. Lithos 112:434–446. https://doi.org/10.1016/j.lithos.2009.04.003

Hon K, Kauhikau J, Denlinger R, Mackay K (1994) Emplacement and inflation of pāhoehoe sheet flows: observations and measurements of active lava flows on Kilauea Volcano, Hawaii. Geol Soc Am Bull 106:351–370. https://doi.org/10.1130/0016-7606(1994)106<0351:EAIOPS>2.3.CO;2

Jónsson J (1978) Geology of Reykjanes. Orkustofnun Jarðhitadeild 7831, 303 pp., Reykjavík

Kress VC, Carmichael ISE (1991) The compressibility of silicate liquids containing Fe2O3 and the effect of composition, temperature, oxygen fugacity and pressure on their redox states. Contrib Mineral Petrol 108:82–92. https://doi.org/10.1007/BF00307328

Kuritani T, Yoshida T, Nagahashi Y (2010) Internal differentiation of Kutsugata lava flow from Rishiri Volcano, Japan: processes and timescales of segregation structures' formation. J Volcanol Geotherm Res 195:57–68. https://doi.org/10.1016/j.jvolgeores.2010.06.003

Manga M, Stone HA (1994) Interactions between bubbles in magmas and lavas: effects of bubble deformation. J Volcanol Geotherm Res. https://doi.org/10.1016/0377-0273(94)90079-5

Marsh BD (2002) On bimodal differentiation by solidification front instability in basaltic magmas, part 1: Basic mechanics. Geochim Cosmochim Acta 66:2211–2229. https://doi.org/10.1016/S0016-7037(02)00905-5

Martin E, Sigmarsson O (2007) Low-pressure differentiation of tholeiitic lavas as recorded in segregation veins from Reykjanes (Iceland), Lanzarote (Canary Islands) and Masaya (Nicaragua). Contrib Mineral Petrol 154:559–573. https://doi.org/10.1007/s00410-007-0209-5

Menand T (2011) Physical controls and depth of emplacement of igneous bodies: a review. Tectonophysics 500:11–19. https://doi.org/10.1016/j.tecto.2009.10.016

Neave DA, Maclennan J, Thordarson T, Hartley ME (2015) The evolution and storage of primitive melts in the Eastern Volcanic Zone of Iceland: the 10 ka Grímsvötn tephra series (i.e. the Saksunarvatn ash). Contrib Mineral Petrol 170:1–23. https://doi.org/10.1007/s00410-015-1170-3

Parmigiani A, Faroughi S, Huber C et al (2016) Bubble accumulation and its role in the evolution of magma reservoirs in the upper crust. Nature 532:492–495. https://doi.org/10.1038/nature17401

Pedersen GBM, Höskuldsson A, Dürig T et al (2017) Lava field evolution and emplacement dynamics of the 2014–2015 basaltic fissure eruption at Holuhraun, Iceland. J Volcanol Geotherm Res 340:155–169. https://doi.org/10.1016/j.jvolgeores.2017.02.027

Philpotts AR, Carroll M, Hill JM (1996) Crystal-mush compaction and the origin of pegmatitic segregation sheets in a thick flood-basalt flow in the Mesozoic Hartford Basin, Connecticut. J Petrol 37:811–836. https://doi.org/10.1093/petrology/37.4.811

Philpotts AR, Shi J, Brustman CM (1998) Role of plagioclase crystal chains in the differentiation of partly crystallized basaltic magma. Nature 395:343–346. https://doi.org/10.1038/26404

Pistone M, Arzilli F, Dobson KJ et al (2015) Gas-driven filter pressing in magmas: insights into in-situ melt segregation from crystal mushes. Geology 43:699–702. https://doi.org/10.1130/G36766.1

Rayleigh JWS (1896) Theoretical considerations respecting the separation of gases by diffusion and similar processes. Philos Mag 42:493–498

Rogan W, Blake S, Smith I (1996) In situ chemical fractionation in thin basaltic lava flows: examples from the Auckland volcanic field, New Zealand, and a general physical model. J Volcanol Geotherm Res 74:89–99. https://doi.org/10.1016/S0377-0273(96)00059-5

Rossi MJ (1997) Morphology of the 1984 open-channel lava flow at Krafla volcano, northern Iceland. Geomorphology 20:95–112. https://doi.org/10.1016/S0169-555X(97)00007-X

Saemundsson K, Jóhannesson H, Hjartarson Á et al (2010) Geological map of Southwest Iceland. Iceland Geosurvey 1:100000

Self S, Thordarson T, Keszthelyi L et al (1996) Inflated pāhoehoe lava flow fields. Am Geophys Union 23:2689–2692. https://doi.org/10.1029/96GL02450

Self S, Keszthelyi L, Thordarson T (1998) The importance of pāhoehoe. Annu Rev Earth Planet Sci 26:81–110. https://doi.org/10.1146/annurev.earth.26.1.81

Sigmarsson O, Thordarson T, Jakobsson SP (2009) Segregations in Surtsey lavas (Iceland) reveal extreme magma differentiation during late stage flow emplacement. Spec Publ IAVCEI 85–104. https://doi.org/10.1144/IAVCEI002.5

Sinton J, Grönvold K, Saemundsson K et al (2005) Postglacial eruptive history of the Western Volcanic Zone, Iceland. Geochem Geophys Geosyst 6:12. https://doi.org/10.1029/2005GC001021

Sisson TW, Bacon CR (1999) Gas-driven filter pressing in magmas. Geology 27:613–616. https://doi.org/10.1130/0091-7613(1999)027<0613:GDFPIM>2.3.CO

Sparks RSJ, Huppert HE, Turner JS et al (1984) The fluid dynamics of evolving magma chambers. Philos Trans R Soc Lond 310:511–534. https://doi.org/10.1098/rspa.1955.0102

Stephenson PJ, Zhang M, Spry M (2000) Fractionation modelling of segregations in the Toomba Basalt, north Queensland. Aust J Earth Sci 47:291–300. https://doi.org/10.1046/j.1440-0952.2000.00780.x

Thomson A, Maclennan J (2013) The distribution of olivine compositions in Icelandic basalts and picrites. J Petrol 54:745–768. https://doi.org/10.1093/petrology/egs083

Thordarson T, Höskuldsson A (2008) Postglacial volcanism in Iceland. Jökull 58:197–228

Thordarson T, Larsen G (2007) Volcanism in Iceland in historical time: volcano types, eruption styles and eruptive history. J Geodyn 43: 118–152. https://doi.org/10.1016/j.jog.2006.09.005

Thordarson T, Self S (1998) The Roza Member, Columbia River Basalt Group: a gigantic pāhoehoe lava flow field formed by endogenous processes? J Geophys Res 103:411–438. https://doi.org/10.1029/98JB01355

Walker GPL (1987) Pipe vesicles in Hawaiian basaltic lavas: their origin and potential as paleoslope indicators. Geology 15:84–87. https://doi.org/10.1130/0091-7613(1987)15<84:PVIHBL>2.0.CO;2

Walker GPL (1991) Structure, and origin by injection of lava under surface crust, of tumuli, "lava rises", "lava-rise pits", and "lava-inflation clefts" in Hawaii. Bull Volcanol 53:546–558. https://doi.org/10.1007/BF00298155

White CM (2007) The graveyard point intrusion: an example of extreme differentiation of snake river plain basalt in a shallow crustal pluton. J Petrol 48:303–325. https://doi.org/10.1093/petrology/egl062

Wilson M (1993) Magmatic differentiation. Geol Soc Lond Mem 16: 205–218. https://doi.org/10.1144/gsjgs.150.4.0611

Zavala K, Leitch AM, Fisher GW (2011) Silicic segregations of the Ferrar Dolerite sills, Antarctica. J Petrol 52:1927–1964. https://doi.org/10.1093/petrology/egr035

Basaltic magmas originate from melting of the Earth's mantle, evolve in transit through the Earth's crust and sometimes surface as orange-glowing lavas. Consequently, these lavas carry the imprint of their mantle source and the subsurface anatomy of their host volcanoes. In this thesis, I follow the evolutionary history of basaltic lavas in Iceland from mantle melting to lava emplacement by utilizing microanalyses of mineral phases, analyses of whole-rock samples and numerical modelling. I give special attention to compositions of primitive olivine macrocrysts, used as indicators of mantle melting conditions, and the Eyjafjallajökull volcanic system, for which I studied crystallization conditions of mineral phases in two primitive lavas. These investigations exposed a signature of deep melting of Earth's mantle below South Iceland and mid-crustal storage and crystallization conditions for the studied Eyjafjallajökull lavas.

Department of Geosciences and Geography A81
ISSN-L 1798-7911
ISSN 1798-7911 (print)
ISBN 978-951-51-4930-5 (paperback)
ISBN 978-951-51-4931-2 (PDF)
http://ethesis.helsinki.fi/

Painosalama
Turku 2020

UNIVERSITY OF HELSINKI
FACULTY OF SCIENCE

UNIVERSITY OF ICELAND